STELLAR OCCULTATION STUDIES OF SATURN'S UPPER ATMOSPHERE

by

Jeffrey Alan Foust

B.S., Geophysics, California Institute of Technology (1993)

Submitted in Partial Fulfillment of the Requirements for the Degree of

DOCTOR OF PHILOSOPHY

in

EARTH, ATMOSPHERIC AND PLANETARY SCIENCES

at the

MASSACHUSETTS INSTITUTE OF TECHNOLOGY

June, 1999

Author _____

Department of Earth, Atmospheric, and Planetary Sciences
April 30, 1999

Certified by _____

Professor James L. Elliot
Thesis Supervisor
Department of Earth, Atmospheric, and Planetary Sciences and
Department of Physics

Accepted by _____

Professor Ronald G. Prinn
Chairman, Department of Earth, Atmospheric, and Planetary Sciences

STELLAR OCCULTATION STUDIES OF SATURN'S UPPER ATMOSPHERE

by

Jeffrey Alan Foust

Submitted to the Department of Earth, Atmospheric and Planetary Sciences on April 30, 1999 in Partial Fulfillment of the Requirements for the Degree of Doctor of Philosophy

Abstract

The properties of Saturn's upper atmosphere are not well-known despite several spacecraft flybys. However, the region of 1-100 μbar can be studied in detail by observing stellar occultations — when the planet passes in front of a star — from groundbased or Earth-orbiting telescopes. We use data from five such occultations: three observed in 1995 by the Faint Object Spectrograph (FOS) on the Hubble Space Telescope (HST), one observed in 1996 at the NASA Infrared Telescope Facility (IRTF) and one in 1989 observed by a different instrument at the IRTF. The data span latitudes from 52° south to 75° north.

We fit isothermal models to each data set and also perform numerical inversions. These analyses show that temperatures in the 1-10 μbar range can vary significantly as a function of season and latitude, ranging from 121 to 160 K, in accordance with radiative transfer models for the atmosphere.

We also search for evidence of gravity wave saturation in Saturn's upper atmosphere, as seen in other planetary atmospheres, by analyzing the power spectra of temperature and density data and by studying the temperature lapse rate in the atmosphere. Our analysis is consistent with saturated gravity waves for all data sets, although gravity wave saturation is not the sole explanation for the spectra.

We take advantage of the wavelength-resolved HST FOS data to study the composition of Saturn's upper atmosphere. We measured the difference in feature times for data taken at two wavelengths, and use the different refractivities of hydrogen and helium, as a function of wavelength to compute the relative amounts of the two elements in the planet's atmosphere. We find that the helium mass fraction is 0.26 ± 0.10, higher than that found using Voyager data, but marginally consistent with theoretical models for the evolution of Saturn's atmosphere, although the large error bars on the results make a definitive conclusion problematic.

Thesis Supervisor: James L. Elliot
Title: Professor of Earth, Atmospheric, and Planetary Sciences and
Professor of Physics

Acknowledgments

I want to thank my advisor, Jim Elliot, for all his guidance during this long, arduous effort that, without him, would have been far longer and more arduous. He provided knowledge, advice, and, when needed, a sharp shove to keep me going. He also provided me the freedom to do my work my way, and make my own mistakes — the best, if most difficult, way to learn.

Other people at MIT also played a key role in this endeavor. Professors Rick Binzel, Tim Dowling, and Jack Wisdom, and Dr. Heidi Hammel, imparted knowledge and provided guidance in and out of the classroom. Fellow graduate students, including Mary Agner, Tom Burbine, Bobby Bus, Joe Harrington, Matt Holman, and Cathy Olkin, shared information and advice. Leslie Young played a similar role first as a graduate student here, and again later as a scientist at Boston University, particularly with the work on saturated gravity waves. Amanda Bosh, who was completing her Ph.D. as I arrived, became a key and valued collaborator (and source of data!) for this project.

There are others inside and outside of MIT who indirectly, and perhaps unknowingly, supported my research efforts, by keeping me balanced and stable, if nothing else. These people include Bruce Mackenzie, Larry Klaes, Roxanne Warniers, Elaine Mullen, and other members of the Boston chapter of the National Space Society; Chris Deards, Lisa Sopata, Wes Watters, Dan Feldkhun, and other members of the MIT chapter of Students for the Exploration and Development of Space; Sudha Jamthe of Web-Net; Dave Cravotta of Final Frontier magazine, Kelly Beatty and Joshua Roth of Sky and Telescope magazine, and Bill Pollock and Karol Jurado of no starch press, all of whom have helped contribute to a fledgling writing career. Without these people I might have finished this thesis somewhat sooner, but in considerably worse shape!

Finally and foremost, I want to thank my mother. Being the only child in a single parent family meant that the bond between mother and son was especially strong, and something I've valued even more as the years pass. She may have never understood what I was doing, but she has always supported me in this or whatever else I've chosen to do. Thank you, Mom.

Table of Contents

List of Figures

List of Tables

Chapter 1
Introduction

Despite flybys of Saturn by three robotic spacecraft (Pioneer 11 in 1979, Voyager 1 in 1980, and Voyager 2 in 1981) there are large gaps in our understanding of the structure of Saturn's atmosphere. Stellar occultations using the ultraviolet spectrometer (UVS) (Broadfoot *et al.* 1977) on the two Voyager spacecraft have probed the atmosphere above 0.01 microbars (μbar) (Festou and Atreya 1982) while infrared and radio science experiments on the spacecraft provided information on Saturn's atmosphere below 1000 μbar (Hanel *et al.* 1981, Tyler *et al.* 1982). The spacecraft data have left an "information gap" in Saturn's upper atmosphere between 0.01 and 1000 μbar (Figure 1.1) Moreover, temperatures measured above 0.01 μbar differ based on results from a solar occultation (Smith *et al.* 1983) and a stellar occultation (Festou and Atreya 1982) observed by the UVS.

The Cassini spacecraft mission to Saturn (Kerridge *et al.* 1992), launched in October 1997 and scheduled to arrive in July 2004, will be able to provide data to fill in this gap. The Composite Infrared Spectrometer (CIRS) will provide global temperature maps in the region of 0.3 microbars to 2 millibars, and the Ultraviolet Imaging Spectrograph (UVIS) and Radio Science Subsystem (RSS) will also examine the vertical temperature and composition profiles of the atmosphere. However, until Cassini arrives, one tool does exist to probe Saturn's atmosphere within this gap — stellar occultations. Using telescopes on the ground and in Earth orbit at infrared and visible wavelengths, one can probe Saturn's atmosphere in the range of 1 to up to 100 μbar, in the middle of the information gap.

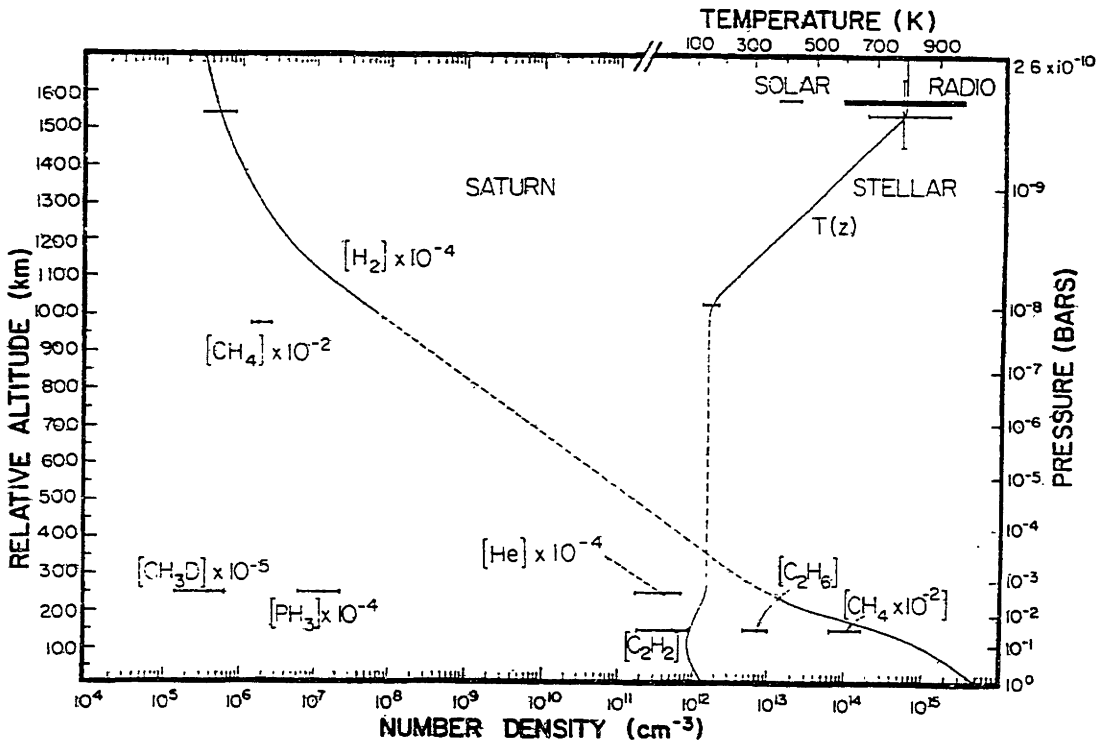

Figure 1.1: Plot of temperature, pressure, number density and altitude for Saturn's upper atmosphere. Note the dashed region between 10^{-3} and 10^{-8} bars, where no data are available. Also note the discrepancy at the top right area of the plot between the results of solar UVS occultation results and stellar UVS and radio science occultation results. From Atreya (1986).

Groundbased observations of stellar occultations by Saturn have provided some information within this gap. Published data from atmospheric observations has dealt with zonal winds in Saturn's stratosphere based on observations of a central flash during an occultation of the star 28 Sgr in 1989 (Nicholson *et al.* 1995). Hubbard *et al.* (1997) has provided the first analysis of Saturn's atmosphere from observations of the immersion and emersion of the star from Saturn's atmosphere, although these data are constrained to within 15° of Saturn's equator. Cooray *et al.* (1998) studied a 1995 occultation near Saturn's north pole. However, the region between these endpoints has yet to be studied in detail, and the use of current and previously-untried analysis techniques can help us better understand Saturn's upper atmosphere and may benefit those planning the science for the Cassini mission.

We choose to study Saturn's atmosphere by observing stellar occultations, when the planet passes in front of a star. Stellar occultations have been used to study the characteristics of a wide range of planets, moons, asteroids, and comets (Elliot 1979; Elliot and Olkin 1996). Their application to Saturn has been limited, as Saturn's bright disk and rings make it difficult to find stars bright enough not to be lost in the glare from Saturn, particularly at visible wavelengths. However, the advent of improved IR arrays and use of infrared wavelengths, where in selected regions the disk of Saturn is quite dark, makes stellar occultations a viable research method to obtain key data on Saturn's atmosphere.

Lightcurves recorded from stellar occultation observations can be used to obtain a wide range of data about the occulting planet. The time of the occultation itself, along with astrometry of the planet and star, can be used to find the radius of the planet at the latitude of the occultation. These can be combined to find a global figure of the atmosphere. Fitting the light curve produced from the occultation observations to an isothermal model gives a scale height for that region of the atmosphere (Baum and Code 1953). This scale height can, in turn, be used in conjunction with the location of the observation with respect to the center of the planet and the local gravity to determine the ratio of atmospheric temperature to mean molecular weight. If the atmosphere is not isothermal, one can fit the data to models that include a thermal gradient (Elliot and Young 1992) and use numerical inversion techniques (French *et al.* 1978) to compute profiles of temperature, pressure, and number density as a function of altitude in the atmosphere.

Spikes in the occultation light curves — sudden brief jumps in the signal from the star during the occultation — can also provide information on the planet's atmosphere. These spikes can be traced to local density variations in the atmosphere which may be

due either to isotropic turbulence (Jokipii and Hubbard 1977) or atmospheric waves (Elliot *et al.* 1977; French and Elliot 1979). An analysis of these variations can provide some understanding of the dynamics of the planet's upper atmosphere. In particular, the power spectrum of temperature and density variations can be calculated and compared to theoretical estimates for spectra from turbulence and saturated gravity waves as well as data from the Earth and, more recently, Jupiter (Young *et al.* 1997) and Titan (Sicardy *et al.* 1998).

Occultation observations of the same event at more than wavelength can also be used to understand the composition of the atmosphere. Saturn's two major atmospheric components are hydrogen and helium, which together make up 99.9% of the atmosphere. However, the helium abundance in Saturn's atmosphere is poorly determined: a helium mass fraction of 0.06 ± 0.05 was computed from Voyager spacecraft observations (Conrath *et al.* 1984). This fraction is significantly below theoretical predictions for Saturn's atmosphere (Stevenson 1980; Stevenson 1982), which require less helium depletion from cosmochemical abundances to account for the planet's excess heat flux. Occultations by Saturn's atmosphere observed at two different wavelengths can take advantage of the difference in refractivity between the wavelengths, which shows up in the data as a time difference in occultation lightcurve features between the two lightcurves. This difference in refractivity can be compared with the known refractivities of hydrogen and helium to find the relative fractions of both constituents in Saturn's atmosphere. Such a technique has previously been applied to Jupiter (Elliot *et al.* 1974).

Our approach is as follows. Chapter 2 discusses the various occultation data sets available to us, and the calibration techniques necessary to convert the data into a usable form. Chapter 3 details two common techniques used to analyze occultation data: isothermal model fits and numerical inversions, and discusses the results of the use of

these techniques on our data (including information about the shape of Saturn's upper atmosphere). Chapter 4 outlines the theory of power spectrum analysis on temperature and density profiles as a way of studying the dynamics of Saturn's upper atmosphere. Chapter 5 discusses the results from the power spectrum analysis technique. Chapter 6 goes over the theory of using occultation lightcurves obtained of the same event at different wavelengths to determine the abundances of hydrogen and helium in Saturn's upper atmosphere, and the results of this technique on spectrally-resolved occultation data. Chapter 7 outlines the results from these various techniques, places them into a greater context of the planet and comparisons to other planets, and provides suggestions for future research. Appendix A describes techniques used to remove background signal from occultation lightcurves obtained by the Faint Object Spectrograph on the Hubble Space Telescope. Appendix B describes the timing calibration performed on data obtained with the NSFCAM infrared camera at the NASA Infrared Telescope Facility. Appendix C discusses the astrometric reduction of that same data. Appendix D lists the *Mathematica*™ notebooks used for these analyses. Appendix E provides a glossary of terms used throughout this thesis.

Chapter 2
Saturn Occultation Data

Introduction

To perform the desired analyses we need to obtain new Saturn stellar-occultation data or reanalyze existing data. A list of stellar occultation candidates was compiled using the Hubble Space Telescope Guide Star Catalog (GSC) by Bosh and McDonald (1992), spanning the period 1991 through 1999. They collected a list of 203 potential occultations of stars by Saturn in this period. Most of these stars are marginal candidates for occultation observations due to any combination of their dimness, high sky-plane velocity (the velocity at which the planet is moving relative to the star as seen by the observer; a high velocity limits the integration time and hence signal-to-noise ratio of any observations), or likelihood to be missed by the planet entirely. However, a number of good candidates could be found on this list, and observations of occultations of two of them are described below, as well as an existing data set from the past occultation of 28 Sgr (Harrington *et al.* 1993).

GSC 5249-01240

Event Parameters

The occultation of GSC 5249-01240 (RA $23^h\ 19^m\ 34^s.66$, Dec $-6°\ 47'\ 9''.8$ in J2000) by Saturn merited special consideration by Bosh and McDonald (1992). The predicted occultation had the lowest sky-plane velocity of any of the 203 events, at 0.9 km/s, because Saturn was near the stationary point in its orbit as seen from Earth. The date of closest approach of Saturn to the star was 1214 UT on 1995 November 20, but Bosh and McDonald noted the occultation would stretch between November 20 and 22 because of the slow velocity of the event, 20 times slower than an occultation observed at

opposition. The star was also moderately bright (a magnitude of 12.3 at a mean wavelength similar to the Johnson *B* bandpass; Bosh and McDonald 1992), which permits shorter integration times.

Ground-based observations of this event were conducted, including observations at the NASA Infrared Telescope Facility (IRTF) at Mauna Kea, Hawaii (see Cooray *et al.* 1998 for a complete discussion of those observations and results). However, the Hubble Space Telescope (HST) provided a unique viewing opportunity: as the velocity of the event was less than the orbital velocity of the HST, the apparent path of the star was not a straight line but a series of loops caused by the parallax of the HST's orbit (see Fig. 2.1). These loops permitted the observation of multiple immersions and emersions over a wide range of latitudes from near Saturn's north pole to equatorial regions.

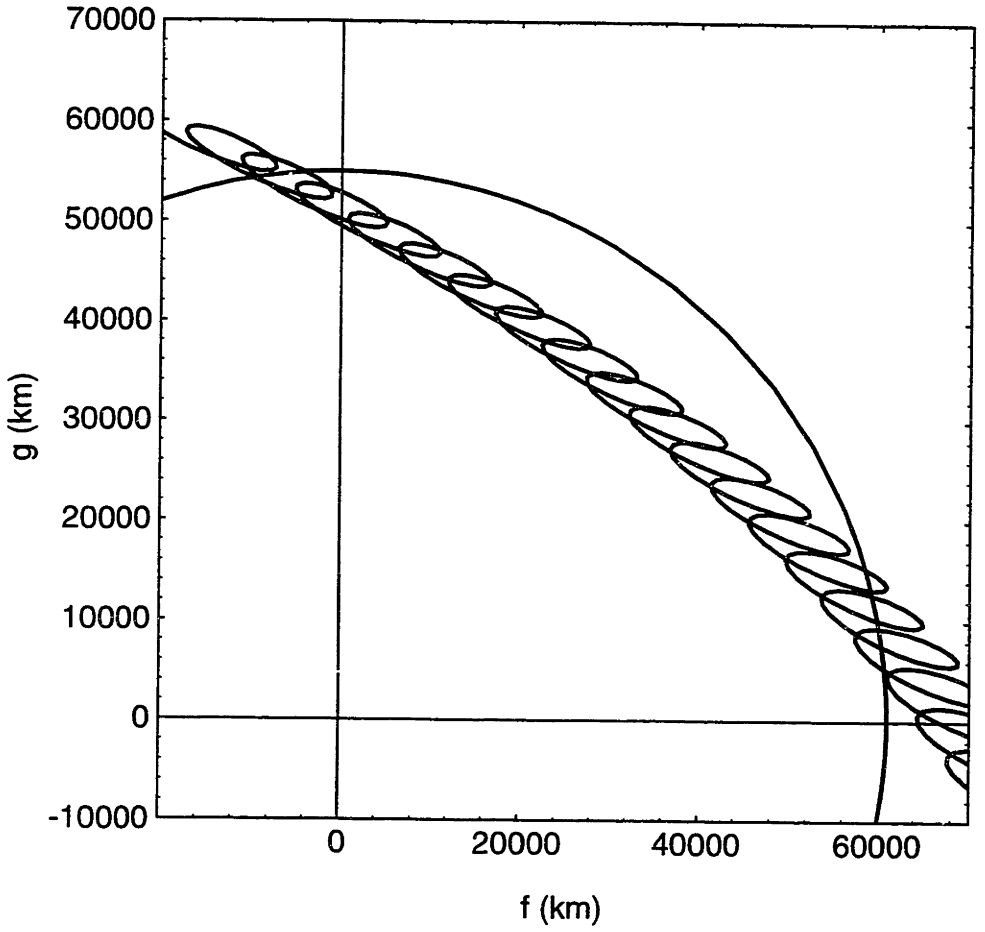

Figure 2.1: The path of GSC 5249-01240 relative to Saturn as seen from the Hubble Space Telescope. The parallax induced by HST's orbit created the looping path seen above. The figure of Saturn, accounting for its ellipticity, is plotted as well. The *f*-*g* coordinate system is used here: the origin of the system is the center of the planet and the *f* and *g* axes are parallel to right ascension and declination, respectively, with *f* increasing to the east. The immersion events were observed at high northern latitudes (upper left) and the emersion events took place at near-equatorial latitudes (lower right).

Data Collection

With the removal of the High Speed Photometer (HSP) during the December 1993 servicing mission, the HST lacked a dedicated instrument for high time resolution observations like occultations. However, the Faint Object Spectrograph (Kinney 1994) is capable of sufficiently high-speed observations in RAPID mode, and no other instrument on the telescope at the time was similarly capable. The FOS was removed during the second Hubble servicing mission in February 1997.

We (Amanda Bosh, PI) used the red digicon on FOS with the G400H disperser and a 0.86-arcsecond aperture. This provides data in the range of 3235-4781 Å with a resolution of 3 Å per diode. We used the FOS in RAPID mode at its fastest speed, with an integration time of 0.25 seconds and an overall cycle time (including dead time) of 0.26 seconds. For most analyses we would simply sum the signal over all diodes to get a single data point at each time, to get data that resembles what would be collected by a photometer. However, in Chapter 6 we discuss an important application of this wavelength-resolved data for determining the ratio of helium to hydrogen in Saturn's atmosphere.

Raw Data

Several attempts were made to observe immersions and emersions of the star using the FOS. Since the observations had to be planned in advance, and because of the limited time available to observe Saturn during each orbit, the times of immersion and emersion had to be estimated based on the planned HST ephemeris. Because of various errors, the occultations were not recorded on all data sets. Table 2.1 lists the nine FOS data sets (using a unique subset of HST's "IPPPSSOOT" root file names; Leitherer 1995) where occultation observations were attempted, and their results. Plots of the raw data, summed over all diodes, are presented in Figures 2.2-2.10.

Table 2.1: Summary of FOS Occultation Observations

Data Set	Start Time (UT)	Length (sec)	Guiding Mode*	Results
0201	1995-11-20 02:27:07	1054.4	FL	no occultation observed
0202	1995-11-20 02:48:35	1054.4	G	possible occultation observed but not reducible
0203	1995-11-20 03:58:38	1399.4	FL	immersion observed
0204	1995-11-20 05:35:08	1744.3	FL	immersion observed
0301	1995-11-20 23:19:21	514.6	FL	no occultation observed
0302	1995-11-20 23:31:53	1054.4	G	no occultation observed
0303	1995-11-21 01:04:14	1054.7	G	star exited aperture during emersion, not reducible
0304	1995-11-21 02:27:10	1054.4	FL	emersion started at end of data set, not reducible
0305	1995-11-21 04:03:42	1054.4	FL	emersion observed

***guiding modes:** FL: fine lock G: gyros

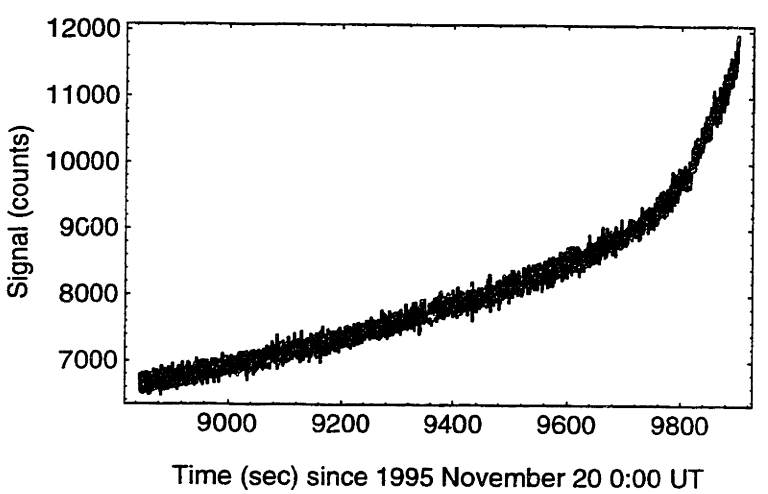

Figure 2.2: The raw, summed data for the 0201 data set

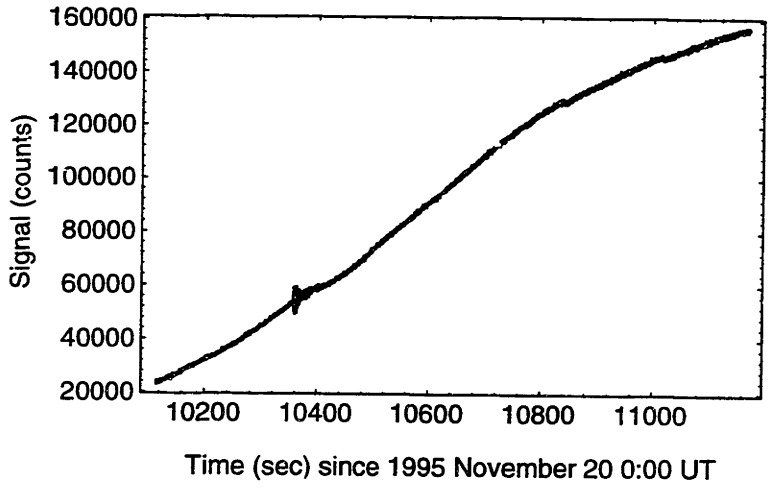

Figure 2.3: The raw, summed data for the 0202 data set

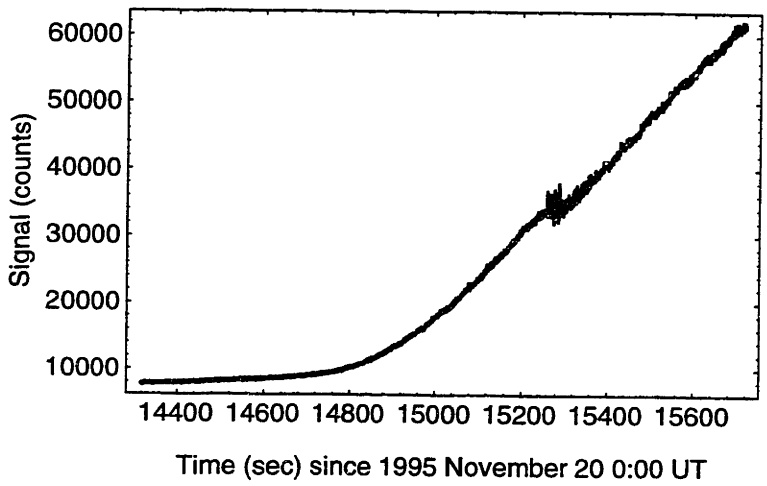

Figure 2.4: The raw, summed data for the 0203 data set. The immersion takes place at approximately 15,300 seconds.

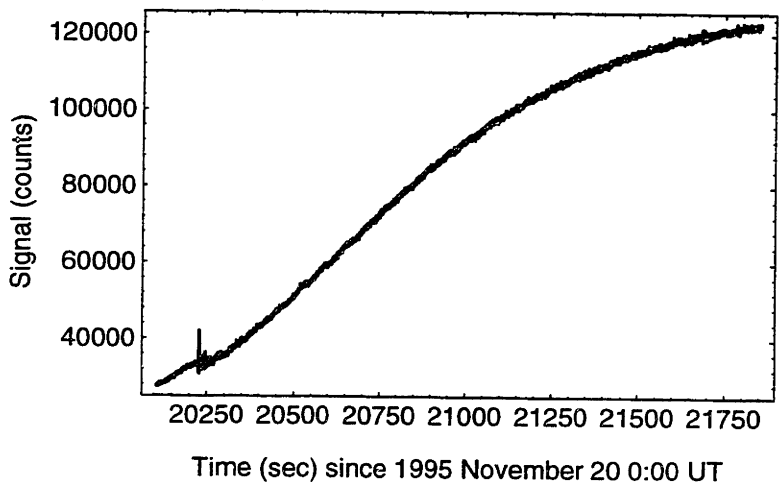

Figure 2.5: The raw, summed data for the 0204 data set. The immersion takes place at approximately 20,250 seconds.

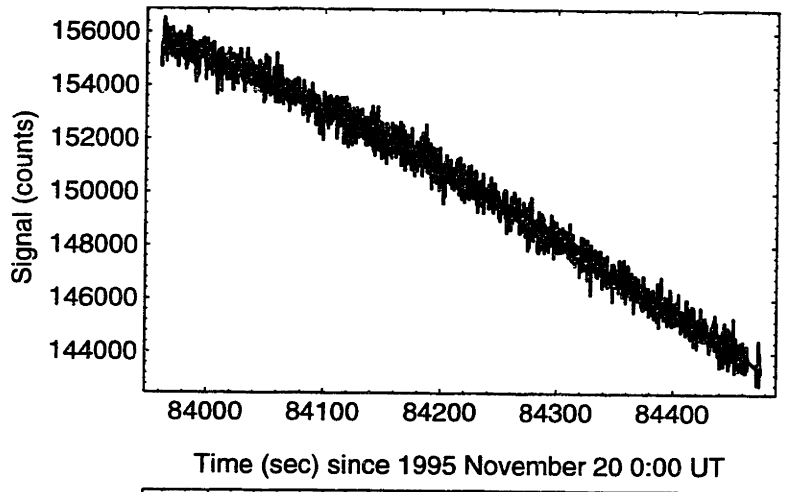

Figure 2.6: The raw, summed data for the 0301 data set. These data are plotted at a different scale than the other sets and hence appear noisier.

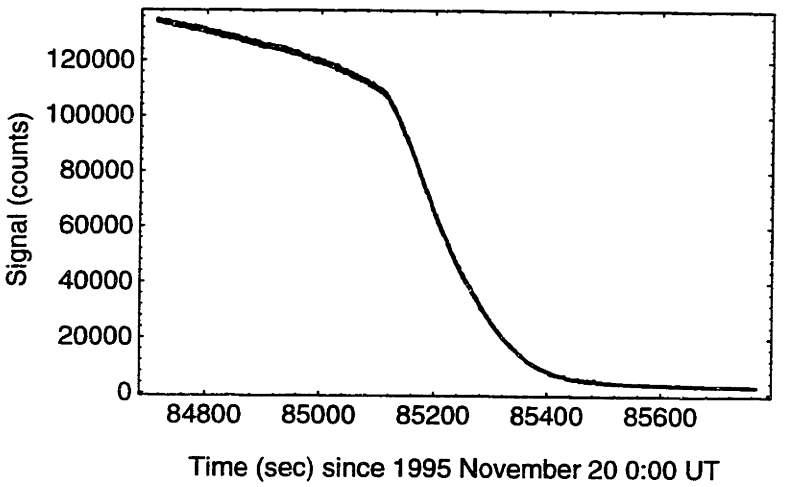

Figure 2.7: The raw, summed data for the 0302 data set

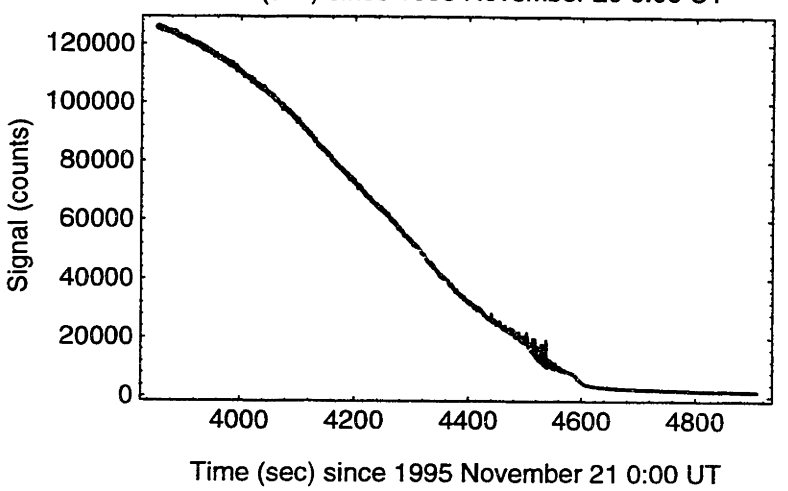

Figure 2.8: The raw, summed data for the 0303 data set

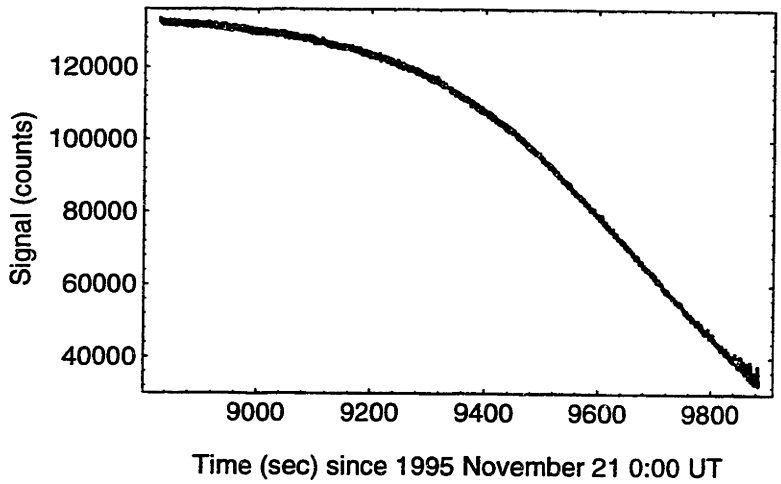

Figure 2.9: The raw, summed data for the 0304 data set

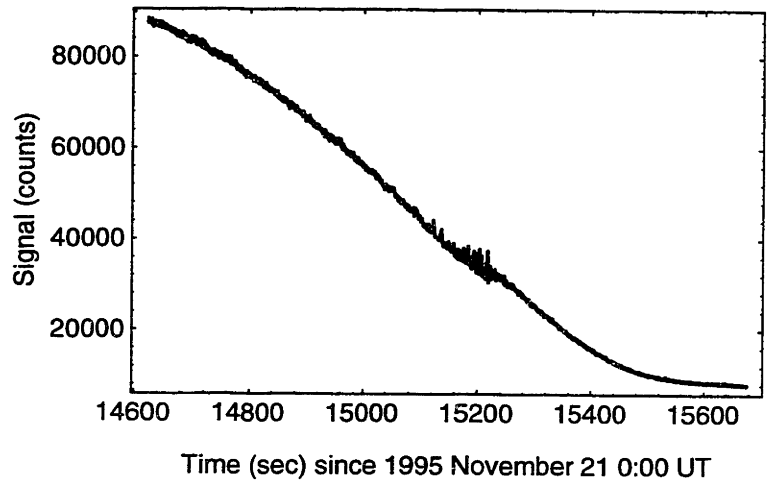

Figure 2.10: The raw, summed data for the 0305 data set. The emersion takes place at approximately 15,200 seconds.

Some of the data sets require comment. The 0202 data sets looks like an immersion was recorded, however, attempts to remove the background signal (as described in Appendix A) failed because of a nonlinearity in the background signal. The HST was using the less-precise gyros, rather than fine lock onto a guide star, for this data set, which may explain the variations. The 0303 data records an occultation, but immediately thereafter there is a sudden drop in the data. The size of the drop is consistent with the signal from the unocculted star, so we believe the star slipped out of the aperture of the FOS at that time. Since only a fraction of the potential signal may have been visible by the FOS at the time of emersion, and because that fraction may have been changing with time, we have chosen not to reduce that data set. As with the 0202 data set,

this was using gyros rather than a guide star lock. Finally, the 0304 data set appears to show the beginning of an emersion at the very end of the set. As the full emersion is not recorded, we have not analyzed that data set.

Calibration

These data were collected in a non-supported mode of the FOS, and as such the data were not processed through the standard analysis pipeline at the Space Telescope Science Institute. This required us to perform a complete reduction of the data before any analysis could begin.

The data included accurate timing from the FOS. Moreover, occultations of the rings by the star were recorded by the FOS after the atmospheric occultations. Timings of ring events permitted an accurate calculation of offsets to the star ephemeris to give accurate positions for all data sets. The distance in *f-g* coordinates (see Elliot *et al.* 1993 for a discussion of this coordinate system) between the star and Saturn was calculated using the DE130 ephemeris (A. Bosh, pers. comm.). Timing of the ring events allowed Bosh to calculate the offsets in the star position from the published values. Those offsets (in the sense of calculated – published values) were –0.071205 ± 0.000073 arcseconds in right ascension and 0.096860 ± 0.000010 arcseconds in declination, corresponding to offsets of 475.58 ± 0.49 km in *f* and –646.93 ± 0.07 km in *g* at Saturn's distance from the Earth.

As the raw data files show, background subtraction is a key issue, complicated by the fact that the HST tracked on the star and not on the planet, so that the amount of Saturn visible in the aperture (and thus the amount of light to be subtracted) varies with time. Techniques attempted and adopted to remove the background signal from these data sets are discussed in Appendix A. The final lightcurves are shown in Figures 2.11-2.13.

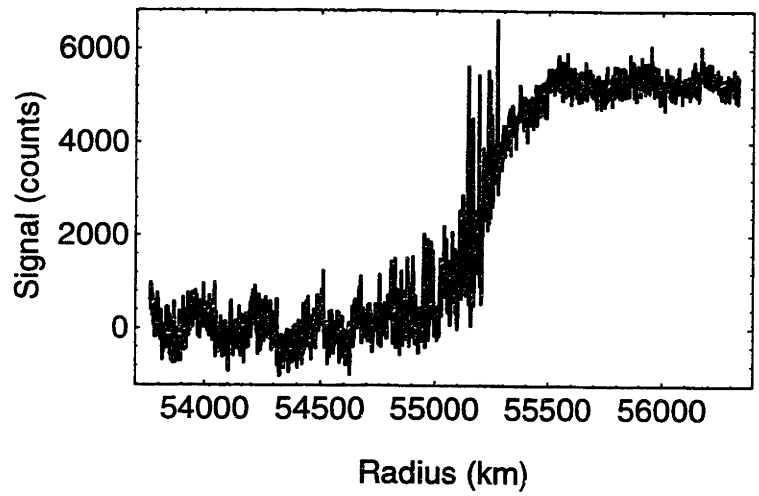

Figure 2.11: The background-subtracted and calibrated signal for the 0203 immersion.

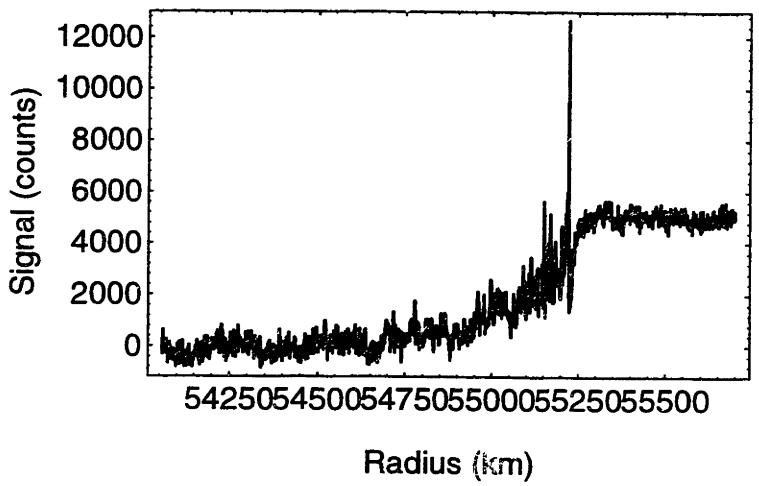

Figure 2.12: The background-subtracted and calibrated signal for the 0204 immersion. The single tall spike at about 55,250 km is caused by Saturn's atmosphere, as is the case with the other spikes.

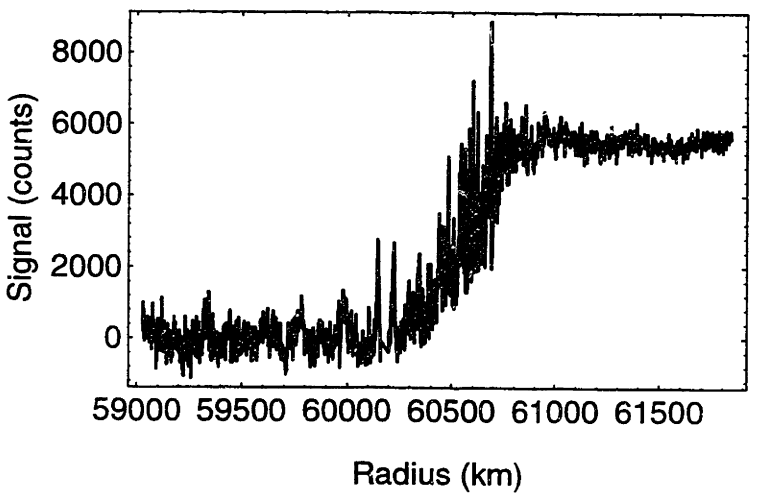

Figure 2.13: The background-subtracted and calibrated signal for the 0305 emersion.

The calibrated data sets, in particular the 0203 and 0204 immersions, show an unusual wave-like pattern. These waves are visible in both the pre- and post-event data, which is unusual: if this was a variation in the light from the star, then it should be visible only in the pre-immersion or post-emersion data. To study this in more detail, we performed a Fourier analysis of segments of pre- and post-event data for all three data sets to search for the period of the variations. The results are shown in Table 2.2.

Table 2.2: Period of Variations in FOS Data

Data Set	Segment	Dominant Period (sec)
0203	1-640 (pre-immersion)	55.4
0203	1100-2200 (post-immersion)	56.4
0204	1-350 (pre-immersion)	30.2
0204	800-1500 (post-immersion)	59.3
0305	1-1000 (pre-emersion)	—
0305	1400-2000 (post-emersion)	66.4

The 0203 data has essentially the same period before and after immersion. The 0204 data set has the same period of the 0203 data set after immersion, but a different value before the immersion. This difference may stem from the limited data set available for the pre-immersion data, which amounts to less than two periods at the frequency seen in the post-immersion data. The 0305 data has a slightly longer period after emersion, but there is no dominant period before the emersion: there are several frequencies visible in the data, and the Fourier data shows a local minimum, not a maximum, at the dominant frequency seen of the other data sets.

Because the variation exists in both the pre- and post-event data, and has the same period for at least the 0203 data, we do not believe that this is an effect of the star or the

occultation. A variation in the star light would not be visible in the post-immersion or pre-emersion data, when only signal from the planet is recorded. Nor should it be an effect of Saturn's atmosphere, as the same variation is seen in the pre-immersion and post-emersion data, when Saturn's atmosphere should have no effect on the star signal.

We conclude this is an effect of the FOS and/or the HST. Other Saturn occultations recorded from ground-based observatories (see Hubbard *et al.* 1997; Cooray *et al.* 1998; and the GSC 0010-00284 occultation discussed below) do not show wave effects in the pre- or post-event data. Cooray *et al.*'s observations were of the same occultation as seen here, at a latitude close to the latitude of the two immersion events. If the aperture of the instrument, or the telescope itself, were oscillating with a period of approximately 55-65 seconds, it would create an effect similar to what we see here: the oscillation would cause more and less of the disk of Saturn to be visible at a given time, increasing or reducing the flux recorded and generating the wave-like features seen here. For all three data sets the telescope was locked onto a guide star, so we do not get the drift we see with the gyros, but some longer-wavelength periodic motion may be possible.

GSC 0010-00284

Event Parameters

A second occultation observed was of the star GSC 0010-00284 (RA: $0^h\ 30^m\ 51^s.02$, Dec: 0° 39' 49".6 in J2000). The geocentric closest approach time of this event was at 1654 UT 1996 July 29. This event had a higher sky-plane velocity than the 1995 event, at 5.1 km/s, although this was still a much slower event than most of the other occultation candidates compiled by Bosh and McDonald (1992). Another advantage of this event was its small impact parameter of 1.04 arcseconds: this meant that the center of

Saturn's disk would pass close to the star during the occultation, raising the possibility of observing a central flash as the star passed through Saturn's evolute (Elliot *et al.* 1977).

Data Collection

We observed this event at the IRTF using the NSFCAM infrared camera (Shure *et al.* 1994; Leggett and Denault 1996). The observations were taken in MovieBurst mode, in which a series of images from a subframe of the IR InSb array is taken in stored in RAM, then written to disk as a single FITS (Wells *et al.* 1981) "image cube" file when the observation is completed. The NSFCAM computer can store up to 64 MB of data, providing a limit on the size of the subframes and the number of integrations possible. The immersion was recorded on a 4800-frame FITS image cube file in MovieBurst mode. We used 0.5-second integrations using a "Spencer" 2.3-μm filter (Leggett and Denault 1996). The observations started at 13:21:06 UT on 1998 July 29 and ended at 14:10:38 UT.

We also attempted to obtain simultaneous visible-light data with the Portable CCD (PCCD) camera (Buie *et al.* 1993) mounted on the optical port of the NSFCAM. Such a system had been used before for simultaneous visible-IR observations, but the field was strongly vignetted (see Appendix III of Olkin 1996 for a complete description.) We attempted to upgrade the optics system to permit a wider field of view for the PCCD during the occultation; however, when we mounted the instrument on the NSFCAM, we found that we could not put both the NSFCAM and PCCD into the same focus. We chose to collect data with only the NSFCAM and used the PCCD only to provide guiding images during the occultation observations.

We also made similar observations of the predicted central flash and emersion using a 2.122-μm filter. However, we recorded no central flash effects and the emersion, which took place during daylight, could not be detected.

Raw Data

A sample image from the MovieBurst file of the immersion is shown in Figure 2.14. For the immersion we used two frames: an 80 × 80 pixel frame that included the star and the relevant region of Saturn, and a 16 × 32 pixel frame centered on the moon Tethys. The latter was recorded as a possible standard for calibration, but not used. The two subframes are combined onto a single image, with a blank section added to pad the data into a rectangular form.

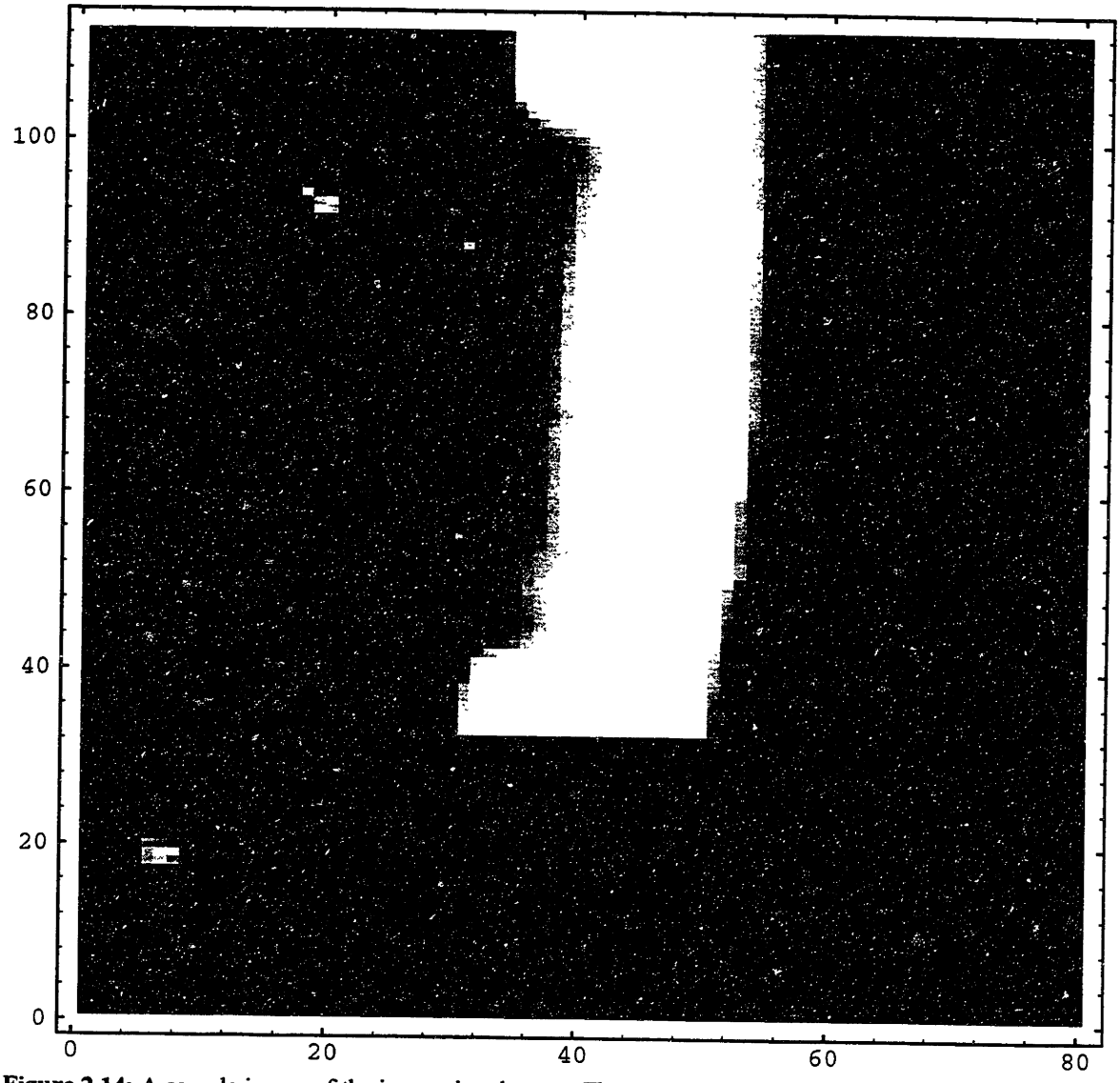

Figure 2.14: A sample image of the immersion data set. The upper portion of the image is an 80 × 80 pixel frame showing the star (upper left) and Saturn. The image is taken at a wavelength where the disk of Saturn is dark, so little of the disk can be seen. The rings form the bright vertical band seen in the middle of the image. The single bright pixel between the star and the rings is a "hot pixel", an instrument artifact. The section in the lower-left is a separate 16 × 32 sub-frame of Tethys, used as a standard for background calibration.

Calibration

We analyzed the frames from the immersion MovieBurst file to generate a lightcurve and simultaneously remove the background signal, rather than do the two in separate steps as with the HST FOS data. We performed a simple, but effective background subtraction. We used a 14 × 12 pixel box in a fixed location in each frame;

this box encompassed the location of the star for each frame. As Saturn's disk was dark at the wavelength used for the occultation, the star contributed all the signal above the background within the box. We summed the signal in the box. We also computed the median signal within the box: since the pixels that contain signal from the star make up only a minority of the total pixels in the box, the median value provides a measure of the background. This median value was multiplied by the number of pixels in the box and subtracted from the signal to provide the background-subtracted signal from the star.

In addition to background subtraction, we needed to calibrate the timing of the data as well as determine the offset from the star from its ephemeris position. Timing calibrations are discussed in detail in Appendix B while astrometry of the occultation is discussed in Appendix C.

The final calibrated lightcurve is shown in Figure 2.15. We note that there is a quadratic trend in the pre-immersion signal. This is likely caused by imperfections in the background-subtraction technique, perhaps because of a small but non-zero contribution by Saturn's disk. However, we do not believe this will impact the later analysis, as we trim much of the pre-immersion data before beginning any model fits or inversions.

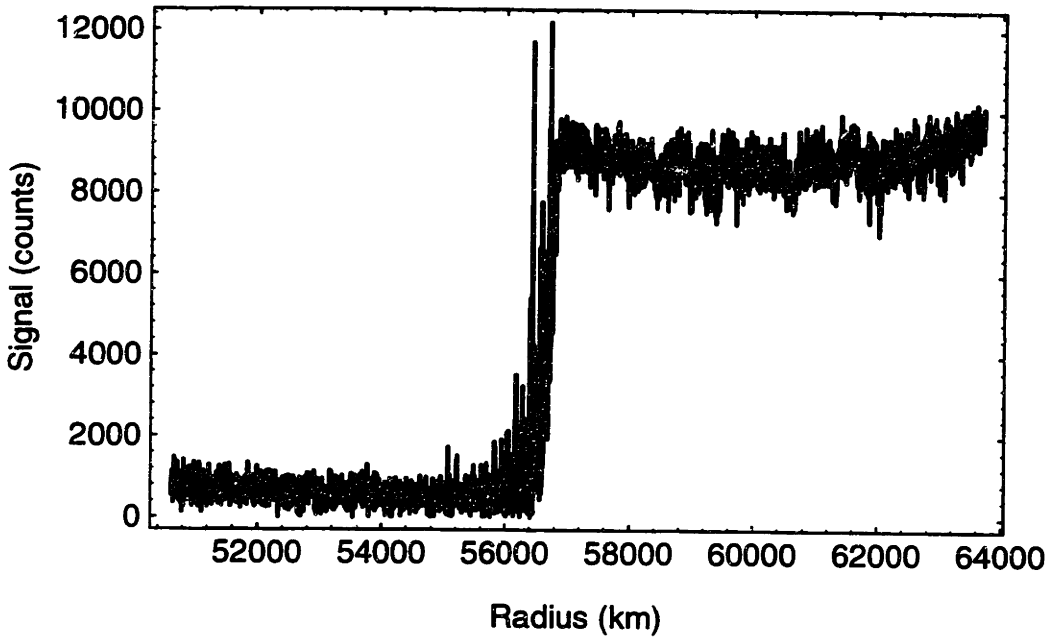

Figure 2.15: The calibrated IRTF 1996 light curve. The data have been background-subtracted, and the timing and astrometry have been calibrated using techniques discussed in Appendices B and C, respectively. The background does leave a residual quadratic curve in the pre-immersion data (between radii of 57,000 and 64,000 km), however, as discussed in the text this is not a major concern for later analysis.

28 Sgr

In addition to these data sets, we also had access to data from a Saturn occultation of the star 28 Sagittrarii (28 Sgr). This occultation was observed with the Rochester infrared camera at the IRTF on 1989 July 6 (Harrington *et al.* 1993). An analysis of this data set, emphasizing the ring segments, is provided by Harrington *et al.* (1993). This data set was also incorporated into the analyses of Hubbard *et al.* (1997), who performed model fits on a set of occultation lightcurves from this event.

The 28 Sgr data had already had the background planet signal removed, but no accurate distance scale in *f*-*g* coordinates. To compute this, we measured the difference between the known position (in right ascension and declination) of 28 Sgr versus the

ephemeris position of the planet for a given time, both in the J2000 epoch. We corrected these values by taking into account the known offset of the star from its measured position, as measured by Elliot *et al.* (1993); the offset of the IRTF from geocentric coordinates; and the offset of the Saturn barycenter from the planet center (Elliot *et al.* 1993). The results are displayed in Figure 2.16. Later analysis of the data set using model fits gave a half-light radius within a few kilometers of the value published by Hubbard *et al.* for these data, so we assume that this distance scale is accurate to within that value.

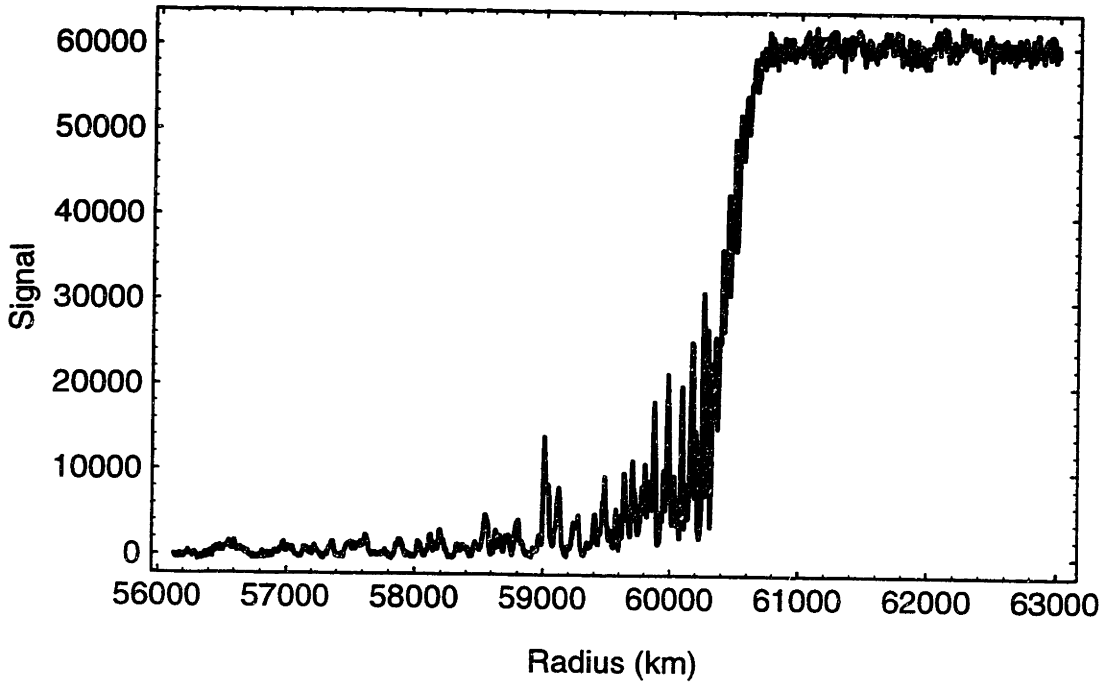

Figure 2.16: The background-subtracted data from the 28 Sgr occultation observed at the IRTF, after the distance scale was recalibrated as described in the text.

Chapter 3
Model Fits and Inversions of Occultation Data

Introduction

Analysis of stellar occultation data sets for atmospheres has traditionally involved the use of two techniques: model fits and inversions. Model fits, both isothermal and with a thermal gradient, can provide an average scale height and its gradient of the planetary atmosphere probed by the occultation near the half-light level, the point in the occultation at which the flux from the star is one-half of the unocculted value. Numerical inversions of occultation data, on the other hand, can provide profiles of refractivity, pressure, and other related parameters as a function of depth in the atmosphere.

Both techniques can prove useful in an effort to understand the structure of a planetary atmosphere. The radii of the half-light levels provided by the model fits can be used to establish the figure of the atmosphere on Saturn, as shaped by gravity, rotation, and high-speed equatorial winds (Hubbard *et al.* 1997). Inversions can be used to probe for changes in density, temperature, and pressure within the atmosphere, which can in turn be used to study dynamical atmospheric phenomena such as gravity wave propagation and saturation (see Chapters 4 and 5).

In this chapter we review the theory and technique of model fits and numerical inversions as used to analyze stellar occultation lightcurves. We also show the application of these techniques to the data and discuss the results of these analyses.

Model Fits

Model fits involve fitting a model for the flux of a star during a stellar occultation versus time or radius. The free parameters of the model that are fit to the data provide the radius of the half-light level and the refractivity scale height in that region, from which the temperature, pressure, and number density can be derived for an atmosphere of known composition in hydrostatic equilibrium.

Theory

The simplest form of a model fit, the isothermal model fit, was introduced by Baum and Code (1953) to fit the lightcurve from the occultation by Jupiter of σ Arietis. Baum and Code made a number of assumptions, including spherical symmetry, an isothermal, homogeneous atmosphere, and an atmospheric scale height much smaller than the radius of the planet to derive a relationship between the observed stellar flux ϕ (normalized to 1 for the unocculted star and 0 when the star is completely occulted) and the angle of refraction θ:

$$\phi = \left(1 - \frac{D\theta}{H}\right)^{-1} \tag{3.1}$$

where D is the distance between the observer and the occulting body and H is the refractivity scale height of the atmosphere.

This simple form, while a close approximation for large planets with isothermal upper atmospheres like Saturn, has been expanded for more general cases Elliot and Young (1992). They note that the flux detected by the observer will be a function of three effects: the differential bending of light rays, the absorption of light by the atmosphere,

and the partial focusing of light by the curvature of the planetary limb. They then derived the relationship:

$$\zeta(r) = \frac{r}{\rho(r)}\left|\frac{dr}{d\rho(r)}\right|\exp\left[-\tau_{obs}(r)\right] \tag{3.2}$$

where $\zeta(r)$ is the flux from the star, r is the distance from the center of the planet to the point of closest approach of a light ray, $\rho(r)$ is the point of arrival of that light ray in the observer's plane, and τ_{obs} is the optical depth along the path of the ray. For these studies Saturn's atmosphere has no relevant extinction, and τ_{obs} is set to zero and ignored. The amount of stellar flux measured by an observer at a radius ρ is the summation of $\zeta(r)$ for all values of r that arrive at ρ. Elliot and Young (1992) note that along the limbs of large planets, the only significant source of the flux would be from the limb nearest the star, so Eq. 3.2 can be rewritten as:

$$\phi(r) = \frac{r}{\rho(r)}\left|\frac{dr}{d\rho(r)}\right| \tag{3.3}$$

For the case where only near limb light is observed, Elliot and Young converted Eq. 3.3 into a function of D and θ:

$$\phi(r) = \frac{1}{(1 + D\theta(r)/r)(1 + Dd\theta(r)/dr)} \tag{3.4}$$

Application to Data

Each background-subtracted data set was analyzed with code developed for *Mathematica*™ (Wolfram 1991). For our model fits we chose to use an existing model function package, *olcNearLimb2*, that allowed one to fit an isothermal model to a data set

based on the equations of Elliot and Young (1992). (As the name suggests, other models take into account any flux from the star refracted by the planet to appear on the far limb, however, since Saturn's radius is much greater than the atmospheric scale height, only the near-limb flux was significant.) The *olcNearLimb2* model was designed to fit the stellar flux versus time, but we chose to use distance from the center of Saturn (in kilometers) as a more convenient scale.

The *olcNearLimb2* model includes up to 14 parameters that can be fit by least squares. However, several of these parameters involved atmospheric extinction, which is not relevant here and can be ignored. Several other parameters were fixed attributes of the data and thus also not included in the fit. To adapt the model to use radius rather than time as its x-coordinate, we set the velocity and time increment (Δt) parameters each to one. In the end we allowed four parameters to be adjusted by the fitting routine: the background and full signal values, the half-light radius r_H, and λ_{Hi}, the ratio of the half-light radius to the scale height.

We used a standard least squares fitting routine to fit the model to the data. Once the best fit was found, we could calculate several parameters from the data. The scale height H can be found by simply dividing the half-light radius by λ_{Hi}:

$$H = \frac{r_H}{\lambda_{Hi}} \tag{3.5}$$

From the definition of scale height, the temperature at the half-light radius in Saturn's atmosphere can be calculated from the gravitational acceleration g at the half-light radius, the mean molecular mass of the atmosphere μ (set to 2.135 for Saturn, from Lindal *et al.* 1985), and the gas constant R:

$$T_h = \frac{H\mu g}{R} \tag{3.6}$$

We note that the value of g above has to take into account both the contribution from gravity itself:

$$g_0 = \frac{GM}{r^2} \tag{3.7}$$

as well as, for rapidly-rotating bodies like Saturn, a centrifugal force that works against gravity. The centrifugal contribution will be a function of both the rotation rate ω and the latitude θ, and modifies g to be:

$$g = \sqrt{\left(g_0 - \omega^2 r\cos^2\theta\right)^2 + \left(\frac{\omega^2 r\sin 2\theta}{2}\right)^2} \tag{3.8}$$

The refractivity at half-light can be computed from the scale height, half-light radius, and the distance D between Saturn and the Earth:

$$\nu_h = \frac{H^{3/2}}{D\sqrt{2\pi r_H}} \tag{3.9}$$

The refractivity, in turn, can be used with the known refractivity at standard temperature and pressure (STP) and Loschmidt's number L to compute the number density of the atmosphere at the half-light radius:

$$n_h = \frac{L\nu_h}{\nu_{STP}} \tag{3.10}$$

The number density and temperature can then, with the Boltzmann constant k, be used to find the half-light pressure:

$$p_h = n_h k T_h \tag{3.11}$$

The half-light radius found by this method is not the actual half-light radius, but the apparent one. Saturn's mass bends light coming from the star, as determined by general relativity, while the atmosphere refracts the light further. Both of these effects can be removed. The *olcNearLimb2* model takes into account the effect of refraction on the half-light radius, but the contribution by general relativity must be computed separately.

From Hubbard *et al.* (1997), the relationship between the observed half-light radius r_H' and the actual half-light radius r_H is

$$r_H' = r_H - D(\theta + \varepsilon_G) \tag{3.12}$$

where D is the Earth-Saturn distance, θ is the angle of refraction caused by the occultation, and ε_G is the gravitational bending of light as predicted by general relativity. (Hubbard *et al.* 1993) provides a function for the gravitational bending:

$$\varepsilon_G = \frac{-4GM}{c^2 r_H} \tag{3.13}$$

where G is the gravitational constant, M is the mass of Saturn, and c is the speed of light. The value for θ comes from the original Baum-Code function for the stellar flux:

$$\phi = \left(1 - \frac{D\theta}{H}\right)^{-1} \tag{3.14}$$

At half light, $\phi = 1/2$, thus $D\theta/H = 1$ and $\theta = H/D$. With these values and the r_H computed from the model fit, we can find the actual half light radius.

To compare the half-light radii for different data sets, we need to convert them to their equivalent values for a standard latitude. Hubbard *et al.* suggest one method to convert the values of the corrected half-light radii into the equivalent equatorial half-light radii. This is done by setting the gravitational potential U, a function of radius and colatitude (90° – latitude) φ, at the location of the half-light level of each data set equal to the same potential at the equator ($\varphi = 90°$), and solving for the equivalent half-light radius a there:

$$U(r_H, \varphi) = U(a, 90°) \tag{3.15}$$

The gravitational potential U is the sum of two terms: a free-space gravitational potential V, defined using the radius, mass of Saturn, and the planet's zonal gravity harmonics, and a rotational potential Q. V is given by:

$$V = \frac{GM}{r}\left[1 - J_2(a_0/r)^2 P_2(\cos\varphi) - J_4(a_0/r)^4 P_4(\cos\varphi) - J_6(a_0/r)^6 P_6(\cos\varphi)\right] \tag{3.16}$$

where a_0 is a reference radius (set to the one-bar level, 60,268 km, from Lindal *et al.* (1985)), J_2, J_4, and J_6 are zonal gravity harmonics (Nicholson and Porco 1988; Campbell and Anderson 1989; Bosh 1994), and P_2, P_4, and P_6 are the corresponding Legendre polynomials.

Q, in turn, can be split into two components. One, Q_0, is a uniform-rotation term, defined as:

$$Q_0 = \frac{\ell^2 \omega_0^2}{2} \tag{3.17}$$

defining ω_0 as the rotation rate of Saturn independent of atmospheric motions (usually measured by the rotation of the planet's magnetic field) and ℓ is the cylindrical coordinate axis measuring distance from the axis of rotation. Added to Q_0 is a second term, ΔQ, that is dependent on the differential rotation rates of the planet, as derived from Voyager data as a function of ℓ(Nicholson *et al.* 1995). Hubbard *et al.* (1997) include an extrapolation of this relationship for regions around the equator, where ΔQ is poorly-known.

Results

The fit parameters (background and full signal level, uncorrected half-light radius, and energy ratio) are shown in Table 3.1. Derived quantities from these values – scale height, temperature, number density, and pressure – are listed in Table 3.2. Parameters used to derive the values in Table 3.2 from the model fit parameters are provided in Table 3.3. Plots of the fits and the data sets are shown in Figures 3.1-3.5.

Table 3.1: Model Fit Parameters

Data Set	Background	Full	r_H (km) (uncorrected)	λ_{Hi}
0203	–0.062 ± 0.004	0.991 ± 0.003	55256 ± 2	1245 ± 37
0204	–0.082 ± 0.006	1.011 ± 0.006	55206 ± 3	1096 ± 35
0305	–0.070 ± 0.005	1.001 ± 0.004	60619 ± 4	1054 ± 39
IRTF 1996	–0.001± 0.013	1.065 ± 0.010	56708 ± 5	1352 ± 100
28 Sgr	–0.009 ± 0.002	1.017 ± 0.002	60385 ± 2	1072 ± 24

Table 3.2: Derived Parameters from Model Fits at Half-Light

Data Set	Scale Height (km)	Temperature (K)	Number Density ($\times 10^{13}$ cm^{-3})	Pressure (μbar)
0203	44.4 ± 1.3	140.3 ± 4.2	7.52 ± 0.34	1.46 ± 0.08
0204	50.4 ± 1.6	159.6 ± 5.0	9.10 ± 0.43	2.00 ± 0.11
0305	57.5 ± 2.1	129.1 ± 4.7	10.59 ± 0.58	1.89 ± 0.13
IRTF 1996	42.0 ± 3.1	121.2 ± 9.1	7.00 ± 0.79	1.17 ± 0.16
28 Sgr	56.4 ± 1.3	129.0 ± 2.9	10.59 ± 0.36	1.88 ± 0.08

Table 3.3: Other Parameters Used to Derive Model Fit Values

Parameter	Value	Reference
ν_{STP}	1.30×10^{-4}	Chapter 6*
M	5.685×10^{26} kg	(USNO 1997)
μ	2.135 amu	(Lindal *et al.* 1985)
ω	1.6378×10^{-4} s^{-1}	(USNO 1997)
g (HST 0203)	12.31 m s^{-2}	Eqs. 3.7-3.8
g (HST 0204)	12.34 m s^{-2}	Eqs. 3.7-3.8
g (HST 0305)	8.75 m s^{-2}	Eqs. 3.7-3.8
g (IRTF 1996)	11.25 m s^{-2}	Eqs. 3.7-3.8
g (28 Sgr)	8.90 m s^{-2}	Eqs. 3.7-3.8

*based on refractivities of helium and hydrogen at 4000 Å, as shown in Chapter 6, using the helium number fraction derived in that chapter.

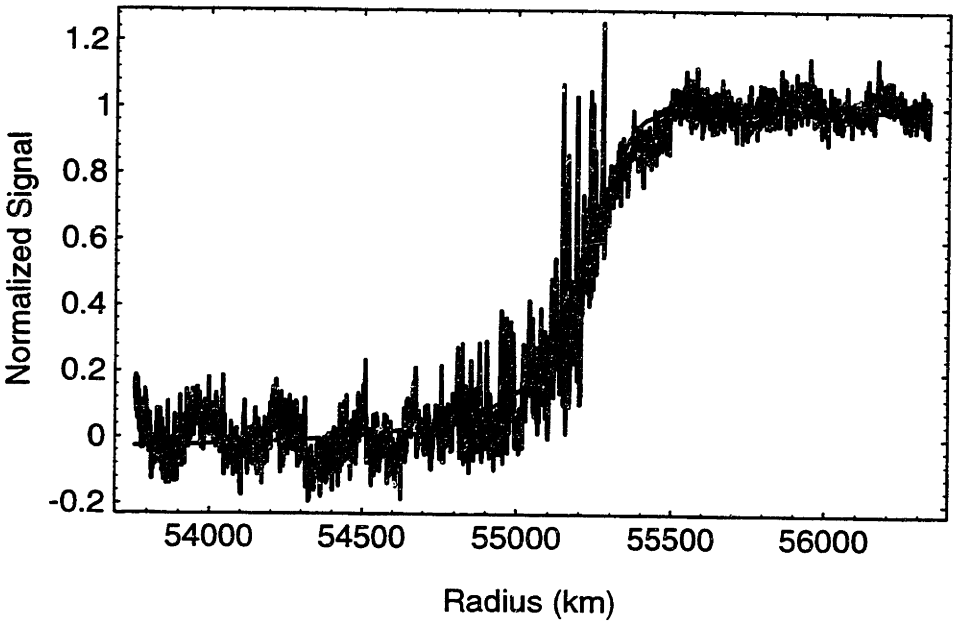

Figure 3.1: Model fit to the 0203 data set. The gray line is the best-fit model to the data (black line). The signal is normalized such that the full unocculted signal from the star is equal to 1.

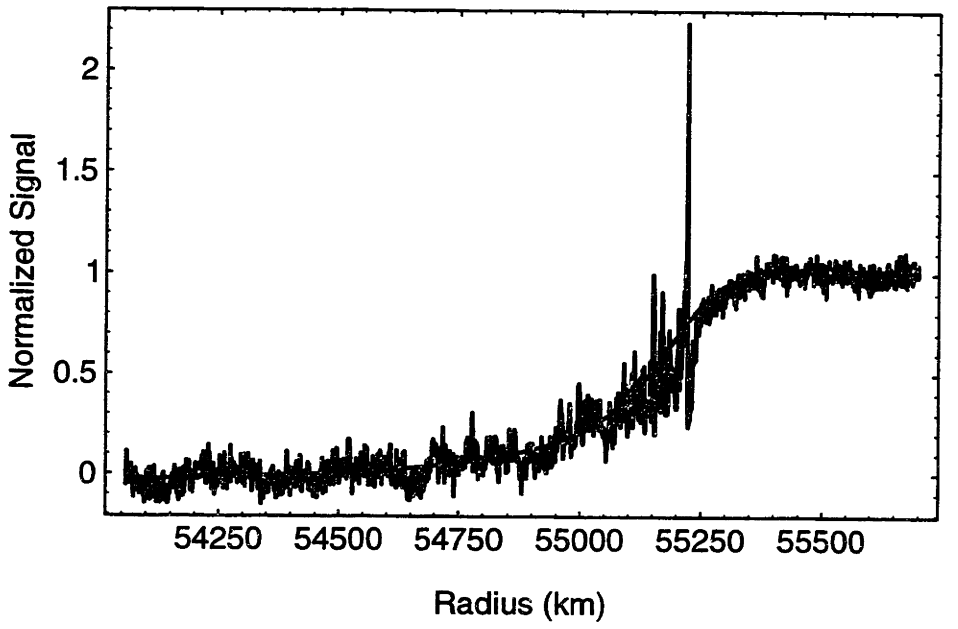

Figure 3.2: Model fit to the 0204 data set. The gray line is the best-fit model to the data (black line). The signal is normalized such that the full unocculted signal from the star is equal to 1.

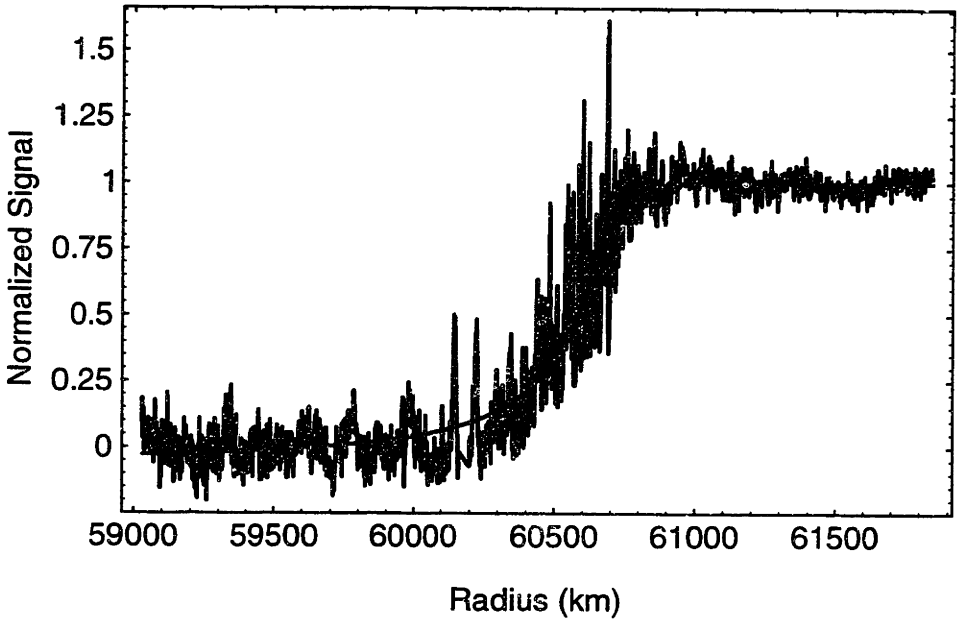

Figure 3.3: Model fit to the 0305 data set. The gray line is the best-fit model to the data (black line). The signal is normalized such that the full unocculted signal from the star is equal to 1.

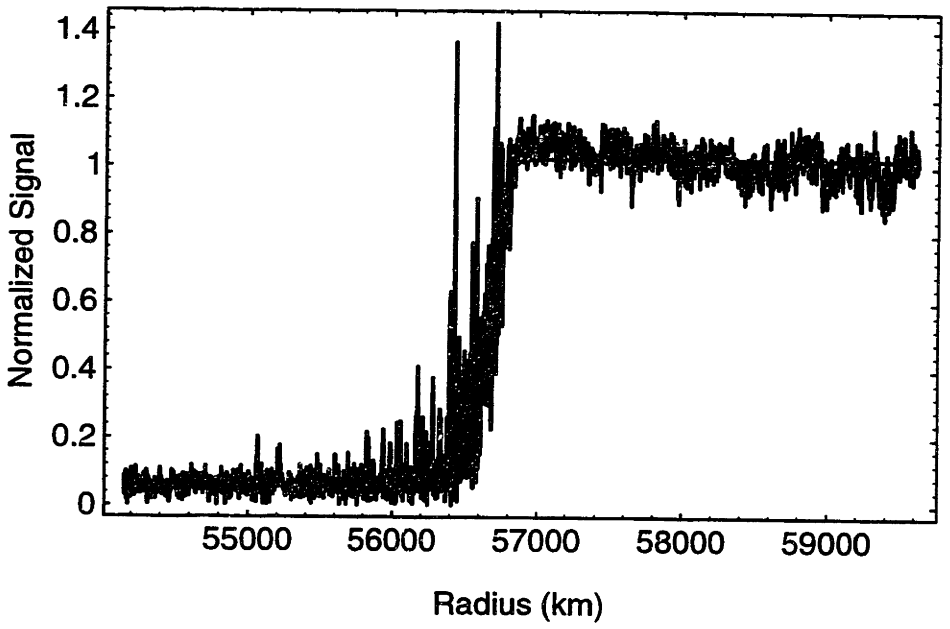

Figure 3.4: Model fit to the IRTF 1996 data set. The gray line is the best-fit model to the data (black line). The signal is normalized such that the full unocculted signal from the star is equal to 1.

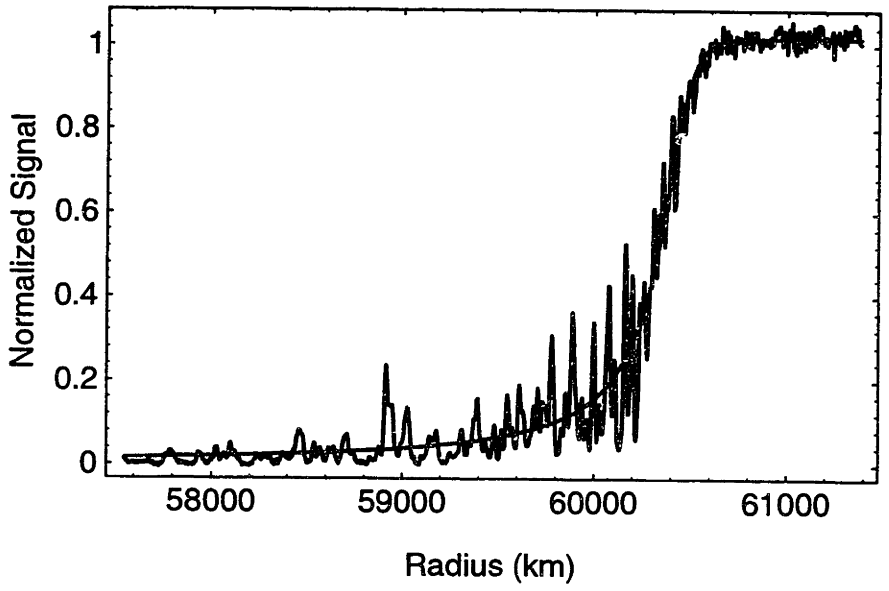

Figure 3.5: Model fit to the 28 Sgr data set. The gray line is the best-fit model to the data (black line). The signal is normalized such that the full unocculted signal from the star is equal to 1.

To check the dependence of the results on the size of the data set used, we removed data from the beginning and end of the HST data sets and reran the model fits. (We did not repeat this for the IRTF data set as we had already trimmed down the size the

data set to accommodate the slope in the pre-immersion data, as described below.) The results are shown in Table 3.4. The fitted parameters do vary as the size of the data sets decreases, although r_H in particular shows little dependence on the size of the data set. The greater variation and increase in errors in the 0204 data set is likely due to the proximity of the immersion to the beginning of the data set: the immersion begins only a few hundred data points into the data set. We thus could not cut even amounts from the beginning and end of the data set without cutting out the immersion itself, so we cut only a fixed amount from the beginning and more from the end. This still left a limited amount of pre-immersion baseline data for the model fit, which certainly contributes to the increasing variation and error in the background and full parameters of the fit.

Table 3.4: Model Fit Results for Different-Sized Data Sets

Data Set	Background	Full	r_H (km) (uncorrected)	λ_{Hi}
0203				
all	–0.061 ± 0.004	0.991 ± 0.003	55256 ± 2	1245 ± 37
cut first/last 100	–0.070 ± 0.004	0.991 ± 0.003	55255 ± 2	1203 ± 37
cut first/last 200	–0.074 ± 0.005	0.989 ± 0.004	55254 ± 3	1190 ± 38
cut first/last 300	–0.091 ± 0.005	0.989 ± 0.005	55252 ± 3	1120 ± 37
cut first/last 400	–0.088 ± 0.006	0.979 ± 0.005	55249 ± 3	1147 ± 42
0204				
all	–0.082 ± 0.006	1.011 ± 0.005	55206 ± 3	1096 ± 35
cut first/last 100	–0.073 ± 0.006	1.014 ± 0.007	55209 ± 3	1125 ± 40
cut first/last 200	–0.088 ± 0.008	1.036 ± 0.010	55212 ± 4	1056 ± 42
cut first 250/last 350	–0.082 ± 0.011	1.046 ± 0.015	55216 ± 4	1065 ± 53
cut first 250/last 500	–0.096 ± 0.017	1.052 ± 0.018	55215 ± 5	1021 ± 62
0305				
all	–0.070 ± 0.005	1.001 ± 0.004	60619 ± 4	1054 ± 39
cut first/last 100	–0.082 ± 0.006	1.000 ± 0.005	60616 ± 4	1016 ± 39
cut first/last 200	–0.082 ± 0.007	1.005 ± 0.005	60618 ± 4	1010 ± 41
cut first/last 300	–0.090 ± 0.008	1.008 ± 0.007	60617 ± 4	984 ± 43
cut first/last 400	–0.095 ± 0.009	1.016 ± 0.009	60619 ± 5	962 ± 47
28 Sgr				
all	–0.009 ± 0.002	1.017 ± 0.002	60385 ± 2	1072 ± 24
cut first/last 100	–0.008 ± 0.002	1.018 ± 0.002	60386 ± 3	1074 ± 27
cut first/last 200	–0.007 ± 0.003	1.016 ± 0.003	60385 ± 3	1084 ± 30
cut first/last 300	–0.007 ± 0.003	1.018 ± 0.004	60386 ± 3	1084 ± 35
cut first/last 400	–0.001 ± 0.004	1.009 ± 0.008	60384 ± 4	1121 ± 46

We note that the errors for the IRTF 1996 data shown in Tables 3.1 and 3.2 are somewhat higher than for the HST data. This is because we used a 650-point subset of 2000-point data set plotted in Figure 3.4, to alleviate the effects of the slope in the per-immersion lightcurve seen in the right half of the figure.

The differences in half-light radius are easily explained by the differences in latitude among the various events, from the two high-latitude immersions (0203 and 0204) to the near-equatorial events (0305 and 28 Sgr). The scale height for the 0305 event most closely matches the mean scale height from the 28 Sgr data sets, 62.3 ± 4.8 km (Hubbard *et al.* 1997), which were also near-equatorial events. The scale heights for the 0203 and IRTF 1996 events are similar to that found by Cooray *et al.* (1998), who observed the same stellar occultation using the ground-based IRTF telescope and found H = 42.8 ± 4.3 km. The 0204 event has a scale height intermediate of the two. This difference as a function of latitude likely stems from the definition of scale height:

$$H = \frac{RT}{\mu g} \tag{3.18}$$

Since R is a constant, and μ is unlikely to change as a function of latitude in a well-mixed atmosphere (see Chapter 6 for an extended discussion of the composition of Saturn's upper atmosphere), H will be dependent on changes in T and g. Because of centrifugal force and Saturn's oblate shape, the half-light surface at higher latitudes is significantly closer to the center of the planet than the equator, and thus have higher values of g, which lower the scale height. This general trend is seen in the data, where the high-latitude 0203 and 0204 events have lower scale heights than the near-equatorial 0305 data set.

The difference in temperatures is consistent with both the mean and range in temperatures from other events. While Hubbard *et al.* recorded a mean temperature of 141 ± 10 K from the 28 Sgr occultation, the temperatures determined from the various occultation data sets ranged from 125 to 158 K, with wide variations for data sets from different stations sampling nearly the same latitude. The error cited by Hubbard *et al.* is simply the standard deviation for the mean temperature from the data sets. Cooray *et al.* record a temperature of 130 ± 10 K from the GSC5429-01240 occultation, somewhat

larger than our IRTF data set. Of interest is the wide range between the 0203 and 0204 data sets, immersions that are less than one degree in latitude and approximately 95 minutes in time apart. This could be explained either by rapid changes and/or longitudinal variations in Saturn's upper atmosphere, or by problems in the reduction or analysis of one or both data sets. Possible problems in the analysis are discussed later in the chapter. In any event, it is difficult to determine any longitudinal or temporal trend in atmospheric variability with just two data points.

The difference in temperatures can also be interpreted as latitudinal, seasonal variations (Figure 3.6). Bezard and Gautier (1985) constructed a radiative seasonal model of Saturn's stratosphere at the 5 mbar level. Their model shows little change in equatorial temperature as a function of time, but does show wide swings of up to 30 K in the temperature of each pole over the course of a Saturnian year, caused by changes in insolation from Saturn's 26°.73 obliquity (USNO 1998). At the time of these occultations (1995 and 1996) the temperature difference between the north and south poles was 25-27 K, near the maximum, and the difference between the north pole and the equator was approximately 5-7 K. This latter difference is similar to the difference we see between the high northern latitude 0203 occultation and the near-equatorial 0305 occultation, but the comparison between the 0204 and 0305 data sets gives a larger difference. The absolute temperature scale is different between the model and data — the model gives an equatorial temperature of 130 K with polar temperatures ranging between 110 and 140 K — but the Bezard and Gautier model applies to the region near the top of the stratosphere, where temperatures are expected to be slightly lower than the mesospheric regions probed by the occultation data.

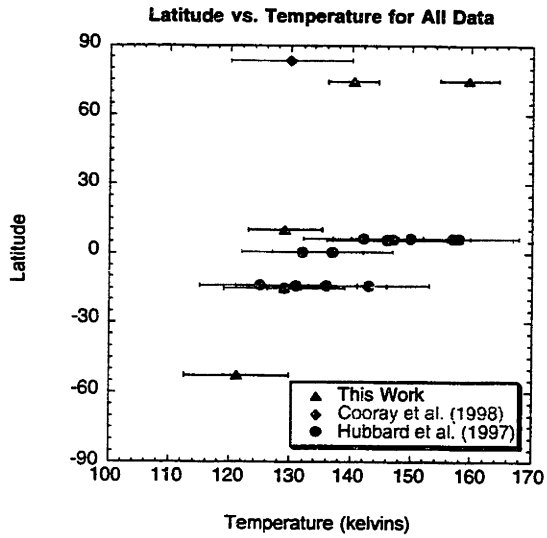

Figure 3.6: A combined plot of latitude versus temperature. This plot displays the half-light temperatures versus latitude for the data from this work (triangles), from Cooray *et al.* (1998) (diamonds), and from Hubbard *et al.* (1997) (circles).

The pressure from the 0203 data set is somewhat similar to the value of 1.61 ± 0.10 μbar found by Cooray *et al.* However, this value is smaller than those from the 0204, 0305, and 28 Sgr data sets and significantly smaller than that from Hubbard *et al.*, who found a mean pressure of 2.43 ± 0.08 μbar from all the 28 Sgr occultation events. The difference in temperature plays a key role in the comparison of the 0203 and the 0204 data sets, which one would otherwise expect to be similar.

The low half-light pressure for the IRTF 1996 data set is linked to the low temperature using Eq. 3.11. The low temperature may be the result of seasonal and latitudinal variations, as described above from the model of Bezard and Gautier (1985), although the differences between the IRTF 1996 temperature and the temperatures at the equator and the north polar regions are greater than those predicted from the Bezard and Gautier model. We will explore these temperature differences in more detail in the section on inversions.

We solve Eq. 3.15 for a for each data set, using the values of V and Q described above. The results are shown in Table 3.5. As expected, the 28 Sgr data closely matches the mean value of 60960 ± 9 km from Hubbard *et al.* However, the 0305 data set has a considerably lower value for a, while the IRTF value is also less than Hubbard *et al.* and that computed by Cooray *et al.*, who found $a = 60987$ from another, higher-latitude, occultation observed at the IRTF. The two immersion data sets, on the other hand, end up with much higher equivalent equatorial radii, even though they are of the same occultation observed by Cooray *et al.* Moreover, the two immersion events are not consistent with each other.

Table 3.5: Equivalent Equatorial Half-Light Radii

Data Set	r_H (km) (corrected)	Latitude (degrees)	a (km)
0203	55298 ± 2	74.12 ± 0.01	61033 ± 2
0204	55248 ± 3	74.68 ± 0.01	61000 ± 3
0305	60657 ± 4	10.19 ± 0.02	60913 ± 4
IRTF 1996	56749 ± 5	–52.73 ± 0.02	60919 ± 5
28 Sgr	60423 ± 2	–15.14 ± 0.01	60970 ± 2

Hubbard *et al.* synthesized a model for Saturn's atmosphere based on their occultation data as well as ultraviolet spectrometer and radio science occultation data collected by the Voyager spacecraft, which probed regions of Saturn's atmosphere above and below, respectively, the region probed by the stellar occultations. This "L+inv" model provides number densities, temperatures, and pressures for values of a between 60,490 and 61,500 km. We used the values of a in Table 6.2 to find temperature and

pressure from the model, and compared those model values to our actual results. The comparison is shown in Table 3.6.

Table 3.6: Comparison of "L+inv" Model Values to Actual Results

Data Set	*a* (km)	Temperature (K)		Pressure (μbar)	
		model	observed	model	observed
0203	61033 ± 2	133.6	140.3 ± 4.2	0.740	1.46 ± 0.08
0204	61000 ± 3	134.1	159.6 ± 5.0	1.279	2.00 ± 0.11
0305	60896 ± 4	138.4	129.1 ± 4.7	6.907	1.89 ± 0.13
IRTF 1996	60939 ± 5	140.1	121.2 ± 9.1	4.761	1.17 ± 0.16
28 Sgr	60970 ± 2	136.6	129.0 ± 2.9	2.098	1.88 ± 0.08

The table clearly shows that the results from the atmospheric model do not compare well to the results from the model fits on each individual data set. Only the 0203 temperature lies within 1 σ of the atmospheric model value, and some of the results, notably the 0305 and IRTF 1996 pressures, are far off from the atmospheric model results. This indicates that there may be problems with the data sets or the application to atmospheric model to these data, particularly the high-latitude events. We believe the latter explanation is more likely, since the data come from three distinct sources (FOS on HST, NSFCAM on IRTF, and Rochester camera on IRTF), and at a wide range of latitudes, yet all fail to reasonably fit the L+inv model. We therefore feel that the atmospheric model may not adequately describe conditions in Saturn's upper atmosphere outside of the equatorial zone.

This problem may be related to the quality of the data for ΔQ, derived from zonal wind profiles computed from Voyager data (Nicholson *et al.* 1995). Figure 3.7 shows the difference in the shape of the atmosphere when ΔQ is used versus when it is not. The

figure shows that while the values of ΔQ used here fit the data at low latitudes reasonably well, they fail to fit the data at higher latitudes. This suggests the wind profiles in these regions is incomplete or has changed since the Voyager flybys, and may explain why the values of a disagree with the Hubbard *et al.* result and their L+inv model.

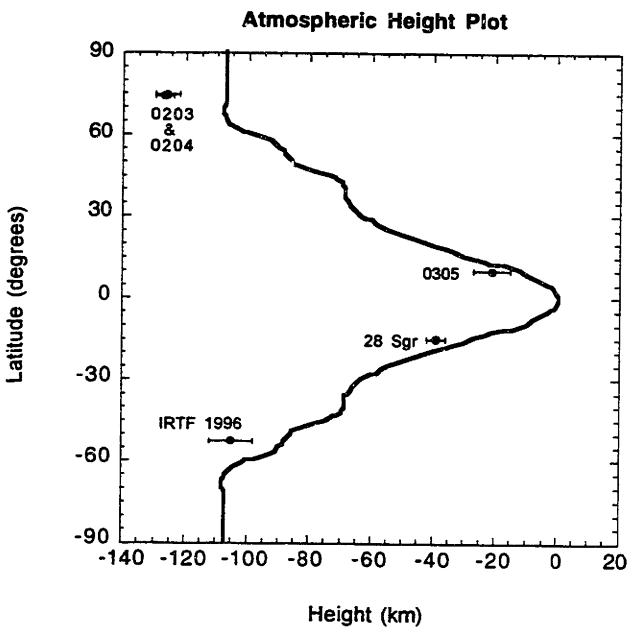

Figure 3.7: A plot of the effects of zonal winds on the "height" (equipotential displacement) of Saturn's atmosphere. The solid line shows the difference in a between the model with ΔQ and the one without as a function of latitude (the difference is represented as the model with ΔQ minus the one without.) The points show the same differences in a for each of the data sets. The figure demonstrates that the zonal wind profile fits the data well at low latitudes, but not at higher latitudes.

Inversions

Fits of occultation lightcurves using isothermal models can provide an average scale height of the atmosphere, but if the atmosphere is not isothermal, then one must use inversions to determine the non-isothermal characteristics of the atmosphere.

While previous research (Atreya 1986) suggested, albeit not conclusively, that Saturn's atmosphere is isothermal in the regime probed by the occultation data sets, isothermal model fits do not take into account sudden variations, or "spikes", in the data. These spikes are caused by small density variations that occur on scales of a few kilometers (Elliot *et al.* 1976), which may be due to turbulence or waves in the atmosphere; thus they contain information about the atmospheric structure. An analysis technique which can recover data about these spikes would be a useful tool in the effort to better understand Saturn's atmosphere at the microbar level.

Theory

Inversion techniques have been used in the study of planetary atmospheres for some time. The theory behind the technique has been described in a number of publications (Kovalevsky and Link 1969; Wasserman and Veverka 1973b; French *et al.* 1978), however, for completeness, the analysis method is described in some detail below.

We start with the Elliot and Young (1992) expression for the flux from an occultation, listed in Eq 3.2. The $\exp(-\tau_{obs}(r))$ accounts for extinction of the light as it passes through the occulting body's atmosphere with an optical depth $-\tau_{obs}(r)$; in this case we assume extinction is negligible and ignore it. If we replace the continuous derivative in Eq. 3.2 with the discrete values Δr and $\Delta\rho$, we can rewrite the equation as:

$$\zeta(r)\rho(r)\Delta\rho(r) = r\Delta r \tag{3.19}$$

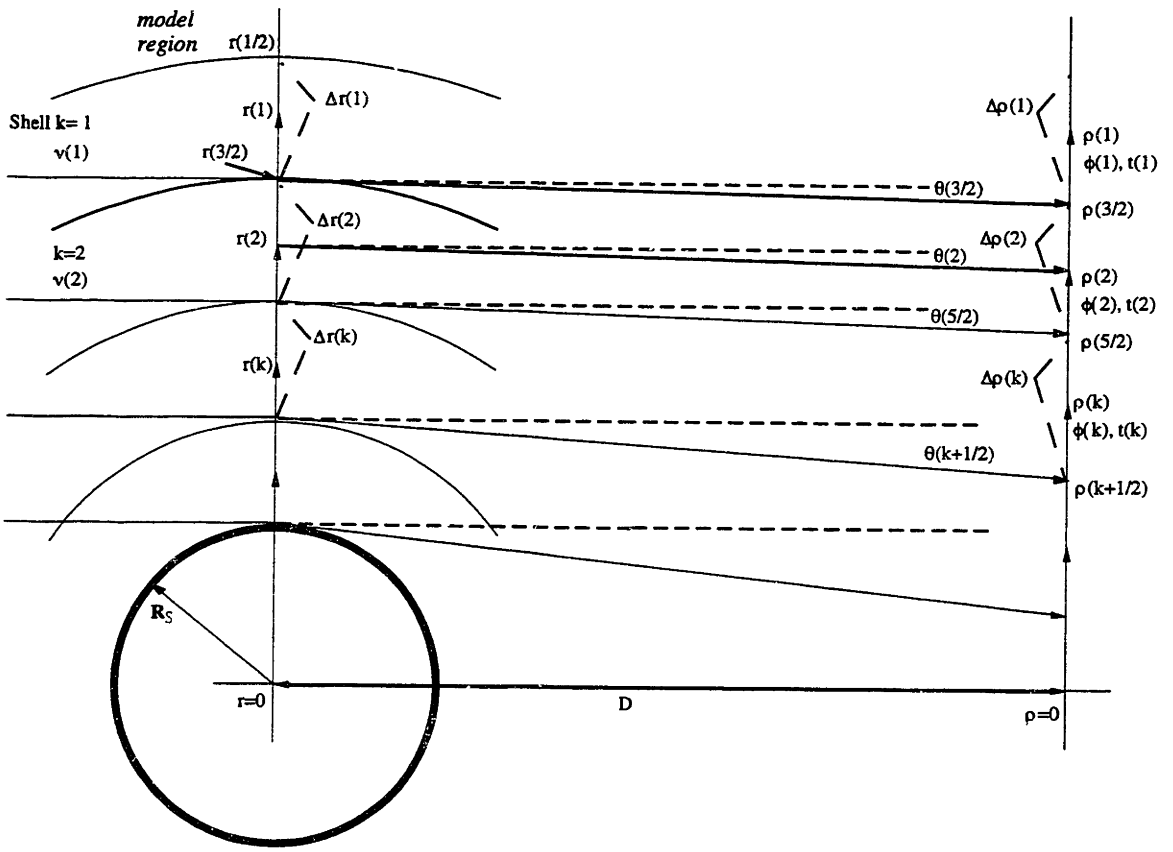

Figure 3.8: Inversion shell architecture. This illustration shows how an inversion of an occultation lightcurve is computed. The atmosphere of the occulting body (left) is divided into a number of shells. The radius r, refraction angle θ, and other quantities can be computed from the known radius in the observer plane ρ, time t, and stellar flux ϕ. From Olkin (1996).

We can use Eq. 3.19 to consider the atmosphere of an occulting body as a set of shells. We define r_1 as the radius of the middle of the first shell, r_2 as the radius of the middle of the second, r_k as the radius of the middle of the kth shell (Figure 3.8). We also define "half-indices" for the radii of the boundaries between the shells: $r_{3/2}$ would be the radius of the boundary between the first and second shell, and $r_{k+1/2}$ would be the radius of the boundary between the kth and k+1th shells. In this definition $r_{1/2}$ is considered as the top of the first shell. By adopting the shorthand notation $\zeta_k = \zeta(r_k)$ and $\rho_k = \rho(r_k)$ we can rewrite Eq. 3.16 as:

$$\zeta_k \rho_k \Delta\rho_k = r_k \Delta r_k \tag{3.20}$$

Eq. 3.20 can be used, with some algebra, to express the difference between the top and bottom of a given shell:

$$r_{k+1/2}^2 - r_{k-1/2}^2 = 2\zeta_k \rho_k \Delta\rho_k \tag{3.21}$$

This can, in turn, be used to find the radius of any boundary radius given we know the value of $r_{1/2}$, the top boundary of the first shell:

$$r_{k+1/2} = \sqrt{r_{1/2}^2 + 2\sum_{i=1}^{k} \zeta_i \rho_i \Delta\rho_i} \tag{3.22}$$

In addition to the radius, the refraction angle θ of a ray passing through the kth layer is given by (Olkin 1996):

$$\theta_{k+1/2} = \frac{\rho_{k+1/2} - r_{k+1/2}}{D} \tag{3.23}$$

where D is the distance between the planet and the observer, assuming θ is small.

Derivation of the function for refractivity as a function of r and θ has been done for large planet atmospheres (using the assumption that the scale height H was much smaller than the radius r) by Wasserman and Veverka (1973b). A refined version of this derivation, which removed the approximations that made the result inaccurate for small planet atmospheres, was reported in Olkin (1996). This updated version will be used in this analysis since it is valid for large-planet atmospheres as well.

Olkin finds the refractivity as a function of radius to be:

$$\nu(r_{k+1/2}) = -\frac{1}{\pi}\left[I_\nu(r_{1/2}, r_{k+1/2}) + \sum_{j=1/2}^{k} \cosh^{-1}\left(\frac{r_j}{r_{k+1/2}}\right)\Delta\theta_j \right] \tag{3.24}$$

where:

$$I_\nu(r_{1/2}, r_{k+1/2}) = \int_{\theta(r_{1/2})}^{0} \cosh^{-1}\left(\frac{r'}{r}\right) d\theta r' \tag{3.25}$$

In Eq. 3.24 the summation represents the contribution of the refractivity from the top of the first shell to the bottom of the *k*th shell. The integral in Eq. 3.25 represents the contribution to the refractivity from the region above the inversion.

The number density $n(r)$ can be found from Eq. 3.10, if we assume that the composition of the atmosphere does not vary in the range probed by the inversion. The pressure can be found using the equation of hydrostatic equilibrium (which requires us to assume that the atmosphere is in hydrostatic equilibrium in the region probed.) Using the number density (and hence refractivity) computed above the expression for the pressure becomes

$$p(r_{k+1/2}) = -\frac{L\mu m_{amu} G M_p}{\pi V_{STP} r_{k+1/2}} \left[I_p(r_{1/2}, r_{k+1/2}) + \sum_{j=1/2}^{k} \left[\cosh^{-1}\left(\frac{r_j}{r_{k+1/2}}\right) - \sqrt{1 - \left(\frac{r_{k+1/2}}{r_j}\right)^2} \right] \Delta\theta_j \right] \tag{3.26}$$

where

$$I_p(r_{1/2}, r_{k+1/2}) = \int_{\theta(r_{1/2})}^{0} \left[\cosh^{-1}\left(\frac{r'}{r}\right) - \sqrt{1 - \left(\frac{r}{r'}\right)^2} \right] d\theta(r') \tag{3.27}$$

Analogous to the expressions for the refractivity, the summation term in Eq. 3.26 is the contribution to the pressure from the top of the first shell to the bottom of the *k*th shell, while the term in Eq. 3.27 provides the contribution to the pressure above the top shell.

Two other quantities, the temperature and the scale height of the atmosphere, can be derived from the inversion. The temperature can be found directly from the perfect gas law:

$$T(r) = \frac{p(r)}{k_B n(r)} \tag{3.28}$$

where k_B is Boltzmann's constant. The scale height $H(r)$ can be computed from its definition:

$$H(r) = \frac{RT(r)}{\mu g(r)} = -\frac{r}{\pi \nu(r)}\left(I_p(r_{1/2}, r_{k+1/2}) + \sum_{j=1/2}^{k}\left[\cosh^{-1}\left(\frac{r_j}{r_{k+1/2}}\right) - \sqrt{1-\left(\frac{r_{k+1/2}}{r_j}\right)^2}\right]\Delta\theta_j \right) \tag{3.29}$$

where R is the ideal gas constant and μ is the mean molecular mass and $g(r)$ is calculated using Eqns. 3.7 and 3.8.

Results

We applied the inversion equations described above to the occultation data with a series of *Mathematica*™ notebooks. The equations described in the previous section were implemented as functions in two existing *Mathematica*™ packages, *occInversions* and

occInversions2, and used in the analysis. The initial conditions for the inversion come from the model fits discussed earlier in this chapter. Because inversions can be highly sensitive to the initial conditions provided, we started our inversions at a number of points corresponding to flux levels in the light curve ranging from $\phi = 0.5$ to 0.9. We established the initial conditions by performing an isothermal model fit to the data down to the specified flux level, as discussed by French *et al.* (1978). Figures 3.9-3.13 show the pressure-vs.-temperature profiles for all four data sets.

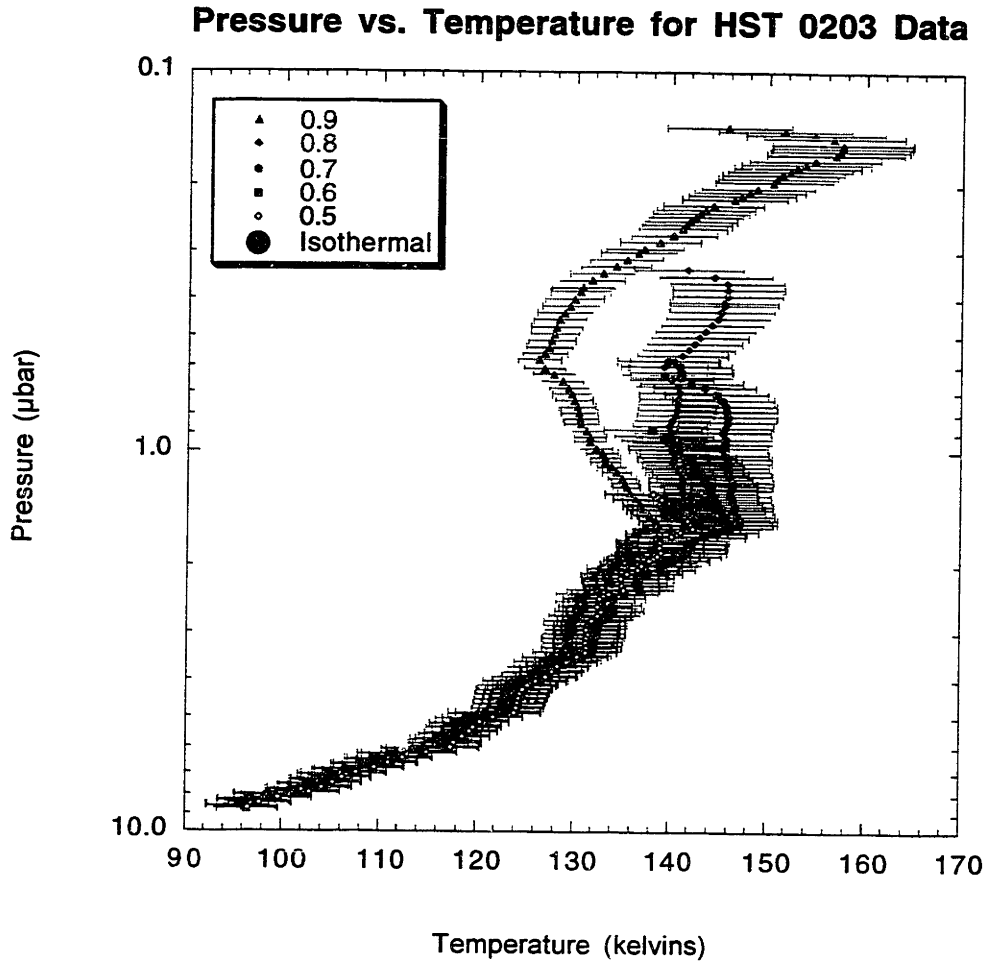

Figure 3.9: Pressure versus temperature inversion profile for the HST 0203 data set (latitude +74.1°). The various curves represent the inversion results based on initial conditions at various points in the occultation light curve, from $\phi = 0.5$ to 0.9. The single large circle is the temperature from the isothermal model fit to the data from Table 3.2

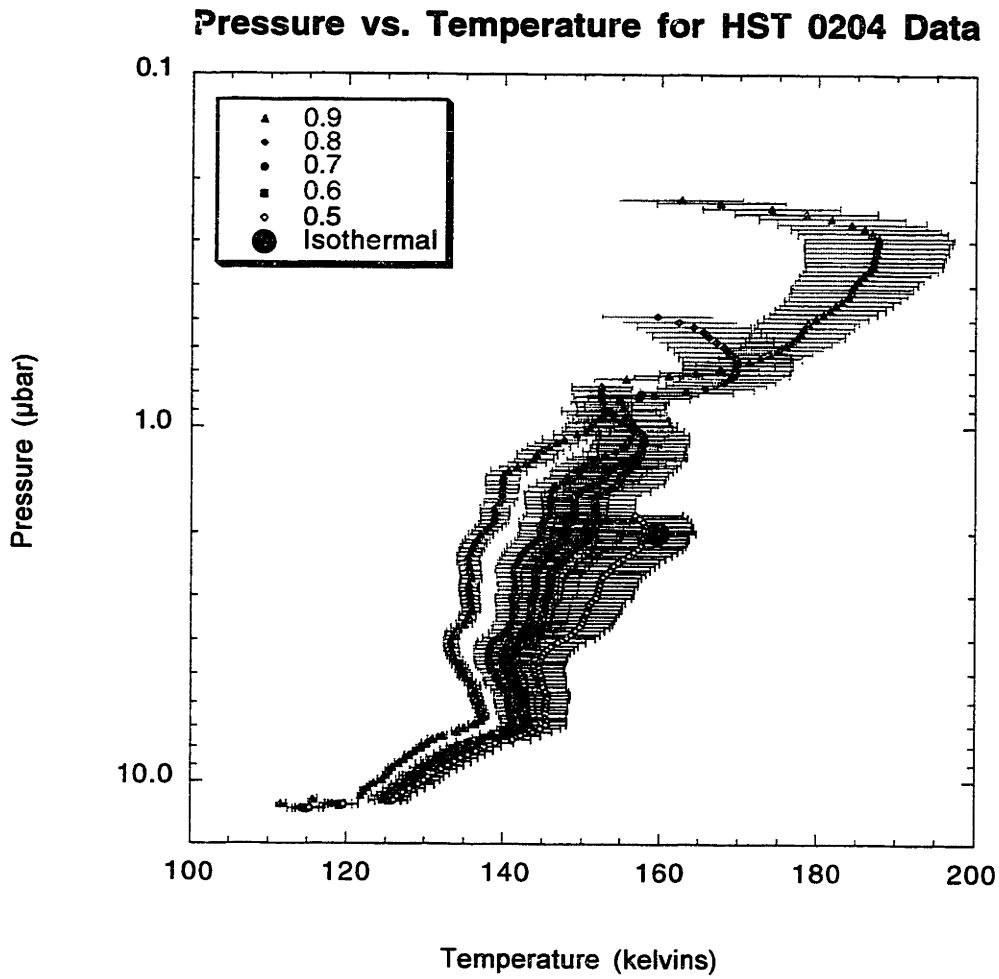

Figure 3.10: Pressure versus temperature inversion profile for the HST 0204 data set (latitude +74.7°). The various curves represent the inversion results based on initial conditions at various points in the occultation light curve, from $\phi = 0.5$ to 0.9. The single large circle is the temperature from the isothermal model fit to the data from Table 3.2

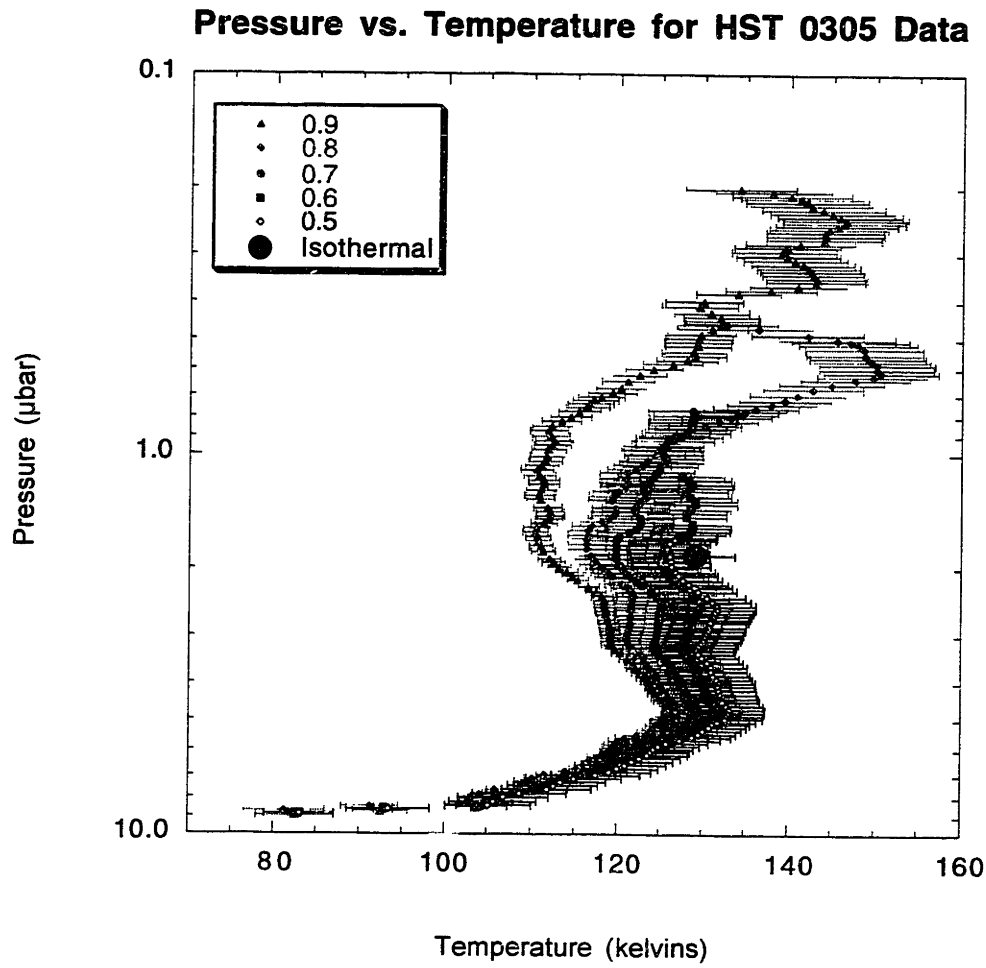

Figure 3.11: Pressure versus temperature inversion profile for the HST 0305 data set (latitude +10.2°). The various curves represent the inversion results based on initial conditions at various points in the occultation light curve, from $\phi = 0.5$ to 0.9. The single large circle is the temperature from the isothermal model fit to the data from Table 3.2

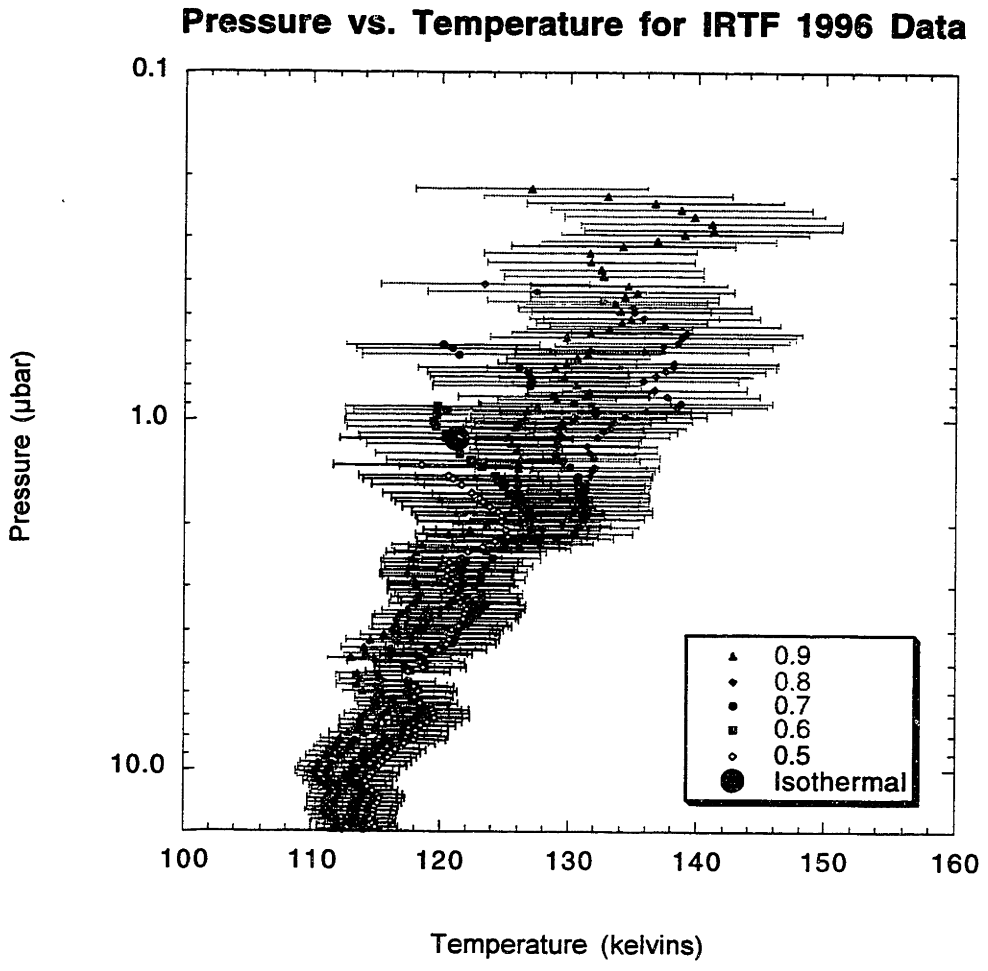

Figure 3.12: Pressure versus temperature inversion profile for the IRTF 1996 data set (latitude –52.7°). The various curves represent the inversion results based on initial conditions at various points in the occultation light curve, from $\phi = 0.5$ to 0.9. The single large circle is the temperature from the isothermal model fit to the data from Table 3.2

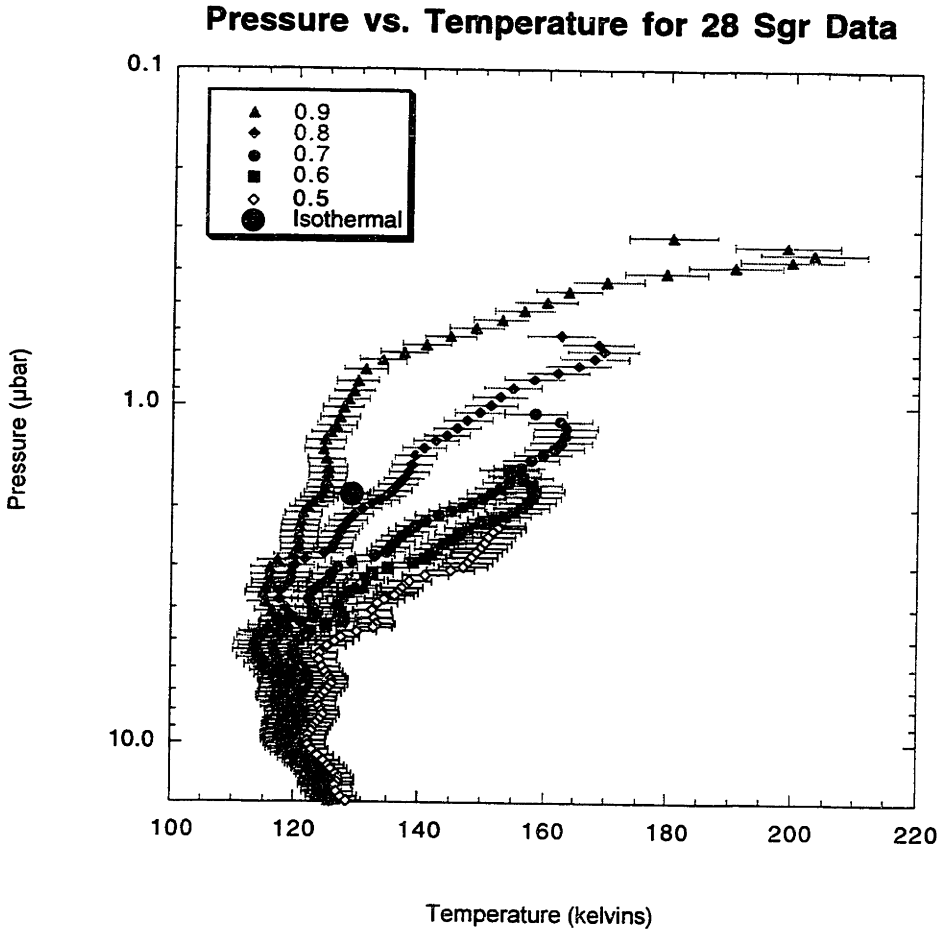

Figure 3.13: Pressure versus temperature inversion profile for the 28 Sgr data set (latitude –15.1°). The various curves represent the inversion results based on initial conditions at various points in the occultation light curve, from $\phi = 0.5$ to 0.9. The single large circle is the temperature from the isothermal model fit to the data from Table 3.2

The HST 0203 inversion shows a markedly different behavior than the 0204 and 0305 data sets, even though it probes the same general region of Saturn's atmosphere as the 0204 data set and does so only approximately 95 minutes before 0204. It is difficult to

see a way where the thermal profile of Saturn's atmosphere would be so spatially and/or temporally variable, so we believe that this may be a problem related to the background subtraction technique used on the data. We attempted several other inversions of the data set by adjusting the parameters of the background subtraction process. (Figure 3.14) In most cases the resulting inversion profiles bore a resemblance to the shape of the 0203 profile shown here, although shifted in temperature. In those cases where the profiles were closer to isothermal in nature, the temperatures were much lower than measured elsewhere in this region of Saturn's atmosphere, including the 0204 data set. As discussed in Appendix A, this is likely because of the uncertainty in the choice of the beginning point of the immersion, as the wavelike pattern overlaid onto the data (see Chapter 2) interferes with the immersion lightcurve. A similar comparison of different background subtraction parameters on the 0204 and 0305 data sets shows that some features of the inversion profiles, including the temperature ranges of the profiles, are sensitive to changes in the parameters (Figures 3.15 and 3.16). However, gross features, including the sharp change in temperature around 6-8 μbar, are not sensitive to the parameters selected and thus are not likely artifacts of the background subtraction process.

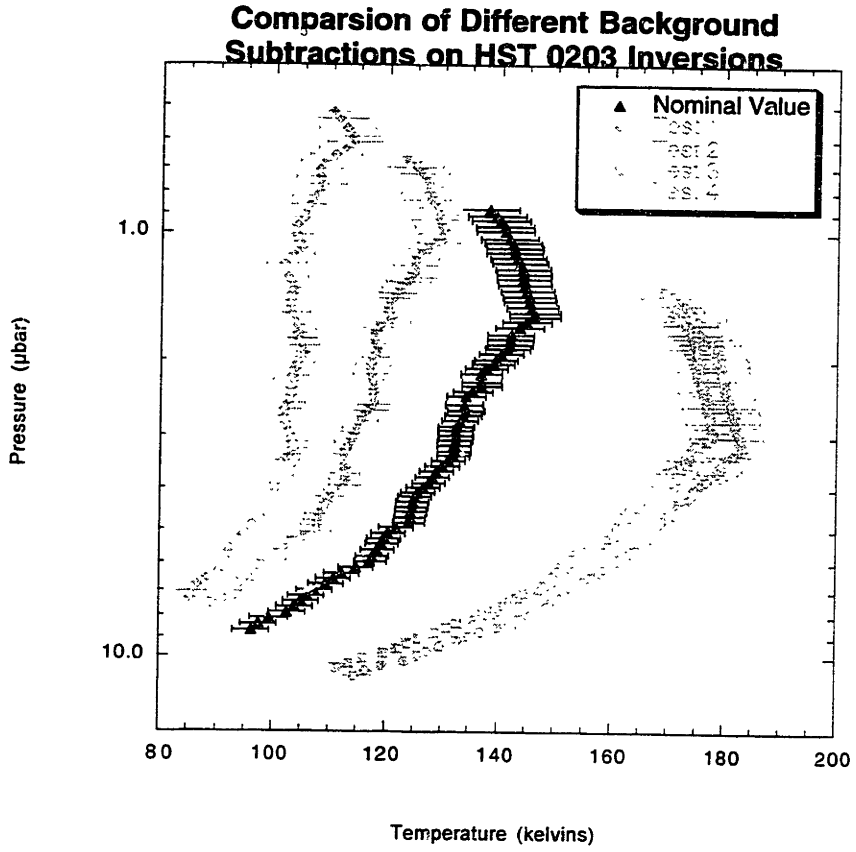

Figure 3.14: A comparison of several 0203 inversion profiles. Each inversion profile shown above used a slightly different background subtraction from the raw data (see Appendix A for more information) to obtain the light curve that was inverted. All the profiles used the same starting point, $\phi = 0.6$, from the model light curve. The version used in Figure 3.9 is shown in black above and denoted as the "Nominal Result"; alternate tests are shown in gray. Note that the shape of the profiles changes dramatically for different background subtraction parameters, and the only profiles that look reasonably isothermal are at very low temperature, much lower than expected for this region of Saturn's atmosphere.

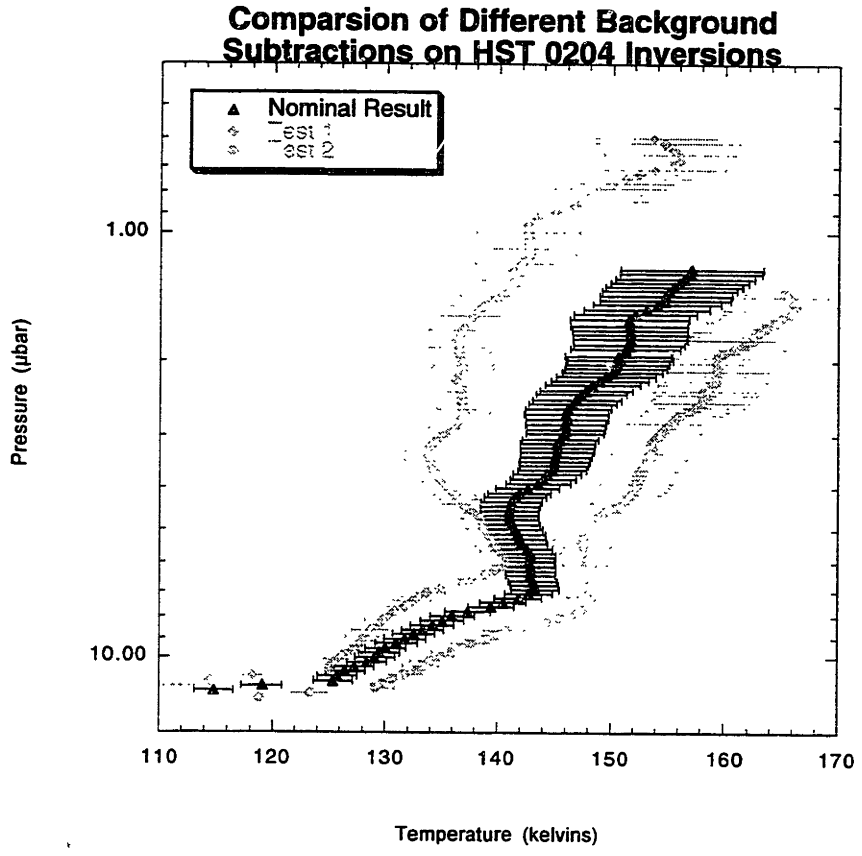

Figure 3.15: A comparison of several 0204 inversion profiles. Each inversion profile shown above used a slightly different background subtraction from the raw data (see Appendix A for more information) to obtain the light curve that was inverted. All the profiles used the same starting point, $\phi = 0.6$, from the model light curve. The version used in Figure 3.10 is shown in black above and denoted as the "Nominal Result"; alternate tests are shown in gray. Unlike the 0203 data, major features in these profiles remain in place even as the background subtraction parameters are altered, although other features and the overall temperature do change.

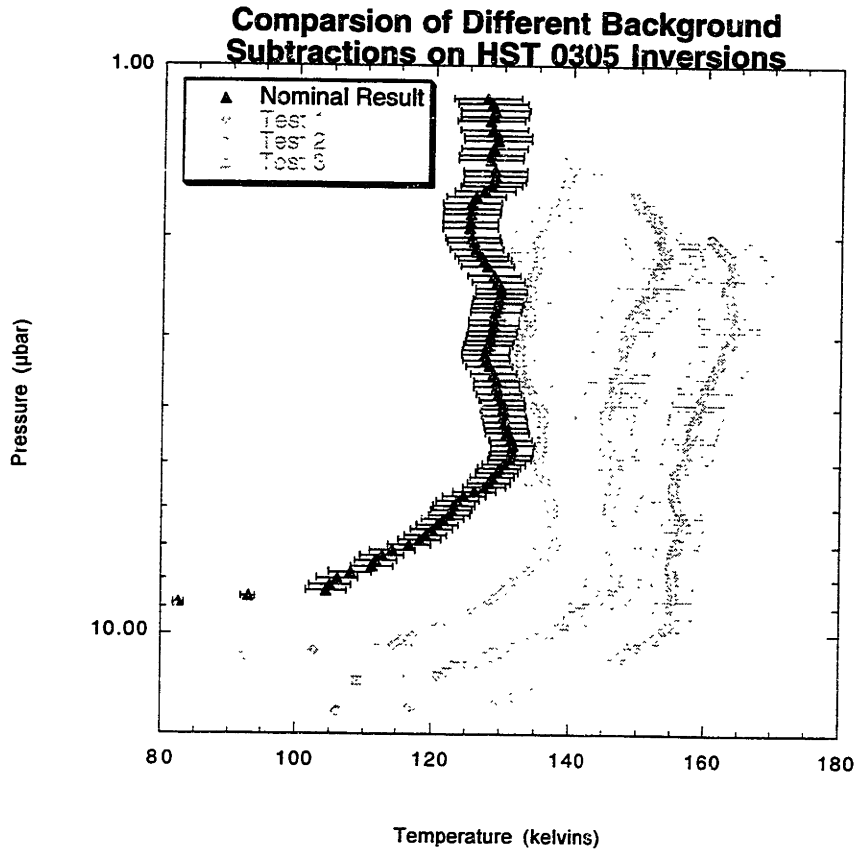

Figure 3.16: A comparison of several 0305 inversion profiles. Each inversion profile shown above used a slightly different background subtraction from the raw data (see Appendix A for more information) to obtain the light curve that was inverted. All the profiles used the same starting point, $\phi = 0.6$, from the model light curve. The version used in Figure 3.11 is shown in black above and denoted as the "Nominal Result"; alternate tests are shown in gray. Unlike the 0203 data, major features in these profiles remain in place even as the background subtraction parameters are altered, although other features and the overall temperature do change.

In Earth's atmosphere temperature decreases with increasing altitude in the mesosphere, as radiative cooling allows more heat to escape than is absorbed by the atmosphere. However, unlike the Earth's atmosphere, Saturn's atmosphere lacks a single, localized atmospheric constituent like ozone that contributes significantly to atmospheric

heating in lower regions; methane, a key absorber of visible and infrared radiation, is well-mixed in Saturn's atmosphere. Thus, we would expect a lesser decrease in temperature in Saturn's mesosphere, or isothermal conditions, a conclusion supported by the temperature profiles recovered from the inversions. If the region probed is near the mesopause, then near-isothermal conditions would be expected as well. High thermal conductivity in the atmosphere can also create isothermal conditions, as Goody and Yung (1989) note, but only at much higher altitudes.

The temperatures calculated are in the range expected from atmospheric models as well. Saturn's atmosphere has a minimum temperature of ~90 K at 100 mbar, the tropopause. Above this level Saturn's temperature increases from the absorption of solar radiation, particularly at infrared wavelengths, by atmospheric components. Bezard and Gautier modeled Saturn's stratosphere to an altitude of 5 mbar by accounting for absorption of visible infrared radiation by CH_4 and emission longward of 7μm by H_2-He, CH_4, C_2H_2, and C_2H_6. This gives 5-mbar temperatures ranging from 110-140 K, depending on latitude and season, as noted earlier in this chapter. Radiative-dynamic models of Saturn's troposphere and stratosphere developed by Conrath *et al.* (1990) and Barnet *et al.* (1992) also found northern regions 10 to more than 20 degrees warmer than southern regions at northern summer solstice and fall equinox, roughly corresponding to 1988 and 1995 respectively.

The warmer temperatures near the north pole compared to the equator and southern hemispheric regions is supported by several factors. Tokunaga *et al.* (1978) explained the warm temperatures near the south pole half a Saturnian year ago by noting that the increased path length and length of the day provides more solar energy to the polar regions in summer than the equatorial zone. Absorption of ultraviolet radiation in polar regions (West 1981; West *et al.* 1983) can also contribute to the higher

temperatures at the poles. Barnet *et al.* (1992) also note the effects of shadowing on the atmosphere from the rings: during the northern summer the ring shadows can reduce the insolation of mid-southern latitudes by more than a factor of 10 from the insolation at high northern latitudes.

One specific feature in the inversion profiles is not easily explained by existing atmospheric models. The HST 0204 and 0305 profiles are very similar, with isothermal profiles around T=130-140 K at pressures down to 5-6 μbar before turning considerably colder at deeper pressures. This is very similar to what Cooray *et al.* (1998) determined from the same occultation observed at the IRTF. They observed an isothermal region with a temperature of 130 K from 2 to 7 μbar, followed by a sharp decrease to 117 K at 10 μbar, followed by another decrease to 115 K at 13 μbar. The HST 0204 profile remains approximately isothermal at 140 K from 2 to 6 μbar before cooling to 120 K at 12 μbar, where it then sharply cools to 110 K. The HST 0305 data remains isothermal at 130 K to 5 μbar, when it cools to 105 K at 8 μbar before sharply cooling to 80 K at 9 μbar. Computation of the thermal lapse rates (discussed in detail in Chapter 5; especially Figures 5.3-5.5) show the lapse rates exceed 1 K/km in these regions, while Cooray *et al.* estimated an overall lapse rate of 0.8 K/km in the 1995 IRTF region (82.5° to 85° latitude).

We consider several possibilities for this change in temperature. Gravity waves that propagate upwards from deeper in the atmosphere may eventually break, releasing their energy by heating the atmosphere. This explanation has been put forward to explain the sudden temperature increase seen in Jupiter's upper atmosphere (Yelle *et al.* 1996; Young *et al.* 1997). However, this increase was more than an order of magnitude larger than seen here, and at lower pressures. Moreover, the role of breaking gravity waves in heating upper atmospheres has recently been questioned (Matcheva and Strobel 1998;

Young *et al.* 1998b). Thus, it is unlikely that breaking gravity waves are contributing to this temperature change.

Dust infall from rings has been explored as a possible cause of an increase in the temperature of the upper Uranian atmosphere that peaks at 8 μbar (Rizk and Hunten 1990). Infalling dust reaches temperatures of up to 200 K, sufficient to warm the Uranian atmosphere in the 1-10 μbar range, where temperatures are similar to those seen in Saturn's upper atmosphere. However, the Uranian data show a temperature increase peaked by the equator, and Rizk and Hunten show that the dust falling from the rings would spread into a band only ~100 km in width. This is insufficient for explaining the Saturnian data, where similar temperature changes are seen both near the equator and near high latitudes.

Another source for infalling material is Saturn's magnetic field. Connerney (1986) showed from Voyager data that latitudinal albedo and temperature variations on Saturn were in magnetic conjugacy with features of Saturn's rings. Connerney noted that the magnetic field would be able to transport ice and dust particles from the ring to the planet, causing the features seen at a variety of longitudes.

The only features noted by Connerney that matches up with our occultation data is the A ring, whose particles are in conjugacy with the southern hemisphere from –48.1 to –51.4 degrees, near the IRTF 1996 immersion; and the inner D ring, from –17.3 to –20.9 degrees, near the 28 Sgr immersion. These data sets, however, are those that do not show a sharp temperature change (with the exception of the 0203 data set, whose difficulties are addressed above). One possibility is that the infall of dust does generate heat (as noted by Rizk and Hunten (1990)) and this offsets a preexisting temperature change seen in the other data sets, assuming the affect covers a slightly wider range than

as listed by Connerney (both the IRTF 1996 and 28 Sgr data sets are 1-2° outside the published extent of the features.) While this may explain why the 1996 IRTF data are different from the other data sets, it does not explain the existence of the sharp temperature change in the first place.

More interesting is the inversion profile of the IRTF data. It, too, shows an approximately isothermal profile, to depths greater than those seen in the HST data or the Cooray *et al.* (1998) data. The temperature of the isothermal region, though, is cooler than the other data sets: temperature of 115-120 K. This result is similar to the half-light temperature obtained from the isothermal model fit, and can be explained by seasonal differences (Conrath and Pirraglia 1983; Bezard and Gautier 1985).

Hubbard *et al.* (1997), whose data sets span from +6° to –15° latitude, see no significant latitudinal variation in temperature from their 1989 28 Sgr occultation observations. However, since these observations took place approximately midway in time between the Voyager observations, with the warmer southern hemisphere, and the 1995-1996 IRTF observation, with the warmer northern hemisphere, it is possible that no latitudinal dependence on temperature existed at that time. However, only one occultation from the southern hemisphere in the mid-1990s has been observed, so we cannot be certain that this was just an aberrant region of Saturn's atmosphere at the time of the observation. Thus, this cannot be construed as conclusive evidence that temperature difference between the northern and southern hemisphere has been measured, but it is strongly suggestive.

Conclusion

It is difficult to generalize about the characteristics of Saturn's upper atmosphere from these data, given the small number of data sets, the regions of the planet they probe, and the inconsistencies among the data sets (particularly between the 0203 and 0204 occultations.) However, there are some key results we can draw from an examination of the data, summarized in Figure 3.17.

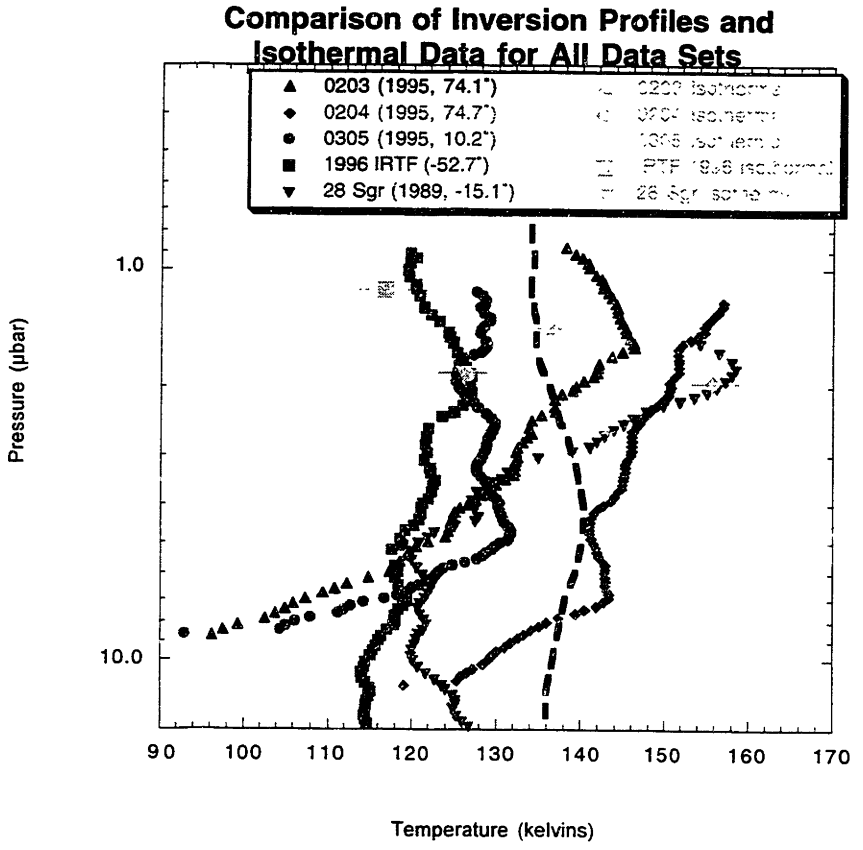

Figure 3.17: A comparison of inversion profiles and isothermal results for all the data sets examined here. For each data set the inversion profile which started at $\phi = 0.6$ of the isothermal model fit is used. Error bars are omitted from the inversion profiles for the sake of clarity.

The half-light temperatures of the data show wide variations that appear to be consistent with seasonal and latitudinal variations as predicted by various atmospheric models. The high northern latitude 0203 and 0204 data are warmer than the near-equatorial 0305 occultation by at least about the amount predicted from the radiative seasonal model of Bezard and Gautier (1985). The southern-hemisphere IRTF 1996 data is also cooler than the equatorial or northern hemisphere data, although the difference is greater than expected from the model. In a direct comparison of IRTF data sets, the southern hemisphere 1996 data is about 13 ± 13 K cooler than the northern hemisphere 1995 data. This is greater than the offset seen in infrared Voyager spectra by Conrath and Pirraglia (1983), who saw a 5 K offset between hemispheres, but with the opposite polarity expected after one-half of a Saturnian year. The errors, though, indicate that this may not be a significant difference.

We also see in some of our data sets, namely the 0204 and 0305 occultations, a sharp temperature gradient at pressures greater than 10 μbar. This gradient is very similar to the one seen in the IRTF 1995 data by Cooray *et al.* (1998), suggesting that a global mechanism, such as aerosols or dust, may be at work. However, the 1996 IRTF data do not show a similar gradient, which may mean whatever process is at work is temporally or spatially limited.

We do note that the results from our model fits do not agree well with the "L+inv" model of Hubbard *et al.* (1997). This is some cause for concern, as the IRTF 1995 occultation studied by Cooray *et al.* (1998) does agree with the model. However, our data come from three distinct sources, were analyzed using similar techniques to Cooray *et al.*, and all disagree with the model. Thus, we believe that the model may not be applicable to Saturn's upper atmosphere at latitudes outside the equatorial zone.

One aspect of the inversion results not discussed here is the small-scale variations seen in the pressure-temperature profiles. Such variations are thought to be indicative of vertical gravity wave propagation in Saturn's upper atmosphere. A detailed analysis of these variations is discussed in Chapters 4 and 5.

Chapter 4
Power Spectra: Theory and Analysis

Theory

Vertically-propagating gravity waves have been extensively studied in the Earth's atmosphere, particularly as a method for explaining wind and temperature fluctuations in the middle atmosphere (Fritts 1989). As the waves propagate upwards through the atmosphere, their amplitude should increase as the density of the atmosphere decreases. However, Fritts (1989) noted that the amplitudes decreased more slowly than predicted, which he interpreted as evidence of gravity-wave saturation. The theory of gravity wave saturation and breakdown is discussed extensively by Lindzen (1981).

There have been efforts to link the saturation of terrestrial atmospheric gravity waves comes with the observed "universality" of the power spectral densities of wind and temperature data, which show little dependence on location, time of day, season, or meteorological conditions (Van Zandt 1982; Dewan and Good 1986; Smith *et al.* 1987). Smith *et al.* advance a simple theory of gravity wave saturation that predicts a power spectral density $P_u(m)$ relationship from wind velocity data that follows a slope of wavenumber to the –3 power:

$$P_u(m) = bN^2 m^{-3} \tag{4.1}$$

where m is the wavenumber, b a coefficient (estimated to be 1/6 by Smith *et al.* (1987)) and N is the Brunt-Väisälä frequency, the buoyancy frequency for vertically-propagating waves:

$$N^2 = \frac{g}{T}\left(\frac{dT}{dz} + \frac{g}{c_p}\right) \tag{4.2}$$

where T is temperature, dT/dz is the lapse rate, g is the acceleration due to gravity, and g/c_p is the adiabatic lapse rate.

Fritts *et al.* (1988) derived a similar expression for the power spectra of temperature data:

$$P_T = A\frac{N^4}{g^2}m^{-3} \tag{4.3}$$

where A is a coefficient. While this equation requires that the power spectrum follow a slope of m^{-3}, this need not always be the case. We can rewrite the equation above for a more general case:

$$P_T = A'\frac{N^4}{g^2}m^{-\beta} \tag{4.4}$$

where β is the exponent. Note that if β is not equal to 3, the coefficient A' will not be unitless, taking on units such that P_T maintains its original units of inverse wavenumber. We can rewrite Eq. 4.4 to keep A' unitless regardless of the slope by normalizing the wavenumber to some value m_0:

$$P_T = A'\frac{N^4}{g^2}m_0^{-3}\left(\frac{m}{m_0}\right)^{-\beta} \tag{4.5}$$

In Eq. 4.5 the coefficient A' is a function of A (from Eq. 4.3), m_0, and β:

$$A' \equiv A(m_0)^{\beta-3} \tag{4.6}$$

The power spectrum for a time series is defined as:

$$P = \frac{2\Delta}{n}|F|^2 \tag{4.7}$$

where Δ is the spacing between adjacent data points, n is the number of data points, and F is the Fourier transform of the data values y and coordinates z:

$$F(m) = \sum_{j=0}^{n-1} y_j e^{2\pi i m z_j} \tag{4.8}$$

It should be noted that this linear saturation theory for gravity waves is not the only one postulated to explain power spectra. Hines (1991) explains the power spectra profiles through Doppler spreading of small waves by large waves. Weinstock (1990) uses nonlinear interactions among waves, while Gardner (1994) uses a "diffusive filtering" explanation similar to Weinstock. However, all these theories agree that gravity wave propagation causes the power spectra observed, and all compute a –3 power law for the spectra.

Other atmospheric phenomena can also create fluctuations in atmospheric temperature and pressure profiles that may not be distinguished from gravity waves. Allen and Vincent (1995) note that convection and inversions can cause such fluctuations, while Weinstock (1990) points to a wide range of interfering phenomena, including wave absorption, reflection, radiation, and wind shears. All these can make it difficult or impossible to retrieve gravity wave data from the atmospheric profiles.

However, Allen and Vincent (1995), in their studies of power spectra from the Earth's atmosphere, note that convection and inversions are far more likely to appear in the troposphere than in the stratosphere, where it is more certain that temperature and density fluctuations are due to gravity waves. For this analysis we will assume that the same is true for Saturn's stratosphere and mesosphere, and that the other effects described by Weinstock are minor. We will come back to this issue in Chapter 5.

Application to Planetary Atmospheres

While power spectrum analysis of atmospheric gravity waves has been performed extensively for the Earth's atmosphere, its application to other atmospheres in the solar system has been limited. This technique has been applied recently to two solar system bodies, Jupiter and Titan.

Upward-propagating gravity waves were detected in data collected by the Atmospheric Structure Instrument (ASI) on the Galileo probe (Young *et al.* 1997). A power spectrum of these gravity waves has a slope ~ –3 (Young *et al.* 1998a), similar to what has been seen on the Earth. Breaking of monochromatic gravity waves – different than what was observed by Galileo – has been suggested as a way to explain a 700 K temperature increase in Jupiter's thermosphere (Yelle *et al.* 1996; Young *et al.* 1997); more recent work, however, suggests that gravity waves are capable of providing only a fraction of the heating necessary to explain the temperature increase (Matcheva and Strobel 1998; Young *et al.* 1998b).

Power spectra from the 1989 occultation of 28 Sgr by Titan have also been computed (Sicardy *et al.* 1998). One dozen lightcurves were analyzed, and Sicardy *et al.* found that the slopes of the power spectra from these lightcurves were in the range of $\beta \sim$

3-4, steeper than predicted by saturated gravity wave theory. They explained their results by noting that both ray crossing from the occultation or the finite diameter of the occulted star could contribute to the abnormally steep spectra by dampening high-frequency components of the spectra.

Sicardy *et al.* ran tests using synthetic data to quantify the effects of ray crossing and stellar diameter. They found that stellar diameter effects smoothed out high frequencies in data whose power spectrum followed a –2 power law, making it appear to have a slope of –3. However, stellar diameter had only a small steepening effect on data that originally had a –3 spectrum. Damping of high-frequency data by ray crossing can, though, cause a –3 spectrum to have a slope closer to –4. They conclude that the slope of their spectra after accounting for these factors should lie in the range of $\beta \sim 2\text{-}3$. A separate analysis of temperature gradient profiles from their data, which show no evidence of superadibaticity, lead them to believe that their data are close to $\beta \sim 3$.

These results suggest there may be a common power spectrum for saturated gravity waves in upper atmospheres, independent of other atmospheric conditions such as composition and temperature. Analysis of power spectra from stellar occultations by Saturn can test this claim.

Data Analysis

The power-spectrum analysis starts with the results of the inversion analysis on each respective data set (see Chapter 3). The inversion of the occultation light curves produces profiles of temperature and pressure, needed to generate and analyze the power spectrum of gravity waves.

The analysis starts by selecting a section of the temperature profile for use generating the power spectrum. Since inversion profiles are initially highly dependent on their initial conditions, we performed these analyses using a number of different profiles corresponding to the initial conditions at points on the lightcurve ranging from $\phi = 0.5$ to 0.9 (See Figures 3.6-3.13).

To compute the Fourier transform of the temperature data, we must evenly space the data in the desired coordinate (here, the logarithm base 10 of the pressure, hereafter "log pressure"). Moreover, the Fourier routines built into *Mathematica*™ work best when the number of data points is an integer power of 2 because of its implementation of the Fast Fourier Transform algorithm (Press *et al.* 1992). To meet these requirements, we compute a spacing in log pressure that allows for the required number of points (usually 64, 128, or 256) with even spacing. The temperature data from the inversion analysis is fit to an interpolation function computed within *Mathematica*™, which is then used to compute new temperature values at the evenly-spaced log pressure intervals. The new temperature versus log pressure data is compared to the original data to ensure the interpolated data remain true to the original.

The temperature data include both short-term variations, related to gravity wave or similar phenomena in the atmosphere, and a long-term trend. As only the short-term variations are of interest, we remove the long-term trend by fitting a line to the data and calculating the difference between the line and the temperature data. This removes the long-term trend while preserving the short-term variations in the data. The temperatures are then converted to a unitless normalized temperature T^* using the function:

$$T^* = \frac{T - \overline{T}}{\overline{T}} \tag{4.9}$$

The T^* profiles for each of the five data sets examined here (see Chapter 2 for a detailed description of each data set) are shown in Figure 4.1.

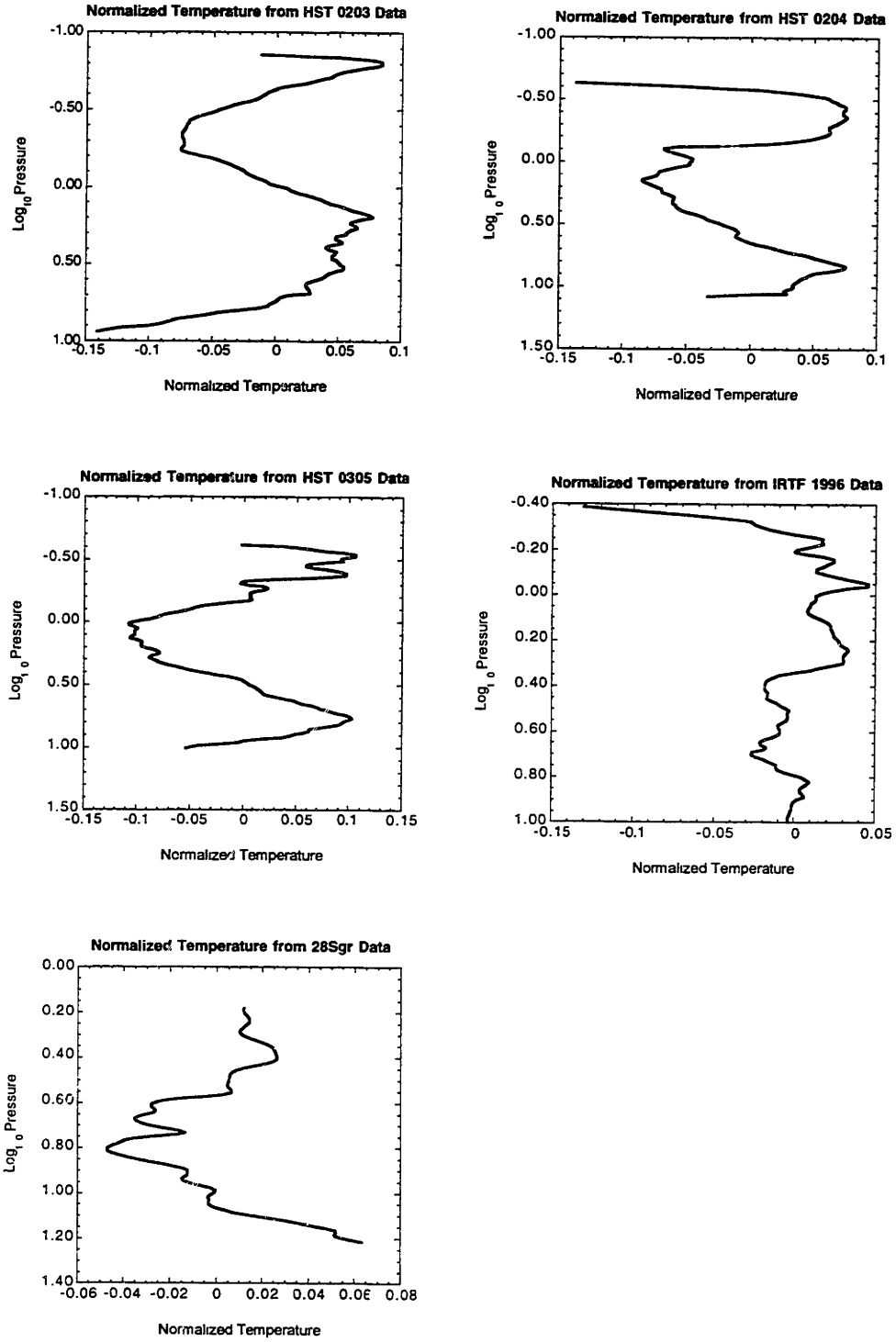

Figure 4.1: Normalized temperature versus pressure. Normalized temperature, as defined by Eq. 4.8, is plotted on the x-axis while the log base 10 of pressure is plotted on the y-axis, for each of the five data sets examined here. These normalized temperatures are used to compute the power spectra discussed below.

It is also possible to compute a power spectrum from the number density, another set of data created by the occultation lightcurve inversion. The log base 10 of the number density is computed and the results are normalized using a form of Eq. 4.8. The normalized density profiles are shown in Figure 4.2. The shapes of the normalized density profiles appear horizontally inverted but otherwise identical to the normalized temperature profiles, which would indicate that both should have similar power spectra. The analysis of either should be suitable for determining the power spectrum of gravity waves in Saturn's atmosphere.

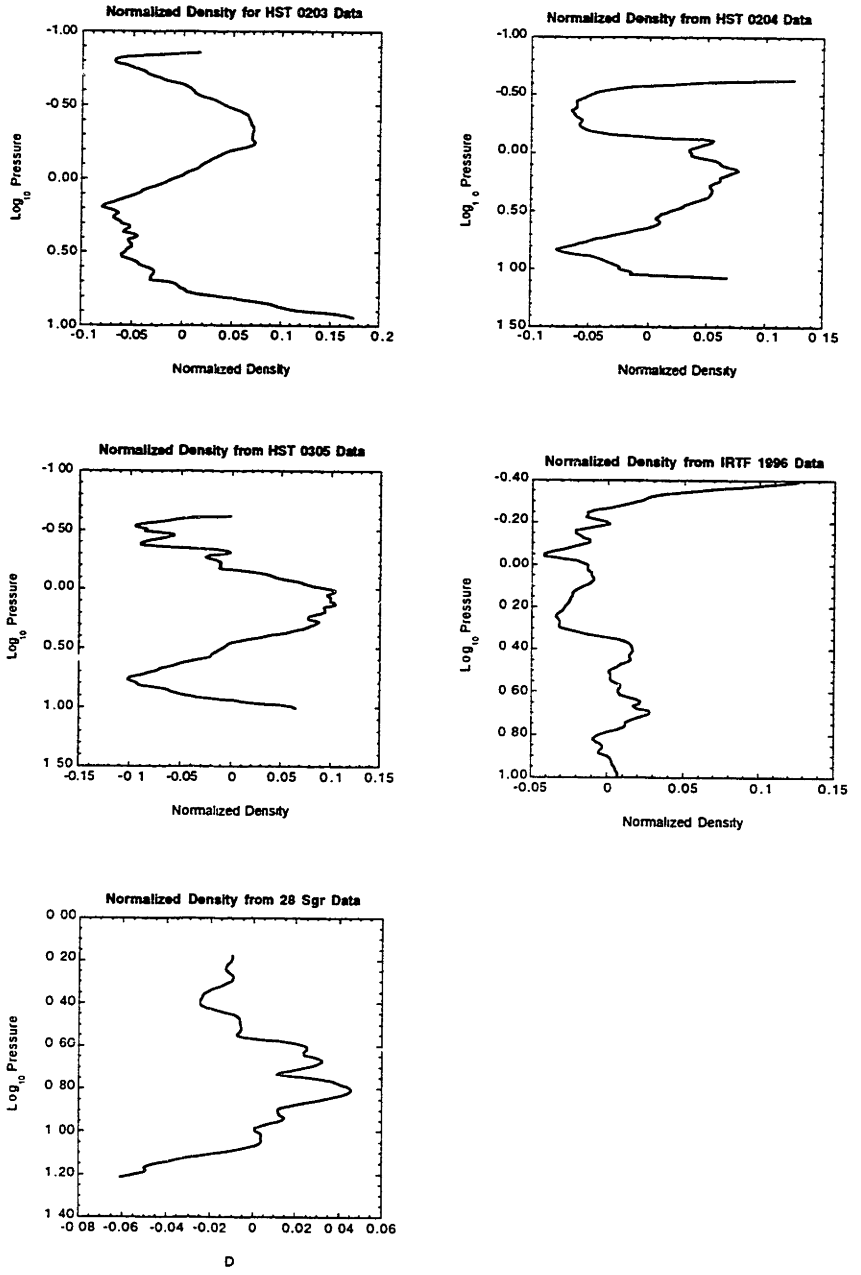

Figure 4.2: Normalized density versus pressure. Normalized density, generated by using Eq. 4.8 on the log base 10 of the number density as opposed to the temperature, is plotted on the x-axis while the log base 10 of pressure is plotted on the y-axis, for each of the five data sets examined here. These normalized densities can be used to compute the power spectra discussed below.

A problem with power-spectrum analysis is from "leakage" of power at high frequencies. Press *et al.* (1992) note that this leakage occurs when the power spectrum of

a data sample is computed with no data window function applied. This means that in effect a square data window is used (1 for the data selected and 0 for all other values). The Fourier transform of a square window includes components at high frequencies, which can introduce spurious noise into a power spectrum analysis.

To prevent this, we multiply a data set by a data window w_j that is unity at the center of the data and drops to zero at both boundaries. Press *et al.* suggest several possibilities:

$$\text{Bartlett:} \quad w_j = 1 - \left| \frac{j - \frac{1}{2}N}{\frac{1}{2}N} \right| \tag{4.10}$$

$$\text{Hann:} \quad w_j = \frac{1}{2}\left[1 - \cos\left(\frac{2\pi j}{N} \right) \right] \tag{4.11}$$

$$\text{Welch:} \quad w_j = 1 - \left(\frac{j - \frac{1}{2}N}{\frac{1}{2}N} \right)^2 \tag{4.12}$$

(The Hann window is also known as the Hanning window; if differs from the Hamming window as the latter uses coefficients of +0.54 and +0.46 in its window function instead of +0.5 and –0.5.) For each window N represents the number of data points and j is the jth data point. A plot of these various data windows is shown in Figure 4.3. The choice among these three data windows is not critical (Press *et al.* 1992). For the present work we chose to use the Hann window.

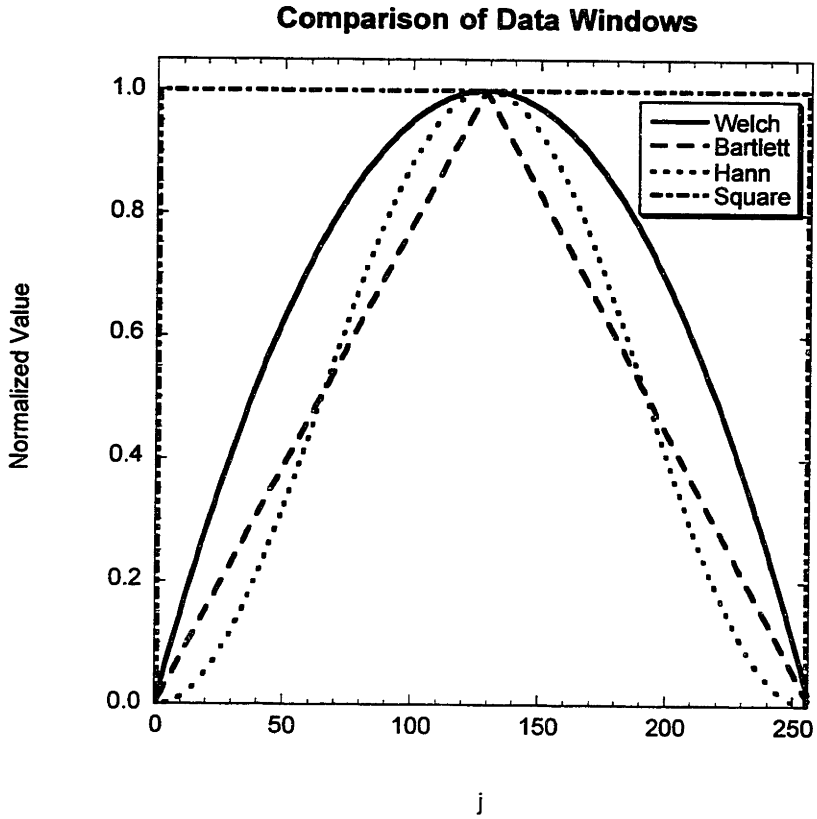

Figure 4.3: A comparison of the Welch, Bartlett, Hann, and square data windows. A hypothetical 256-element data set is used to plot the data windows, using Eqs. 4.10-4.12.

A power spectrum can now be computed from the normalized, detrended, windowed temperature or density data, evenly spaced in log pressure. We use *Mathematica*™*'s* built-in *Fourier* function to compute the Fourier transform coefficients b_s, defined as (Wolfram 1991):

$$b_s = \frac{1}{\sqrt{n}} \sum_{r=1}^{n} a_r e^{2\pi i(r-1)(s-1)/n} \tag{4.13}$$

To correct for the difference between this definition and our preferred definition given in the previous section, we multiply the result from the *Fourier* function by $\sqrt{n}$. The power spectrum is then calculated as described in Eq. 4.7.

The wavenumbers that correspond to this power spectrum are in the form 1/log pressure, a unitless quantity. A more desirable unit for the wavenumber would be 1/length, either 1/meters or 1/kilometers. To compute this we note the relationship between scale height and pressure:

$$p_1 = p_0 e^{-z/H} \tag{4.14}$$

where p_1 is the pressure at altitude z, p_0 is the reference (z=0) pressure, and H is the scale height. Taking the log base 10 of both sides, we get:

$$\log_{10}(p_1) = \log_{10}(p_0) - \frac{z}{H}\log_{10}(e) \tag{4.15}$$

After some algebra, Eq. 4.14 can be written as:

$$z = -\frac{H}{\log_{10}(e)}\left(\log_{10}(p_1) - \log_{10}(p_0)\right) \tag{4.16}$$

Since the data are evenly spaced in log pressure, the right-hand side of Eq. 4.16 will be a constant, and we can write the difference in altitude between neighboring points as:

$$\Delta z = -\frac{H}{\log_{10}(e)}\Delta\left(\log_{10}(p)\right) \tag{4.17}$$

This value can now be used to compute wavenumbers in units of 1/length, so that for N data points, the jth wavenumber k_j is given by:

$$k_j = \frac{j}{N\Delta z} \tag{4.18}$$

We can now fit Eq. 4.5 to this relationship between power spectrum and wavenumber, after first computing the Brunt-Väisälä frequency. The results of these analyses will be discussed in the next chapter.

Chapter 5
Power Spectra: Results and Discussion

Results

Five data sets were examined with the techniques described in Chapters 2 and 4. Three were HST FOS data from the November 1995 occultation of GSC 5249-01240; two, 0203 and 0204, were immersions in far northern latitudes (~75°) and one, 0305, was an emersion in the northern near-equatorial region. The fourth was an occultation of GSC 0010-00284 in July 1996, an immersion in mid-southern latitudes, observed with the NSFCAM at the IRTF. The fifth was an occultation of 28 Sgr in July 1989, in northern near-equatorial latitudes, observed at the IRTF with the Rochester camera. Full details regarding the data sets are available in Chapter 2; the inversion techniques used to obtain the density and temperature profiles used here are discussed in Chapter 3.

Using the method described in the previous chapter, we performed this power spectrum analysis on multiple inversion profiles representing different starting conditions between $\phi = 0.5$ and 0.9. We also compared the spectra for temperature variations and number density variations. In each case we spaced the data evenly in log base 10 pressure, using 64 or 128 data points, depending on the number of points in the original sample. We computed the normalized density or temperature, multiplied it by the Hann data window (Eq. 4.11), and then computed the power spectrum. We then fit the power spectrum to Eq. 4.5, using a least-squares fit to find the amplitude A' and slope β. We used three values for m_0, 10^{-3}, 10^{-4}, and 10^{-5} m^{-1}, that spanned the range of wavenumbers sampled by the data to check that the results were independent of the reference wavenumber selected. The results from the temperature data are shown in Tables 5.1 - 5.5 and the results from the number density data are shown in Tables 5.6 - 5.10.

Table 5.1: Power Spectrum Results from HST 0203 Temperature Data

Data Set	# Points	$m_0 = 10^{-3}$		$m_0 = 10^{-4}$		$m_0 = 10^{-5}$	
		A'	β	A'	β	A'	β
$\phi = 0.9$	128	0.0038 ± 0.0021	3.37 ± 0.23	0.0035 ± 0.0011	3.38 ± 0.23	0.0036 ± 0.0024	3.37 ± 0.23
$\phi = 0.8$	128	0.00013 ± 0.00007	3.73 ± 0.25	0.00013 ± 0.00005	3.73 ± 0.25	0.00013 ± 0.00011	3.73 ± 0.25
$\phi = 0.7$	128	0.0025 ± 0.0010	3.46 ± 0.19	0.0024 ± 0.0007	3.47 ± 0.19	0.0024 ± 0.0015	3.47 ± 0.19
$\phi = 0.6$	128	0.00048 ± 0.00022	3.65 ± 0.23	0.00045 ± 0.00017	3.66 ± 0.23	0.00046 ± 0.00037	3.66 ± 0.23
$\phi = 0.6$	64	7.16 ± 4.20	2.65 ± 0.24	7.48 ± 2.38	2.65 ± 0.24	7.71 ± 3.91	2.67 ± 0.24
$\phi = 0.5$	64	0.031 ± 0.020	3.18 ± 0.28	0.030 ± 0.012	3.19 ± 0.28	0.031 ± 0.027	3.19 ± 0.28

Table 5.2: Power Spectrum Results from HST 0204 Temperature Data

Data Set	# Points	$m_0 = 10^{-3}$		$m_0 = 10^{-4}$		$m_0 = 10^{-5}$	
		A'	β	A'	β	A'	β
$\phi = 0.9$	128	0.0031 ± 0.0010	3.42 ± 0.13	0.0030 ± 0.0005	3.43 ± 0.13	0.0030 ± 0.0010	3.42 ± 0.13
$\phi = 0.8$	128	0.00052 ± 0.00021	3.54 ± 0.17	0.00052 ± 0.00013	3.54 ± 0.17	0.00050 ± 0.00027	3.55 ± 0.17
$\phi = 0.7$	128	0.0015 ± 0.0005	3.47 ± 0.16	0.0015 ± 0.0004	3.48 ± 0.16	0.0015 ± 0.0008	3.48 ± 0.16
$\phi = 0.6$	128	0.000020 ± 0.000006	3.92 ± 0.16	0.000020 ± 0.000005	3.92 ± 0.16	0.000020 ± 0.000010	3.92 ± 0.16
$\phi = 0.6$	64	0.0030 ± 0.0017	3.40 ± 0.22	0.0027 ± 0.0008	3.42 ± 0.22	0.0028 ± 0.0017	3.41 ± 0.22
$\phi = 0.5$	128	0.00000097 ± 0.00000025	4.24 ± 0.16	0.00000102 ± 0.00000028	4.24 ± 0.16	0.00000114 ± 0.00000067	4.24 ± 0.16
$\phi = 0.5$	64	0.000023 ± 0.000014	3.90 ± 0.28	0.000021 ± 0.000008	3.90 ± 0.28	0.000023 ± 0.000018	3.90 ± 0.28

Table 5.3: Power Spectrum Results from HST 0305 Temperature Data

Data Set	# Points	$m_0 = 10^{-3}$		$m_0 = 10^{-4}$		$m_0 = 10^{-5}$	
		A'	β	A'	β	A'	β
$\phi = 0.9$	128	0.00011 ± 0.00006	3.68 ± 0.21	0.000111 ± 0.00003	3.68 ± 0.21	0.00011 ± 0.00006	3.68 ± 0.21
$\phi = 0.8$	128	0.0000023 ± 0.0000011	4.11 ± 0.22	0.0000023 ± 0.0000007	4.11 ± 0.22	0.0000023 ± 0.0000015	4.11 ± 0.21
$\phi = 0.7$	128	0.0000049 ± 0.0000017	4.10 ± 0.17	0.0000050 ± 0.0000012	4.10 ± 0.17	0.0000050 ± 0.0000027	4.10 ± 0.17
$\phi = 0.6$	128	0.0000029 ± 0.0000012	4.15 ± 0.18	0.0000030 ± 0.0000008	4.15 ± 0.18	0.0000030 ± 0.0000018	4.15 ± 0.18
$\phi = 0.6$	64	0.00034 ± 0.00022	3.66 ± 0.24	0.00034 ± 0.00011	3.67 ± 0.24	0.00035 ± 0.00023	3.66 ± 0.24
$\phi = 0.5$	128	0.00000037 ± 0.00000017	3.36 ± 0.21	0.00000036 ± 0.00000014	3.38 ± 0.20	0.00000036 ± 0.00000029	3.37 ± 0.20
$\phi = 0.5$	64	0.0062 ± 0.0030	4.38 ± 0.23	0.0057 ± 0.0015	4.38 ± 0.23	0.0058 ± 0.0033	4.38 ± 0.23

Table 5.4: Power Spectrum Results from IRTF 1996 Temperature Data

Data Set	# Points	$m_0 = 10^{-3}$		$m_0 = 10^{-4}$		$m_0 = 10^{-5}$	
		A'	β	A'	β	A'	β
$\phi = 0.9$	128	0.056 ± 0.034	3.10 ± 0.25	0.057 ± 0.020	3.11 ± 0.25	0.057 ± 0.043	3.10 ± 0.25
$\phi = 0.8$	128	0.0021 ± 0.0011	3.46 ± 0.22	0.0019 ± 0.0006	3.48 ± 0.22	0.0020 ± 0.0014	3.47 ± 0.22
$\phi = 0.8$	64	0.038 ± 0.040	3.16 ± 0.38	0.037 ± 0.018	3.17 ± 0.38	0.037 ± 0.035	3.17 ± 0.38
$\phi = 0.7$	64	0.322 ± 0.213	2.94 ± 0.25	0.340 ± 0.110	2.94 ± 0.25	0.318 ± 0.210	2.94 ± 0.25
$\phi = 0.6$	64	0.151 ± 0.085	3.02 ± 0.23	0.155 ± 0.046	3.03 ± 0.23	0.151 ± 0.097	3.02 ± 0.23
$\phi = 0.5$	64	1.90 ± 1.34	2.75 ± 0.30	1.99 ± 0.81	2.74 ± 0.30	1.77 ± 1.60	2.77 ± 0.30

Table 5.5: Power Spectrum Results from 28 Sgr Temperature Data

Data Set	# Points	$m_0 = 10^{-3}$		$m_0 = 10^{-4}$		$m_0 = 10^{-5}$	
		A'	β	A'	β	A'	β
$\phi = 0.9$	128	0.000077 ± 0.000030	3.76 ± 0.17	0.000077 ± 0.000030	3.76 ± 0.17	0.000076 ± 0.000030	3.76 ± 0.17
$\phi = 0.9$	64	1.928 ± 1.389	2.74 ± 0.26	2.061 ± 0.704	2.74 ± 0.26	1.590 ± 1.091	2.76 ± 0.26
$\phi = 0.8$	64	0.000033 ± 0.000023	3.89 ± 0.28	0.000032 ± 0.000012	3.90 ± 0.28	0.000031 ± 0.000025	3.90 ± 0.28
$\phi = 0.7$	64	0.0093 ± 0.0048	3.32 ± 0.21	0.0085 ± 0.0023	3.33 ± 0.21	0.0087 ± 0.0051	3.33 ± 0.21
$\phi = 0.6$	64	0.000096 ± 0.000051	3.81 ± 0.23	0.000090 ± 0.000027	3.82 ± 0.23	0.000092 ± 0.000060	3.82 ± 0.23
$\phi = 0.5$	64	0.0150 ± 0.0059	3.30 ± 0.171	0.0145 ± 0.0034	3.30 ± 0.17	0.0147 ± 0.0077	3.30 ± 0.17

Table 5.6: Power Spectrum Results from HST 0203 Number Density Data

Data Set	# Points	$m_0 = 10^{-3}$		$m_0 = 10^{-4}$		$m_0 = 10^{-5}$	
		A'	β	A'	β	A'	β
$\phi = 0.9$	128	0.0037 ± 0.0020	3.36 ± 0.22	0.0034 ± 0.0011	3.37 ± 0.23	0.0035 ± 0.0023	3.37 ± 0.22
$\phi = 0.8$	128	0.00011 ± 0.00007	3.72 ± 0.26	0.00011 ± 0.00004	3.72 ± 0.26	0.00011 ± 0.00009	3.72 ± 0.26
$\phi = 0.7$	128	0.0021 ± 0.0008	3.46 ± 0.19	0.0019 ± 0.0001	3.47 ± 0.19	0.0020 ± 0.0013	3.46 ± 0.19
$\phi = 0.6$	128	0.00018 ± 0.00008	3.73 ± 0.23	0.00018 ± 0.00007	3.73 ± 0.23	0.00018 ± 0.00014	3.73 ± 0.23
$\phi = 0.6$	64	1.81 ± 1.04	2.77 ± 0.23	1.88 ± 0.58	2.77 ± 0.23	1.085 ± 1.06	2.78 ± 0.24
$\phi = 0.5$	64	0.014 ± 0.009	3.23 ± 0.28	0.013 ± 0.005	3.25 ± 0.28	0.013 ± 0.011	3.24 ± 0.28

Table 5.7: Power Spectrum Results from HST 0204 Number Density Data

Data Set	# Points	$m_0 = 10^{-3}$		$m_0 = 10^{-4}$		$m_0 = 10^{-5}$	
		A'	β	*A'*	β	*A'*	β
$\phi = 0.9$	128	0.0055 ± 0.0020	3.37 ± 0.14	0.0052 ± 0.0010	3.38 ± 0.14	0.0053 ± 0.0021	3.37 ± 0.14
$\phi = 0.8$	128	0.00081 ± 0.00033	3.51 ± 0.17	0.00081 ± 0.00020	3.51 ± 0.17	0.00081 ± 0.00043	3.51 ± 0.17
$\phi = 0.7$	128	0.000046 ± 0.000022	3.83 ± 0.21	0.000045 ± 0.000014	3.83 ± 0.21	0.000045 ± 0.000031	3.83 ± 0.21
$\phi = 0.6$	128	0.000015 ± 0.000006	3.93 ± 0.16	0.000016 ± 0.000004	3.93 ± 0.16	0.000016 ± 0.000009	3.93 ± 0.16
$\phi = 0.6$	64	0.0021 ± 0.0011	3.43 ± 0.22	0.0019 ± 0.0006	3.44 ± 0.22	0.00019 ± 0.0012	3.44 ± 0.22
$\phi = 0.5$	128	0.0000007 ± 0.0000002	4.24 ± 0.16	0.0000008 ± 0.0000002	4.24 ± 0.16	0.0000008 ± 0.0000005	4.24 ± 0.16
$\phi = 0.5$	64	0.000015 ± 0.000009	3.92 ± 0.27	0.000015 ± 0.000005	3.92 ± 0.27	0.000015 ± 0.000012	3.92 ± 0.27

Table 5.8: Power Spectrum Results from HST 0305 Number Density Data

Data Set	# Points	$m_0 = 10^{-3}$		$m_0 = 10^{-4}$		$m_0 = 10^{-5}$	
		A'	β	*A'*	β	*A'*	β
$\phi = 0.9$	128	0.000054 ± 0.000027	3.77 ± 0.20	0.000052 ± 0.000014	3.77 ± 0.20	0.000051 ± 0.000028	3.77 ± 0.20
$\phi = 0.8$	128	0.0000022 ± 0.0000014	4.13 ± 0.23	0.0000022 ± 0.0000007	4.13 ± 0.23	0.0000022 ± 0.0000015	4.13 ± 0.23
$\phi = 0.7$	128	0.0000039 ± 0.0000015	4.12 ± 0.17	0.0000038 ± 0.0000009	4.12 ± 0.17	0.0000038 ± 0.0000020	4.12 ± 0.17
$\phi = 0.6$	128	0.0000021 ± 0.0000007	4.18 ± 0.19	0.0000019 ± 0.0000005	4.18 ± 0.19	0.0000019 ± 0.0000012	4.18 ± 0.19
$\phi = 0.6$	64	0.00024 ± 0.00015	3.69 ± 0.24	0.00026 ± 0.00008	3.70 ± 0.24	0.00022 ± 0.00015	3.69 ± 0.24
$\phi = 0.5$	128	0.00000024 ± 0.00000014	4.40 ± 0.24	0.00000025 ± 0.00000014	4.40 ± 0.24	0.00000025 ± 0.00000021	4.40 ± 0.24
$\phi = 0.5$	64	0.0035 ± 0.0018	3.41 ± 0.20	0.0033 ± 0.0009	3.42 ± 0.20	0.0033 ± 0.0019	3.42 ± 0.20

Table 5.9: Power Spectrum Results from IRTF 1996 Number Density Data

Data Set	# Points	$m_0 = 10^{-3}$		$m_0 = 10^{-4}$		$m_0 = 10^{-5}$	
		A'	β	*A'*	β	*A'*	β
$\phi = 0.9$	128	0.042 ± 0.025	3.12 ± 0.25	0.041 ± 0.014	3.13 ± 0.25	0.041 ± 0.031	3.12 ± 0.25
$\phi = 0.8$	128	0.0019 ± 0.0010	3.46 ± 0.22	0.0018 ± 0.0006	3.48 ± 0.22	0.0018 ± 0.0013	3.47 ± 0.22
$\phi = 0.8$	64	0.061 ± 0.060	3.11 ± 0.35	0.062 ± 0.029	3.12 ± 0.35	0.058 ± 0.051	3.11 ± 0.35
$\phi = 0.7$	64	0.425 ± 0.268	2.92 ± 0.24	0.446 ± 0.140	2.91 ± 0.24	0.413 ± 0.261	2.92 ± 0.24
$\phi = 0.6$	64	0.190 ± 0.107	3.00 ± 0.23	0.196 ± 0.078	3.00 ± 0.23	0.188 ± 0.120	3.00 ± 0.23
$\phi = 0.5$	64	1.64 ± 1.18	2.76 ± 0.31	1.72 ± 0.72	2.76 ± 0.31	1.22 ± 1.13	2.78 ± 0.31

Table 5.10: Power Spectrum Results from 28 Sgr Number Density Data

Data Set	# Points	$m_0 = 10^{-3}$		$m_0 = 10^{-4}$		$m_0 = 10^{-5}$	
		A'	β	*A'*	β	*A'*	β
$\phi = 0.9$	128	0.000082 ± 0.000031	3.76 ± 0.17	0.000082 ± 0.000020	3.76 ± 0.17	0.000081 ± 0.000044	3.76 ± 0.17
$\phi = 0.9$	64	1.947 ± 1.441	2.75 ± 0.27	2.106 ± 0.732	2.74 ± 0.26	1.651 ± 1.111	2.76 ± 0.27
$\phi = 0.8$	64	0.000031 ± 0.000022	3.91 ± 0.28	0.000029 ± 0.000011	3.91 ± 0.28	0.000029 ± 0.000023	3.91 ± 0.28
$\phi = 0.7$	64	0.011 ± 0.006	3.31 ± 0.20	0.010 ± 0.003	3.32 ± 0.20	0.010 ± 0.006	3.32 ± 0.20
$\phi = 0.6$	64	0.000093 ± 0.000050	3.83 ± 0.23	0.000087 ± 0.000027	3.83 ± 0.23	0.000089 ± 0.000059	3.83 ± 0.23
$\phi = 0.5$	64	0.014 ± 0.006	3.30 ± 0.17	0.014 ± 0.003	3.31 ± 0.17	0.014 ± 0.008	3.31 ± 0.17

We note that the results for both A' and β are approximately the same regardless of the reference wavenumber m_0 used, although different values of m_0 give different errors, with $m_0 = 10^{-4}$ providing the smallest errors. We also note that the results are approximately the same whether number density or temperature data are used. This is expected both by inspection of the normalized temperature and number density profiles (Figures 4.1 and 4.2, respectively) as well as by Makhlouf *et al.* (1990), who note that normalized temperature and normalized density vary only in sign in the case of hydrostatic equilibrium and the linearized perfect gas law.

Since our primary interest is with β, the slope of the power spectrum, we selected as the "best" result from each data set (the result with the smallest error in β). Those values, for both temperature and number density power spectra, are shown in Table 5.11. Plots of the power spectra are shown in Figures 5.1 and 5.2.

Table 5.11: Summary of Power Spectrum Fit Results

Data Set	Temperature		Number Density	
	A'	β	A'	β
0203	0.0024 ± 0.0007	3.47 ± 0.19	0.0019 ± 0.0001	3.47 ± 0.19
0204	0.0030 ± 0.0005	3.43 ± 0.13	0.0052 ± 0.0010	3.38 ± 0.14
0305	$5.0 \pm 1.2 \times 10^{-6}$	4.10 ± 0.17	$3.8 \pm 0.9 \times 10^{-6}$	4.12 ± 0.17
IRTF 1996	0.0019 ± 0.0006	3.48 ± 0.22	0.0018 ± 0.0006	3.48 ± 0.22
28 Sgr	0.015 ± 0.003	3.30 ± 0.17	0.014 ± 0.003	3.31 ± 0.17

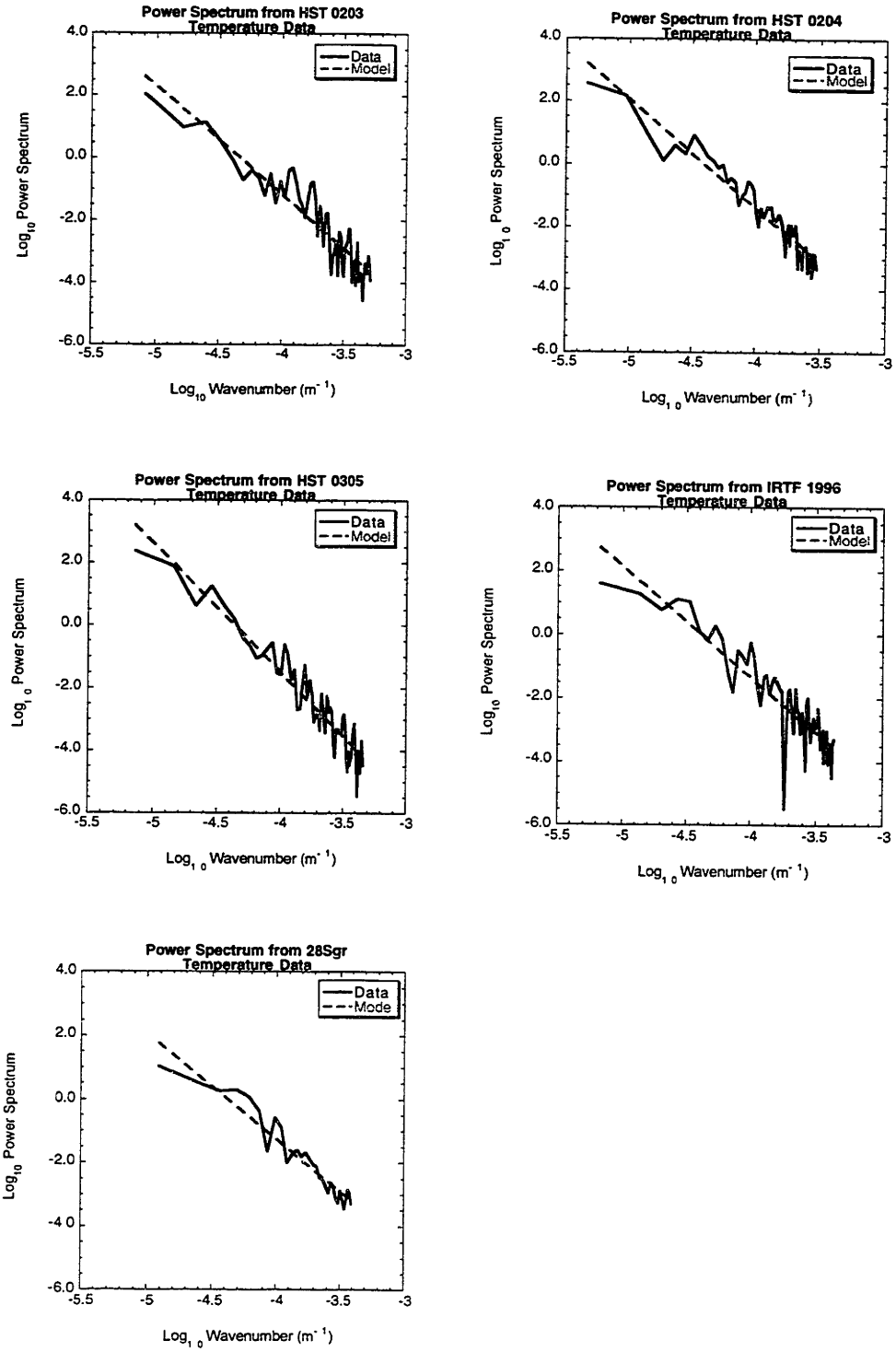

Figure 5.1: Power spectra from temperature data. The log base 10 of the power spectrum of the normalized temperature (in units of meters/cycle) is plotted against the log base 10 of wavenumber (in units of inverse meters) for each of the five data sets. The solid line represents the data, while the dashed line is the best fit model from Eq. 4.5.

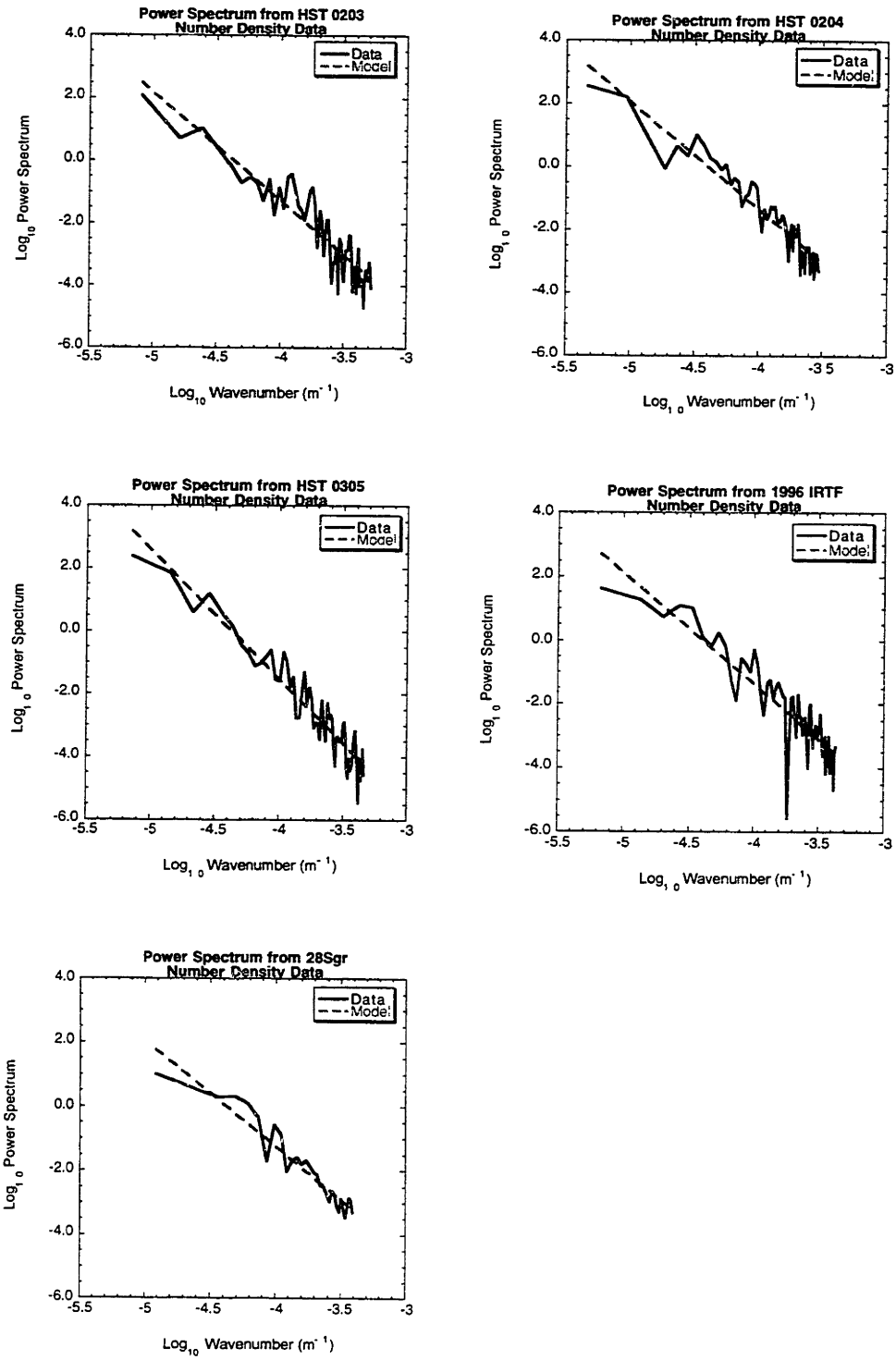

Figure 5.2: Power spectra from number density data. The log base 10 of the power spectrum of the normalized number density (in units of meters/cycle) is plotted against the log base 10 of wavenumber (in units of inverse meters) for each of the five data sets. The solid line represents the data, while the dashed line is the best fit model from Eq. 4.5.

The above results were computed using a Hann data window (Eq. 4.11). We also tested the Bartlett (Eq. 4.10) and Welch (Eq. 4.12) data windows, using $m_o = 10^{-4}$ and the best-fit data sets as used in Table 5.11, to see if the results would differ. These are shown in Table 5.12. With the exception of the 0305 data set, the Welch and Bartlett data window functions produce values of β that are consistent within those computed using the Hann window. This is consistent with the conclusions of Press *et al.* (1992), who noted that there is little practical difference among the three data windows.

Table 5.12: Comparison of Welch and Bartlett Data Window Functions

Data Set	Welch		Bartlett	
	A'	β	*A'*	β
0203 (temp.)	.0038 ± .0011	3.44 ± 0.18	.0008 ± .0003	3.60 ± 0.24
0203 (density)	.0046 ± .0014	3.40 ± .020	.0022 ± .0007	3.46 ± 0.21
0204 (temp.)	.0034 ± .0006	3.43 ± 0.14	.0025 ± .0005	3.44 ± 0.14
0204 (density)	.0065 ± .0013	3.37 ± 0.15	.0037 ± .0008	3.40 ± 0.15
0305 (temp.)	.0043 ± .0009	3.44 ± 0.14	.0006 ± .0001	3.64 ± 0.15
0305 (density)	.0145 ± .0029	3.31 ± 0.14	.0013 ± .0003	3.54 ± 0.14
IRTF 1996 (temp.)	.0091 ± .0029	3.33 ± 0.22	.0045 ± .0013	3.40 ± 0.20
IRTF 1996 (density)	.0070 ± .0020	3.36 ± 0.20	.0043 ± .0013	3.40 ± 0.21
28 Sgr (temp.)	.010 ± .003	3.35 ± 0.21	.0038 ± .0010	3.44 ± 0.19
28 Sgr (density)	.010 ± .003	3.36 ± 0.20	.0037 ± .0010	3.45 ± 0.19

The temperature lapse rate provides additional insight regarding the potential saturation of gravity waves. Smith *et al.* (1987) note that a monochromatic gravity wave will saturate when wave perturbations cause the lapse rate to become superadiabatic. We

can compute the lapse rate from the inversion profiles and look for regions where the lapse rate exceeds the adiabatic lapse rate of approximately –0.6 to –0.9 K/km (the lapse rate, g/c_p, is a function of latitude, due to its dependence on the gravitational acceleration g). Plots of log pressure versus lapse rate are shown in Figure 5.3 through 5.5: Figure 5.3 shows all the data with their own y-axes, Figure 5.4 shows the data with a common y-axis that spans the full range of the data for all 5 data sets, and Figure 5.5 shows the data with a common y-axis which includes the range of log pressure common to all data sets.

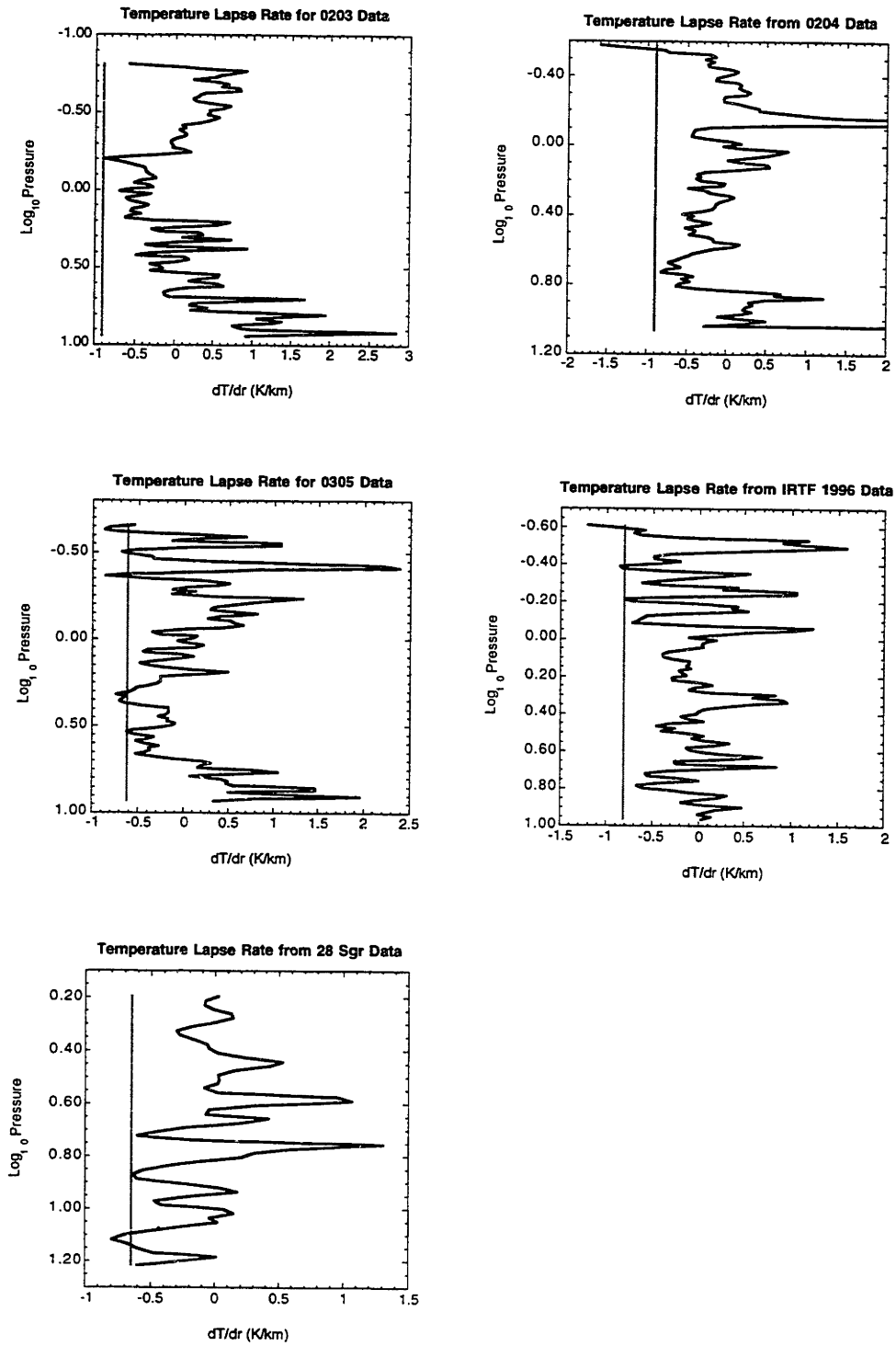

Figure 5.3: Lapse rate plots for each data set. Plotted is the log pressure, on the y-axis, versus the lapse rate in K/km. The adiabatic lapse rate, ranging from -0.6 to -0.9 K/km as a function of latitude, is shown as a gray vertical line. Each data set shows evidence of lapse rates meeting or exceeding the adiabatic limit, suggesting that gravity wave saturation is occurring in Saturn's upper atmosphere.

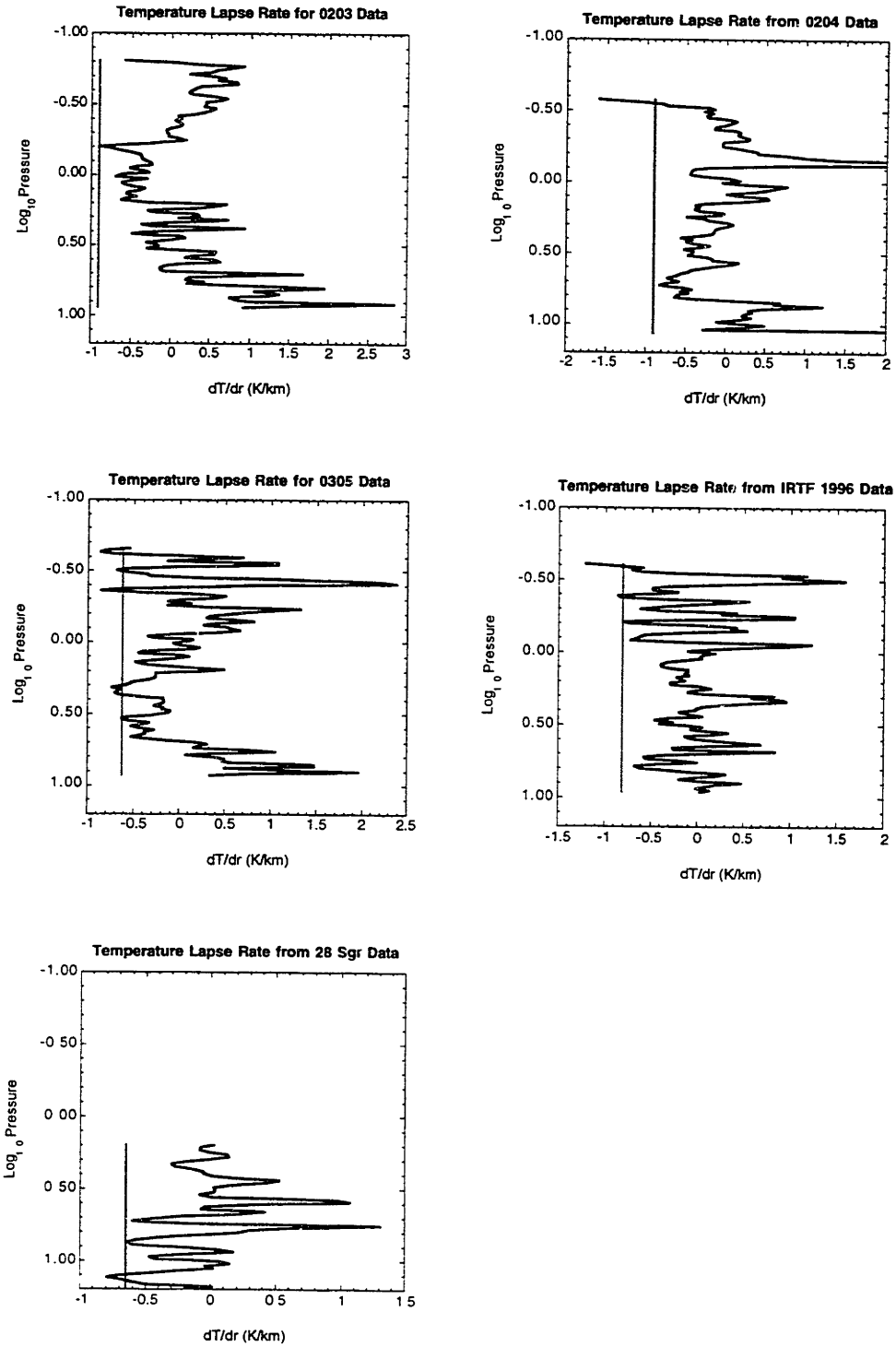

Figure 5.4: Same as Figure 5.3, but with a common *y*-axis for all plots, ranging from –1.0 to 1.2.

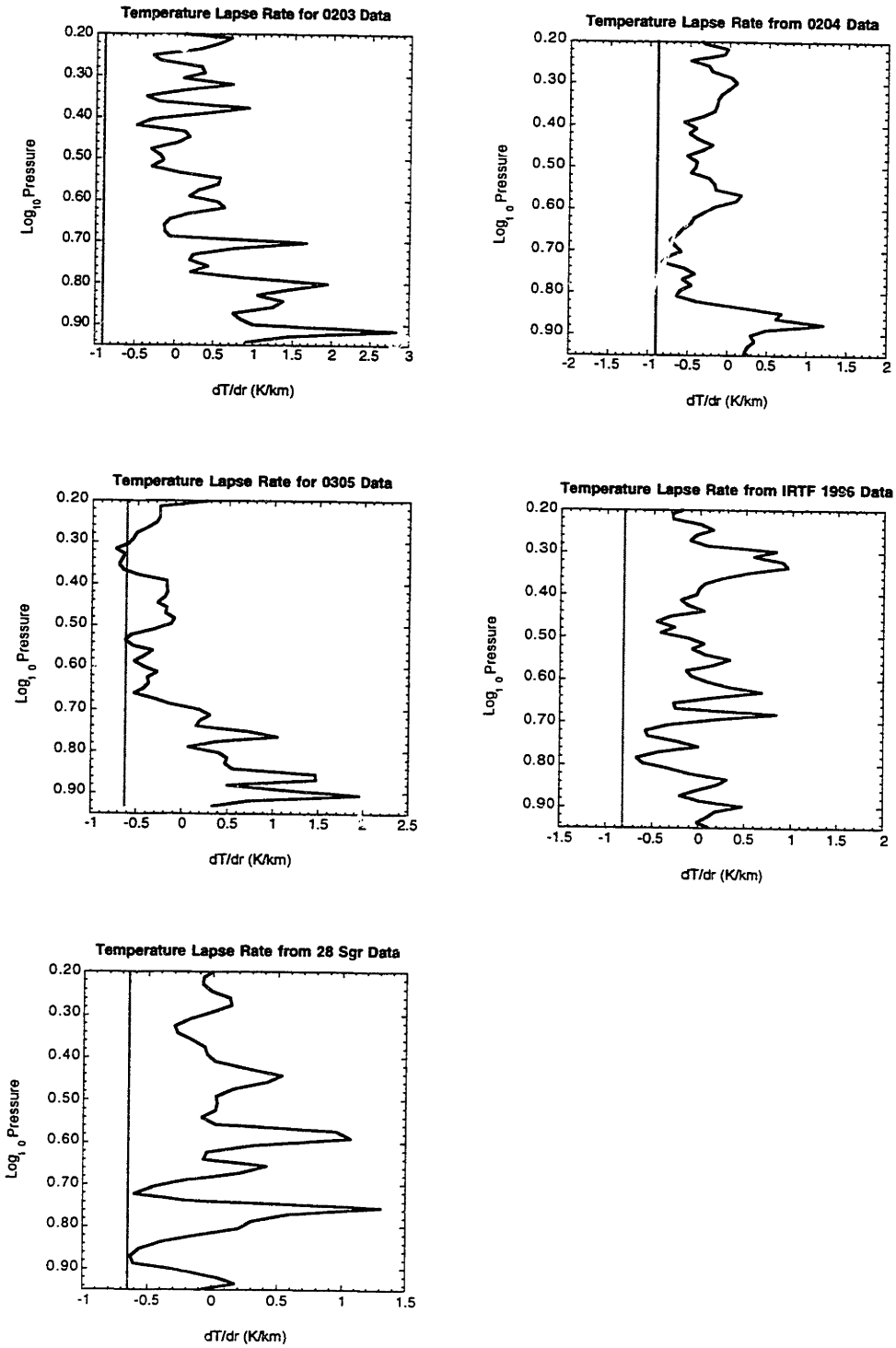

Figure 5.5: Same as Figure 5.3, but with a common y-axis for all the plots, ranging form 0.2 to 0.95.

Another way to examine the data is by studying the relationship between A' and β for the various data sets. As shown in Eq. 4.6, the amplitude A' is a function of β, as well as the reference wavenumber m_0 and the original amplitude A, so we would expect some variation in A' as a function of β. Plotting A' versus β on a logarithmic-linear scale (Figure 5.6) shows that nearly all the data points from the temperature and number density analyses (as displayed in Tables 5.1 – 5.10) fall along a line. We can fit a function to this data of the form:

$$A'(\beta) = 10^{c-d\beta} \tag{5.1}$$

where a least-squares fit yields $c = 15.82 \pm 0.30$ and $d = 5.65 \pm 0.11$

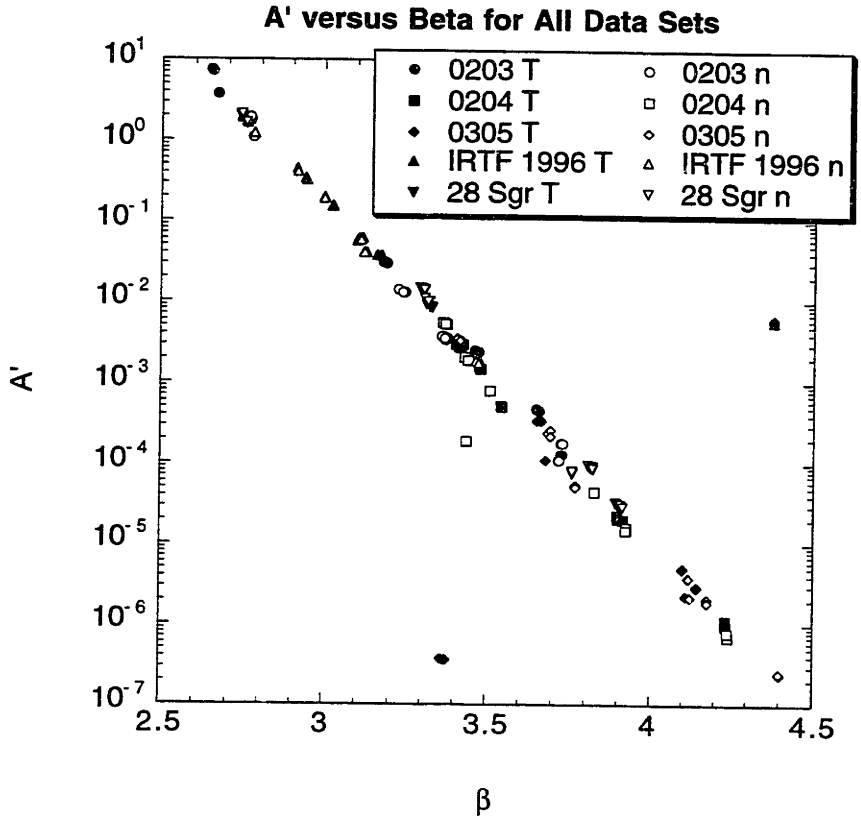

Figure 5.6: A plot of A' versus β. This figure shows the relationship between A' and β for the temperature (T) and number density (n) data sets analyzed here. The data come from Tables 5.1 – 5.10. Note that nearly all the data points fall on the same line in this logarithmic-linear plot.

We can use Eq. 5.1 to find the value of A' at $\beta = 3$, the point at which, according to Eq. 4.6, $A' = A$. Using the values provided above we find that $A = 0.07 \pm 0.07$ at $\beta = 3$. We can now compare this value to terrestrial data, where β is fixed at 3. Smith *et al.* (1987) estimate that, for temperature data from saturated gravity waves in the Earth's upper atmosphere, A is approximately 0.1, similar to our result.

Discussion and Conclusions

Our analysis of the power spectra from these data yields several key points. For nearly all our data sets, we find that the slope β falls in the range of 3 to 4. This is steeper than predicted by gravity wave saturation theory, which predicts β of 3. However, Sicardy *et al.* (1998) note that two characteristics of stellar occultation observations, the projected diameter of the star and ray crossing caused by variations in the occulting body's atmosphere, can artificially steepen power spectra. Their analysis of these effects (discussed in Chapter 4) showed that ray crossing in particular can cause data with an original slope of –3 to appear to be closer to –4. Thus, we conclude that similar effects here mean the actual value of β is in the range of 2 to 3.

Our method of analysis allows β to be a free parameter, while terrestrial gravity wave saturation theory fixes β at 3. This makes comparisons of amplitudes between our results and terrestrial data difficult, as our amplitude A' is a function of β. To permit a meaningful comparison, we fit a function to our data to determine the value of A' at β of 3, where A' is equal to the original amplitude A of terrestrial theory. We find A' of 0.07 ± 0.07, which is very similar to the theoretical value of $A = 0.1$ predicted by Smith *et al.* (1987).

Our studies of the temperature gradients of our data sets showed that in all cases the gradient approached, but did not routinely exceed, the adiabatic lapse rate. This is consistent with the observations of Sicardy *et al.* (1998), who found that the temperature gradients in their data also approached but did not exceed the adiabatic lapse rate. Such behavior is consistent with the saturation of gravity waves, which occurs when the amplitude of the waves matches the adiabatic limit. We also see no evidence that wave amplitudes are dependent on the inverse square root of the density; Dewan and Good

(1986) note that unsaturated vertically propagating waves would show such a dependence, while saturated gravity waves would not.

These attributes of our data are strongly consistent with observations that are interpreted as evidence of gravity wave saturation in the Earth's atmosphere. Fritts *et al.* (1988), using radar data, found that both the amplitudes and the slopes of power spectra of velocity and temperature data closely matched theoretical predictions for gravity wave spectra in the stratosphere. Allen and Vincent (1995), using temperature data collected by radiosondes above Australia, found spectral amplitudes and slopes consistent with gravity wave saturation theory. They do note that their slopes in the stratosphere are somewhat smaller then theory, with values of β around 2.5, but note that horizontal drift of the radiosondes would distort the vertical wavenumber power spectra in a way that would create shallower slopes. Nastrom *et al.* (1997), using measurements of velocity and temperature taken from balloons above Illinois, got spectra with β of 3 in the stratosphere, although the mean amplitudes differed from theory by a factor of 3.

Our data shares many characteristics with these terrestrial data sets: our power spectra have the approximately the slopes (when adjustments for stellar occultation artifacts as discussed by Sicardy *et al.* (1998) are taken into account) and the amplitude of our spectra are consistent with the theoretical amplitude for power spectra from temperature data. We see no evidence for a $\rho^{-0.5}$ dependence in the amplitudes of our data, and the temperature gradients of our data approach, but do not exceed, the adiabatic lapse rate. These conditions, when seen in terrestrial power spectra, have been interpreted as evidence of gravity wave saturation. Thus, we find that our results are consistent with gravity wave saturation in Saturn's upper atmosphere.

As we noted in Chapter 4, though, we need to note that gravity waves are not the only mechanism for generating the power spectra from these data. Allen and Vincent (1995) note that convection and inversions can cause fluctuations in temperature and density profiles similar to those generated by gravity waves, while Weinstock (1990) noted a number of phenomena, from wind shear to wave reflection, that can contribute to the data. While Allen and Vincent (1995) note that convection and inversion is more likely to happen in the lower atmosphere, with gravity wave phenomena likely to dominate in the upper atmosphere, our data cannot in and of itself be considered conclusive evidence of gravity wave propagation and saturation in Saturn's upper atmosphere, but rather suggestive that the phenomenon is occurring.

These and other results suggest the possibility of a common gravity wave power spectra in upper atmospheres. As noted in Chapter 4, gravity wave saturation is a well-studied phenomenon in the Earth's atmosphere, and data from the Galileo probe suggests that gravity waves are also saturating in Jupiter's upper atmosphere. Our results as well as the data from Sicardy *et al.* bring to four the number of planetary atmospheres where gravity wave saturation may have been observed, and suggests this may be a common phenomenon. This subject will be discussed in additional detail in Chapter 7.

Chapter 6
A Method for Finding the Helium/Hydrogen Ratio of Saturn's Upper Atmosphere from Multi-Wavelength Stellar Occultation Data

Introduction

The physical characteristics of the giant planets of the solar system, like Saturn, inhibit the escape of even the lightest elements, meaning that the composition of these planets should closely resemble the composition of the dust and gas cloud from which the solar system formed. However, planetary evolution can alter the atmospheric compositions from their original mix. Smoluchowski (1967) first argued that helium could differentiate from hydrogen in planetary interiors as they cooled. Once a planet cooled beyond a specific point, droplets of helium could condense in the atmosphere and migrate to the center of the planet, depleting the atmosphere of helium and liberating gravitational energy as they fall to the center. The larger the planet, the longer it would hold onto its primordial heat of formation and the longer the onset of helium precipitation would be delayed.

Evolutionary models of Jupiter indicated that that planet should still have enough internal heat to prevent helium precipitation. This was borne out by Voyager spacecraft data, which showed the planet's atmosphere had a helium mass fraction Y of 0.18 ± 0.04, somewhat below the solar value of 0.28 (Gautier *et al.* 1981). Saturn, however, should have lost most of its primordial internal heat, according to interior models (Slattery 1977; Zharkov and Trubitsyn 1978; Hubbard *et al.* 1980), yet the observed heat flux (Hanel *et*

al. 1983) exceeds the model predictions. Additional heat from the precipitation of helium was predicted by Stevenson (1980) to explain the mismatch between model and data.

Conrath *et al.* (1984) used infrared spectra and radio occultation data from the Voyager spacecraft to measure the composition of Saturn's atmosphere. The radio occultation provides a profile of the ratio of the temperature to the mean molecular weight. Different temperature profiles, corresponding to different mean molecular weights, were computed and used to generate spectra, which were then compared with the measured infrared spectrum to find the mean molecular weight that best fit the data. They found $Y = 0.06 \pm 0.05$ (corresponding to a number fraction f(He) of 0.037 ± 0.024), significantly lower than the solar abundance and implying that helium precipitation was taking place in Saturn's atmosphere. Since then there have been no further published measurements of the helium fraction of Saturn's atmosphere.

The large error bars on the Conrath *et al.* result provide no more than an upper limit on the fraction of helium in Saturn's atmosphere. Additional, improved measurements of the ratio would raise our understanding of Saturn's atmosphere as well as its internal structure. Refined measurements of the helium content would provide one way to estimate how long helium precipitation has been taking place within Saturn. Variations in the amount of helium as a function of time or planetary latitude might indicate the atmosphere is not well-mixed. In this chapter we propose a new version of one technique to measure the helium fraction of Saturn's atmosphere using multi-wavelength stellar occultation data and attempt to apply this technique on a set of HST FOS data.

Theory

The use of timing differences in lightcurve features ("spikes") of stellar occultations at different wavelengths to determine the helium fraction was first suggested by Brinkmann (1971). Brinkmann noted that light rays of different wavelengths will traverse almost exactly the same path through a planetary atmosphere but will be refracted by different angles by the atmosphere because of differences in refractivity of the atmosphere as a function of wavelength. Brinkmann predicted that observation of an occultation by Jupiter, at wavelengths of 3000 and 6000 Å, would produce time scale shifts between 1.8% (pure He atmosphere) and 6.1% (pure H_2.). Such time differences could be measured by taking the difference in arrival times of spikes visible in the lightcurves at both wavelengths.

Brinkmann's approach was critically reviewed by Wasserman and Veverka (1973a), who found that Brinkmann's technique for an isothermal atmosphere not only depended on the timing of spikes but on the intensity of the background occultation curve. Measurement of the background occultation signal is necessary for accurate determinations of the timing differences. The signal must be measured to better than ±5% accuracy to get meaningful values of the amounts of hydrogen and helium in the atmosphere of a giant planet.

The theory was revised and expanded by Elliot *et al.* (1974). They start with the function for the angle of refraction for a monochromatic light ray passing through an atmosphere with closest approach distance r_1 to the planet:

$$\theta(r_1) = \int_{-\infty}^{+\infty} \frac{1}{n(r)} \frac{dn(r)}{dr} dx \qquad (6.1)$$

where $n(r)$ is the index of refraction, as a function of distance from the center of the planet, and x is along the direction of travel for the ray (Figure 6.1). By noting that the refractivity $\nu(r)$ is simply $n(r) - 1$ and that $n(r) \sim 1$, one can rewrite (6.1) as:

$$\theta(r_1) \equiv \int_{-\infty}^{+\infty} \frac{d\nu(r)}{dr} dx \tag{6.2}$$

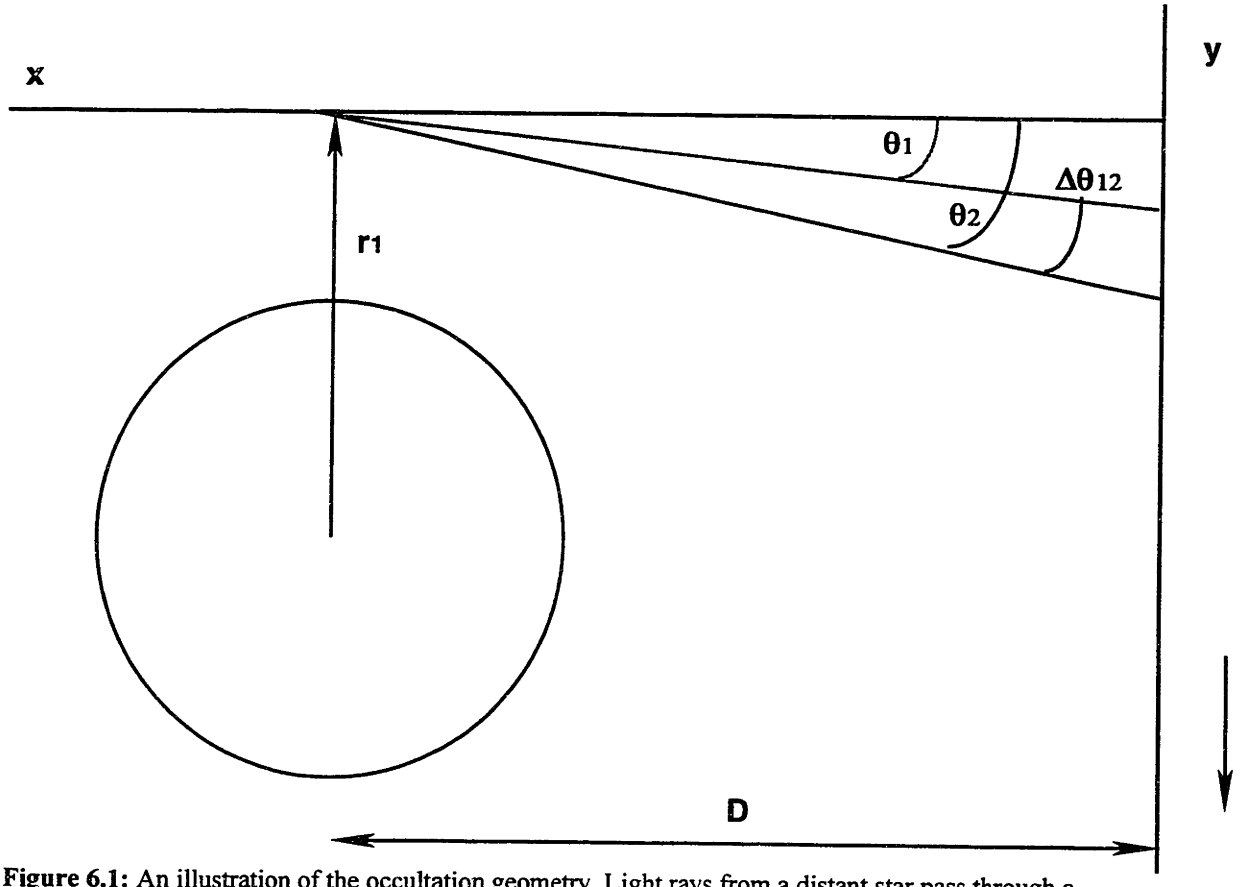

Figure 6.1: An illustration of the occultation geometry. Light rays from a distant star pass through a planetary atmosphere with a closest approach distance r_1. A ray of light of wavelength λ_1 is bent by the angle θ_1, while a ray of wavelength λ_2 is bent by θ_2. Here $\theta_2 > \theta_1$ and, for the refractive behaviors of hydrogen and helium, $\lambda_2 < \lambda_1$. These differences in refraction angles are detected by the observer, at a distance D from the planet and is moving at a velocity v relative to the planet, as a delay in the arrival of the signal. The delay increases as the refractive angle grows. After Elliot *et al.* (1974).

Different refraction angles will result when light of different wavelengths pass through the atmosphere, as refractivity is also a function of wavelength. (For this analysis we will consider the atmosphere well-mixed at all altitudes probed by the occultation, so that the ratio of two refractivities is independent of altitude.) Consider light at two wavelengths λ_1 and λ_2. The difference in the refraction angles between the two wavelengths is:

$$\Delta\theta_{12} = \theta_1 - \theta_2 = \int_{-\infty}^{+\infty} \frac{d\nu_1(r)}{dr} dx - \int_{-\infty}^{+\infty} \frac{d\nu_2(r)}{dr} dx = \frac{\nu_1 - \nu_2}{\nu_2} \theta_2 \tag{6.3}$$

From geometry, we can also show:

$$\Delta\theta_{12} = -\tau_{12}\left(\frac{\upsilon}{D}\right) \tag{6.4}$$

where τ_{12} is the difference in arrival times between corresponding parts of a light curve observed at the two different wavelengths, υ is the relative velocity of the observer to the planetary limb, and D is the distance from the observer to the planet.

If we consider ϕ_2, the normalized flux of light from the star in wavelength λ_2, we can use the relationship between the flux and the refraction angle derived by Goldsmith (1963):

$$\frac{1}{\phi_2} = 1 + D\frac{d\theta_2(r_1)}{dr_1} \tag{6.5}$$

We can also note from geometry that:

$$dy = -\upsilon dt_2 = dr_1 + Dd\theta_2(r_1) \tag{6.6}$$

Combining Eqs. 6.5 and 6.6 in such a way to eliminate dr_1 provides an expression for the refraction angle θ_2:

$$\theta_2 = -\frac{\upsilon}{D}\int_{t_0}^{t_2}\left(1-\phi_2(t')\right)dt' + \theta_0 \tag{6.7}$$

where t_2 is the time the occultation feature was observed in the light curve at wavelength λ_2, t_0 is an arbitrary starting time, and θ_0 is the refraction angle at the starting time t_0.

Equation 6.7 can now be combined with Eqs. 6.3 and 6.4 to show:

$$\frac{\nu_1-\nu_2}{\nu_2}\left(-\frac{\upsilon}{D}\int_{t_0}^{t_2}\left(1-\phi_2(t')\right)dt' + \theta_0\right) = -\tau_{12}\left(\frac{\upsilon}{D}\right) \tag{6.8}$$

If we set t_0 arbitrarily far back so that it represents a time before the immersion begins (or far enough forward so that it represents a time after the emersion ends), θ_0 will be zero and can be discarded from Eq. 6.8. We can also define, for simplicity, a new variable Θ such that:

$$\Theta \equiv \int_{t_0}^{t_2}\left(1-\phi_2(t')\right)dt' \tag{6.9}$$

Therefore, Eq. 6.8 can now be written as:

$$\tau_{12} = \left(\frac{\nu_1-\nu_2}{\nu_2}\right)\Theta = \left(\frac{\nu_1}{\nu_2}-1\right)\Theta = \left(\nu_{ratio}-1\right)\Theta \tag{6.10}$$

Since τ_{12} can be found from the two lightcurves, and Θ can be computed from the reference lightcurve, the refractivity ratio ν_{ratio} can be found from two lightcurves of the same occultation event, taken at different wavelengths. This technique has an advantage over that of Wasserman and Veverka (1973a) in that no estimate of the background flux at the time of each spike is necessary, reducing that source of error, although the integration of 1- ϕ will introduce its own error.

This refractivity ratio can, in turn, be used to find the relative composition of a two-component atmosphere. If the component gases, generalized here as A and B, and their refractivities are known, the relationship between them and the refractivity ratio is:

$$\frac{\nu_1}{\nu_2} = \frac{f(A)\nu_A(\lambda_1) + f(B)\nu_B(\lambda_1)}{f(A)\nu_A(\lambda 2) + f(B)\nu_B(\lambda_2)} \tag{6.11}$$

where f(A) and f(B) are the number fractions for gases A and B, respectively, while ν_A and ν_B represent their refractivities at wavelengths λ_1 and λ_2 .

Elliot *et al.* (1974) used data from the 1971 May 13 occultation of β Scorpii by Jupiter to determine the abundance of hydrogen and helium in the Jovian atmosphere. They had simultaneous lightcurves at three wavelengths – 3530, 3934, and 6201 Å – with a time resolution of 0.01 sec. They noted that the difference in refractivities of helium and hydrogen as a function of wavelength should create differences in the arrival times of spikes in the occultation lightcurves created by density differences in the atmosphere.

In their analysis, Elliot *et al.* identified a number of spikes seen in the lightcurves and determined the time at the peak of each spike. The difference in arrival times for each spike in different lightcurves was computed. The refractivity ratio was calculated using

these differences and values of Θ computed from the lightcurve. Their best data found $f(\mathrm{He}) = 0.16^{+0.19}_{-0.16}$, equivalent to a helium-to-hydrogen ratio of $0.19^{+0.35}_{-0.19}$. Despite the large error, this result compares favorably with the helium-to-hydrogen ratio obtained from the Galileo probe data of 0.156 ± 0.006 (Niemann 1996; Von Zahn and Hunten 1996).

Technique

The technique used on the HST FOS data has its basis in that used by Elliot *et al.* The FOS data consist of 512 columns, one for each diode in the detector. For the Saturn occultation observations the red digicon on the instrument was used in conjunction with the G400H grating, yielding a wavelength range of 3235 to 4781 Å and a resolution of 3.00 Å per diode (Kinney 1994). This theoretically gives 130,816 different combinations of diodes that could be tested. However, since approximately 15 diodes are dead (return no signal) and the amount of signal on a single diode is quite small, especially at blue wavelengths, it is more efficient to sum the signal over a range of diodes and then compare these "virtual" diodes.

The raw signal files for each data set were grouped into sets of four virtual diodes, each consisting of data from 128 physical diodes. The signals for each group of 128 diodes were summed together at each time step to create the signal for the virtual diodes.

As no background subtraction had been performed on the raw data, some analysis was necessary to remove the signal from Saturn from the data. As our interest in the data was limited to a small subset of the data during and immediately after immersion, or during and immediately before emersion, a less rigorous subtraction than that used for model-fitting and inversions (see Chapter 3) could be used. Data segments of

approximately 1000 points (260 seconds) around the time of immersion or emersion were used. In these segments, the contribution of Saturn to the total signal varied approximately linearly. To remove this signal, a line was fit to a post-immersion or pre-emersion section of the data. At those times the contribution to the signal should be only from Saturn, thus the line should provide the total contribution of Saturn as a function of time in the data segment. The line is then subtracted from the data, returning the signal from the star alone. The full star signal is then normalized to 1.

To maximize the differences in timing in lightcurve features, only the red virtual diode (4397–4781 Å) and the blue virtual diode (3235–3619 Å) are compared. Unlike Elliot *et al.*, who pre-selected a set of spikes visible in each lightcurve for timing comparisons, we chose to begin with the full lightcurve. This technique allows the comparison of smaller features that exist in both lightcurves but which may be overlooked in an analysis.

In this analysis, an interpolation function of order 1 (linear interpolation) is fit to the red diode data. The interpolation function allows us to compare time shifts that are not integral multiples of the time resolution of the data, approximately 0.259 seconds. The data are then shifted in time using Eq. 6.10 with an estimate of the value of the refractivity ratio ν_1/ν_2 (values of Θ are computed using Eq. 6.9, with the background-subtracted signal summed over all diodes used as the reference lightcurve.) The unshifted blue data are then subtracted from the shifted red data, and the sum of the squares of these residuals is computed for all data points. This analysis is performed on a range of values for the refractivity ratio; the best-fit ratio is the one that minimizes the sum of the square of the residuals.

The error in the refractivity ratio is computed as follows. Consider the "curvature matrix" α, the inverse of the covariance matrix, where each term of the matrix is defined as:

$$\alpha_{kl} = \frac{1}{2}\frac{\partial^2 \chi^2}{\partial p_k \partial p_l} \tag{6.12}$$

where p_k and p_l are parameters of the model fit and χ^2 is the traditional goodness-of-fit measure (Press *et al.* 1992):

$$\chi^2 = \sum_i^N \left(\frac{d_i - m_i}{\sigma_i} \right)^2 \tag{6.13}$$

where d_i is the ith data point and m_i is the model value corresponding to the ith data point. For this case the only parameter of the model is the refractivity ratio, thus the curvature matrix simplifies into the single term:

$$\alpha = \frac{1}{2}\frac{\partial^2 \chi^2}{\partial (\nu_{ratio})^2} \tag{6.14}$$

Press *et al.* note that not only is the curvature matrix the inverse of the covariance matrix, but the diagonal terms of the covariance matrix are the squares of the errors for each parameter. In this case the square of the error of our parameter, σ_p, is simply:

$$\sigma_p{}^2 \equiv \alpha^{-1} = 2\left(\frac{\partial^2 \chi^2}{\partial (\nu_{ratio})^2} \right)^{-1} \tag{6.15}$$

The best fit is defined as the model that minimizes the value of χ^2. As the expected value of χ^2 for the best fit is simply the number of points N minus the number of constraints (here, 1) (Taylor 1982), we can find the value of σ in Eq. 6.13:

$$\sigma^2 = \frac{\min\left(\sum_i (d_i - m_i)^2\right)}{N-1} \tag{6.16}$$

where $\min\left(\sum_i (d_i - m_i)^2\right)$ is the minimum value of the sum of the squared residuals between data and model. Therefore, a generalized expression for χ^2 becomes:

$$\chi^2 = \frac{(N-1)\sum_i (d_i - m_i)^2}{\min\left(\sum_i (d_i - m_i)^2\right)} \tag{6.17}$$

This can then be inserted into Eq. 6.15 which, when simplified, yields:

$$\sigma_p{}^2 = \frac{2\min\left(\sum_i (d_i - m_i)^2\right)}{N-1}\left(\frac{\partial^2\left(\sum_i (d_i - m_i)^2\right)}{\partial(\nu_{ratio})^2}\right)^{-1} \tag{6.18}$$

The number of points N and the minimum sum of squared residuals can be easily determined. The remaining derivative can be computed by computing the sum of squared residuals for various refractivity ratios and then fitting the data, using a simple least-squares fit, to a second order polynomial (parabola) of the form:

$$\sum_i (d_i - m_i)^2 = c_2(\nu_{ratio})^2 + c_1(\nu_{ratio}) + c_0 \tag{6.19}$$

The second derivative of Eq. 6.19 is simply $2c_2$, thus, Eq. 6.18 reduces to:

$$\sigma_p{}^2 = \frac{2\min\left(\sum_i (d_i - m_i)^2\right)}{N-1}(2c_2)^{-1} \tag{6.20}$$

The error in the best-fit refractivity ratio can now be computed by taking the square root of Eq. 6.20.

A problem with using this technique on all data points is that the data include not only spikes, but noise as well. To remove the noise, an isothermal model is fit to both the red and blue data sets prior to the comparison. If the data for either the red or blue lightcurves fall below a predetermined offset from the isothermal model, called the *threshold*, those data are excluded from the comparison. The value of the offset is found by the value that produces the tightest fit to the data, using a parabola fit described above. This process is similar to that used by Elliot et al. to pre-select spikes in the light curves; however, here that selection is done automatically and in such a way that minimizes the error, which together should improve the quality of the results.

One can use the refractivity ratio and error to find the fraction of helium and hydrogen in Saturn's atmosphere. This requires a knowledge of the refractivities of the gases as a function of wavelength. Elliot *et al.* used helium refractivities measured by Mansfield and Peck (1969) and computed a fit to existing measurements of hydrogen refractivity. Since Elliot *et al.*, Peck and Huang (1977) have more accurately measured hydrogen refractivities in the visible and infrared. In addition, Smith *et al.* (1976) have measured refractivities for several gases, including helium and hydrogen, in the near ultraviolet. These new values are used in this analysis.

The variation of refractivity with wavelength is usually expressed in a Sellmeier equation of the form:

$$\nu = \frac{a}{b - m^2} \tag{6.21}$$

where a is a constant representing oscillator strength, b is a constant for effective absorption frequency, and m is the wavenumber (inverse wavelength), measured in units of inverse microns. While the previous works computed their own Sellmeier functions from their own data, we chose to combine the data sets (which do not overlap in wavelength/wavenumber space) and fit our own Sellmeier functions to them.

Figure 6.2 shows the plot of refractivities versus wavenumber for the helium data. Fitting a Sellmeier function to the data, using a standard least-squares fit, produces $a = 1.50438 \pm 0.00658 \times 10^4$ and $b = 433.87 \pm 1.87$. The reduced χ^2 from this fit is 1.32, indicating that the function fits the combined data well. By comparison, using just their data, Mansfield and Peck found $a = 1.470091 \times 10^{-2}$ and $b = 423.98$ (they did not provide error estimates with their results).

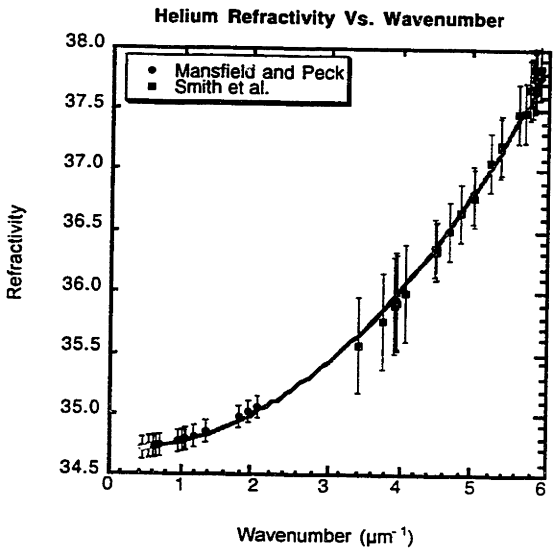

Figure 6.2: A plot of refractivity vs. wavenumber (in units of inverse microns, μm^{-1}), for helium. Circles represent data from Mansfield and Peck, while squares represent data from Smith *et al.* The line is the best fit plot to the data using the Sellmeier function (Eq. 6.21), as discussed in the text.

As a comparison, we also fit the refractivity data to a function of wavelength, rather than wavenumber, using a function of the form:

$$\nu = c + d\lambda^{-2} \tag{6.22}$$

where c and d are constants without necessarily any physical meaning, and λ is the wavelength in nanometers. A fit to the combined data yielded $c = 3.4664 \pm 0.00067 \times 10^{-5}$ and $d = 8.61579 \pm 0.00058 \times 10^{-2}$. (Figure 6.3) The reduced χ^2 here was 2.86, making this a slightly worse fit than the fit using the Sellmeier equation. We chose to use the better Sellmeier fit in the later analysis.

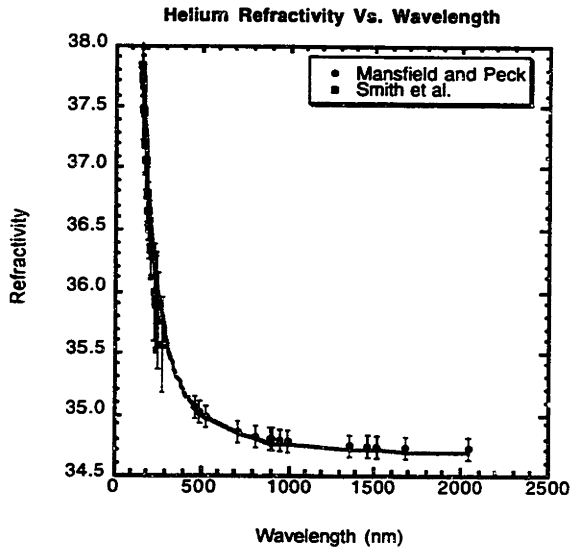

Figure 6.3: A plot of refractivity vs. wavelength (in units of nanometers) for helium. Circles represent data from Mansfield and Peck, while squares represent data from Smith *et al.* The line is a best-fit line to the data using Eq. 6.22, as discussed in the text.

Similarly, we tried fitting a Sellmeier equation to the combined hydrogen refractivity data. The best fit to the data yielded $a = 1.71399 \pm 0.00349 \times 10^4$ and $b = 126.357$. However, the χ^2 from this fit is 98.6, indicating a poor fit. A fit using Eq. 6.22 achieved $c = 1.35067 \pm 0.00128 \times 10^{-4}$ and $d = 1.3708 \pm 0.0250$, but with the astronomically high χ^2 of 5040! (Figure 6.4) Neither function fit the data well.

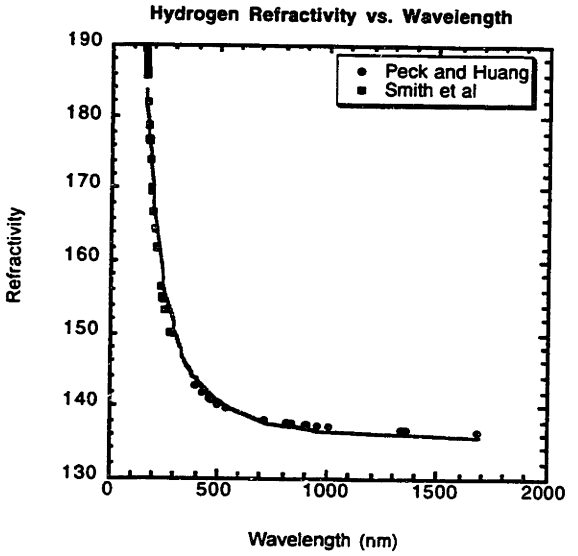

Figure 6.4: A plot of refractivity vs. wavelength (in nanometers) for hydrogen. Circles represent data from Peck and Huang, while squares represent data from Smith *et al.* The line represents the best fit to the data using Eq. 6.22, although the fit appears quite poor, as discussed in the text.

Peck and Huang expressed their best fit to their data in the form of a two-term Sellmeier function of the form:

$$\nu = \frac{a_1}{b_1 - m^2} + \frac{a_2}{b_2 - m^2} \tag{6.23}$$

where a_1 and a_2 are similar to a and b_1 and b_2 similar to b in Eq. 21. Fitting the data to this equation yields $a_1 = 1.34 \pm 0.03 \times 10^4$, $a_2 = 1.02 \pm 0.03 \times 10^4$, $b_1 = 343 \pm 300$, and $b_2 = 105.3 \pm 8.6$. (Figure 6.5) The χ^2 for this fit is 6.51. Peck and Huang get a somewhat different answer when they combine their data with that from Smith *et al.*, with $a_1 = 1.48956 \times 10^{-2}$, $a_2 = 4.9307 \times 10^{-3}$, $b_1 = 180.7$ and $b_2 = 92$ (no errors are given for their results.) Huang and Peck discarded two of their data points from their fit that were included in this fit; excluding these data, however, makes no appreciable difference in our results.

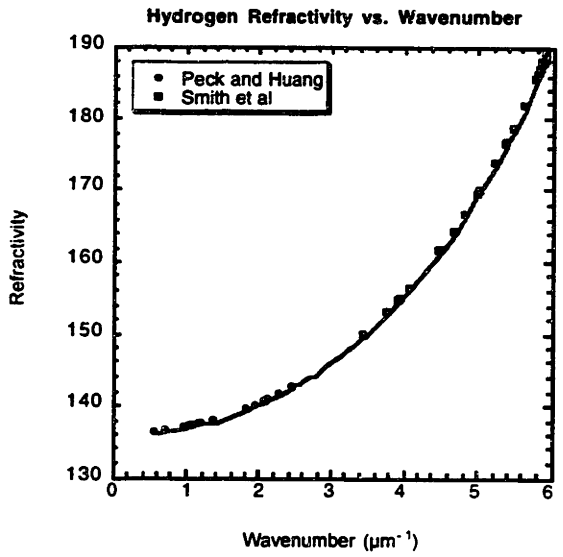

Figure 6.5: A plot of refractivity vs. wavenumber (in units of inverse microns, μm^{-1}) for hydrogen. Circles represent data from Peck and Huang, while squares represent data from Smith *et al.* The line represents the best fit to the data using a two-term Sellmeier function (Eq. 6.23) as discussed in the text.

These refractivity equations can be used to find the refractivity of helium and hydrogen at the desired wavelengths, which here are the middle wavelengths of the red and blue virtual diodes, 4589 and 3427 Å respectively. We use these refractivities and the refractivity ratio found from the data in Eq. 6.11. Since we assume that helium and hydrogen are the only components of Saturn's atmosphere, we can define $f(H_2) = 1 - f(He)$ and rewrite Eq. 6.11 as:

$$\frac{\nu_{4589}}{\nu_{3427}} = \frac{f(He)\nu_{He}(4589\text{Å}) + (1 - f(He))\nu_{H_2}(4589\text{Å})}{f(He)\nu_{He}(3427\text{Å}) + (1 - f(He))\nu_{H_2}(3427\text{Å})} \tag{6.24}$$

This can then be solved for $f(He)$:

$$f(He) = \frac{\nu_{H_2}(4589\text{Å}) - \frac{\nu_{4589}}{\nu_{3427}}\nu_{H_2}(3427\text{Å})}{\left(\nu_{H_2}(4589\text{Å}) - \nu_{He}(4589\text{Å})\right) + \frac{\nu_{4589}}{\nu_{3427}}\left(\nu_{He}(3427\text{Å}) - \nu_{H_2}(3427\text{Å})\right)} \quad (6.25)$$

The errors in this helium number fraction can be computed from the errors in the refractivity ratio:

$$\sigma_{f(He)} = \sqrt{\left(\frac{\partial f}{\partial(\nu_{4589} / \nu_{3427})}\right)^2 \sigma^2_{\nu_{4589}/\nu_{3427}}} \quad (6.26)$$

where the derivative in the above equation is:

$$\frac{\partial f(He)}{\partial(\nu_{4589} / \nu_{3427})} = \frac{-\nu_{H_2}(3427\text{Å})}{\left(\nu_{H_2}(4589\text{Å}) - \nu_{He}(4589\text{Å})\right) + \frac{\nu_{4589}}{\nu_{3427}}\left(\nu_{He}(3427\text{Å}) - \nu_{H_2}(3427\text{Å})\right)} +$$

$$\frac{\left(\nu_{He}(3427\text{Å}) - \nu_{H_2}(3427\text{Å})\right)\left(\nu_{H_2}(4589\text{Å}) - \frac{\nu_{4589}}{\nu_{3427}}\nu_{H_2}(3427\text{Å})\right)}{\left(\left(\nu_{H_2}(4589\text{Å}) - \nu_{He}(4589\text{Å})\right) + \frac{\nu_{4589}}{\nu_{3427}}\left(\nu_{He}(3427\text{Å}) - \nu_{H_2}(3427\text{Å})\right)\right)^2} \quad (6.27)$$

The helium mass fraction Y can be computed using the function:

$$Y = \frac{f(He)m_{He}}{f(He)m_{He} + f(H_2)m_{H_2}} \quad (6.28)$$

or, by noting that $f(H_2) = 1 - f(He)$:

$$Y = \frac{f(He)m_{He}}{f(He)(m_{He} - m_{H_2}) + m_{H_2}} \quad (6.29)$$

The error in Y is thus:

$$\sigma_Y = \sqrt{\left(\frac{m_{He}}{f(He)\left(m_{He} - m_{H_2}\right) + m_{H_2}} - \frac{m_{He}}{f(He)\left(m_{He} - m_{H_2}\right)} \right)^2 \sigma^2_{f(He)}} \qquad (6.30)$$

Analysis

The first key aspect of the analysis of the three FOS data sets using the above technique was the selection of a subset of the full data set for analysis. We chose to select sets of 1000 points at around the time of immersion or emersion for the background subtraction. The background subtraction process was similar to the linear method described in Appendix A, but applied separately to data from each diode and not to the summed data set. See Figures 6.6-6.8 for examples of the background subtraction results from the red virtual diode; data from the blue virtual diode are similar. Once the background was removed from the data, we selected a smaller subset, of 575 (0203 and 0204) or 700 (0305) points, either starting just at the time of immersion or ending at the time of emersion, for analysis. Using larger data sets would not have been more effective, since the additional data would have consumed more computer time and would have diminishing returns as the spikes and occultation features faded with time. Θ was calculated using the background-subtracted signal from all the diodes.

The background subtraction, as seen in Figure 6.6-6.8, is far from ideal and not as good as that when data from all the diodes are summed and used, as described in Appendix A. This is likely because of the limited amount of data available for each virtual diode to reduce errors. However, since we are interested primarily in the spikes in

the light curves, the analysis can adjust for this by moving the threshold for rejecting data up and down relative the model lightcurve to reduce the effect of these features.

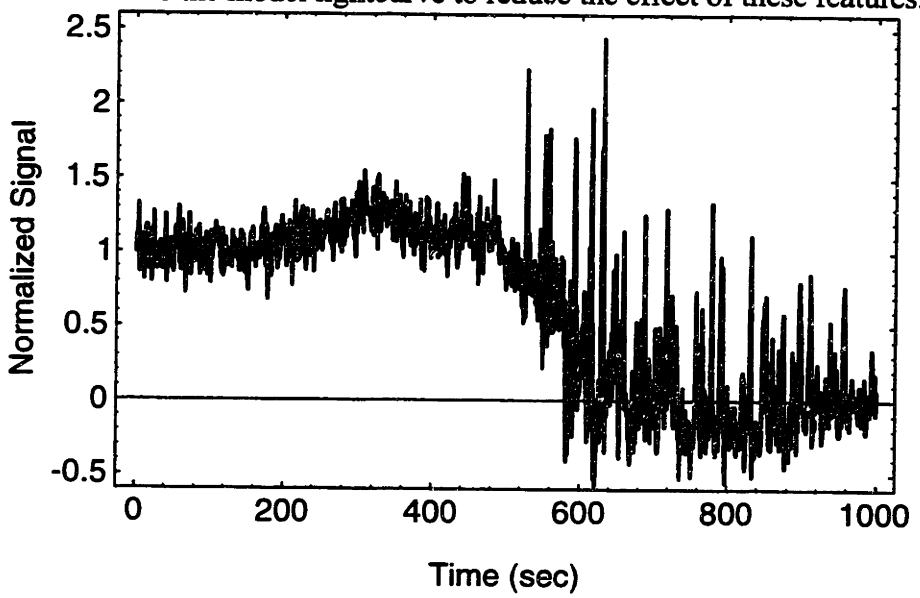

Figure 6.6: The background-subtracted red signal from the 0203 data. Time in seconds is on the x-axis, and normalized signal is on the y-axis. This data is the result of using the last 350 points as the basis for subtracting the background.

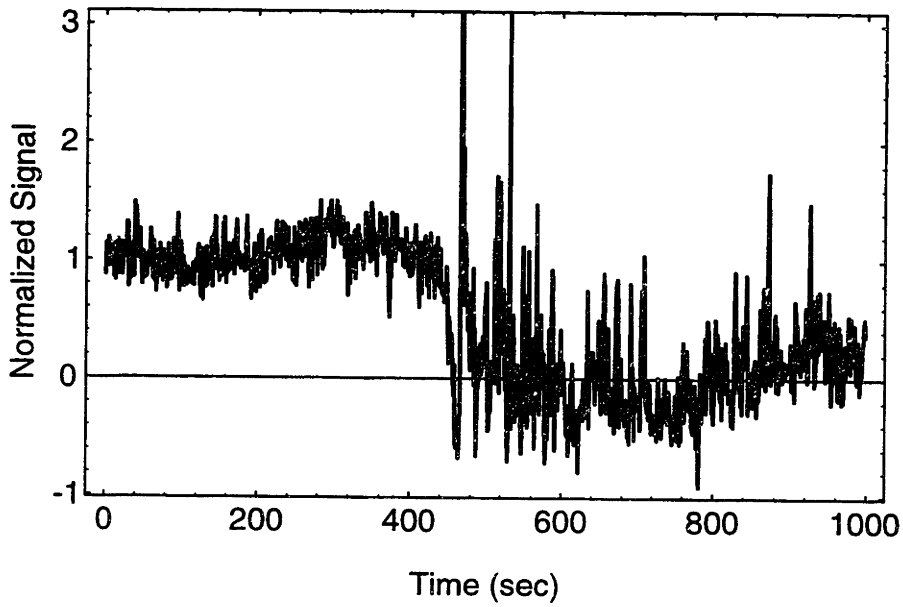

Figure 6.7: The background-subtracted red signal from the 0204 data. Time in seconds is on the x-axis, and normalized signal is on the y-axis. This data is the result of using the last 500 points as the basis for subtracting the background.

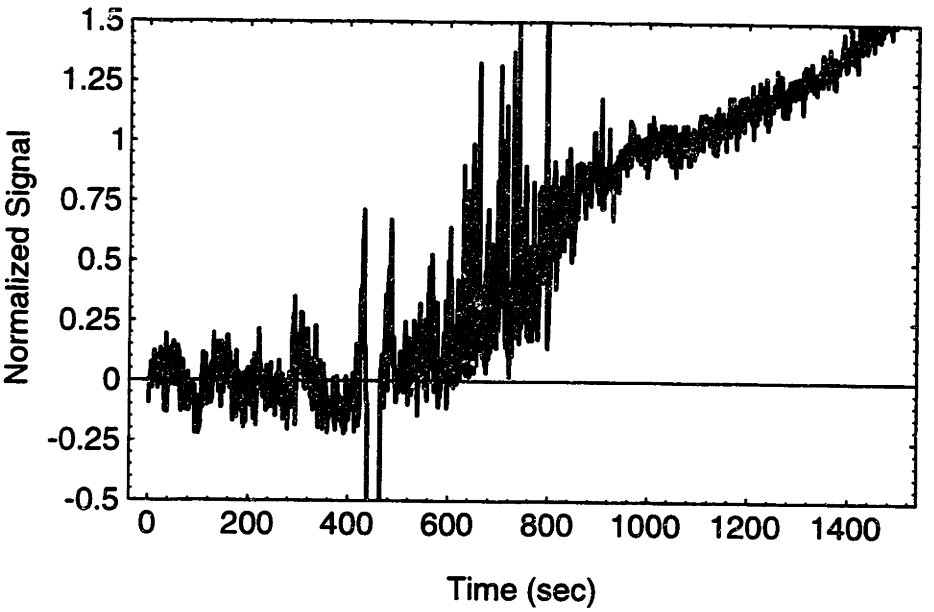

Figure 6.8: The background-subtracted red signal from the 0305 data. Time in seconds is on the x-axis, and normalized signal is on the y-axis. These data are the result of using the first 350 points as the basis for subtracting the background. Note that this background subtraction technique works poorly on the post-emersion data, however, our concern is on the data up through the emersion, so this is not a problem for this analysis.

As described in the previous section, we eliminated noise from the analysis by comparing the data to isothermal models. Separate models were computed for the red and blue data. The offsets (defined as data–model) between these models and the data were computed, if a data point fell below the threshold in either the red or blue data, that data point was excluded from the analysis in both data sets. We varied the threshold value to minimize the error. Plots of the sum of squared residuals versus refractivity ratios for each of the three data sets are shown in Figures 6.9 - 6.11, with the best-fit results listed in Table 6.1. The residual plots have a "jagged" appearance because of the existence of many local minima and maxima as the red and blue lightcurves are adjusted to one another.

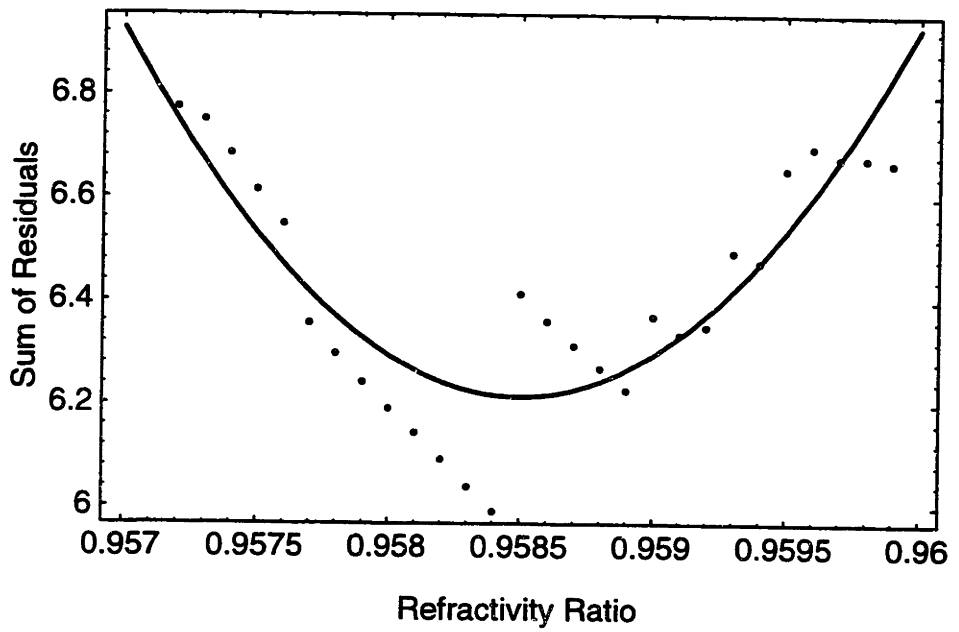

Figure 6.9: A plot of the sum of the squared residuals versus refractivity ratio for the 0203 data. The background subtraction and threshold value used here correspond to the best-fit value shown in bold in Table 6.1.

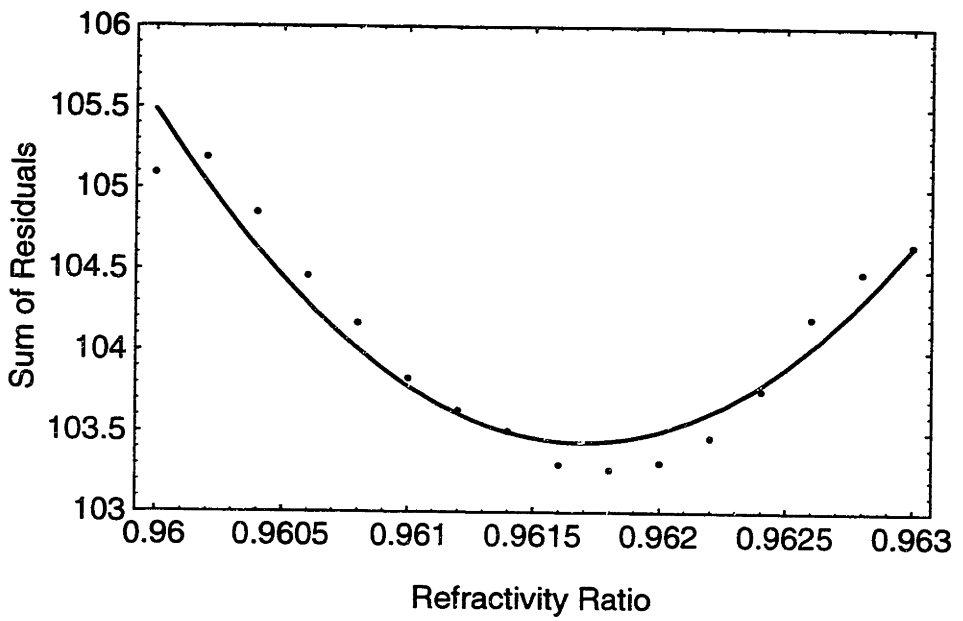

Figure 6.10: A plot of the sum of the squared residuals versus refractivity ratio for the 0204 data. The background subtraction and threshold value used here correspond to the best-fit value shown in bold in Table 6.2.

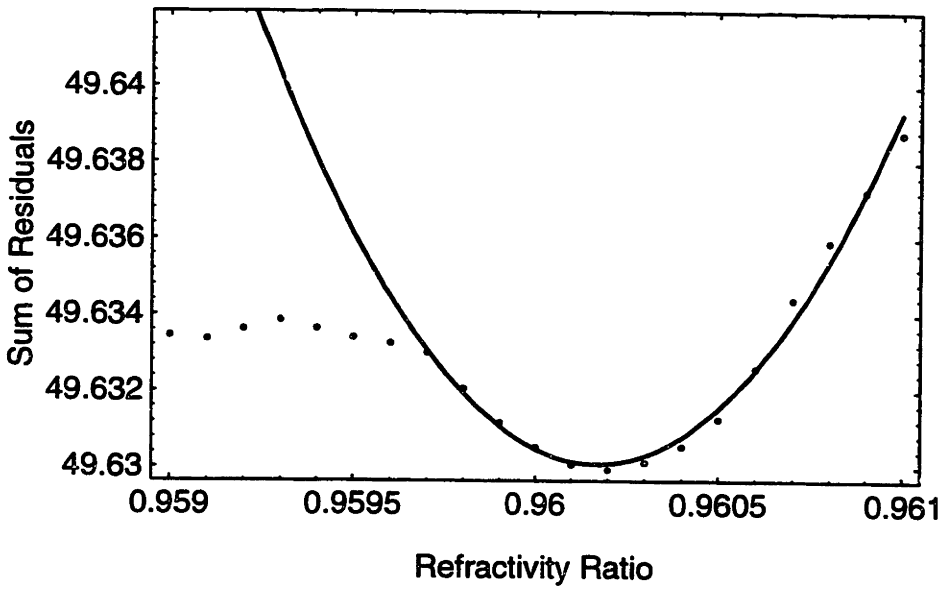

Figure 6.11: A plot of the sum of the squared residuals versus refractivity ratio for the 0305 data. The background subtraction and threshold value used here correspond to the best-fit value shown in bold in Table 6.3. The seven points on the left side of the plot were excluded from the fit.

Table 6.1: Initial *f*(He) and *Y* Results from HST FOS Data

Data Set	Refractivity ratio	*f*(He) (1 σ)	*Y*
0203	0.9586 ± 0.0002	0.0021 ± 0.0225	0.004 ± 0.046
0204	0.9618 ± 0.0005	0.337 ± 0.039	0.502 ± 0.044
0305	0.9602 ± 0.0024	0.194 ± 0.246	0.323 ± 0.344

The three data sets gave significantly different results. When the wavelengths of 3427 and 4589 Å were used to compute *f*(He), the results were non-physical, with *f*(He) either less than 0 or greater than 1. Instead, the wavelengths for the endpoints of the data were used, 3235 and 4781 Å, which provided more reasonable results for *f*(He) listed in Table 6.4. While the values of *f*(He) from the 0203 and 0204 data sets lie within the error bars of the 0305 result, the errors on the 0305 result are so large as to make it useless in an effort to precisely determine *f*(He). The errors on the 0203 and 0204 values are encouraging low, but the *f*(He) values are far apart from each other.

These results suggest two possible conclusions: that the data are not of high enough quality to extract f(He) using refractivity ratios, or that the technique itself is flawed.

Alternative Analysis

One problem that is clear from looking at the data is that the background subtraction of the data is imperfect, as evidenced by the irregular lightcurves displayed in Figures 6.6-6.8. While there may be little that can be done to improve the quality of the lightcurves using the current background subtraction technique, there may be ways to improve the quality of the lightcurve used for computing Θ, another key parameter of this analysis. The background subtraction techniques used on the summed data have also been imperfect, which may contribute to problems in the calculation of Θ and thus the refractivity ratio.

As an alternative technique, we used only the red and blue virtual diode data to generate a lightcurve to be used to compute Θ. Taking advantage of the fact that the colors of the star and of Saturn were somewhat different, we took the ratio of the red to the blue data. The data were smoothed using a moving boxcar average of the five points before and after each point to remove point-to-point random noise. Those data (Figures 6.12-6.14) show changes before and after an immersion or emersion: a slight change for the 0203 and 0204 immersion events, near Saturn's north pole, and greater for the 0305 emersion event near Saturn's equator. The smoothing generates an oscillation seen in all three data sets with a minimum period, from Fourier analysis, of ~7 seconds (multiples of this are also seen in the Fourier data). It is not clear if this is an artifact of the smoothing process—the minimum period is approximately 2.5 times longer than the smoothing interval—or if this a high-frequency "jitter" present in the data but lost in the point-to-

point noise when the data are not smoothed. The oscillation is not seen if the data are binned rather than smoothed, and the final results are the same for either method.

We then fit an isothermal model to this light curve (Chapter 3), fitting not only for r_H and λ_{Hi} but also the background and full signal values and the slope of the lightcurve (Table 6.2). The background was then subtracted from the data using the equation

$$\phi_{new}(t) = \phi_{old}(t) - [b - r(t) \cdot m] \tag{6.31}$$

where b and m are the background and slope values, respectively, from the isothermal model fit, r is the distance from the center of Saturn, ϕ_{old} is the original ratio data and ϕ_{new} is the background-subtracted data. The data are then normalized so that the full pre-immersion or post-emersion signal is 1. This new light curve can then used in place of the original background subtraction technique to generate Θ; alternatively, the model fit itself can be used to generate Θ, with the advantage of removing any anomalous noise in the data that could affect Θ and hence the refractivity ratios and helium fractions. We choose using the mode fit value of Θ in our analysis.

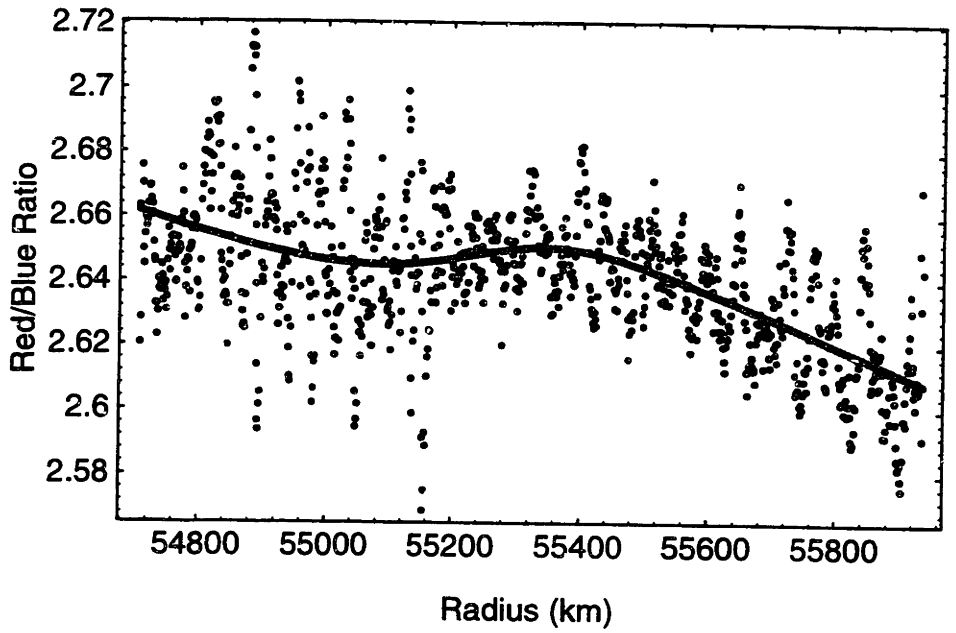

Figure 6.12: Red/blue ratio data versus distance for the 0203 data set. The ratio of red signal to blue signal is plotted on the y-axis, and distance from the center of Saturn is denoted on the x-axis. The gray line represents the best-fist isothermal model to the data. The immersion is visible in these data and can be fit to, although smoothing is required to bring out the difference between the pre- and post-immersion data.

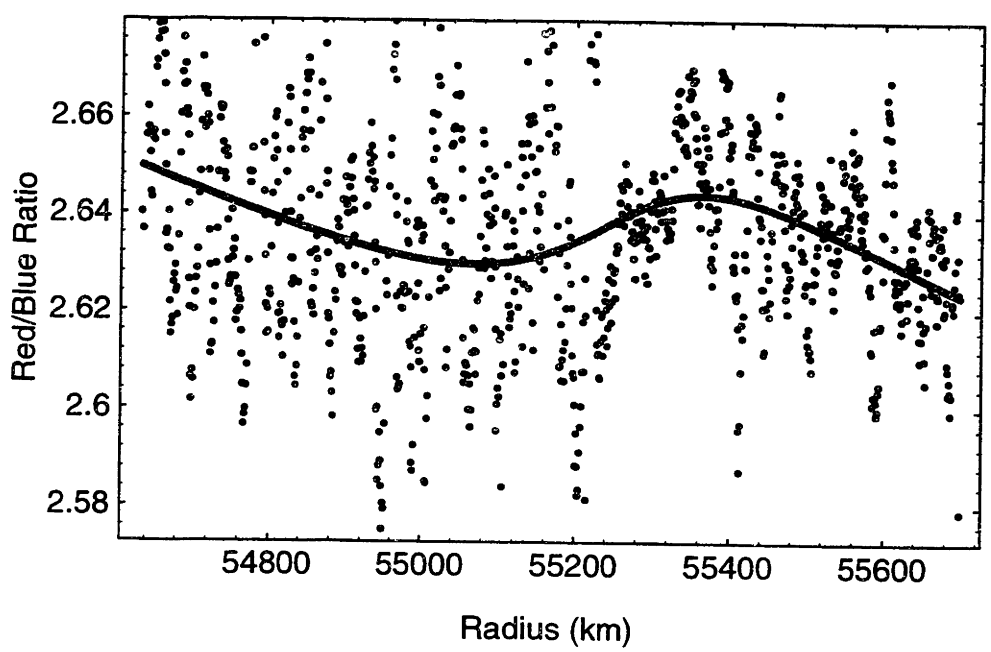

Figure 6.13: Red/blue ratio data versus distance for the 0204 data set. The ratio of red signal to blue signal is plotted on the y-axis, and distance from the center of Saturn is denoted on the x-axis. The gray line represents the best-fist isothermal model to the data. As with the 0203 data, the immersion is visible in these data and can be fit to, although smoothing is required to bring out the difference between the pre- and post-immersion data.

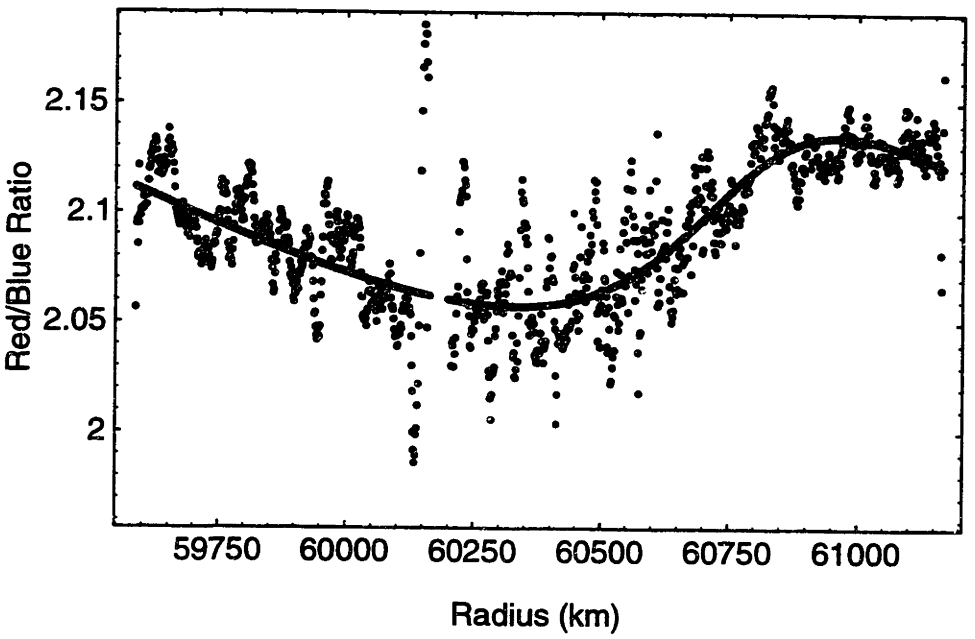

Figure 6.14: Red/blue ratio data versus distance for the 0305 data set. The ratio of red signal to blue signal is plotted on the y-axis, and distance from the center of Saturn is denoted on the x-axis. The gray line represents the best-fist isothermal model to the data. We note that while this data set has been smoothed to the same degree as the 0203 and 0204 sets, the difference between pre- and post-emersion signal is strong enough to be detected even without any smoothing.

Table 6.2: Parameters from the Isothermal Model Fits of the Color Ratio Data

Data Set	Background	Slope $\times 10^4$	Full	r_H (km)	λ_{Hi}
0203	7.28 ± 0.50	–0.84 ± 0.09	7.34 ± 0.51	55217 ± 18	736 ± 204
0204	6.80 ± 1.00	–0.76 ± 0.18	6.86 ± 1.02	55234 ± 15	984 ± 373
0205	9.54 ± 2.05	–1.25 ± 0.35	9.78 ± 2.12	60700 ± 26	619 ± 195

The results show a much better consistency among the various data sets for the refractivity ratio, as shown in Table 6.3 and Figures 6.15-6.17. However, the error bars here are large, and using the midpoint values for the wavelengths to generate the helium number and mass fractions exacerbate this. There results are consistent with a hydrogen-helium atmosphere on Saturn, but the errors prevent us from drawing further conclusions on its composition.

Table 6.3: Results from HST FOS Data Using Model Fit Values of Θ (128 diodes)

Data Set	Refractivity ratio	*f*(He)	*Y*
0203	0.9702 ± 0.0014	0.07 ± 0.24	0.13 ± 0.42
0204	0.9700 ± 0.0008	0.03 ± 0.15	0.06 ± 0.28
0305	0.9710 ± 0.0015	0.19 ± 0.21	0.32 ± 0.30

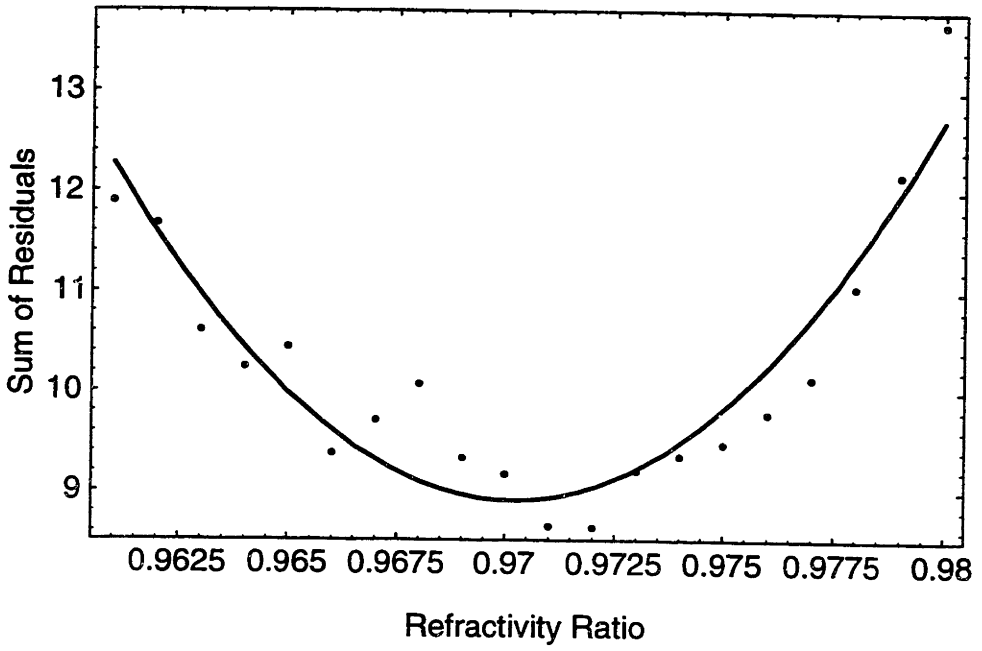

Figure 6.15: A plot of the sum of squared residuals versus refractivity ratio for the 0203 data. The line represents the best-fit solution to the data, used for determining the data.

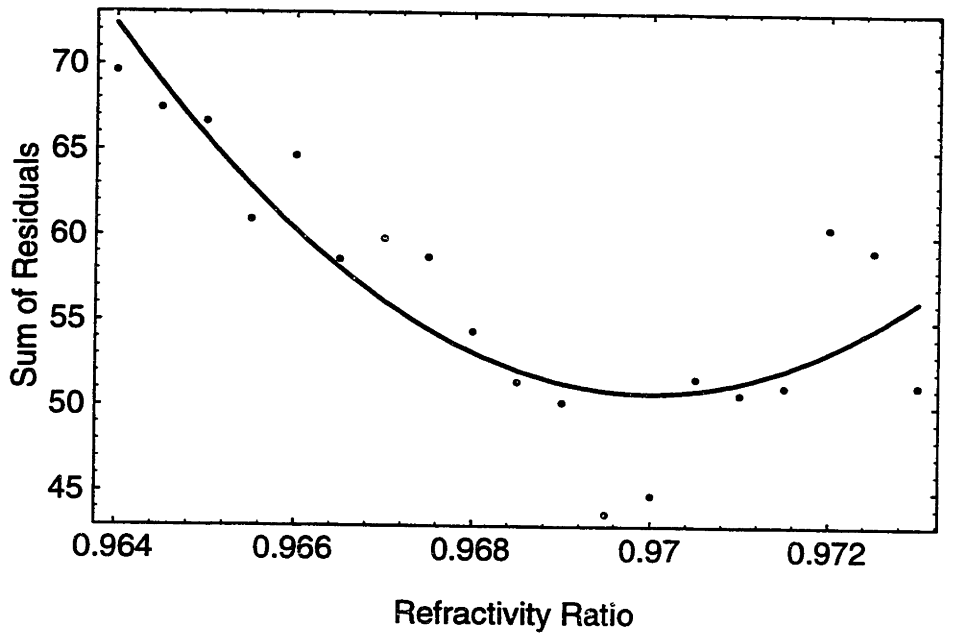

Figure 6.16: A plot of the sum of squared residuals versus refractivity ratio for the 0204 data. The line represents the best-fit solution to the data, used for determining the data.

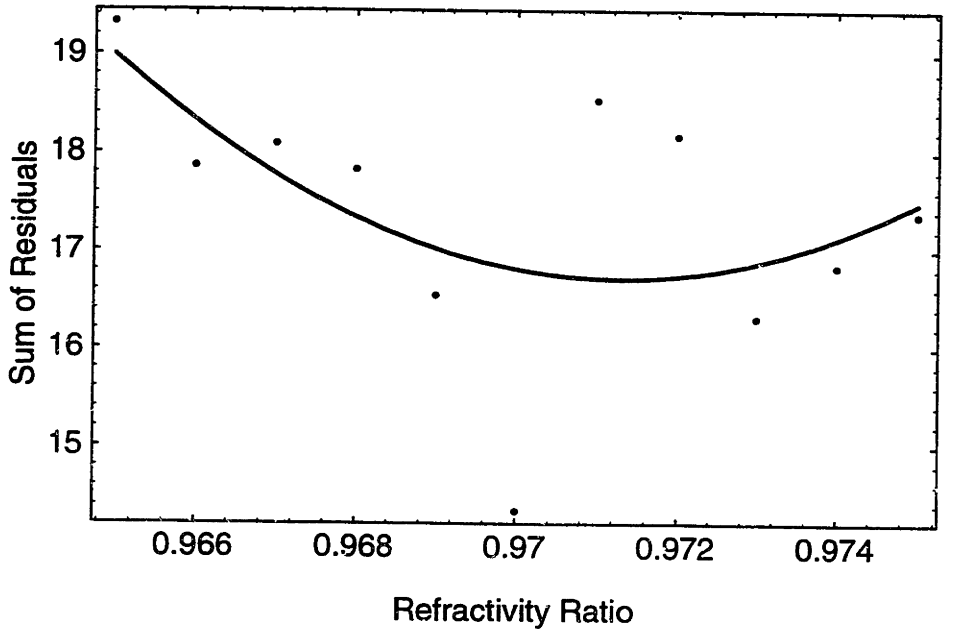

Figure 6.17: A plot of the sum of squared residuals versus refractivity ratio for the 0305 data. The line represents the best-fit solution to the data, used for determining the data.

One possible cause for the large errors in the 128-diode data is the large span of wavelengths summed together to create the virtual red and blue diodes, which would tend to smear out differences. To test this, we halved the data used, summing data from 64

diodes from each end of the data set. These results, shown in Table 6.4, show that the errors are reduced, but are still relatively large, as shown in the helium number and mass fractions in the table. These results are consistent with a hydrogen-helium atmosphere and Saturn, and appear to be larger than the results from the Voyager data found by Conrath *et al.* (1984).

Table 6.4: Results from HST FOS Data Using Model Fit Values of Θ (64 diodes)

Data Set	Refractivity ratio	f(He)	Y
0203	0.9660 ± 0.0009	0.22 ± 0.10	0.36 ± 0.13
0204	0.9652 ± 0.0009	0.13 ± 0.12	0.23 ± 0.19
0305	0.9650 ± 0.0009	0.10 ± 0.13	0.18 ± 0.21

To the test the validity of these results, we performed a number of tests to see how changing the data affected the results. We tested to determine the sensitivity of the results to different amounts of smoothing of the red/blue ratio data used to calculate Θ. The red/blue ratio data sets were smoothed by averaging the 3 points before and after each data point, and again using 7 points before and after each data point. We also tested the effects of using no smoothing, but found that the isothermal model could not properly fit the 0203 or 0204 data, likely because of the small difference between the pre- and post-immersion signal in the ratio data for those events. The results are summarized in Table 6.5. Increasing the number of points used in the averaging for the 0203 and 0204 data has only a small impact, while decreasing it has a much greater impact, perhaps because of the introduction of more point-to-point noise. Note that using no smoothing at all on the 0305 data produces a result similar to that obtained using the standard ±5 smoothing. However, unlike the smoothed results, the refractivity ratio varied considerably using the unsmoothed data if only a few points were removed from the data set.

Table 6.5 Effects on Refractivity Ratio of Different Smoothing Techniques (128 diodes)

Points Averaged for Smoothing	Refractivity Ratio		
	0203	0204	0305
± 3	0.9729 ± 0.0025	0.9690 ± 0.0010	0.9705 ± 0.0018
± 5	0.9702 ± 0.0014	0.9700 ± 0.0008	0.9710 ± 0.0015
± 7	0.9737 ± 0.0026	0.9700 ± 0.0015	0.9702 ± 0.0021
none	N/A	N/A	0.9703 ± 0.0015

To further test the effect of the number of diodes used on the results, we ran tests using only the 10 diodes at each end of the FOS data. The results, shown in Table 6.6 and Figures 6.18-6.20, show that the results are reasonably consistent with the larger diode sets, although the 10 diode set does not further reduce the errors, as was the case when going from 128 to 64 diodes.

Table 6.6: Results from HST FOS Data Using Model Fit Values of Θ (10 diodes)

Data Set	Refractivity ratio	*f*(He)	*Y*
0203	0.9617 ± 0.0014	0.26 ± 0.13	0.41 ± 0.16
0204	0.9597 ± 0.0007	0.03 ± 0.08	0.06 ± 0.15
0305	0.9613 ± 0.0010	0.22 ± 0.10	0.36 ± 0.13

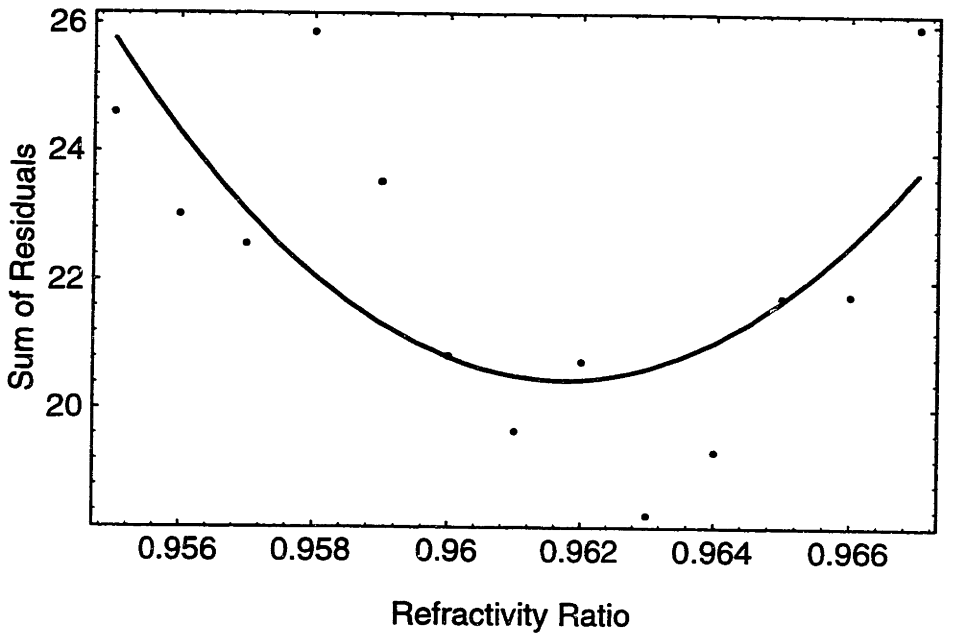

Figure 6.18: A plot of the sum of squared residuals versus refractivity ratio for the 0203 data, using only the 10 diodes from the red and blue end of the data. The line represents the best-fit solution to the data, used for determining the error in the minimum refractivity ratio.

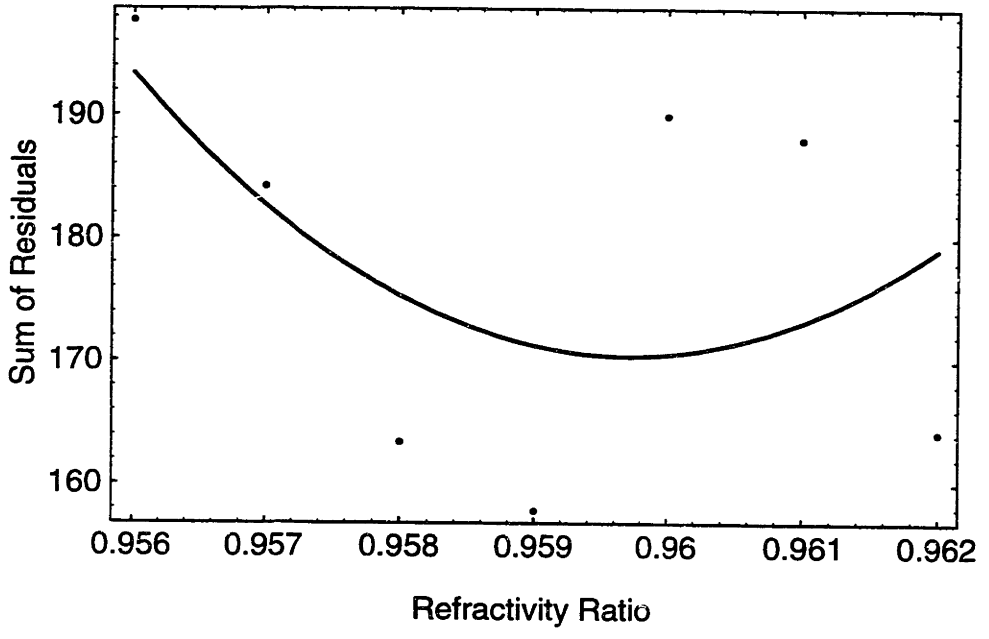

Figure 6.19: A plot of the sum of squared residuals versus refractivity ratio for the 0204 data, using only the 10 diodes from the red and blue end of the data. The line represents the best-fit solution to the data, used for determining the error in the minimum refractivity ratio.

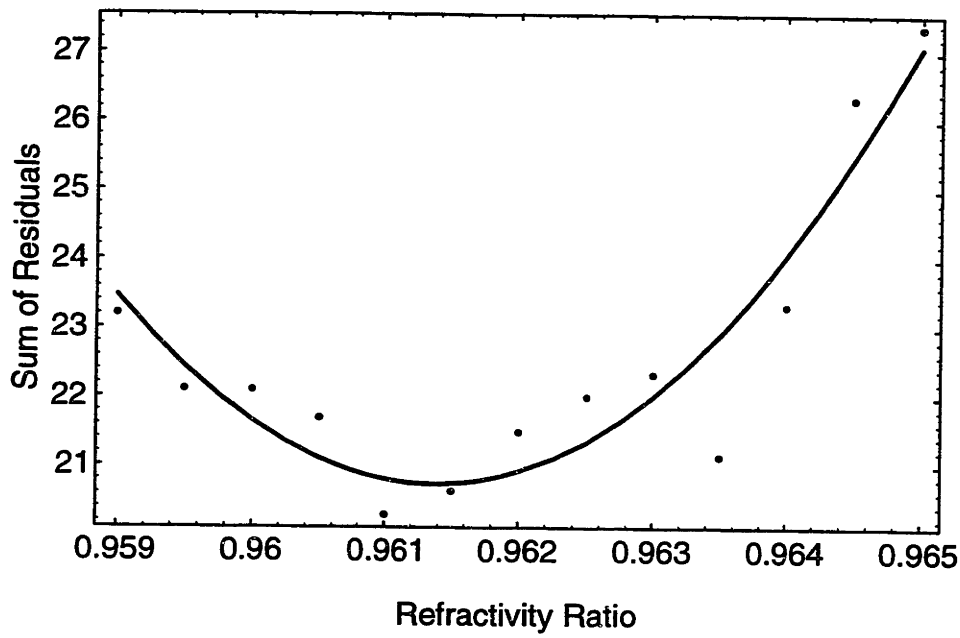

Figure 6.20: A plot of the sum of squared residuals versus refractivity ratio for the 0305 data, using only the 10 diodes from the red and blue end of the data. The line represents the best-fit solution to the data, used for determining the error in the minimum refractivity ratio.

Another source of error is the error in the refractivity functions for hydrogen and helium created by fitting one- and two-term Sellmeier functions to the refractivity data. If these errors are included, Eq. 6.26 becomes:

$$\sigma_{f(He)} = \sqrt{\begin{aligned}&\left(\frac{\partial f}{\partial(\nu_{4589}/\nu_{3427})}\right)^2 \sigma^2_{\nu_{4589}/\nu_{3427}} + \left(\frac{\partial f}{\partial(\nu_{He}(4589\text{Å}))}\right)^2 \sigma^2_{\nu_{He}(4589A)} + \\ &\left(\frac{\partial f}{\partial(\nu_{He}(3427\text{Å}))}\right)^2 \sigma^2_{\nu_{He}(4589A)} + \left(\frac{\partial f}{\partial(\nu_{H_2}(4589\text{Å}))}\right)^2 \sigma^2_{\nu_{H_2}(4589A)} + \\ &\left(\frac{\partial f}{\partial(\nu_{H_2}(3427\text{Å}))}\right)^2 \sigma^2_{\nu_{H_2}(4589A)}\end{aligned}} \qquad (6.32)$$

The derivatives in Eq. 6.32 can be found in a manner similar to that shown in Eq. 6.27. The errors in Eq. 6.32 beyond the error in the refractivity ratio (which comes from the occultation data) can be found from error analysis of the Sellmeier equations at the

appropriate wavelengths. We found errors in helium refractivity of 0.215×10^{-6} and 0.218×10^{-6} at 4589 and 3427Å respectively, or less than one percent of the refractivity at those wavelengths from the equation, and errors in hydrogen refractivity of 9.022×10^{-6} and 9.717×10^{-6} at 4589 and 3427Å respectively, equal to approximately 6 percent of the hydrogen refractivity values.

However, when we inserted these values into Eq. 6.32, we found errors in the helium number fraction of order 1, far higher than any other source of error. While this indicates that the results are sensitive to errors in the refractivity functions, it should also be noted that the error information available for the hydrogen and helium refractivities is far from ideal. The error bars for the refractivity data shown in Figures 6.2-6.5 are inferred from the information published in the papers from which they were obtained, as explicit error information was generally not available. The errors shown in the figures are conservative and thus may be overestimates of the actual error. As both Mansfield and Peck (1969) and Peck and Huang (1977) did not publish errors to their best-fit Sellmeier functions for helium and hydrogen refractivity, no comparison with the errors from our results are possible. Because of these uncertainties in the errors in the published data and results, we have chosen to neglect errors from the refractivity functions at this time, although it should be considered if and when more precise data are available.

Error in Θ

We also need to take into account the error contribution to the ratio by errors in Θ itself. By combining Eqs. 6.7 and 6.9 we can generate an expression for Θ as a function of the refraction angle θ:

$$\Theta = -\frac{D}{\upsilon}\theta \tag{6.33}$$

where υ is the velocity of the occultation and D is the Earth-Saturn distance. From Figure 6.1 we can also derive a geometric expression for θ:

$$\theta = \frac{y - r}{D} \tag{6.34}$$

By combining Eqs. 6.33 and 6.34 we get:

$$\Theta = -\frac{y - r}{\upsilon} \tag{6.35}$$

We note that, for isothermal atmospheres, r is equal to:

$$r = r_h - H\ln\left(\frac{1}{\phi} - 1\right) \tag{6.36}$$

Substituting Eq. 6.36 into Eq. 6.35 and simplifying yields:

$$\Theta = -\frac{y - r_h + H\ln\left(\frac{1}{\phi} - 1\right)}{\upsilon} \tag{6.37}$$

Computing the error in Θ above, we find:

$$\sigma_\Theta{}^2 = \frac{\sigma_y{}^2}{\upsilon^2} + \frac{\sigma_{r_h}{}^2}{\upsilon^2} + \left(\frac{\ln\left(\frac{1}{\phi} - 1\right)}{\upsilon}\right)^2 \sigma_H{}^2 + \left(\frac{H}{\upsilon\phi(1-\phi)}\right)^2 \sigma_\phi{}^2 + \left(\frac{\Theta}{\upsilon}\right)^2 \sigma_\upsilon{}^2 \tag{6.38}$$

We note that the error in y is insignificant, so the first term of Eq. 6.38 can be ignored. Similarly, the error in the velocity υ will be insignificant, so the last term can be ignored. The error in ϕ will be very small (see Chapter 3), and thus that term can also be ignored. The errors in the half-light radius r_h and the scale height H are of the same magnitude, but the largest effect on the error in Θ will come from the error in H near the top and the bottom of the lightcurve, when $\left|\ln\left(\frac{1}{\phi}-1\right)\right|$ is greater than 1.

This analysis shows that the best way to explore the errors in the refractivity ratio is to adjust the value of H and test its effects on the refractivity ratio analysis. We performed this by changing the value of H by $\pm 1\sigma$ and recomputing the model light curve (based on an isothermal model which includes H as one of its parameters), from which Θ is calculated. The results, shown below in Table 6.7, show that the best-fit refractivity ratio changes by approximately 1 σ or less when H was changed by 1 σ.

Table 6.7: Effects of Changing H on Refractivity Ratios (128 diodes)

Data Set	Normal	-1σ	$+1\sigma$
0203	0.9702 ± 0.0014	0.9698 ± 0.0020	0.9690 ± 0.0017
0204	0.9700 ± 0.0008	0.9710 ± 0.0012	0.9700 ± 0.0010
0305	0.9710 ± 0.0015	0.9710 ± 0.0015	0.9700 ± 0.0010

Summary and Discussion

Tests have shown that the technique outlined here can recover the refractivity ratio for the two mean wavelengths of observations, and thus provide the fraction of helium in Saturn's atmosphere (provided that the noise levels are sufficiently low).

However, with the current data and technique we are limited in the quality of the results and the conclusions that can be drawn from them. We find weighted means for the refractivity ratio from the three HST FOS data sets of 0.9604 ± 0.0005 using 10 diodes of data, 0.9654 ± 0.0005 using 64 diodes of data, and 0.9702 ± 0.0006 using 128 diodes of data. Using the 64-diode set as a representative sample, we find a helium fraction f(He) of 0.153 ± 0.064 and a helium mass fraction Y of 0.264 ± 0.096. The implications of this from a comparative planetology standpoint will be discussed further in Chapter 7.

We note that these values are higher than that found by Conrath *et al.* (1984), who found $Y = 0.06 \pm 0.05$ from Voyager data. In contrast, Stevenson (1980) notes that a drop in Y from 0.25 to 0.15 would be sufficient to generate the observed heat flux for at least 2 billion years, while greater drops would not add to the heat flux and would be difficult to reconcile with theoretical solubility models. In a revised work, Stevenson (1982) says that depletion of helium by a factor of two from cosmic abundances is sufficient to generate the observed heat flux. Gautier and Owen (1989), in a summary of work by several groups, find protosolar values of Y in the range 0.27-0.28. Our results show that Saturn has a helium content in its atmosphere higher than found by the Voyager data, but is also higher than predicted by Stevenson's (1980) theory, although the large error bars on our results make it uncertain whether this is a significant difference.

There are indications (Conrath, pers. comm.) that the Voyager data were miscalibrated, by comparing the Voyager results for Jupiter (Gautier *et al.* 1981) with Galileo data (Niemann 1996; Von Zahn and Hunten 1996), which gave a higher value for Y than the Voyager data. A reanalysis of the Voyager Saturn data by Conrath is in progress, and preliminary results suggest that the helium fraction derived from Voyager data is higher than originally published, bringing that data into closer accord with the FOS results.

Future Use of the Technique

The results could be improved with the use of higher-quality data sets. Three attributes of any future data sets that would improve their quality for this analysis are:

1) Use higher time resolution. The FOS data had a resolution of 0.26 seconds. At this low time resolution, spikes and other features in the occultation light curve can be smoothed out. Since the light curve at one wavelength will be smoothed out differently than the light curve at another wavelength (because one will be shifted in time compared to another, as illustrated in Figure 6.21) it becomes more difficult to match up identical features at different wavelengths.

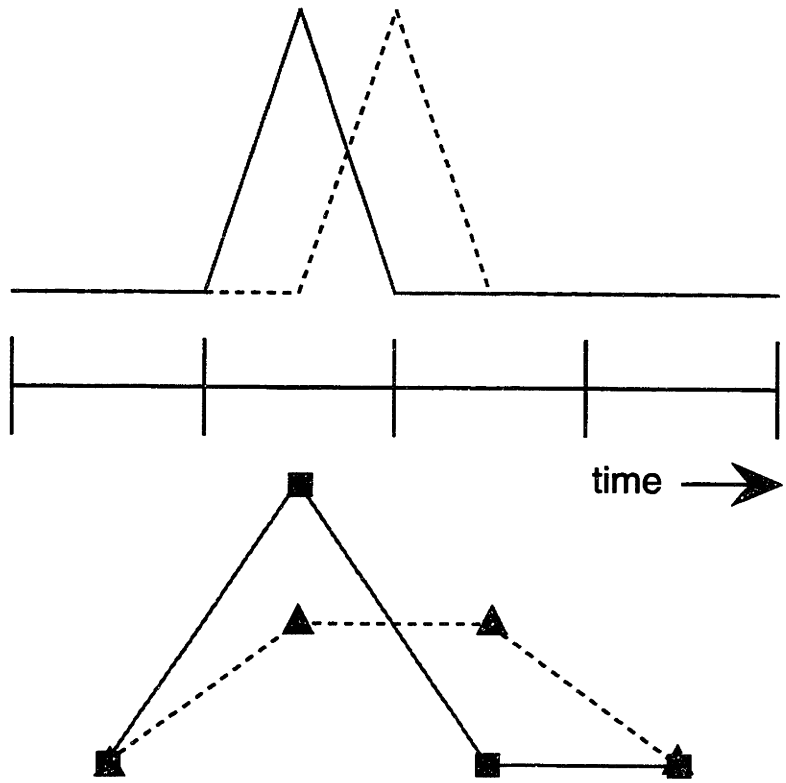

Figure 6.21: The effects of low time resolution. This cartoon illustrates one detrimental effect of using low time resolution data to compute refractivity ratios. The top half shows the actual signal of an occultation event, including a "spike", at two wavelengths with differing refractivities such that the "blue" (dashed) signal is delayed relative to the "red" (solid) signal. Time is plotted on the horizontal axis using arbitrary but equal segments. The bottom shows the data collected by a hypothetical instrument that records one data point per time segment. Since all the signal from the spike in the red data arrives within one time segment, the data collected matches the actual signal well. However, since the signal from the spike in the blue data is evenly split between two time segments, the data recorded by the instrument is a poor match to the actual signal. This mismatch causes problems when one tries to compute refractivity ratios by shifting the data sets. Using a higher time resolution increases the sampling and improves the fidelity of the data.

Elliot *et al.* (1974) used photometer data with a resolution of 0.01 sec for their analysis of f(He) in Jupiter's atmosphere. Samples of their data illustrate that many light curve features are smaller than 0.25 seconds in duration and feature similarities that might be lost if the data were smoothed out at a much lower time resolution, which is dependent on the shadow velocity of the event: faster events require higher time resolution. Such high data rates would be difficult to duplicate with modern CCD

systems, although systems optimized for high data rates and reading out only small subframes on the CCD could approach those data rates.

A guideline for the minimum data rate comes from the Fresnel scale, which limits the resolution of features to $\approx \sqrt{\lambda D}$. At Saturn's distance from the Earth and at the average FOS wavelength of 4000 Å, the Fresnel scale works out to approximately 0.75 km. The occultations observed by the FOS took place at velocities of 4-5 km/sec, so the Fresnel length scale works out to a time scale of 0.15-0.19 sec. Moreover, the Nyquist sampling theorem requires that data be sampled at twice the highest frequency present in the data. Applied here (where we are integrating, not sampling, signal), would require an interval of 0.075-0.095 sec. This requires a considerably faster data rate than the FOS data, which had an interval of 0.26 sec.

2) Make measurements at blue and ultraviolet wavelengths. The plots of refractivity versus wavelength and wavenumber (Figures 6.2-6.5) show that refractivity increases dramatically at shorter wavelengths. This means that even a small difference in wavelengths can result in larger refractivity differences than larger differences at longer wavelengths, where the refractivity curve is flat. The FOS data were taken in the bend in the curve of refractivity versus wavelength (Figures 6.3 and 6.4)

A problem with this approach is that common CCD detectors are usually less sensitive at shorter wavelengths than at longer visible and infrared wavelengths, and ground-based ultraviolet observations are problematic at best because of increasing atmospheric extinction at shorter wavelengths. Moreover, while the use of short wavelengths limits the amount of background flux from the occulting planet, it also makes observations of stars, particularly cooler, redder stars, more difficult. However, a spaceborne ultraviolet-optimized instrument with a moderate aperture (like the Hubble

Space Telescope, provided a suitably high-speed instrument were available) could observe occultations in the ultraviolet and short visible wavelengths without the problems of terrestrial telescopes

Another disadvantage of this approach is that it required even faster instruments that that needed for the FOS data. Using the Fresnel scale arguments shown above in point 1, moving the wavelength down to 2500 Å would reduced the Fresnel scale to under 0.6 km, with a corresponding change in the time scale (assuming occultation velocities of 4-5 km/sec) to 0.12-0.15 sec. Data taken at even shorter wavelengths, or data of an occultation event with a typical velocity of 25 km/sec, would further complicate matters.

3) Collect data at three or more wavelengths. Using only two wavelengths allows for only one refractivity ratio comparison and thus one value of f(He). Adding a third wavelength to the data permits two additional refractivity ratios and values of f(He) and permits one to check that the results are consistent with one another. If one value is inconsistent with the other two, or if all three are inconsistent with one another, it may imply problems with the data or the analysis that could not be detected using only a pair of wavelengths. Such a comparison could have been possible with the FOS data, as the instrument samples over a continuous series of wavelengths, but the problems computing the refractivity ratio over the greatest difference in wavelength would have been amplified trying to match up data over shorter spans of wavelength.

Better data could improve the quality of the helium mass fraction of Saturn's atmosphere, which could in turn be used to refine models of Saturn's interior, particularly the contribution helium precipitation has played on the composition of the interior. With

present data, though, we are able to confirm that helium precipitation is occurring in Saturn's atmosphere, at levels in accordance with existing theoretical predictions.

Chapter 7
Conclusions

Summary

Model Fits and Inversions

The model fit and inversion analysis of the five Saturn-occultation data sets explored here has provided results on Saturn's atmospheric structure that were compared with existing atmospheric models. The data sets confirmed latitudinal and seasonal variations in Saturn's temperature, with data collected in Saturn's north polar regions at the end of northern summer substantially warmer than equatorial or southern hemispheric data. Existing models of the atmospheric profile in this region, such as the L+inv model of Hubbard *et al.* (1997), may not be valid outside the equatorial regions, based on data collected at mid and high latitudes. Also, a new phenomenon was discovered: several data sets, including two of our HST FOS inversion profiles as well as IRTF data of the same event collected by Cooray *et al.* (1998) show a sharp downturn in temperature below 6-10 μbar. Latitudinal and seasonal effects cannot explain this downturn, nor can insolation effects or infalling dust or ice particles from the rings.

Gravity Wave Spectra

The inversion profiles of all five data sets examined in this work show small-scale variations in temperature and number density, which may be caused by vertically-propagating gravity waves. We constructed the power spectra of both the temperature and number density data from these profiles and fit them to theoretical functions (Fritts *et al.* 1988; Dewan 1997) for gravity wave spectra. Several key characteristics of these data, including the amplitudes and –3 slope of the power spectra as well as the temperature gradients of the data—which approach but do not exceed the adiabatic lapse rate—are all consistent with terrestrial observations which have been interpreted as saturating gravity

waves. However, other atmospheric phenomena, including convection, inversions, and shear, can also generate similar power spectra.

Helium/Hydrogen Ratio

We studied the relative abundances of hydrogen and helium, the two primary components of Saturn's atmosphere. Our HST FOS data sets were resolved in wavelength as well as time, and since the refractivity of these two components is a function of wavelength changes sharply at the wavelengths recorded in the FOS data, we can compare differences in refractivity at two wavelengths to find the ratio of the two atmospheric species. Our results yield a helium mass fraction Y of 0.26 ± 0.10. This value is significantly higher than reported by Conrath *et al.* (1984) from Voyager observations, but is marginally consistent with theoretical models for helium rainout in Saturn's atmosphere (Stevenson 1980; Stevenson 1982). However, the large error bars on the result make any definitive conclusions regarding the composition of Saturn's atmosphere problematic.

Comparative Planetology

Gravity Wave Spectra

Saturn is not the only planet for which power spectra of gravity waves have been determined. As noted in Chapter 4, gravity-wave spectra have been computed from theoretical models and sounding data for the Earth's atmosphere using a number of different techniques (Dewan and Good 1986; Smith *et al.* 1987; Fritts *et al.* 1988). Young *et al.* (1998) constructed the power spectra of upward-propagating gravity waves as detected by the Galileo probe in Jupiter's atmosphere. Sicardy *et al.* (1998) used stellar occultation data in a manner similar to this work to compute the power spectrum of

gravity waves in Titan's atmosphere. In all cases β, the logarithmic slope of the power spectrum, was approximately –3, the theoretical prediction for saturated gravity waves (Van Zandt 1982; Smith *et al.* 1987; Dewan 1997), although other atmospheric phenomena, including convection, inversions, and shear, can also generate similar spectra.

Some have previously suggested a "universality" of gravity waves in planetary atmospheres (Van Zandt 1982; Dewan 1997), which can be explored by further research into the power spectra of gravity waves in other atmospheres. There is already some evidence for saturated or breaking gravity waves in the upper atmospheres of other planets. Barnes (1990) argues that breaking gravity waves at altitudes of 40-80 km in the Martian atmosphere may adjust circulation patterns, explaining anomalous heating observed in the middle atmosphere above some regions of the planet. Previously, Krasnopolsky (1975) argued that a steep temperature gradient observed at altitudes of 160-200 km in the Martian atmosphere was caused by breaking and dissipating gravity waves.

Hinson and Jenkins (1995) and Leroy (1994) have shown evidence that vertically-propagating gravity waves exist in the atmosphere of Venus. In particular, Hinson and Jenkins found that the atmosphere in the region where gravity waves were observed had a lapse rate approximately the same as the adiabatic lapse rate in a region 35-60 km above the surface, suggesting that the gravity waves were saturated in that region. Lellouch *et al.* (1994) postulated that a variation in the mesopsheric zonal flow in the atmosphere of Venus may be caused by breaking gravity waves.

Temperature profiles of Neptune's atmosphere from several stellar occultations by the planet. Roques *et al.* (1994) have shown evidence of a 25 K increase in

temperature above 3 μbar. Roques *et al.* have interpreted this as evidence for gravity waves breaking in the planet's upper atmosphere. Models of Neptune's atmosphere also point to evidence of gravity wave breaking as the source for heating in the planet's atmosphere (McHugh and Friedson 1996).

These analyses strongly suggest that saturated gravity waves exist in the atmospheres of Venus, Mars, and Neptune, however, no gravity wave power spectra have been computed for these cases. As temperature profiles already exist for these bodies, calculation of the power spectra would be a straightforward way to obtain additional evidence for the existence of upward-propagating gravity waves in these atmospheres.

Hydrogen/Helium Ratio

Saturn's atmosphere is considerably depleted in helium relative to both solar ratios and the ratios observed in other gas giants. (Figure 7.1 and Table 7.1) Jupiter also shows a depletion of helium, although improved results from the Galileo probe (Niemann 1996; Von Zahn and Hunten 1996) now permit only a slight depletion from solar ratios. However, both Uranus and Neptune show results consistent with solar ratios, ruling out any significant helium depletion in these planets' atmospheres.

Table 7.1: Helium Mass Fractions for Solar System Gas Giants and Sun

Planet	Y	Reference
Jupiter	0.18 ± 0.04	Gautier *et al.* (1981)
	0.24 ± 0.01	Von Zahn and Hunten (1996)
Saturn	0.06 ± 0.05	Conrath *et al.* (1984)
	0.26 ± 0.10	This work
Uranus	0.26 ± 0.05	Conrath *et al.* (1987)
Neptune	0.26 ± 0.05	Conrath *et al.* (1991); Conrath *et al.* (1993)
Sun/Solar Neighborhood	0.28 ± 0.05	Heasley and Milkey (1978)
	0.28 ± 0.02	Pagel (1982)

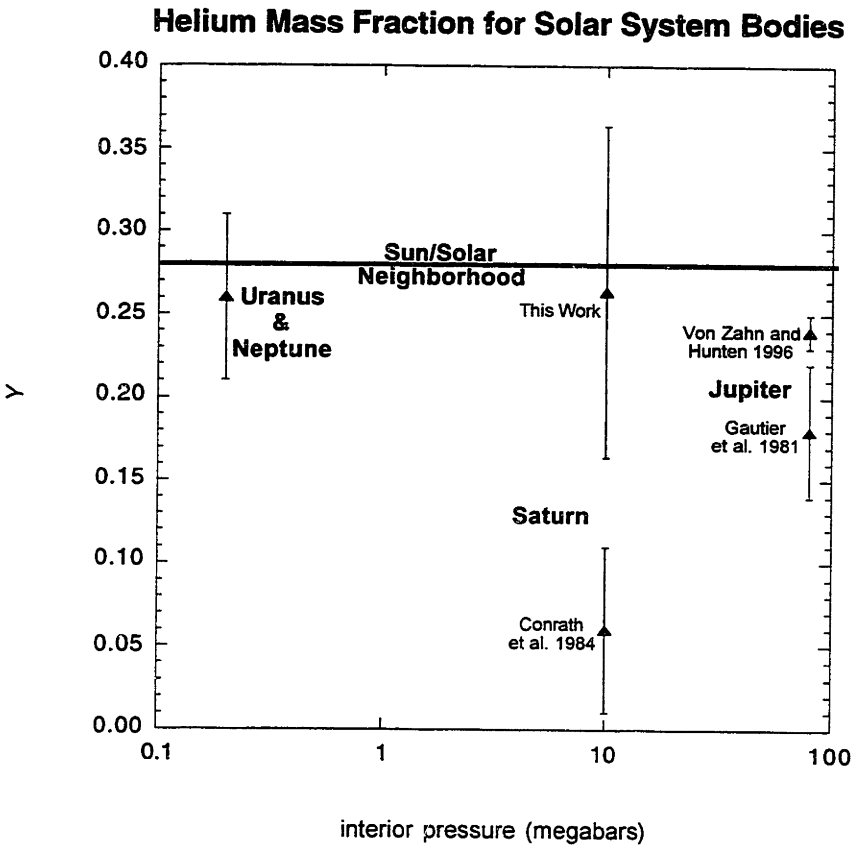

Figure 7.1: A plot of helium mass fractions for solar system bodies. The data plotted above is the same data shown in Table 7.1, shown here as a function of peak interior pressure experienced by the hydrogen inside each planet. Note the slight depletion of helium in Jupiter and the greater depletion in Saturn. Also note that the initial results for both Jupiter and Saturn, based on Voyager data, have been revised upward by Galileo probe data and this work. Uranus and Neptune maintain near-solar helium mass fractions because the hydrogen in their interiors does not reach high enough pressures to convert into a metallic form.

Gautier and Owen (1989) explain this difference in values for Y on the internal pressures of the gas giants. At pressures greater than 3×10^6 bars, when hydrogen exists in a metallic form, helium will become immiscible within the hydrogen once temperatures drop below 10^4 K (Stevenson 1982). On Saturn this occurs after about 2 billion years, as the core loses its initial heat of formation, at which point helium begins

to rain out of the atmosphere to collect in the core of the planet. This estimate for the time, though, is based solely on measurements of Saturn's current heat flux; Stevenson (1982) points out that uncertainties in theoretical solubility estimates for helium in metallic hydrogen make it difficult to make absolute theoretical predictions on the date helium precipitation began or helium mass fraction.

This process also occurs inside Jupiter, but since the planet is larger, it lost its heat more slowly, and thus has retained more helium in its atmosphere, explaining the helium mass fraction that is slightly depleted compared to solar levels, but still higher than Saturn's. Uranus and Neptune, on the other hand, have peak hydrogen pressures of only 2 $\times 10^5$ bars at the edge of their rock-ice cores (Hubbard and Stevenson 1984), below the level at which hydrogen can exist in metallic form. Helium will not become saturated and rain out in the interiors of these worlds, and thus should retain their primordial helium quantities in their atmospheres. This is borne out by the data, which show helium mass fractions near solar levels for both Uranus and Neptune.

Future Plans

Future Occultations

Stellar occultation studies provide a useful "snapshot" of the atmosphere of the planet in the microbar pressure range, at a given time and latitude of the planet. However, a single occultation data set provides no information on spatial or temporal variability in the atmosphere in that range. While the data sets used in this work do provide better spatial and temporal resolution that previous works, the combined Saturn occultation data sets available are rather sparse. Additional data sets at different times and latitudes would be useful to understand spatial and temporal variations in temperature as well as look for any variations in the gravity wave power spectra.

One way to obtain additional data is through additional stellar occultation observations. Bosh and McDonald (1992) list a set of Saturn occultation candidate stars through the end of 1999. While most of the list has already been exhausted, four good candidate events remain for the end of 1999, and are listed below in Table 7.2. The "best observing locations" listed below are based on the portions of the Earth at night that can view the event at the closest approach time (given in the first two columns of the table.) Based on the geometry and velocity of the event, the best places to observe immersion and/or emersion may be elsewhere.

Table 7.2: Upcoming Saturn Stellar Occultation Events in 1999

Date	Time (UT)	GSC Star	V Mag.	Vel. (km/s)	Best Obs. Locations
1999 Oct 15	0503	0647-00237	13.0	17.5	N. and S. America
1999 Nov 24	1027	0645-00956	12.9	18.4	Western. N. America, Hawaii, Australia
1999 Dec 3	0431	0645-01130	9.1	6.4	N. and S. America
1999 Dec 31	0031	0645-00845	13.2	6.1	Eastern N. and S. America, W. Europe

Of particular interest in the 1999 December 3 event, which will feature not only a bright star but a slow immersion and emersion speed, which will improve the resolution of the data. The 1999 December 31 event also has a low velocity, but with a considerably dimmer star.

Groundbased observations have been successfully conducted at the NASA Infrared Telescope Facility (IRTF), using their NSFCAM infrared camera. This has

proven to be a capable instrument for Saturn occultation observations, both of the 1996 event in this work as well as a 1995 occultation (Cooray *et al.* 1998). An advantage of infrared wavelengths is that the observations can be performed in wavelength bands where the planet is relatively dark, making the observations easier to conduct. Saturn occultation observations can also be considered at other wavelengths and other observatories, depending on the availability of high-speed instruments.

Another option for observing stellar occultations is through airborne astronomy. Aircraft equipped with telescopes can fly to regions of the planet where a particular event is visible on the Earth, and can observe the event at altitude to avoid inclement weather. The Stratospheric Observatory for Infrared Astronomy (SOFIA), a 747SP aircraft equipped with a 2.5-meter telescope, will be available to observe occultations in 2001. One of the instruments available on SOFIA will be the High-Speed Occultation Photometer and Imager (HOPI), a visible-light CCD camera capable of intervals as short as 0.5 milliseconds.

Our Hubble Space Telescope data came from the Faint Object Spectrograph, an instrument removed from the telescope during the second servicing mission in February 1997. Alternative instruments are available, however. The Fine Guidance Sensors (Benedict *et al.* 1992) are capable of collecting data with time intervals as small as 0.025 sec at wavelengths from 4600 to 7000 Å. Although the FGS was successfully used for observations of a stellar occultation by Triton in 1997 (Elliot *et al.* 1998), but the FGS could not be used for Saturn occultations because its brightness limit would be exceeded. The Space Telescope Imaging Spectrograph (Woodgate *et al.* 1997) is capable of extremely high time-resolution data: intervals as small as 0.000125 sec at wavelength ranges of 1100-3000 Å are possible in TIME-TAG mode. This would be very useful for further studies of the helium fraction in Saturn's atmosphere, as both the small time

intervals and the ultraviolet wavelengths used would greatly improve the quality of the data.

Cassini

The Cassini spacecraft mission to Saturn (Kerridge *et al.* 1992; Matson 1996) was launched 1997 October 15 and is scheduled to arrive at Saturn in July 2004 for a four-year primary mission. Cassini will be able to provide extensive data on Saturn's atmosphere at a frequency not possible from the occasional stellar occultation. The instrument will also be able to determine the composition of Saturn's atmosphere.

There are several instruments on Cassini that will be able to probe the structure and composition of Saturn's atmosphere in the microbar and adjacent regions. The Composite Infrared Spectrometer (CIRS) (Kunde *et al.* 1996) is a set of spectrographs that will be able to detect thermal emissions from Saturn at wavelengths from 7 to 1000 μm to a resolution of one to two scale heights. In particular, the instrument will be able to provide limb profiles at a wavelength of 7.7 μm to pressure levels above 1 μbar (Taylor *et al.* 1998); however, Taylor *et al.* note that limited sampling in temporal and spatial domains will make measurements of upper altitude waves difficult. Complementary studies of regions of the atmosphere above and below the microbar range will be provided by the Ultraviolet Imaging Spectrograph (UVIS) and Radio Science Subsystem (RSS) instruments, respectively.

These instrument characteristics make Cassini particularly well-suited for studies of the temperature and pressure profiles of the atmosphere, as the instrument will be able to provide repeated close looks at the atmosphere over the course of several years. Since Cassini will arrive at Saturn nearly half a Saturnian year after the 1995 FOS and 1996 IRTF observations, Cassini's data will complement those observations by studying the

changes in the temperature profiles in the northern and southern hemispheres in different seasons. As Cassini will be at Saturn nearly a full Saturnian year after the Voyager 1 and 2 flybys, its data will serve as a check on the previous Voyager results. Cassini's CIRS data should also provide an additional check on the helium mass fraction of the atmosphere.

One area Cassini data may not be of help is studies of gravity wave propagation. The limited resolution of the CIRS instrument is far less than the resolution available from Earth-based stellar occultation studies, and that better resolution is needed to resolve small-scale gravity waves. Future studies of gravity waves in Saturn's upper atmosphere will have to continue to rely on Earth-based stellar occultation observations until a future spacecraft with a higher-resolution instrument and/or an atmospheric probe is sent to Saturn.

Appendix A
Background Subtraction of FOS Emersion Data

Introduction

In the absence of a high speed photometer on the Hubble Space Telescope (HST), the Faint Object Spectrograph (FOS) could be used to take high time-resolution spectrally-resolved data until its removal from HST in February 1997. The signal recorded by the instrument could then be analyzed to look for differences in the lightcurves for different wavelengths, or they could be summed to provide a single value for the signal measured for each integration, like an ordinary photometer.

Unlike high-speed imaging data obtained by instruments like PCCD and NSFCAM, where information about the location of the star, planet, and any other background effects can be determined, FOS data provide only the total signal that passed through the entrance aperture, requiring other techniques to determine and remove the background. This is a critical problem with the occultations observed by the FOS: in each case the HST tracked the star, rather than remaining fixed on the limb of the planet, so the amount of background from the disk of the planet varies with time. Therefore, a technique is needed to calculate the background signal level and remove it from the data.

Limb Modeling Technique

The primary source for background signal in these data is from the disk of Saturn. Because the disk of the planet is much larger than the aperture of the FOS, and because the disk of the planet is not uniform in brightness, a successful removal of the planet

signal requires knowledge of the location of the aperture on Saturn's disk at any given time. This information is available for the FOS data in the form of f and g coordinates of the star, if we assume that the star is centered in the aperture. FOS observations are conducted in an effort to get the target within 0.04 arcsec of the center of the aperture (Leitherer 1995), so this assumption is valid if the relative error between the coordinates of the star and the ephemeris of Saturn is negligible.

To compute the brightness of the portion of the disk visible in the aperture, we use the technique of Linear Limb Darkening discussed in Karkoschka and Tomasko (1992) (hereafter KT92). This technique allows one to compute the reflectivity of an object using the angle of the incident and reflected rays, the phase angle of the observations, and the full-disk and half-disk geometric albedos of the object. The half-disk albedo of a planet is defined as the geometric albedo of the disk of a planet from the center to one-half its radius. For a uniform disk the two albedos would be equal; for a limb-darkened disk the half-disk albedo would be greater than the full-disk albedo. KT92 define the reflectivity as:

$$I / F = p(\alpha)\{g + 2.5(h - g)(1.5\mu_1 - 1)\}\mu_0 / \mu_1 \qquad \text{(A.1)}$$

where I/F is the reflectivity, $p(\alpha)$ is the phase angle function, g is the full-disk geometric albedo and h is the half-disk albedo, μ_0 is the cosine of the zenith angle of the incident ray, and μ_1 is the average of the cosines of the zenith angle for the incident and reflected rays.

Karkoschka and Tomasko, in their studies of Saturn, published values of g and h based on wavelength and latitude on the planet. While the latitude range includes the latitudes probed in the FOS occultation data sets, the shortest wavelengths listed, 460 nm,

is at the red end of the FOS data. To compensate we used a linear extrapolation of g and h down to 400 nm, the center of the FOS data. This seems a reasonable assumption, since both g and h follow a linear trend below 650 nm (Figure A.1). This method gives the following functions for $g(\lambda)$ and $h(\lambda)$:

$$g(\lambda) = -0.280487 + 0.001408\lambda$$
$$h(\lambda) = -0.511257 + 0.0020835\lambda \qquad \text{(A.2)}$$

With this method we compute g to be 0.2827 and h to be 0.3221 at 400nm.

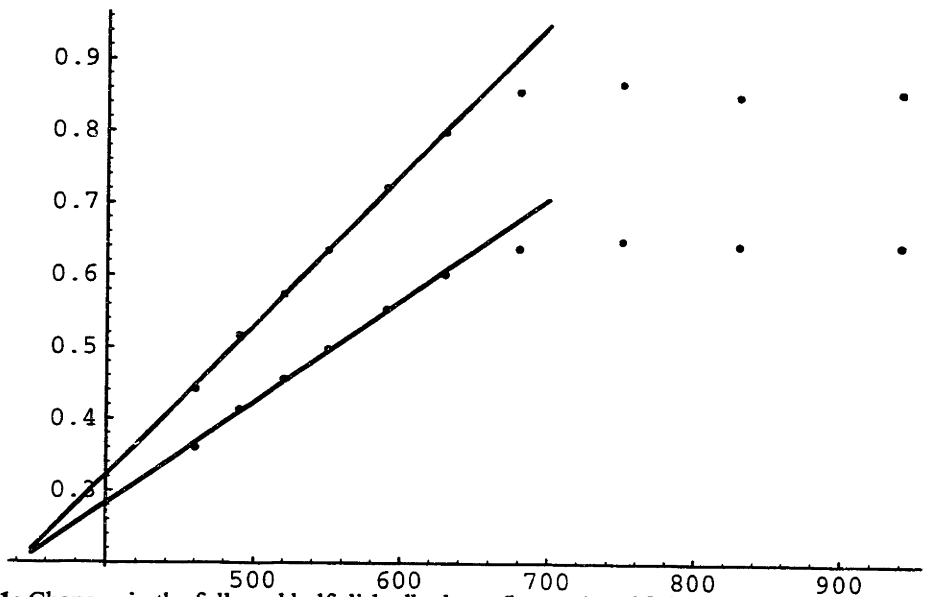

Figure A.1: Changes in the full- and half-disk albedos g (bottom) and h (top) as a function of wavelength, displayed on the x-axis here in nanometers. The points give the values of g and h from KT92. The lines are the least-square fits to the points below 680 nm wavelength. The lines are extrapolated to values less than 400 nm, the wavelength used to find the values of g and h for the limb darkening analysis.

This limb darkening function can then be used to construct a model lightcurve of the light from the disk of Saturn. For each data point we consider the aperture of the FOS, which is 0".86 in diameter, or 5,745 km at Saturn's distance from Earth at the time of the observations. We then superimpose on this aperture a 5800 × 5800 km grid centered on the aperture, with each grid element 50 × 50 km. For each grid element we compute whether its center is within the aperture, and discard those that are not. For each

remaining grid element we check to see if it is within the disk of the planet at that time. We do this by assuming a simple elliptical shape for the planet and using the f and g value of each grid element to see if would be within the disk. For those that are within the disk, the reflectivity is computed using Eq. A.1. The reflectivities computed for all the grid elements are summed to provide the total reflectivity of the planet as seen at the FOS at that time. This process is repeated for other data points. In practice, the background curve is very smooth, and thus only every 50th or 100th data point needs to be calculated with interpolation sufficient for the remainder of the data, making this procedure less computationally expensive. The results are then scaled to the actual signal recorded, and the fit is compared.

This technique, however, did not provide a satisfactory result: the model fit the data well at those times when the disk of the planet dominated the signal, but failed to accurately model the background as the disk moved out of the aperture. (Figure A.2) One possible explanation for this is an incorrect extrapolation of g and h to shorter wavelengths as described above. Another is that the albedos may not be accurate near the limb, a concern noted by KT92. A third possibility is that scattered light caused by the point-spread function (PSF) of the FOS may play a significant role in the distribution of signal, especially as the disk exits the aperture, contributing to the poor fit. These concerns are all addressed below.

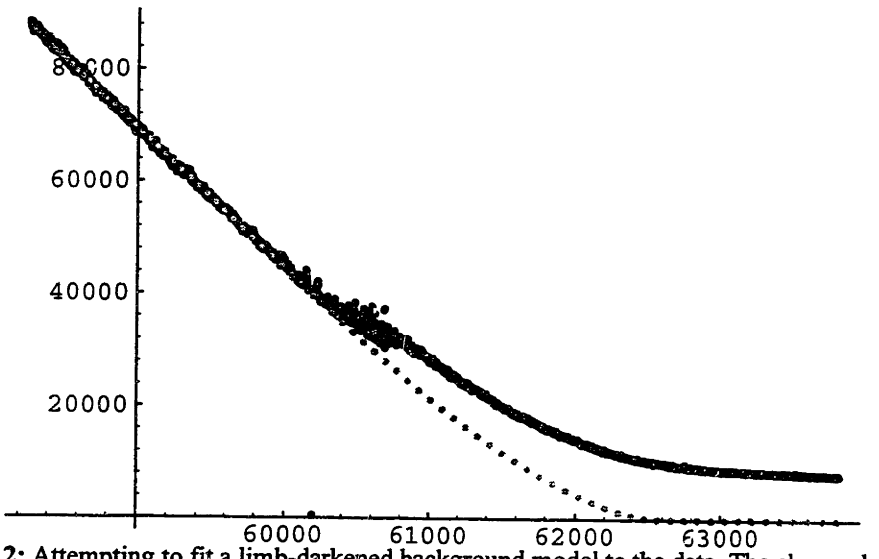

Figure A.2: Attempting to fit a limb-darkened background model to the data. The above plot displays signal counts vs. radius (in km) for the 0305 data set. The black line is the actual data, the gray circles are the background model. Note the poor fit of the background model to the data after the emersion event (the series of oscillations in the data at around the 60,500 km level).

One solution to the problems described above is to incorporate the limb-darkening model into the overall isothermal model for Saturn's atmosphere. In this case g and h become two additional parameters in the least-squares fit (with the background and full signal levels, the half-light radius, and energy ratio.) The isothermal model is then run on the raw (no background subtraction) data, and the least-squares iteration finds the combination of these values that best fits the data.

For this procedure to succeed, we must know how the background model behaves to different values of g and h. Model lightcurves are calculated as described above (except that a 100 × 100 km grid is used to expedite the calculations) for values of g and h from 0.15 to 0.35 in increments of 0.01. All the models can be fit by a simple polynomial expression:

$$S = c_0\left[c_1(r-c_2)^2 + c_3\right] \tag{A.3}$$

where S is the signal, r is the distance from the center of the disk to the center of the FOS aperture at a given time, and c_0, c_1, c_2, and c_3 are coefficients of the fit that are all functions of g and h. The addition of a linear term to Eq. A.3 does not improve the fit. In cases where the computed value of S was less then zero the result was set equal to zero, since the negative result corresponded with the extrapolation of the polynomial beyond the point where the disk of the planet was no longer visible in the aperture. The coefficients were computed for each set of g and h values used in the models, and polynomial fits for c_1, c_2, and c_3 were then computed (it proved more expedient to have the model interpolate the value of c_0 from the array of g, h and c_0 values computed above because of nonlinearities in the behavior of c_0 for some values of g and h.) The polynomial fits for c_1, c_2, and c_3 were:

$$c_1(g,h) = 0.00131g + 0.00503h \tag{A.4}$$

$$c_2(g,h) = 67760 + 168900g - 17600h - 402000gh - 151800g^2 + 579100h^2 + 279200g^2h + 268600gh^2 + 45750g^3 - 622700h^3 \tag{A.5}$$

$$c_3(g,h) = -14790 - 1.0220\times10^6 g + 1.0211\times10^6 h + 1.919\times10^7 gh - 9.0886\times10^6 g^2 - 1.0607\times10^7 h^2 + 6.567\times10^6 g^2h - 2..665\times10^7 gh^2 + 3.9896\times10^6 g^3 + 1.6580\times10^7 h^3 \tag{A.6}$$

We incorporated this background model as a module in the overall isothermal model fit and ran the fit on the data from the 0305 emersion event, the only HST FOS data set which accurately recorded an emersion. This resulted in a somewhat better fit, especially for the data just past the emersion itself, but failed to fit the signal towards the end of the data set as the disk of Saturn exited the aperture, leaving only the star and any remaining background signal (Figure A.3).

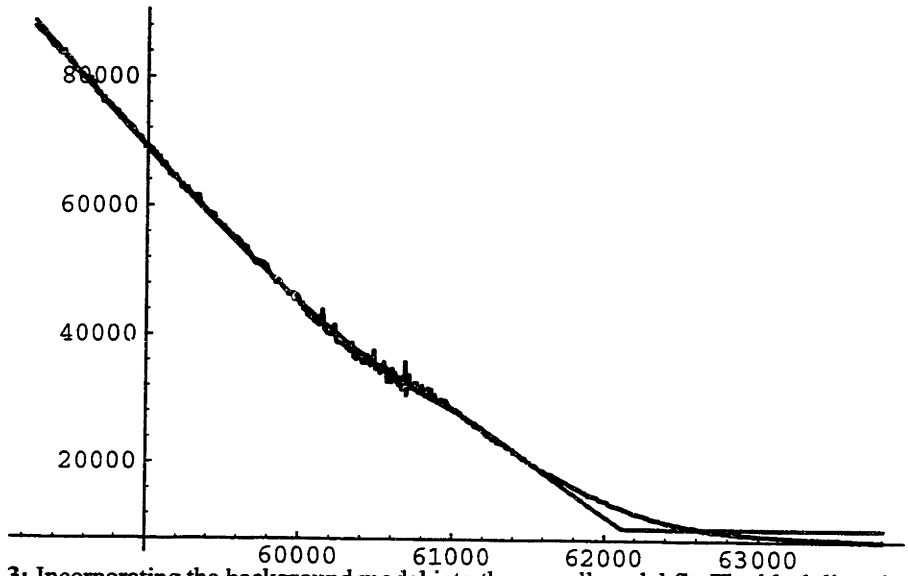

Figure A.3: Incorporating the background model into the overall model fit. The black line above shows the raw 0305 data, and the gray line is the best-fit model to the data using an isothermal model fit which incorporates a limb-darkening model. Note that the fit still does not fit the data well after the emersion event.

The model runs above assume perfect optics: that is, when the disk of the planet has just exited the aperture, it no longer contributes any signal. In reality light from the disk is still recorded after the exact limb of the planet leaves the aperture because of the PSF (point-spread function) of the FOS, which spreads the light out to a small degree, contributing to the signal recorded. This effect needs to be included to create a more realistic model of the background signal.

A PSF for the FOS was determined (Koratkar 1996) but the PSF files were taken off the Space Telescope Science Institute's Web site in early 1997 when errors were discovered in the PSF. A corrected PSF was never provided before support for the FOS ended in late 1997 (E. Smith, pers. comm.). In the absence of *a priori* knowledge of the PSF, we used a simple Gaussian function as the PSF:

$$G(x) = e^{-x^2/\sigma^2} \tag{A.7}$$

The width (σ) of the Gaussian was determined by trial and error and eventually set at 1135 km, or approximately 0".175 at Saturn's distance from the Earth. (The value of σ could have been an additional parameter in the fit, but its inclusion would have made the model fit procedure run much more slowly as new Gaussians were computed.) The Gaussian was then convolved with the background model described above.

This resulted in a very realistic model of the background light. The model, which included the background signal as well as the star signal, closely matched the data (Figure A.4). When the background model computed in the model fit is subtracted from the raw data, the resulting signal—which should represent the signal from the star only —resembles a typical occultation lightcurve. (Figure A.5)

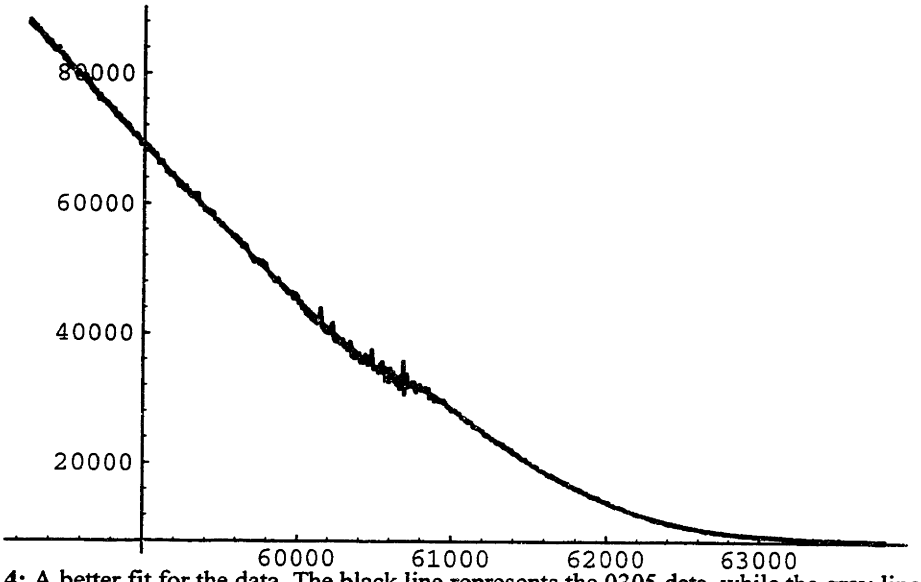

Figure A.4: A better fit for the data. The black line represents the 0305 data, while the gray line is the best-fit model using the limb-darkened background model and a Gaussian function convolved with the model. The fit is very good.

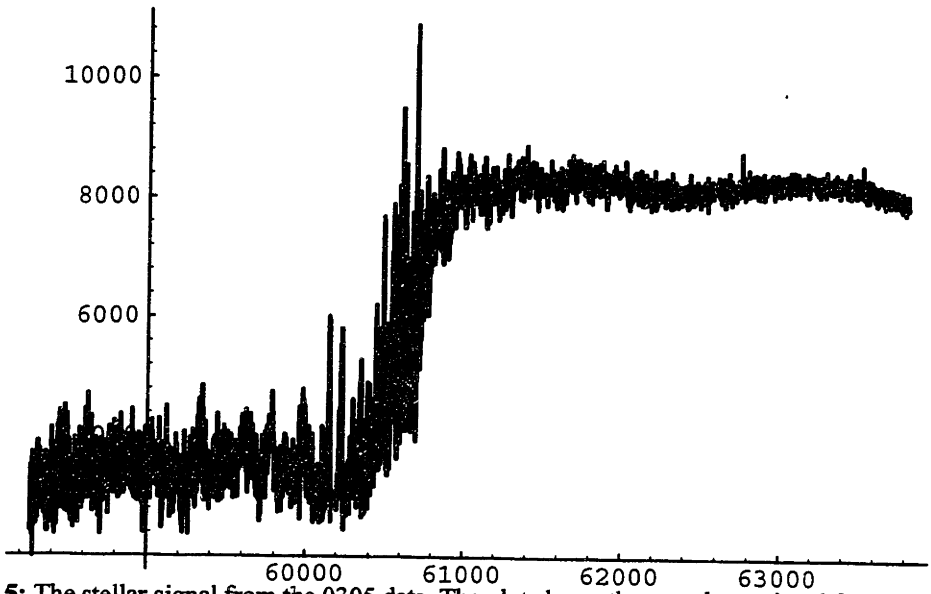

Figure A.5: The stellar signal from the 0305 data. The plot shows the actual star signal from the 0305 data set, found by subtracting the best-fit background model from the raw data. The data resembles a typical occultation light curve. Note the constant offset from zero of the data and the undulations in the post-emersion data on the right, evidence that the background signal has not been completely removed.

Linear Fitting Technique

The problem with the limb-modeling technique, however, is that an offset from the f and g coordinates of the star must be included in the analysis. While the object of the observations was to guide on the star in the center of the aperture, even a small offset of the star from the center of the aperture could have a considerable impact on the limb-fitting technique described above. This is especially true for those data sets taken when the HST was using the less precise gyros for pointing the spacecraft rather than a fine lock on a guide star. Moreover, unless the tracking rate of the HST was continuously adjusted during the occultation the star would drift from the center of the aperture during the occultation itself as refraction decreases the star's motion relative to the disk. The fits shown in Figures A.4 and A.5 assume an offset of 600 km in both f and g, values chosen because they appeared to fit the data well by a simple visual inspection. To rigorously test this would require computing limb darkening functions for a wide range of f and g

offsets, incorporating these into the model, and including the offsets as more parameters of the model fit. Because of the amount of time required to compute the limb darkening functions (12-24 hours for a single set of conditions, using a *Mathematica*™ 2.2.2 kernel running on a Hewlett-Packard Series 9000 Model 735/125 workstation), this technique becomes undesirable. Moreover, this effort would have to multiplied by a factor of three, since the process would have to be repeated for each data set (the results for only one data set, 0305, were presented here.)

We therefore sought alternative methods of removing the background from the data that were far less computationally intensive. This meant abandoning a physical model for the background flux in favor of a simple empirical model that could successfully remove the background contribution to the data. We noted that, for regions of the summed raw data immediately after immersion or before emersion, when the only contributor to the signal is the flux from Saturn, the signal varied linearly with time. We therefore fit lines to the post-immersion and pre-emersion data near the time of immersion or emersion of the form

$$signal = c_1 r + c_0 \tag{A.8}$$

where c_0 and c_1 are parameters of the fit and r is the radius. We used that fit to subtract Saturn's signal from the data. Plots of the raw data and the best linear fit to the background are shown in Figures A.6-A.8, and the fit parameters are listed in Table A.1.

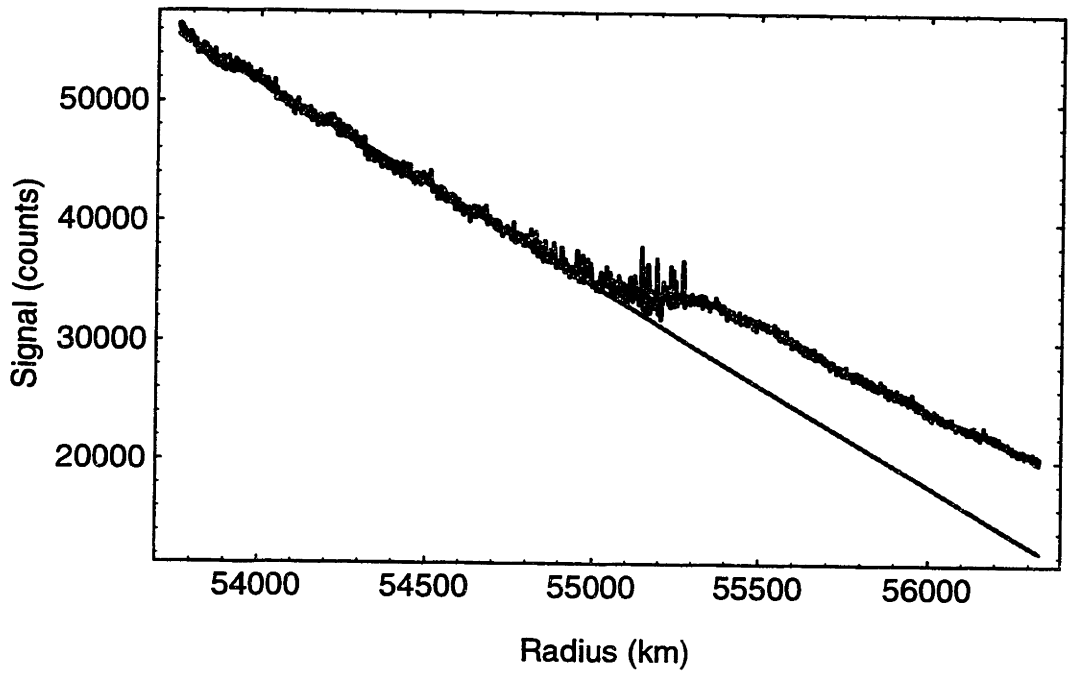

Figure A.6: Linear fit to the background for the 0203 data set. The black line is the raw, summed data from the 0203 data set, while the gray line represents the best fit to the post-immersion data (the leftmost 1000 points shown above.) This line is subtracted from the data to remove Saturn's contribution to the data.

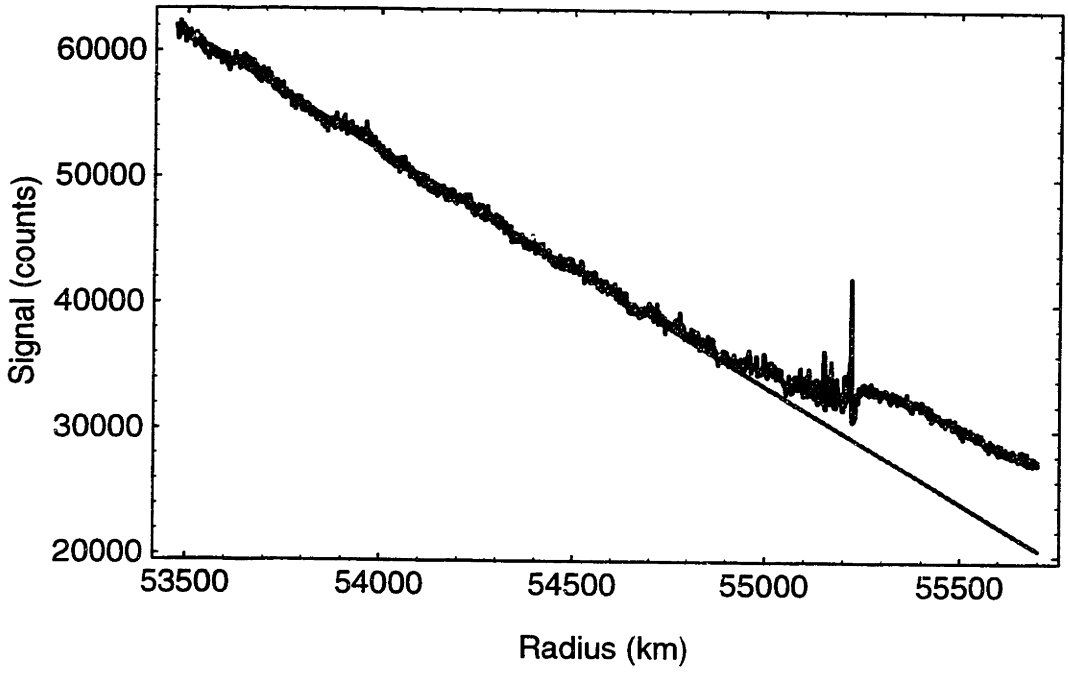

Figure A.7: Linear fit to the background for the 0204 data set. The black line is the raw, summed data from the 0204 data set, while the gray line represents the best fit to the post-immersion data (the leftmost 1000 points shown above.) This line is subtracted from the data to remove Saturn's contribution to the data.

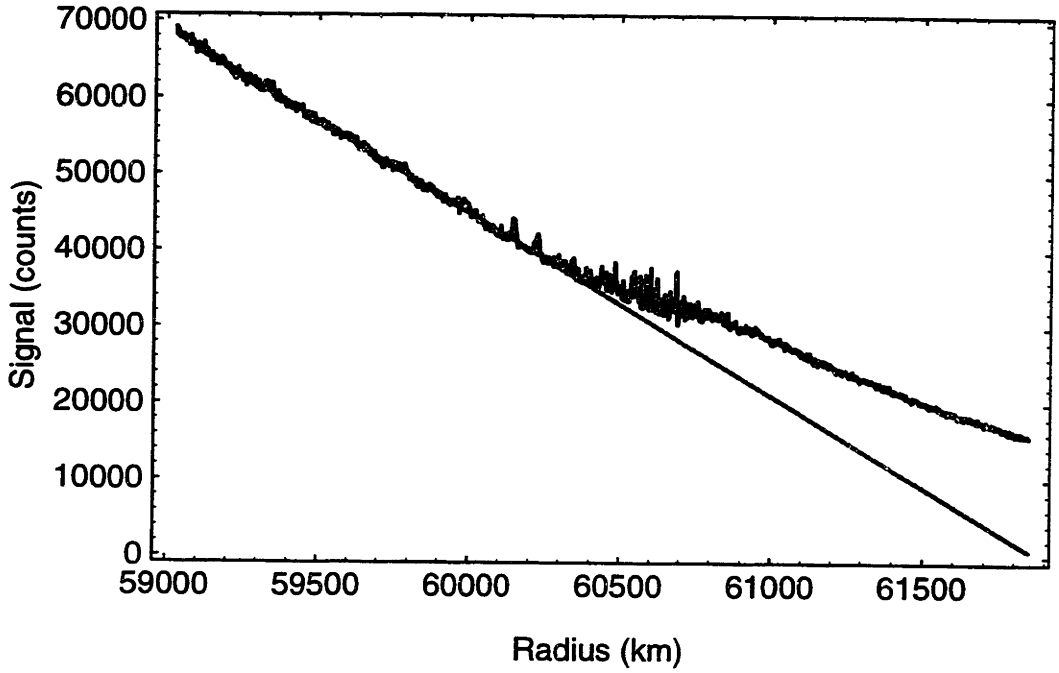

Figure A.8: Linear fit to the background for the 0305 data set. The black line is the raw, summed data from the 0305 data set, while the gray line represents the best fit to the post-immersion data (the leftmost 900 points shown above.) This line is subtracted from the data to remove Saturn's contribution to the data.

Table A.1: Linear Fit Parameters

data set	points used	c_0	c_1
0203	4000-5000	959300 ± 2100	−16.810 ± 0.039
0204	1000-2000	1053600 ± 1900	−18.547 ± 0.036
0305	1000-1900	1479900 ± 2600	−23.916 ± 0.043

The coefficients of the fit for the 0203 and 0204 data sets are similar, albeit not within their errors. As both immersions took place in approximately the same region of Saturn and separated by less than two hours, this agreement is expected. The values for the 0305 event are different, as this emersion event took place near the equator, where the flux from Saturn's disk may be different, and scattered light from Saturn's rings may also play a role.

One complication to this technique is that it would cause the post-emersion and pre-immersion data – where both the planet and star are contributing to the total flux – to curve upwards. Since the star's contribution to the post-emersion/pre-immersion signal should be a constant, one explanation is that the linear fit is not taking into account the scattered light from Saturn visible in the aperture. To correct this, we fit a quadratic curve to the post-emersion/pre-emersion line of the form:

$$signal = c_2 r^2 + c_1 r + c_0 \tag{A.9}$$

where c_0, c_1, and c_2 are coefficients of the fit. We use that fit to remove the curve from that data, making it a straight line. Plots of the background-subtracted data and the best fit functions are shown in Figures A.9-A.11. The fit parameters are listed in Table A.2.

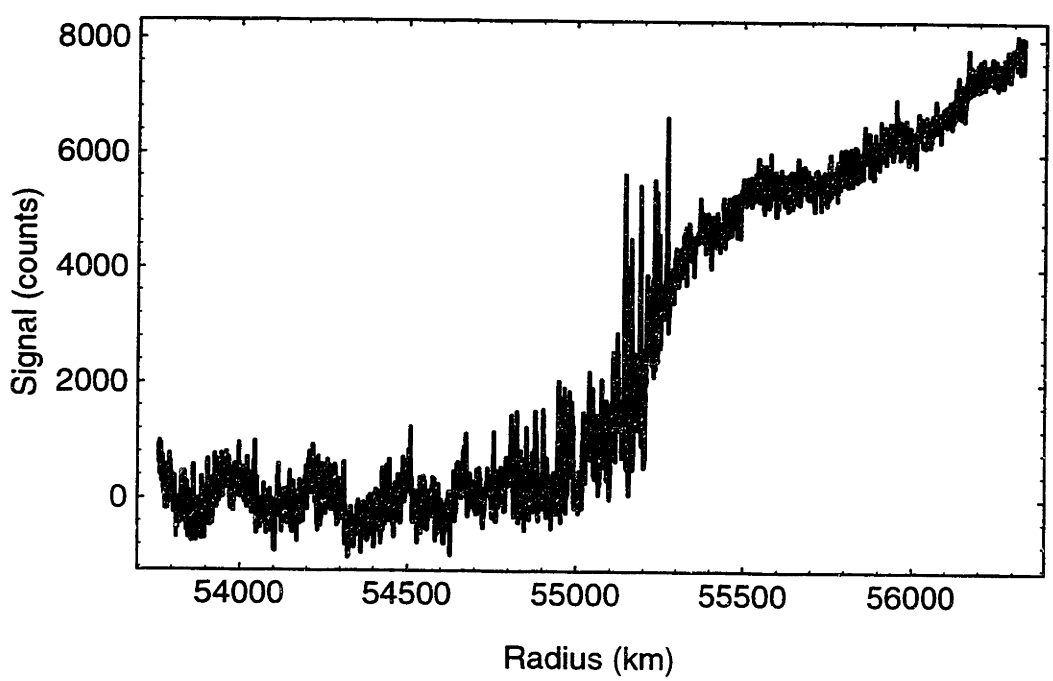

Figure A.9: Secondary background subtract fit to 0203 data. The black line is the signal from the 0203 data set with the linear background subtraction applied. The gray line is the best fit for a quadratic function to fit the rising pre-immersion signal. This function is used to make the pre-immersion signal constant.

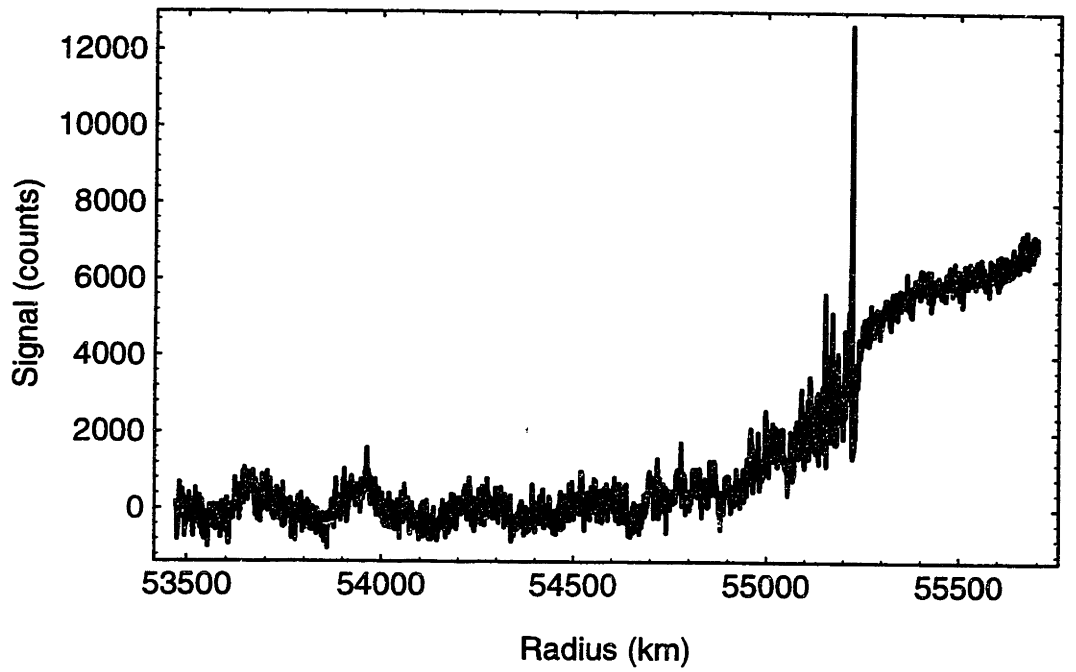

Figure A.10: Secondary background subtract fit to 0204 data. The black line is the signal from the 0204 data set with the linear background subtraction applied. The gray line is the best fit for a quadratic function to fit the rising pre-immersion signal. This function is used to make the pre-immersion signal constant.

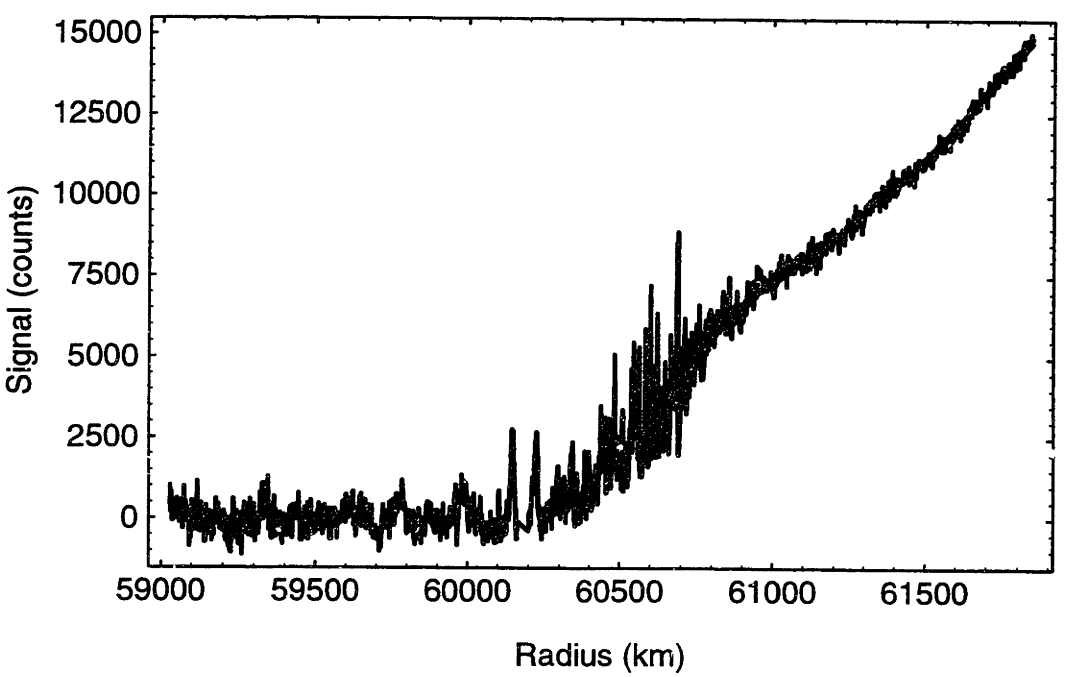

Figure A.11: Secondary background subtract fit to 0305 data. The black line is the signal from the 0203 data set with the linear background subtraction applied. The gray line is the best fit for a quadratic function to fit the rising post-emersion signal. This function is used to make the post-emersion signal constant.

Table A.2: Parameters from Secondary Background Fit

data set	range	c_0	c_1	c_2
0203	2800-3425	9960000 ± 570000	–359 ± 20	0.00324 ± 0.00018
0204	1-350	20770000 ± 4190000	–751 ± 151	0.00680 ± 0.00136
0305	2360-3000	10240000 ± 470000	–342 ± 15	0.00285 ± 0.00012

The 0203 and 0305 fits have similar parameters, even though they represent data sets taken from different regions of the planet. This could mean that the rise is signal is something characteristic of the star itself and not of the disk and/or rings of Saturn. However, the values for 0204 are different. Note, though, that the data set sampled was much smaller (since the immersion took place near the beginning of the data set) and the errors are up to an order of magnitude higher, so the difference in values may be an effect of the small data sample available for the quadratic fit.

This technique gives background-subtracted light curves of the form expected for such an event. The curves are shown in Figures A.12-A.14. Of some concern is the 0203 data set, where the signal begins its drop at around 55,400 km, levels off briefly, then continues its drop as the immersion progresses. Such behavior would not be expected for a typical occultation and is not seen in the 0204 or 0305 data sets. One possibility is that the beginning of the immersion is being lost in the undulations visible in the signal before and after the immersion (the possible sources of such wave-like activity are discussed in Chapter 2). The effects of this on isothermal model and inversion analysis is discussed in Chapter 3.

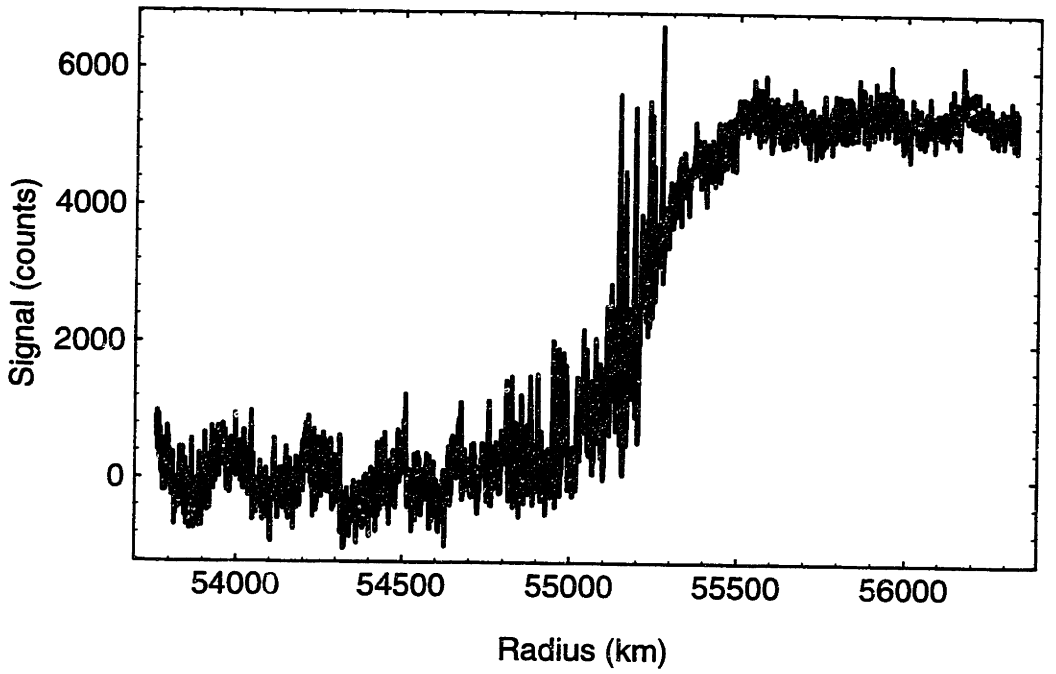

Figure A.12: The background-subtracted signal for the 0203 event.

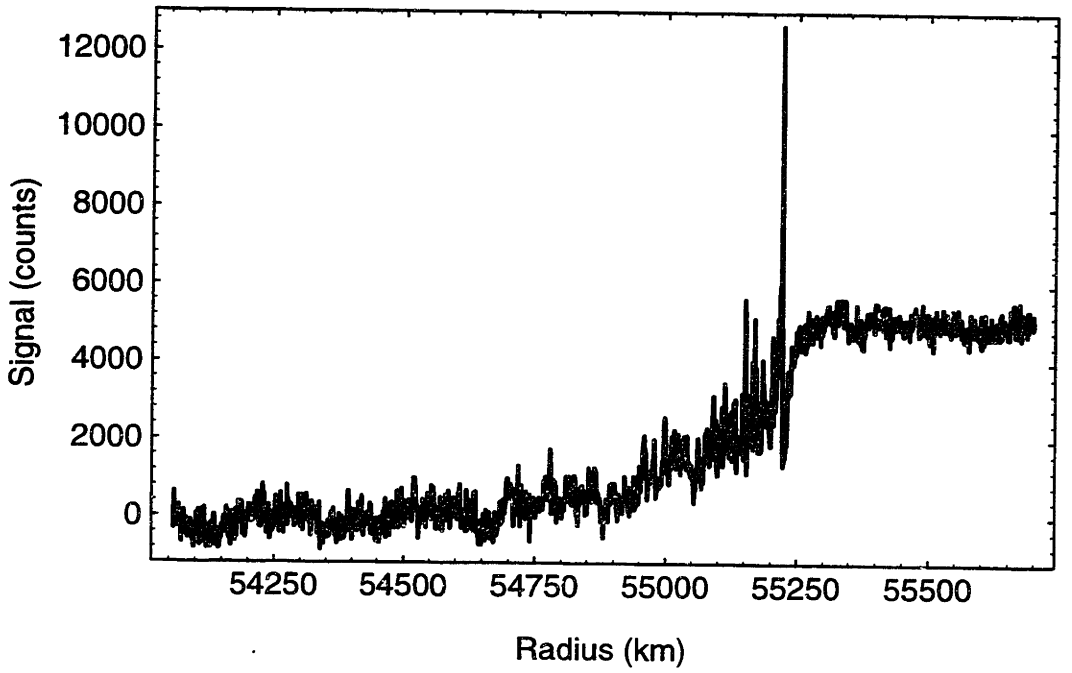

Figure A.13: The background-subtracted signal for the 0204 event.

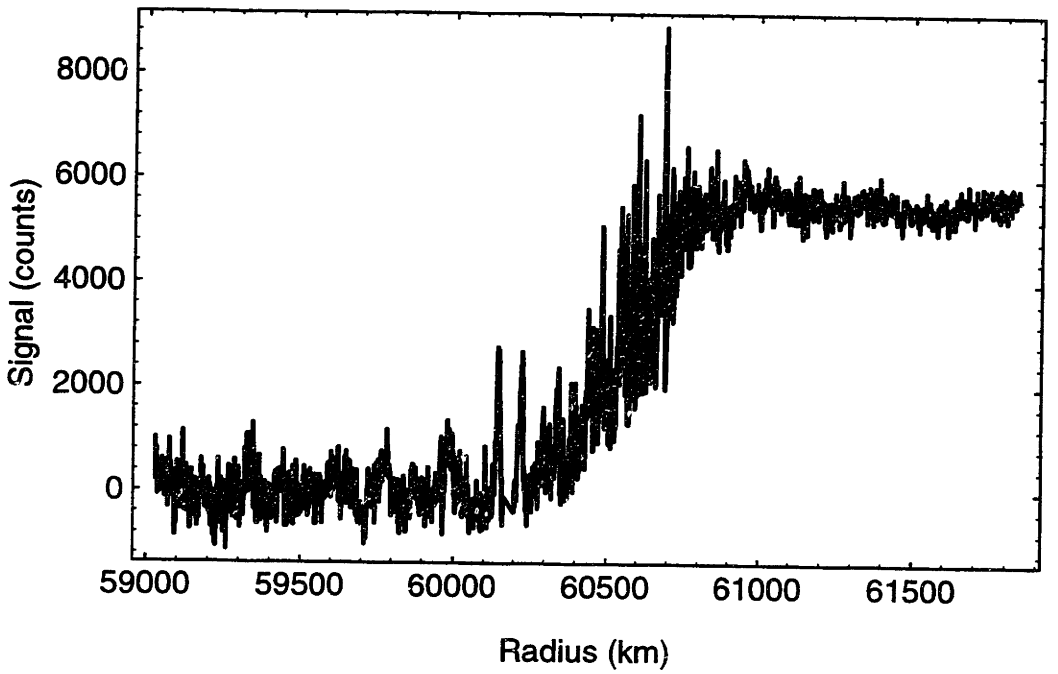

Figure A.14: The background-subtracted signal for the 0305 event.

Conclusion

The ideal model would use solely known physical parameters of the planet, star, telescope, and instrument, to determine the contribution to the total signal from sources other than the star, and to remove that undesired signal. However, for unusual data sets like the HST stellar occultation sets discussed here, such purely physical techniques are not satisfactory. The need to account for everything from the known motion of Saturn with respect to the star to unknown parameters such as the full- and half-disk albedos of the disk at these wavelengths and the position and motion of the star relative to the center of the aperture make attempts to construct physical models too computationally-intensive to be completed in a reasonable time.

Empirical methods, such as the linear fit used above, are less satisfying because they do not use a rigorous physical model to understand the sources of the background

signal and to remove them. However, they are far easier to implement and produce the best results. The results from this empirical method, shown above, do provide a reasonable removal of the background and permit further analysis of the data.

Appendix B
LED Timing Calibration for NSFCAM

Introduction

When NSFCAM is used in Movie or MovieBurst mode, the integration time listed in the headers of the data files does not provide the accurate timing necessary for the analysis of occultation data, since the time base is provided by the instrument computer clock. In addition to any errors caused by inaccuracies in the timing oscillator of the instrument computer, the integration time provided tells how many seconds the image is exposed in each frame, but does not give the *cycle time*, or the time between the start of one integration and the start of the next integration. The difference between the cycle time and the integration time, referred to here as the *dead time*, is the overhead needed to transfer the data out of the instrument's InSb array and into the instrument computer's memory and to reset the instrument for the next frame. This time will vary based on the number, size, and location of the subframes on the array: in general, the more total pixels in the subframe(s), the longer the dead time needed to read out the data.

While the dead time can be estimated from the timing properties of the electronics, a more accurate way to determine the dead time, and hence the cycle time, is through the analysis of a set of observations of a calibrated light source that turns on and off with a known, accurate pattern. The preferred method for doing this is to take MovieBurst mode observations of a light-emitting diode (LED), flashing at an accurately-known period (controlled by the clock in a GPS receiver). The analysis of these data can be used to calibrate the computer clock, and repeated measurements can test its stability over time. If the clock is stable, this calibration can provide the accurate timing necessary for the occultation data.

For this and previous timing calibrations with the NSFCAM camera at the IRTF, an infrared LED was placed in the optical path of the telescope. The LED is connected to a GPS receiver, which generates an output trigger to turn the LED on and off. The system is configured to turn the LED on for 100 ms at the beginning of each second, then off for 900 ms. This pattern is repeated for the duration of the timing observations using MovieBurst mode on NSFCAM, generating a time series of light pulses with an accurate period that can be used to find the cycle time of the observing mode.

Previous Work

LED timing calibrations have been used with NSFCAM on several occasions, starting with a 1994 occultation by Saturn of GSC5815-01190. Smith (1995) developed the analysis technique for the LED timing observations taken during this event. This technique has since been used on similar data sets from NSFCAM observations of occultations by Saturn, Titan, and Triton in 1995.

The readout of a NSFCAM image involves several steps (Leggett and Denault 1996). First, the InSb array is reset, pixel by pixel, by setting the charge of each pixel to zero. Then the array is read out sequentially in a "pedestal" read. After a period of time to allow charge to accumulate, the array is read out once again sequentially in a "sample" read. The NSFCAM computer stores the difference between the sample and pedestal reads. The integration time, as displayed in the header in the FITS file of the data, is the time between the beginning of the pedestal read and the beginning of the sample read (Leggett and Denault 1996). Since the data are read out sequentially, the start and end times for each pixel will be slightly different and vary by the readout time; however, the integration time for each pixel will be the same.

NSFCAM also allows more than one non-destructive read (NDR), where the pixels in the array are read without resetting their values. The number of pedestal and sample reads performed by NSFCAM is each equal to the value of NDR set by the observer. Increasing the number of NDRs reduces the read noise but increases the dead time, and hence the cycle time, since additional pedestal and sample reads are required. As with single reads, the integration time is equal to the time from the first pedestal read to the first sample read (Leggett and Denault 1996). (see Figure B.1) The data stored by the NSFCAM computer are the differences between the sum of the sample reads and the sum of the pedestal reads for each pixel.

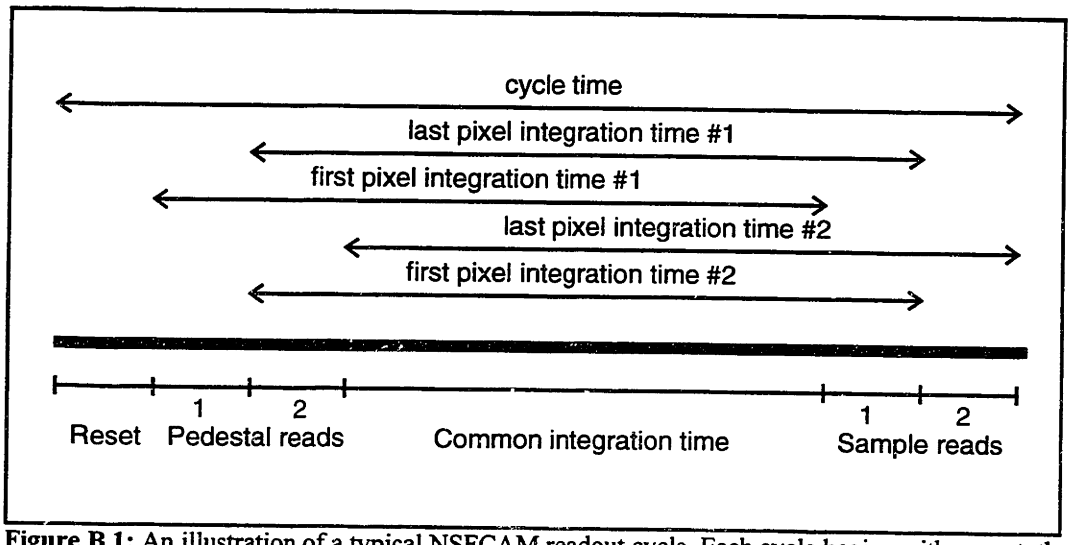

Figure B.1: An illustration of a typical NSFCAM readout cycle. Each cycle begins with a reset, then a number of pedestal reads as set by the value of NDR. This is followed by a common integration time when no reads take place. The cycle is concluded with a number of sample reads equal to the value of NDR. In this example NDR is equal to two. The figure illustrates the integration times for the first and last pixel in the array for both reads. Note that while the absolute times between reads for different pixels are different, the interval of the integration time is unchanged. Time in the cycle not allocated to integration time is considered to be dead time.

Smith knew for his data set that the integration time was set so that the data would have a cycle time of approximately 250 ms. Since the cycle time was not quite 250 ms, there was a discernible pattern as the LED flashes shifted from one set of frames to an adjacent one. A useful landmark for measuring this shift is a pair of adjacent frames with

similar signal counts: this is a sign that the LED signal is shifting between frames (Figure B.2). By measuring the number of frames apart these pairs of frames are, Smith calculated the difference in the cycle time from 250 ms. Smith also found that the start time of the data set, taken from the GPS and printed in the header of file, is offset from the beginning of the first frame of data by only a few milliseconds, and is thus not a significant source of timing error.

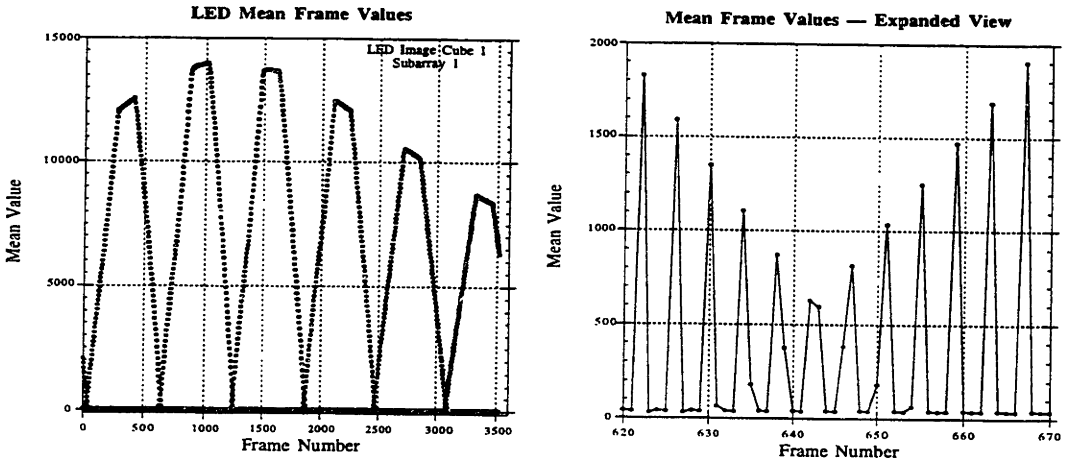

Figure B.2: An example of the transition effect from Smith (1995). The plot on the left shows the long-term effects of the LED transition, while the frame on the right is a close-up which shows the transition of the LED signal from one frame to the next, where the two adjacent frames have nearly equal LED values.

Olkin (pers. comm., 1997) discusses two methods to find the cycle time of a data set when no good estimate of the cycle time is available. One method is to construct a model of the LED timing pulse and then fit it to the data, using the cycle time and the dead time of the system as parameters for the fit. However, Olkin notes that this does not work well because the abrupt changes in the model make a least-squares fit difficult. Instead, Olkin counted the number of frames between spikes in the data (Figure B.3) and compared that value to the expected number of frames between spikes in the data from

the model, given a specific cycle time. From this one can get the cycle time and thus the dead time of the data.

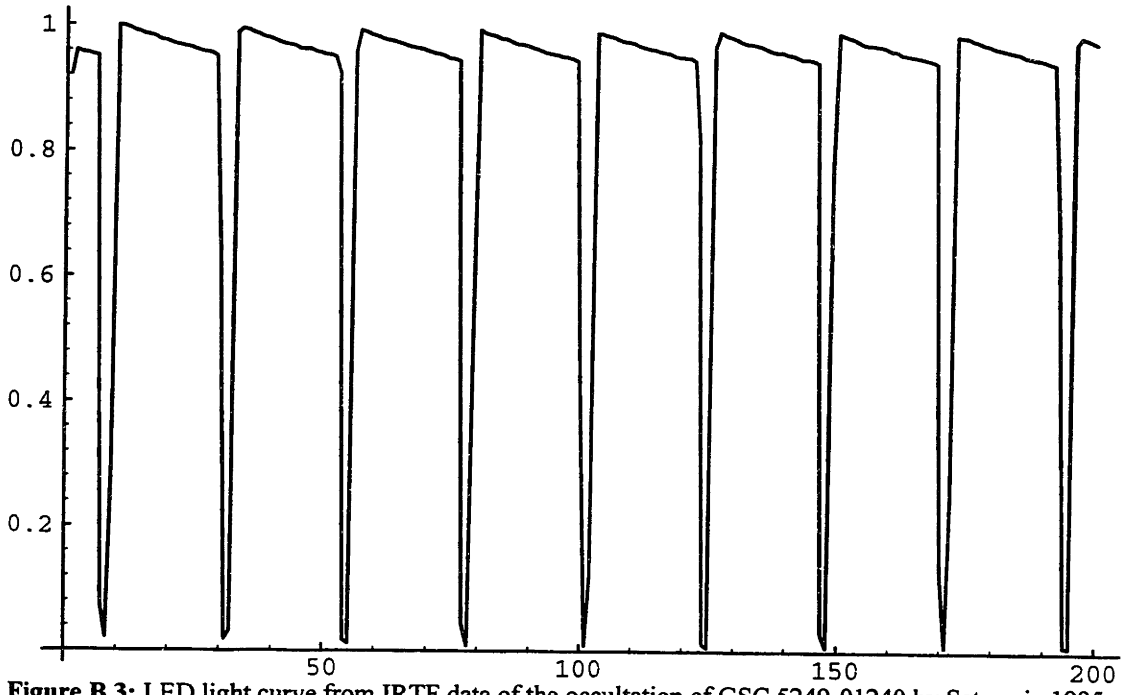

Figure B.3: LED light curve from IRTF data of the occultation of GSC 5249-01240 by Saturn in 1995. Note the regular series of dips in the light curve, which can be used with a model to find the cycle time and dead time of the observations. From Olkin (pers. comm., 1997)

Technique

We recorded LED timing exposures on 1996 July 29 after observing a Saturn occultation. Using MovieBurst mode on NSFCAM, we took exposures of 1000, 2000, and 4800 frames each with the LED in place, using the setup described in the first section of this appendix. We used subframes of the same number and size as those used during the immersion, but the subframes themselves were erroneously placed in different locations on the CCD than during the immersion. The effects of this error will be discussed below. For these data the number of non-destructive reads (NDR) was set to two.

The analysis techniques described in the previous section do not work for the LED timing data collected during the 1996 Saturn occultation. The 1996 timing data appears significantly different from previous timing data sets with no obvious "peaks" or "valleys" visible in the 1996 data (Figure B.4).

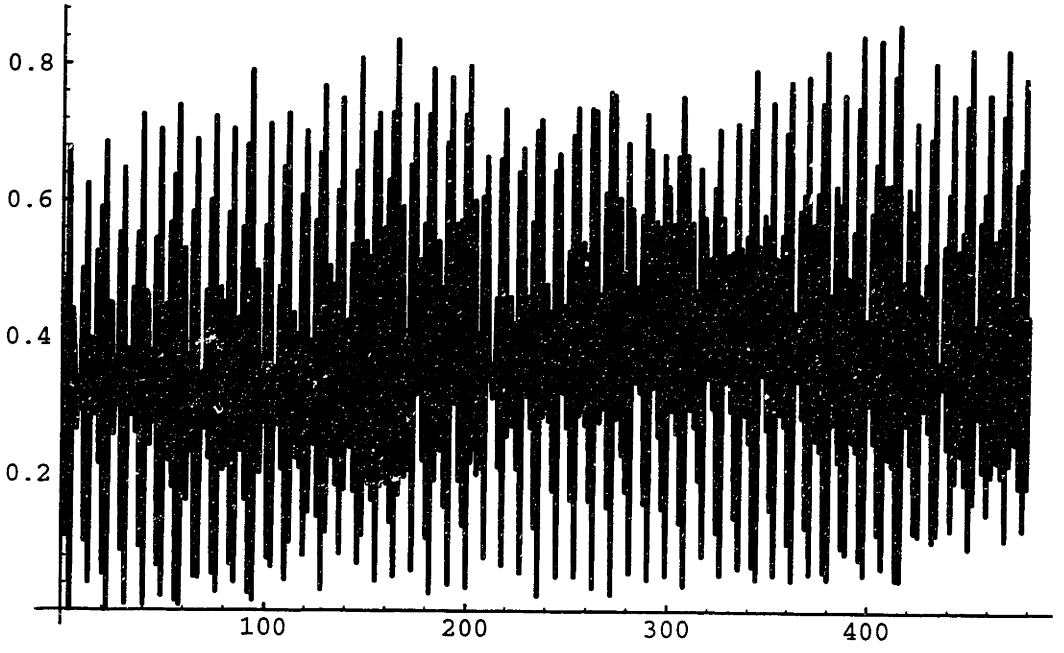

Figure B.4: LED timing data from the 1996 event. The signal from the first 480 frames (10%) of a 4800-frame LED timing calibration are displayed. The signal has been normalized to values between zero and one, corresponding to the minimum and maximum values of the data set. Note that unlike the timing data displayed in Figure 3, there is no obvious pattern or peaks and/or dips in the data that could be used with existing techniques to determine the cycle and dead time of the data.

In an attempt to find some pattern in the data, we fit a simple sine curve to the data using least squares. The amplitude and zero-offset of the curve was fixed, and the frequency and phase shift of the curve was determined from the fit process. We started by fitting the curve to the first ten points of each data set, and then used the frequency and phase shift parameters from that fit as the start of a new fit using twice as many points. This process was repeated until the entire data set was included in the fit (Figure B.5).

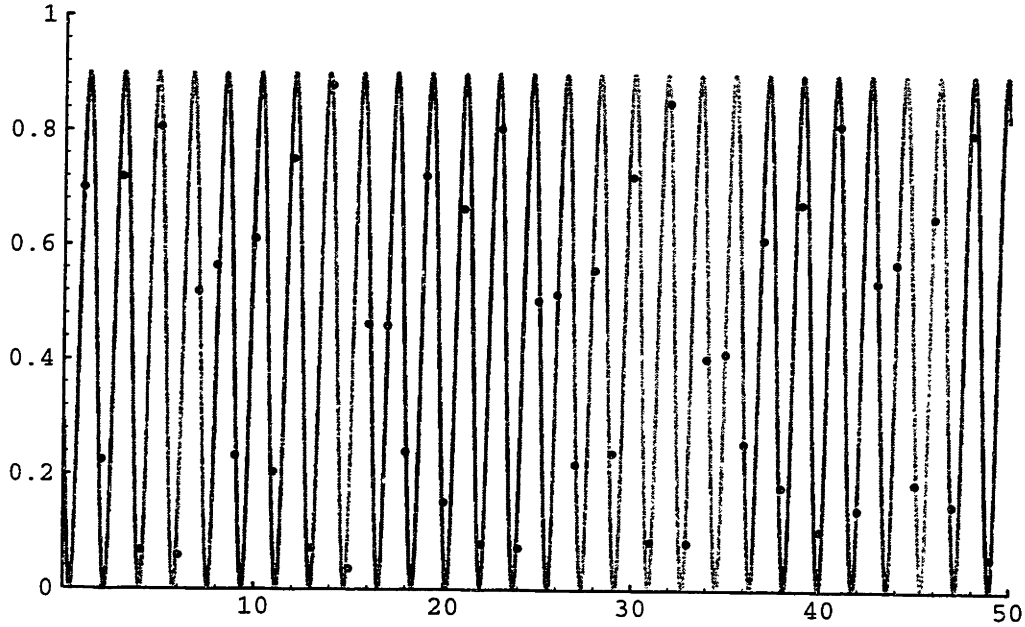

Figure B.5: A comparison of the data (black dots) and least-squares fit of a sine wave (gray curve). The above set from the first 50 frames of a 4800-frame data set is representative of the quality of the fit for the entire data set. The period of the sine wave is 1.79891 frames, or 0.55589 seconds.

For the 4800-frame data set the least-squares fit resulted in a period of 1.7989058 ± 0.0000019 frames. Since the GPS signal driving the LED has a period of 1 second, the cycle time of the data is 1/1.7989058, or 0.55589347 ± 0.0000006 seconds. The integration time of each frame was 0.5 seconds (based on data in the FITS header of each file), so the actual dead time is 0.05589347 seconds, or 55.9 ms.

We used this technique on the two other LED timing tests taken during the event, one with 1000 frames and the other with 2000 frames. All three were taken in immediate succession, in the order of the 1000-frame exposure, 2000-frame exposure, and the 4800-frame exposure. The cycle time derived from the sine curve fit to the 2000-frame data matches the 4800-frame data to within their errors. The fit to the 1000-frame data produces a cycle time that is 7 – 7.5 sigma greater than that derived from the 2000- and 4800-frame data (see Table B.1). However, the 1000-frame data was not as good as the longer data sets: there was a significant long-term increase in the mean signal values in

addition to the variation seen in the longer data sets. This data set had to be normalized in sets of 10 frames each, instead of normalizing over the entire data set as was done with the longer data sets. While this removed the trend in the data, it may have introduced other effects which may have impacted the results of the fit.

Table B.1: Cycle Time Results from LED Timing Data

File Name	# Frames	Cycle Time & Error (sec)
data2199.movie	1000	0.5559039 ± 0.000014
data2200.movie	2000	0.55589354 ± 0.0000039
data2201.movie	4800	0.55589347 ± 0.0000006

Data in the FITS header of the LED timing files confirms this result. The FITS header produced by NSFCAM data includes a keyword entry named "FRM_RATE." According to NSFCAM software designer Tony Denault (personal communication), FRM_RATE is defined as the amount of time it takes to perform a single readout of the array, be it a reset, pedestal read, or sample read. As the integration time is defined as the time between the first pedestal read and the first sample read, there is a time equal to three reads of the array where data are not collected, and hence is a dead time between frames.

For the first pixel sequentially read, the integration time would include the time for the two pedestal reads and the intermediate time between the pedestal and sample reads, and would end at the beginning of the first sample read. The integration time would not include the time for the rest of the sample reads or for the reset of the frame. Similarly, for the last pixel read out, the integration time would begin at the end of the first pedestal read, when the final pixel was read out, and continue to the end of the first sample read, when the pixel was read out again. It would not include the second sample

read, the reset read, or the time for the first pedestal read up until that pixel was read out (see Figure B.1).

The length of FRM_RATE is determined by the number and location of the subframe(s) on the image. For all the LED timing data FRM_RATE is equal to 18.79 ms. If the dead time is three times the value for FRM_RATE, the dead time from this method becomes 56.37 ms, less than 0.5 ms longer than the value from the sine curve fit discussed above. Since the timing of the computer used to determining FRM_RATE is based on an oscillator with much less accuracy than the GPS timing used to generate the LED pulses, it is reasonable to conclude that the results of these two methods are consistent within their respective errors.

The timing from the FRM_RATE value and the timing from the LED calibration can be used to determining the accuracy of the timing in the NSFCAM computers. Since the cycle time should be the same whether we calculate it from LED calibrations or FITS file header information, the GPS-derived cycle time of 0.5589347 seconds should equal the FITS-header-derived time of 0.55637 seconds. The GPS timing is far more accurate than computer timing, therefore the error in the computer timing is approximately 0.1%.

However, an examination of the start and end times for some data sets gives a different answer for the dead time. The start and end times for the 4800-frame MovieBurst file of the immersion event of the occultation itself were recorded by the observers (Bosh, Foust, and Elliot) in the log book. For the file, "data0174.movie", the start time was recorded as 13:21:06 UT and the end time as 14:10:38 UT. The duration of the file was thus 49:32, or 2,972 seconds. Assuming a negligible delay time at the beginning or end of the file, this gives a cycle time of 619.2 ms, or a dead time of 119.2

ms. This is significantly larger than 56.37 ms dead time from the FRM_RATE variable in the FITS header.

One explanation for this difference is that the starting and ending times in the observing log book may be in error. The difference in dead times (62.73 ms) over 4800 frames is 301.1 seconds, or just over five minutes. It seems unlikely that the observers could have erred in the starting and/or ending times by five minutes. Another possible source of error is the timing within the instrument computer. Since it uses an oscillator with much less accuracy than the GPS, errors in the timing could contribute to the offset between the deadtimes determined by the GPS timing and the deadtime obtained from the computer-generated start and stop times. However, as noted above, the error in computer timing is approximately 0.1%, which is far too small to account for the difference described here.

Another possibility is that the difference in times is not a dead time at all, but the delay in transferring the data from the *Nsfpc*, the computer where the data collected in MovieBurst mode are temporarily stored in RAM, to a disk on another IRTF computer, where the file is converted into a FITS image cube. The start and end times recorded in the logbook include the time it takes to transfer the data from the instrument computer and write them on disk. The size of the 4800-frame file is approximately 82 MB (in addition to the 64 Mb of RAM for data storage in the instrument computer, the file size includes zero-padding necessary to fit the two subframes into a single rectangular image.) For the 301-second delay to be fully accounted by the delay in transferring the data, the transfer rate of the data would have to be 0.27 MB/sec. Tony Denault (pers. comm., 1997) estimates that the transfer rate is approximately 1-2 MB/sec, somewhat faster than the required rate. However, it is not impossible that, given the condition of the computer

system at the time of the observation, the transfer rate was running below the estimate by Denault.

Results and Conclusions

From sine wave fits to the LED timing data as well as the information contained in the FRM_RATE entry in the FITS header, the dead time of the data is about 56 ms, with an overall cycle time for each frame of 556 ms. This assumes that the discrepancy between the dead time from the sine curve fits and FRM_RATE value and the dead time from the difference in the recorded start and end times of the data can be explained as time spent transferring the data after the end of the exposure, or by errors in the oscillator that provides the timing for the computer (see Table B.2).

Table B.2: Comparison of Cycle Time from Various Methods

Method	Cycle Time (seconds)
LED timing calibration	0.55589347 ± 0.0000006
FRM_RATE value	0.55637
Start and end times in logbook	0.6192

The sine curve fit to the data also helps resolve another feature of the data: the lack of an obvious period with spikes and/or dips, unlike previous LED timing sets. When the data are folded into the period derived from the least-squares fit, a distinctive curve forms (Figure B.6). This combination of two exponential curves resembles the charging and discharging of a capacitor. This result suggests that the LED was not blinking on and off throughout the course of the LED timing observations, as expected, but was on all the time and only varying in brightness. This also explains why the LED is

visible in every frame of the timing data, when, given the exposure times and expected pattern of LED flashes, it should not have been visible in every frame.

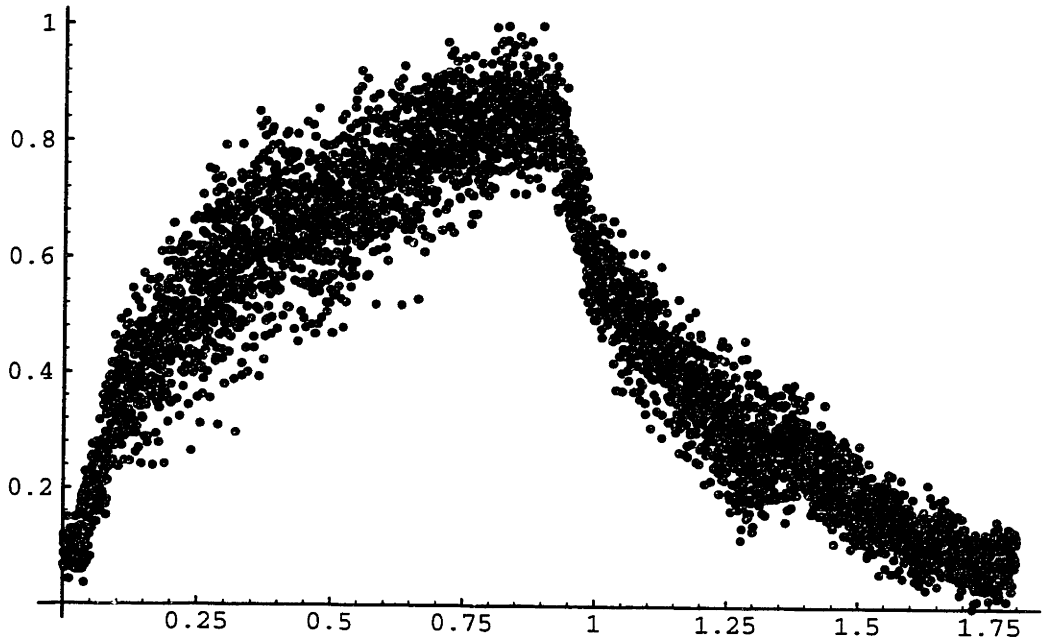

Figure B.6: The LED timing data wrapped to a period. The 4800-frame LED timing data set above has been wrapped to the period of the least-squares fit of 1.79891 frames. Note that the result is a pair of exponential curves: one rising up and leveling off, then one falling and leveling off. This is similar to the charging and discharging of a capacitor, evidence that the LED was always on, and only varying in brightness, during the LED observations.

There is one additional complication to this work. The subframes used for the LED timing data are the same size but not in the same location as the subframes used to record the immersion event of the occultation. The occultation data has a 16×32 pixel frame starting at (112, 16) and a 80×80 pixel frame starting at (88, 136). The LED timing data had a 80×80 frame starting at (96, 64) and a 16×32 frame starting at (168, 200). The difference in locations may have a difference in the read time of the arrays. This is confirmed by examining the value of FRM_RATE in the header of the occultation data: there FRM_RATE is 17.05 ms, compared to 18.79 ms in the LED data. This would imply that the dead time in the occultation data itself is 3×17.05 ms, or 51.15 ms, and thus the cycle time is 0.551155 seconds. To find the true cycle time of the immersion data, we have to take into account the timing error in the NSFCAM computer, as noted

earlier in comparison with the more accurate timing derived from the GPS. Assuming the computer time is 0.1% longer than the GPS time, as before, the revised cycle time for the immersion data set becomes 0.550604 seconds.

If we assume that the error for this revised cycle time is the same as that from the 4800-frame LED test, we can determine the effects of that error on the timing of the occultation data. The half-light level of the occultation took place at approximately frame 2600 of a 4800-frame observation. If we assume that the timing error is cumulative, then the error in the half-light time would be $2600 \times 6 \times 10^{-7}$, or 0.002 seconds. The velocity of the event at the time of occultation is 4.96 km/sec, so an error of 0.002 seconds in the half-light time would correspond to an error of approximately 0.01 km in the half-light radius. This error is much smaller than other errors from the occultation analysis.

Message from Tony Denault

Return-Path: denault@irmanoa1.IFA.Hawaii.Edu
Received: from irmanoa1.ifa.hawaii.edu by hale.IFA.Hawaii.Edu (4.1/hale1.1)
id AA02753; Mon, 3 Mar 97 10:30:09 HST
Received: by irmanoa1.ifa.hawaii.edu (SMI-8.6/SMI-SVR4)
id KAA03819; Mon, 3 Mar 1997 10:24:17 -1000
Date: Mon, 3 Mar 1997 10:24:17 -1000
From: denault@irmanoa1.IFA.Hawaii.Edu (Tony Denault)
Message-Id: <199703032024.KAA03819@irmanoa1.ifa.hawaii.edu>
To: jeff
Subject: Re: Question about NSFCAM FITS header entry
Cc: bryant@irmanoa1.IFA.Hawaii.Edu
X-Sun-Charset: US-ASCII

>
> Hi,
> We have some NSFCAM data taken last July in MovieBurst mode, and
> are wondering about one of the lines in the header of the FITS files:
>
> FRM_RATE= 18.79 / In msec. Fastmode=Off SlowCnt=1 NDR=2
>
> The NSFCAM manual doesn't seem to explain this, and since we're trying to

> get our timing as exact as possible with these data, we're curious to know
> what this time or rate here means. If you could give us some information
> on this, or let us know who to contact about this, we'd appreciate it.
>

Frame rate is the amount of time needed to do a single readout
of the array. A single readout could be a reset, pedestal, or sample
frame. So if you were in ARC_D readout mode with 2 NDR then a single
image would consist of:

[RESET][PED][PED][...][SAMPLE][SAMPLE]

where
[RESET] is a Reset frame.
[PED] is a pedestal frame (2 ndr).
[...] a pause between pedestal & reset (len depends on integrations time).
[SAMPLE] is a sample frame (2 ndr).

each [RESET], [PED], or [SAMPLE] is 18.79 ms in lenght.

Tony

Appendix C
Astrometric Solution for the 1996 Saturn Occultation

Introduction

Proper analysis and interpretation of data collected during an occultation requires precise knowledge of the location and relative motion of the occulting body and the star being occulted as seen from the perspective of the observer. Without this knowledge one does not know which part of the planet was probed by the star.

The catalog position of the star and the ephemeris of the occulting body provide an estimate of the precise location of the event. However, both are subject to errors, which can have a significant impact on the results of the occultation analysis: a 1-arcsec error the position of one of the bodies is equal to approximately 6,500 km at Saturn's distance from the Earth at the time of the 1996 IRTF observations. Thus these positions require a correction based on observations of the star, occulting body, and any other objects that can improve the accuracy of the positions.

Technique

Past stellar occultations by Saturn have relied on the observation of occultations of the star by ring features to compute a distance scale for the event (Hubbard *et al.* 1997; Cooray *et al.* 1998). However, the path of Saturn relative to the star for the 1996 occultation kept it clear of the rings both before atmospheric immersion and after atmospheric emersion, so an alternative method is needed to find where the star probed Saturn's atmosphere. In our case we chose observations of the star, Saturn, and several of its moons to provide an astrometric solution for this event.

In a two-hour period prior to the occultation of GSC 0010-00284 by Saturn, the observers (A. Bosh, J Foust, J. Elliot) took 54 images of the star, Saturn, and several of its moons (Enceladus, Mimas, Rhea, and Tethys) for later astrometric analysis. The observers also took three images of the stars Tr59 and Tr60 (McDonald and Elliot 1992) to determine the pixel scale and rotation angle of the detector relative to the J2000 celestial coordinate system. These images were taken in full-frame (256×256 pixel) mode at a pixel scale of 0.3 arcseconds per pixel.

We later analyzed the images to find the *x-y* positions of the objects. The *ipMargAnal* routine, part of the *imageProcessing Mathematica*™ package included in the group software on "astron.mit.edu", was used to compute the centers of the star and Saturnian moons. Since it is difficult to compute the center of a complex image, such as the disk of a large body with rings, the center of Saturn in the images was not determined.

The right ascension and declination of Saturn and its moons were computed with the *simple_eph* program using the DE403 and sat-95-96.bsp ephemerides obtained from the Jet Propulsion Laboratory. As a check, another set of ephemerides were calculated using the pre-RPX (ring plane crossing) Saturn Ephemeris Generator 1.1 (http://ringside.arc.nasa.gov/www/tools/ephem_sat.html), provided by the PDS Planetary Rings Node. The two sets of ephemerides were identical to within 15 milliarcseconds. The position of the star came from version 1.2 of the HST Guide Star Catalog (GSC), available online (http://www-gsss.stsci.edu/gsc/gsc12/gsc12_form.html) (Table C.1).

Table C.1: GSC 1.2 position for GSC 0010-00284 (J2000)

RA	Dec
$0^h\ 30^m\ 50^s.99$	$0°\ 39'\ 49".7$

For the later analysis of the occultation data, we adopted a *f-g* coordinate system (Elliot *et al.* 1993) centered at the center of Saturn, with the *f* axis parallel to right ascension and the *g* axis parallel to declination. For simplicity, we considered the center of the *f-g* plane fixed and track the motion of the star in the plane, even though the star is actually fixed and the planet moving. Using the difference between star position from the GSC catalog and the center of Saturn from its ephemeris, we obtained provisional *f* and *g* positions for the star.

We used the observations of the stars Tr59 and Tr60 (McDonald and Elliot 1992) to find the pixel scale and rotation of the images. The distance, in pixels, between the two stars is compared with the known distance between the two stars to find the pixel scale in arcseconds per pixel and kilometers per pixel (Table C.2). The rotation angle of the *x-y* plane of the image relative to the sky (and hence the *f-g* plane) comes from the difference in the position angles of the stars between the detector frame and the sky. The angle is defined here as the difference between the *y* axis of the image and *f* axis of the *f-g* coordinate system.

Table C.2: Pixel Scales and Rotation Angle from the Tr59/60 Data

Pixel Scale (arcsec/pixel)	0".2976 ± 0".0014
Pixel Scale (km/pixel)	1937.9 ± 9.1
Rotation Angle (degrees)	1°.0914 ± 0°.0043

Since the goal of this analysis is to find the exact position of the path of the star relative to Saturn, the ideal technique would be to compare the distance between the star and Saturn in the frame, rotated into the *f-g* plane, with the predicted difference from the catalog position of the star and the planetary ephemeris. However, since it is difficult to

find an exact position for the center of Saturn, an alternate technique must be adopted. The moons of Saturn visible in the image, whose centers can be determined, are a viable alternative.

Not all the moons visible in the images are useful for this technique. Mimas is dim and is lost in the glare from Saturn's rings in most images, so it is excluded from the analysis. Enceladus is missing from several images when it is lost off the top of the frame when the telescope is moved. Moreover, Amanda Bosh (pers. comm.) expressed concern that the Enceladus positions may not be as accurate as those for other moons. For these reasons, Enceladus was excluded from the analysis. The two remaining moons, Rhea and Tethys, were used in the analysis.

In this analysis, the x and y pixel positions of Rhea, Tethys, and the star were determined for each frame. The distance between Rhea and the star and Tethys and the star, in x and y, was determined and converted into arcseconds using the pixel scale from the Tr59/Tr60 analysis. The x-y distances were converted into f-g (and thus right ascension and declination) distances using:

$$\begin{bmatrix} f \\ g \end{bmatrix} = \begin{bmatrix} \sin\theta & -\cos\theta \\ \cos\theta & \sin\theta \end{bmatrix} \begin{bmatrix} x \\ y \end{bmatrix} \tag{C.1}$$

where θ is the angle of rotation between the f-g and x-y axes, provided in Table C.2. This provided the distance from each moon to the star in right ascension and declination, which could, in conjunction with the ephemeris position of each moon, be used to find the right ascension and declination position of the star. This position can be compared to the catalog position of the star to find offsets in f and g, designated f_0 and g_0, that be applied to the f and g positions of the star computed previously.

Results

The *f* and *g* offsets found using Tethys and Rhea are not the same, even within their errors. (Table C.3) This is a significant difference which has a considerable impact on the *f* and *g* position of the star.

Table C.3: f_0 and g_0 using Rhea and Tethys

Moon	f_0 (km)	g_0 (km)
Rhea	5290 ± 180	–3640 ± 260
Tethys	7130 ± 460	–2330 ± 200

Another aspect of this difference can be seen in the offsets in the distance between Rhea and Tethys. Figure C.1 shows the offset between the ephemeris and measured distance between the two satellites, in right ascension (*f*) and declination (*g*). There is a considerable amount of scatter in the offsets over very short periods of time. The mean offset (Rhea–Tethys) in right ascension is –0.334 ± 0.095 arcsec and the mean offset in declination is –0.190 ± 0.072 arcsec.

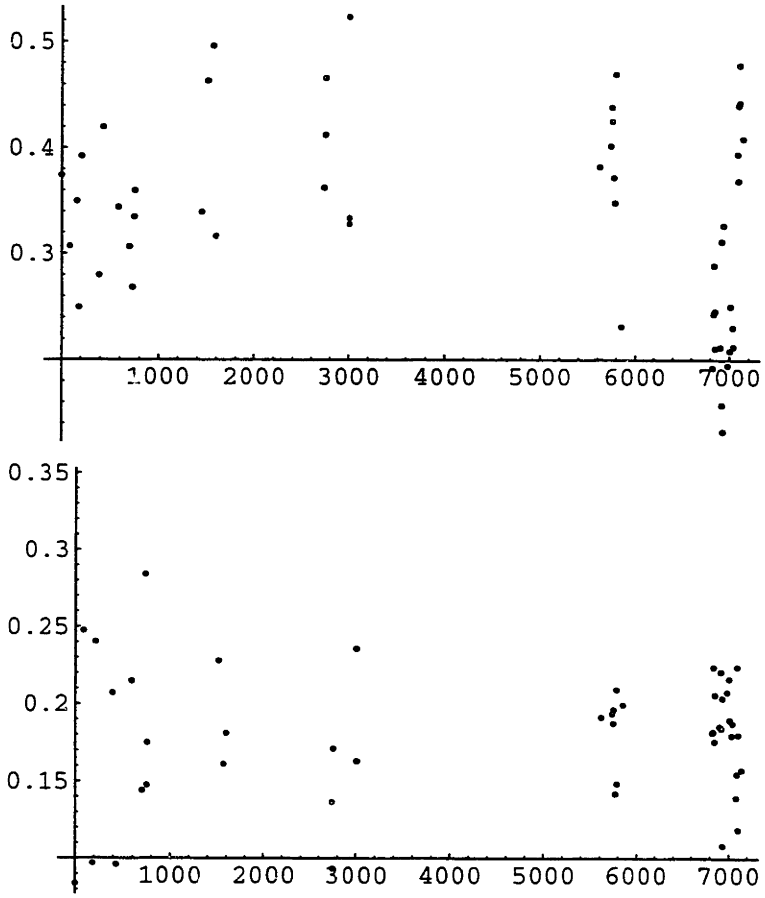

Figure C.1: Offsets in right ascension (top) and declination (bottom) for the distance between Rhea and Tethys. The offset is defined here as the difference between the distance as measured on the images, using centers computed by *ipMargAnal*, and as computed from the ephemeris. The y-axis measures this offset in arcseconds, and the x-axis shows time in seconds from the first image. Note the large scatter in positions over very short periods of time.

The scatter in these positions is undesirable. An alternate method is needed to check these results and try to improve the precision of the positions and distances measured in the images. One method is to fit a point-spread function (PSF) to one object and then use that PSF to find the center of another specified object. This allows one to compute accurate distances between the centers of two objects with identical PSFs.

We used the *doFit* routine, an existing package that does PSF fitting, on the 54 images and the distances between the star and Rhea and the star and Tethys were

computed. However, the scatter in the distances between Rhea and Tethys did not appreciably change: the mean offset (Rhea-Tethys) between the distances computed from the ephemeris and the distances computed using *doFit* were –0.363 ± 0.104 arcseconds in right ascension and –0.145 ± 0.062 arcseconds in declination. The scatter in the offsets (Figure C.2) appears little different than the scatter found using the *ipMargAnal* positions.

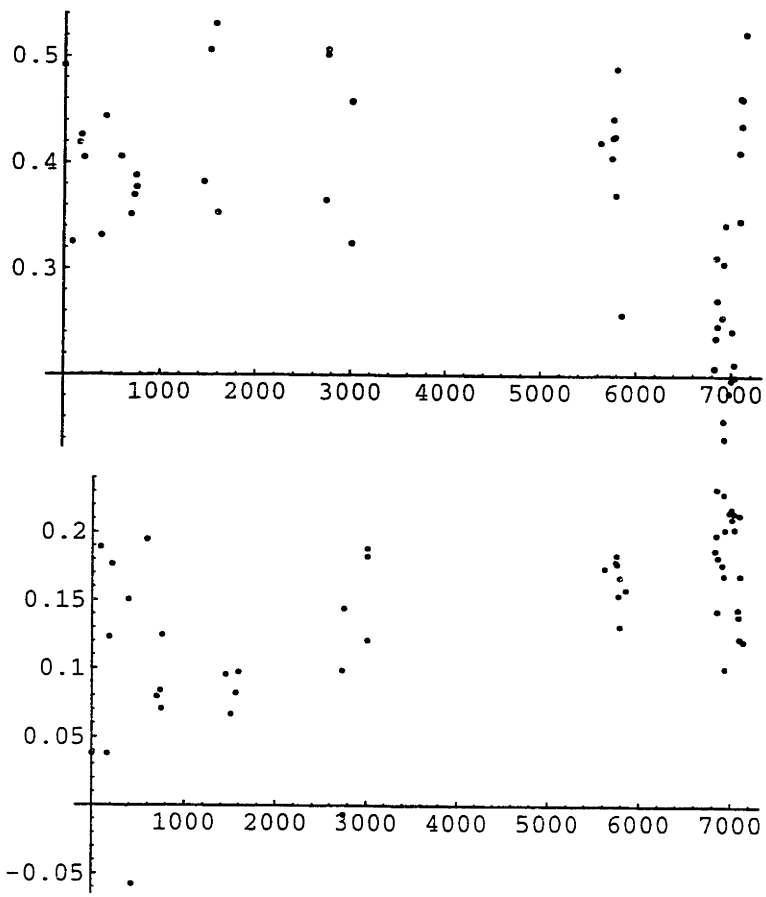

Figure C.2: Offsets in right ascension (top) and declination (bottom) for the distance between Rhea and Tethys. The offset is defined here as the difference between the distance as measured on the images, using centers computed by *doFit,* and the distance as computed from the ephemeris . The *y*-axis measures this offset in arcseconds, and the *x*-axis shows time in seconds from the first image. Note the large scatter in positions over very short periods of time, and the similarity to the scatter shown in Figure C.1.

In this case, *doFit* does little, if anything, to reduce the scatter in the positions. This means that the scatter is due to either variations in the ephemeris for the moons or variations in the actual positions of the moons as seen in the images. We can test this by looking at the ephemeris positions as calculated and looking for evidence of variations or other problems which might explain the scatter. The distances between Rhea and Tethys as computed by the ephemeris are shown in Figure 3.

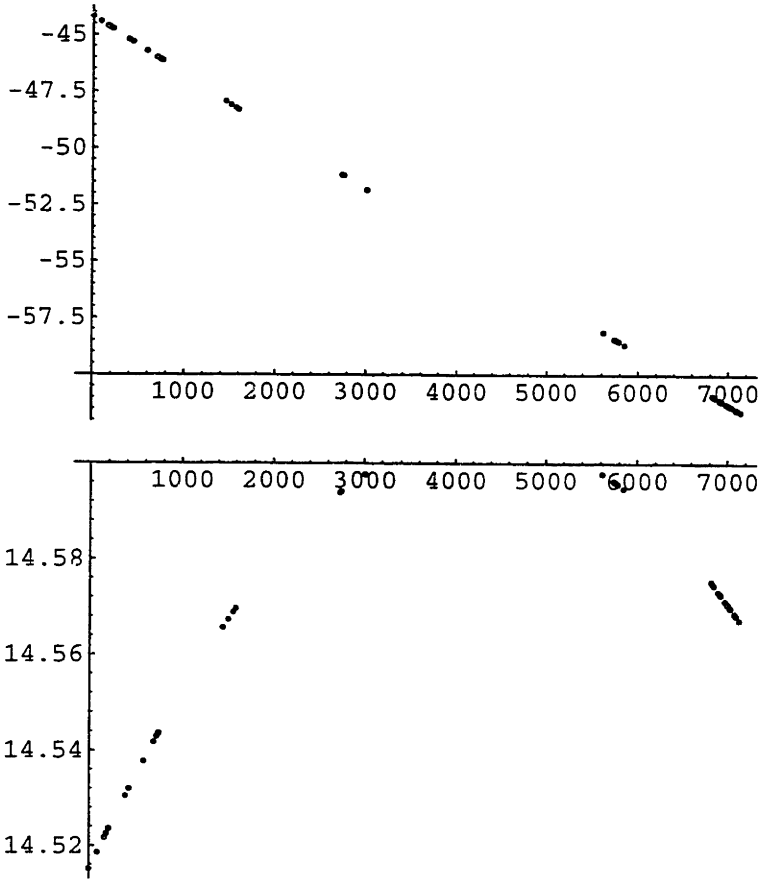

Figure C.3: The distance between Rhea and Tethys as computed by the ephemeris in right ascension (top) and declination (bottom). The *y*-axis is distance (Rhea–Tethys) in arcseconds, and the *x*-axis is time in seconds from the first image. Although the declination distance is nonlinear, both curves follow smooth paths with no sign of irregularities which could explain the scatter in the offsets seen in Figures C.1 and C.2.

Although the declination distance is not linear, the smooth nature of both curves provides no evidence of variations which could explain the scatter seen in the offsets. As an example, the variation in positions for the last set of declination positions (at a time of around 7000 seconds) is less than 0.02 arcseconds. However, the scatter seen in the declination offsets at that time is over 0.1 arcseconds, or more than five times the scatter seen in the ephemeris positions. Thus, it seems most likely that the source of the scatter is the positions of the moons from the images themselves, perhaps due to seeing effects, and other techniques will not be able to improve on this scatter.

To check this conclusion the *f* and *g* residuals from the difference between the star and Rhea and the star and Tethys were plotted against one another (Figure C.4). The *f* residuals show a very high degree or correlation, with a correlation coefficient of 0.91. The *g* residuals have a much lower correlation coefficient of 0.12, but the plot still shows a noticeable correlation between the two sets of residuals.

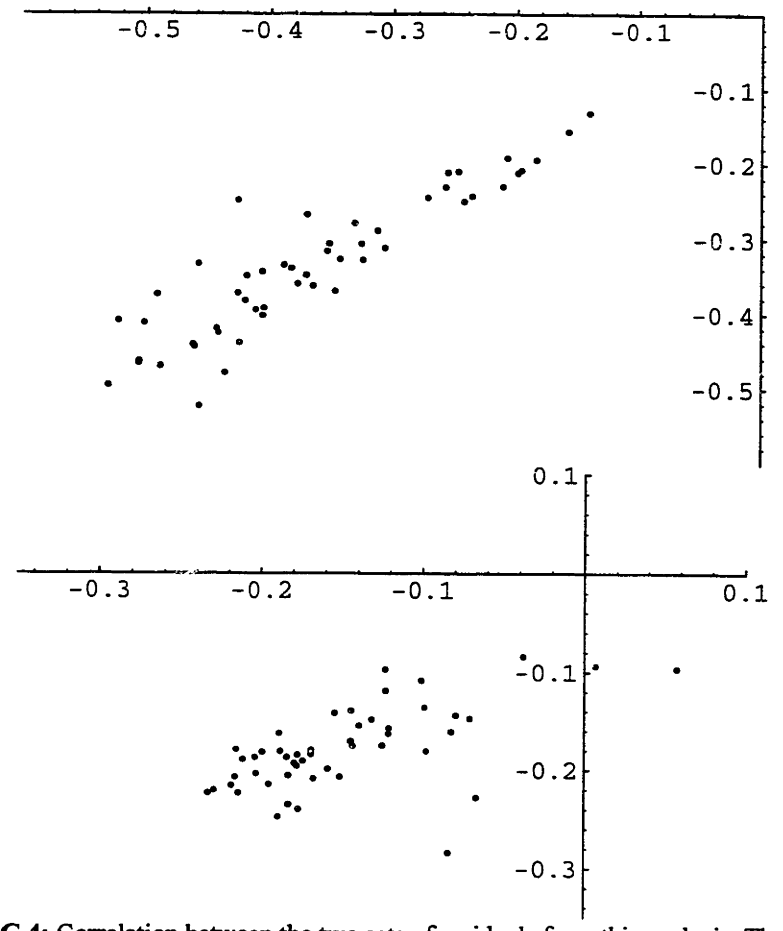

Figure C.4: Correlation between the two sets of residuals from this analysis. The top plot compares *f* residuals and the bottom compares *g* residuals. On each plot the residuals (differences between the star-Rhea and star-Tethys distances) from *doFit* are plotted on the *x*-axis and residuals from *margAnal* are plotted on the *y*-axis. There is a strong correlation between the two sets of *f* residuals while the *g* residuals show a weaker, but still noticeable, correlation.

We can compare the differences in the Rhea and Tethys offsets with the errors in the ephemeris positions for these bodies. Jacobson (1997) notes that both Rhea and Tethys have the same errors: 500 km in the radial direction and in the out-of-plane direction, and 1000 km in the "downtrack" direction, along the orbital path. Because the inclination of the orbits of both moons is very small (1°.86 for Tethys and 0°.35 for Rhea (USNO 1997)), and because the orbits are observed here edge-on, the error in declination, and hence *g*, will come from the out-of-plane error, while the error in right ascension σ_α, and hence *f*, will be a contribution of the radial and downtrack errors, as a function of the position of each moon in its orbit:

$$\sigma_\alpha = |R\sin\varphi| + |D\cos\varphi| \qquad \text{(C.2)}$$

where R is the radial error and D the downtrack error, while φ is the angular position of the moon (defined such that φ is 90° for eastern elongation). For these observations φ changes from 40° to 65°.9 for Tethys and from 12° to 18°.6 for Rhea. We then find that the right ascension error changes from 1080 to 1107 km for Rhea and from 1087 to 865 km for Tethys. The declination error is a constant 500 km for both bodies. These errors are several times larger than the errors shown in Table C.3. However, they are still insufficient to reconcile the large differences between the two data sets.

Alternate Technique

Since the analysis described above produces two very different answers for the *f* and *g* offsets depending on the data used, another analysis is needed to provide an independent result that can be compared to the results from the previous method. This new analysis should use new data and/or a new analysis technique to avoid any errors introduced into the previous analysis.

Previously, we noted that Saturn had been excluded from the analysis using *ipMargAnal*, and later *doFit*, since its complex shape made it difficult for the software to find accurate centers using their fitting routines. However, it is possible to use another technique to locate the center of Saturn in the images. The new technique is based on simple rules of geometry and straightforward analysis methods.

From basic geometry, the diameter of a conic section, such as an ellipse, is defined as the locus of the midpoints of a set of parallel chords. Different diameters can

be defined by using different sets of parallel chords. Since any diameter of an ellipse passes through its center, the exact location of the center can be found by determining the intersection of two different diameters. (Figure C.5)

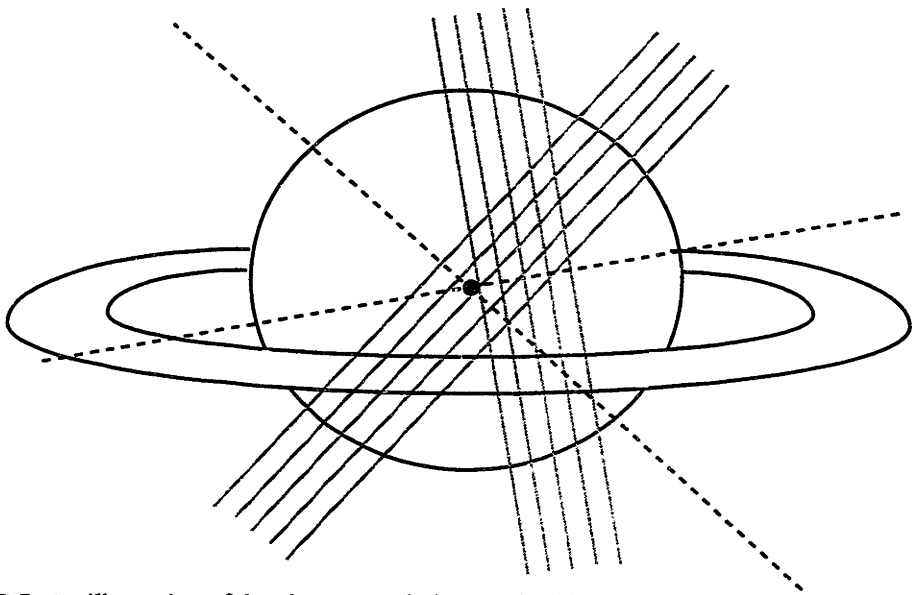

Figure C.5: An illustration of the alternate technique to find the center of Saturn. The gray lines are parallel chords which pass through the disk of Saturn. The midpoints of the chords form diameters of the ellipse, shown above as dashed lines. The intersection of the lines is at the center of the ellipse.

Define the equation of a chord as $y = mx + c$, where m is the slope and c is the y-intercept of the chord. The chord intercepts the ellipse at two points, (x_1,y_1) and (x_2,y_2). The midpoint of the chord, (x_m,y_m) is simply found by:

$$x_m = \frac{x_1 + x_2}{2}$$
$$y_m = \frac{y_1 + y_2}{2} \qquad \text{(C.3)}$$

We can take the equation for the chord and substitute it into the general form of the equation for the ellipse:

$$\frac{x^2}{a^2}+\frac{y^2}{b^2}=1 \tag{C.4}$$

Substituting $mx + c$ for y and simplifying gives:

$$\left(a^2m^2+b^2\right)x^2+\left(2a^2mc\right)x+a^2\left(c^2-b^2\right)=0 \tag{C.5}$$

This equation has two roots, which correspond to the points x_1 and x_2, the two points where the chord intersects the ellipse. The sum of these roots is expressed by:

$$x_1+x_2=-\frac{2a^2mc}{a^2m^2+b^2} \tag{C.6}$$

Using the definition of the midpoint from Eq. C.6, we can now state:

$$x_m=-\frac{a^2mc}{a^2m^2+b^2} \tag{C.7}$$

By substituting for x instead of y in the general equation for the ellipse and following the same steps, we can obtain an expression for the y value of the midpoint:

$$y_m=\frac{b^2c}{a^2m^2+b^2} \tag{C.8}$$

We can now find the equation of the line formed by the midpoints of a set of parallel chords, by taking the ratio of y_m to x_m:

$$\frac{y_m}{x_m}=-\frac{b^2}{a^2m} \tag{C.9}$$

thus,

$$y_m = -\frac{b^2}{a^2 m} x_m \tag{C.10}$$

This is the equation of a straight line that passes through the center of the ellipse (which in the general form of the equation of an ellipse is defined as the point (0,0)). When the location of the center of the ellipse is unknown, two such lines can be derived from two different sets of parallel chords, one set with a different slope than the other: the location of the intersection of the lines is the center of the ellipse.

This technique can be applied to the Saturn data by taking the limb of Saturn to be an ellipse. We generated two sets of parallel chords, taking care to make sure the chords pass through the limb of the planet on both sides and do not encounter Saturn's ring system, which would invalidate this method. The point where the chord passes the limb is found by finding the pixel location where the counts exceed a certain level well above the background; in this case, 5000 counts. The midpoint is then computed between the two points the chord crosses the limb, and a line is fit to the set of midpoints. The intersection of two such lines, computed using two sets of chords, provides the center of Saturn on a particular image.

This process was repeated for 32 of the 54 astrometric frames taken prior to the occultation event (only those images taken in the K band were used; the remaining 22, taken using filters at 2.12 and 2.3 μm, featured little light coming from the disk of Saturn, making this technique usable on those images.)

With the positions of the center of Saturn, as well as positions of the center of the star from previous analyses, we could now directly compare the distance between the star

and Saturn between the images and the ephemeris, without the need of using positions of Rhea, Tethys, or the other moons. We did this by simply translating the x-y pixel distances on the image into f-g distances in kilometers, using the rotation angle and pixel scale in Table 2. The offsets f_0 and g_0 come directly from comparing the two sets of distances.

This analysis results in another, different set of values for f_0 and g_0. We found f_0 to be 4088 ± 490 km and g_0 to be 0 ± 360 km. These results are very different from the results found using the moons Rhea and Tethys, and cannot be used to confirm, or refute, either result.

Conclusion

The three different analyses presented here resulted in three different results for the offsets f_0 and g_0. It may be impossible to determine which one is correct from those results alone, but we can use the different offsets in lightcurve analysis to see which one or ones gives the most reasonable results. We applied the three sets of offsets to the data set and computed isothermal model fits for each set (see Chapter 3 for a complete description of the model fit technique.) As with the other data sets, we fit for four parameters: the background and full signal levels, the uncorrected half-light radius, and the ratio of half-light radius to scale height (also known as the energy ratio.) (Table C.4) We also computed atmospheric attributes, such as scale height, temperature, and pressure, based on those conditions (Table C.5). We corrected the half-light radius to account for general relativity effects, and found the equivalent equatorial half-light radius (Table C.6).

Table C.4: Model Fit Parameters

Data Set	Background	Full	r_H (km) (uncorrected)	λ_{Hi}
Tethys offset	–0.001± 0.013	1.065 ± 0.010	56708 ± 5	1352 ± 100
Rhea offset	–0.002± 0.013	1.065 ± 0.010	58958 ± 5	1412 ± 106
Saturn offset	–0.002± 0.013	1.063 ± 0.010	57105 ± 5	1381 ± 103

Table C.5: Derived Values from Model Fits

Data Set	Scale Height (km)	Temperature (K)	Pressure (μbar)
Tethys offset	42.0 ± 3.1	116.7 ± 8.7	1.13 ± 0.15
Rhea offset	41.8 ± 3.1	106.0 ± 7.9	1.00 ± 0.13
Saturn offset	41.4 ± 3.1	112.2 ± 8.4	1.06 ± 0.15

Table C.6: Equivalent Equatorial Half-Light Radii

Data Set	r_H (km) (corrected)	Latitude (degrees)	*a* (km)
Tethys offset	56749 ± 5	–52.73 ± 0.02	60939 ± 5
Rhea offset	58997 ± 5	–52.05 ± 0.02	63724 ± 5
Saturn offset	57146 ± 5	–48.89 ± 0.02	60976 ± 5

Using Table C.6 we can discard the Rhea offset as a viable solution, since it gives an equivalent equatorial half-light radius that is far higher than the other two data sets or the result from Hubbard *et al.* (1997). However, both the data sets using the Tethys-derived offset and the Saturn-derived offset have similar results, and it is difficult to select between the two.

Fortunately, as Table C.5 shows, data sets using all three offsets generate similar solutions for atmospheric parameters such as scale height, temperature, and pressure. Thus, the choice of a particular offset will only have an effect on studies of the absolute half-light radius and precise location of the immersion. For the studies conducted in Chapter 3, we chose to use the Tethys offsets as they had marginally smaller errors in half-light radius and energy ratio.

Appendix D
Mathematica™ Notebooks

This appendix lists the *Mathematica*™ notebooks used in generating results for this thesis, divided by chapter and appendix section. These notebooks are all stored on the machine lowell.mit.edu, in folders contained in "Internal HD:Local Files:Projects:Saturn". In some cases on the most recent version of the notebook is listed; past versions are archived in the same folder as the one listed for the given notebook.

Chapter 1

None used

Chapter 2

Period of variations in FOS data:	1995-FOS:wave test 1.0.m
1996 IRTF lightcurve:	1996 GSC 0010-00284:IRTF Observations:Model Fits:lightcurves 1.0.4.t
28 Sgr lightcurve:	1989 28 Sgr:28Sgr f&g calibration 1.0.m

Chapter 3

Model fits:	1995-FOS:Immersion:Model Fits:model fit lb 0203 1.1.m
	1995-FOS:Immersion:Model Fits:model fit lb 0204 1.1.m
	1995-FOS:Emersion:Model Fits:model fit lb 0305 1.1.m
	1996 GSC 0010-00284:IRTF Observations:Model Fitsmodel fit 1996 IRTF 1.1.m
	1989 28 Sgr:model fit 28Sgr 1.0.m
Inversions:	1995-FOS:Immersion:Inversions:inversion 0203 1.41.m
	1995-FOS:Immersion:Inversions:inversion 0204 1.31.m
	1995-FOS:Emersion:Inversions:inversion 0305 1.12.m
	1996 GSC 0010-00284:IRTF Observations:Inversions:inversion IRTF96 1.61.m
	1989 28 Sgr:inversion 28Sgr 1.2.1.m

Chapter 4

Normalized temperature and number density: Power Spectra:power spectrum 0203 1.4.m

Power Spectra:power spectrum 0203 1.4.m

Power Spectra:power spectrum 0305 1.3.m

Power Spectra:power spectrum IRTF96 1.4.m

Power Spectra:power spectrum 28Sgr 1.3.m

Chapter 5

Power spectra and lapse rates: Power Spectra:power spectrum 0203 1.4.m

Power Spectra:power spectrum 0203 1.4.m

Power Spectra:power spectrum 0305 1.3.m

Power Spectra:power spectrum IRTF96 1.4.m

Power Spectra:power spectrum 28Sgr 1.3.m

Chapter 6

Refractivities of hydrogen and helium: 1995-FOS:refractivities 1.0.m

Refractivity ratio determination: 1995-FOS:Immersion:Color Tests:color test 0203 1.2.1.m

1995-FOS:Immersion:Color Tests:color test 0204 1.2.1.m

1995-FOS:Emersion:Color Tests:color test 0305 1.2.1.m

Chapter 7

None used

Appendix A

Physical model background subtraction tests on 0305 data:

1995-FOS:Emersion:Background Subtraction:background subtraction 1.53.b.m

Linear background subtraction: 1995-FOS:Immersion:linear bkgr subt 0203 1.0.m

1995-FOS:Immersion:linear bkgr subt 0204 1.0.m

1995-FOS:Emersion:linear bkgr subt 0305 1.0.m

Appendix B:

LED timing tests: 1996 GSC 0010-00284:IRTF Observations:Timing:led data 1.02.m

Appendix C

Rhea-Tethys offsets:

1996 GSC 0010-00284:IRTF Observations:Prediction/Astrometry:Rhea/Tethys offsets 1.0.m

Event astrometry notebooks (only most recent listed):

1996 GSC 0010-00284:IRTF Observations:Prediction/Astrometry:Saturn_predict_960729_2.42.m

Saturn chord technique:

1996 GSC 0010-00284:IRTF Observations:Prediction/Astrometry:saturn center chords 1.3.m

Appendix E
Glossary

This glossary is based on Olkin (1996) with contributions from other sources cited in the references section.

28 Sgr — a star that was occulted by the planet Saturn on 1989 July 3.

absolute magnitude — the apparent magnitude of an object if it were at a distance of 10 parsec

adiabat — the trajectory in pressure-temperature space followed by a parcel of matter which undergoes changes in volume without exchanging heat with its surroundings

arcsecond — one part in 3600 of a degree, sometimes abbreviated as arcsec

ASI — Atmospheric Structure Instrument on the Galileo atmospheric probe

Astronomical Unit (AU) — average distance between the Earth and Sun. 1.4959787×10^{11} m

bar — a unit of pressure: 1×10^{6} dyne/cm^{3}. The standard atmospheric pressure at Earth's surface (termed "one atmosphere") is 1.013 bar

Brunt-Väisälä frequency — The buoyancy frequency for vertically-propagating atmospheric waves

CCD — charge-couple device

chords — an occultation light curve or just the immersion or emersion section

CIRS — Cassini Infrared Spectrometer instrument

correlation coefficient — a dimensionless quantity taking values from −1 to +1 measuring the degree of linear association between two variates. A value of −1 indicates a perfect negative linear relationship, +1 a perfect positive relationship.

curvature matrix — the inverse of the covariance matrix

cycle time — time from the beginning of one integration to the beginning of the next, it includes both the full integration time plus any dead time (see below)

data window — a function that is convolved with a power spectrum to reduce the problem of power "leakage" at high frequencies. Common data windows include the Hann, Bartlett, and Welch.

dead time — the time between integrations

declination — the angular distance on the celestial sphere north or south of the celestial equator. It is measured along the hour circle passing through the celestial object.

digicon — an instrument that accelerates electrons emitted by a photocathode onto a linear array of diodes

diurnal aberration — the component of stellar aberration (see stellar aberration) resulting from the observer's diurnal motion about the center of the Earth

emersion — that portion of an event (in this case a stellar occultation) in which one object (the star) reappears from behind another (the occulting body).

energy ratio — a parameter in the model of Elliot and Young (1992). It is the ratio of the half-light radius to the scale height at the half-light radius.

ephemeris — a tabulation of the positions of a celestial object in an orderly sequence for a number of dates

extinction — the scattering or absorption of photons

***f*-*g* plane** — a coordinate system centered on a planet, with the f axis aligned with right ascension and the g axis aligned with declination, as defined by Elliot *et al.* (1993)

FGS — Fine Guidance Sensors on the Hubble Space Telescope

FITS Flexible Image Transport System, a commonly-used format for storing astronomical data

flat-field image an image of an evenly illuminated field

FOS Faint Object Spectrograph on the Hubble Space Telescope from 1990-1997

frame transfer a method for reading out a CCD to minimize dead time. The recorded image is transferred to a different part of the detector after the exposure and read out during later integrations.

FWHM full width at half maximum

geocentric with reference to, or pertaining to, the center of the Earth

geometric albedo the ratio of brightness of an object to the brightness of a perfectly diffusing disk of the same radius at the same distance from the Sun

GPS Global Positioning System, a system of satellites that transmit time signals that allow users with GPS receivers to determine an accurate time and position

gravity wave a type of wave generated in stably-stratified atmospheres when a vertically-displaced parcel of air undergoes buoyancy oscillations. Such waves are also called buoyancy waves.

GSC Guide Star Catalog for the Hubble Space Telescope

GSC 5249-01240 star occulted by Saturn on 1995 November 20-21

GSC 0010-00254 star occulted by Saturn on 1996 July 29

guiding mode method used to guide the Hubble Space Telescope, options are either fine lock on a guide star (more accurate) or gyros on spacecraft

half-disk albedo the geometric albedo of the central region of a body out to one-half of the object's radius

half-light radius — the radius (typically in the planet plane) probed by a stellar occultation when the flux from the occulting star equals half its unocculted value

HOPI — High-speed Occultation Photometer/Imager, an instrument planned for the SOFIA aircraft

HSP — High-Speed Photometer instrument on the Hubble Space Telescope 1990-1993

HST — Hubble Space Telescope

hydrostatic equilibrium — the condition of stability that exists when gravitational forces are exactly balanced by counteracting gas and radiation pressure

immersion — that portion of an event (in this case a stellar occultation) in which one object (the star) disappears behind another (the occulting body).

impact parameter — the closest approach distance (usually measured in arcsec) between two celestial bodies.

IRTF — Infrared Telescope Facility. Located on Mauna Kea, Hawaii.

K filter — center wavelength 2.21 μm and a FWHM of 0.39 μm

L+inv model — a model developed by Hubbard et al. (1997) to explain the temperature and pressure profiles in Saturn's atmosphere between 60,500 and 61,500 km in equatorial radius

lapse rate — the change in temperature versus altitude in the atmosphere

LED — light-emitting diode

lightcurve — the record of observed flux from a body or bodies

light travel time — the interval of time required for light to travel from a celestial body to the Earth. During this interval the motion of the body in space causes an angular displacement of its apparent place from its geometric position.

Linear Limb Darkening — a model developed by Karkoschka and Tomasko (1992) to compute the reflectivity of an object using the angle of the incident and reflected waves, the phase angle of the observations, and the full- and half-disk albedos of the object

linearized perfect gas law — a relationship where the change in temperature over initial temperature equals the change in pressure over initial pressure minus the change in density over the initial density

magnetosphere — the region of space surrounding a rotating, magnetized sphere

magnitude — a measurement on a logarithmic scale of the brightness of a celestial object considered as a point source

mesosphere — the region of an atmosphere above the stratosphere and below the thermosphere were temperatures are unchanged or slightly falling with altitude

microbar — μbar, 10^{-6} bar

NSFCAM — an astronomical instrument for imaging in the infrared at the IRTF

Nyquist sampling theorem — a theorem which requires that data be sampled at twice the highest frequency present in the data

occultation — the obscuration of one celestial body by another of greater apparent diameter

oblateness — the ratio of the difference between the equatorial and polar radii to their mean value

PCCD — a Portable CCD instrument designed to perform high-speed imaging for occultation observations. Four PCCD systems exist.

photometry — a measurement of the intensity of light usually specified for a specific wavelength range

pixel scale — the ratio of the distance (in arcseconds or other units) between two objects and the distance in pixels between the two objects on a CCD image

planet plane — the plane parallel to the shadow plane at the occulting body. See Figure 5.1.

R filter — center wavelength = 700 nm, passband = 220 nm

refraction — the bending of a light ray as it passes through an atmosphere

right ascension — angular distance on the celestial sphere measured eastward along the celestial equator from the equinox to the hour circle passing through the celestial object

rotation angle — the angle between the right ascension and declination axes and the orientation of the CCD image

RSS — Radio Science Subsystem on the Voyager and Cassini spacecraft

saturation — the condition when a gravity wave's amplitude does not increase as density decreases.

scale height — the distance in an atmosphere over which the pressure or number density changes by a factor of e. For an isothermal atmosphere the pressure and density scale heights are equal.

Sellmeier equation — equation used to express the refractivity of an element or compound as a function of wavenumber.

shadow plane — the plane perpendicular to the direction of the occulted star whose origin is at the center of the Earth.

shadow velocity — the velocity of an occultation shadow as seen from an observer.

SOFIA — Stratospheric Observatory For Infrared Astronomy, due to be operational in 2002

"Spencer 2.3" a filter used on the NSFCAM at the IRTF, it has a central wavelength of 2.28 μm and a FWHM of 0.17 μm

STIS Space Telescope Imaging Spectrograph

stratosphere an upper layer of a planetary atmosphere, above the troposphere and below the thermosphere, characterized by a vertical temperature gradient which is stable against convection

subframe a subsection of an array detector

subsolar the point on a planet where the Sun is at the local zenith

thermal conductivity the ability to transfer heat through contact between, but not exchange of, particles

thermosphere the region of temperature rise due to ionospheric heating

threshold in studies of the helium/hydrogen ratio, the offset from the isothermal model fit to a lightcurve used to determine which data points to accept or reject in the analysis.

topocentric with reference to, or pertaining to, a point on the surface of the Earth, usually with reference to a coordinate system.

tropopause the boundary between the troposphere and stratosphere (or for Triton, the thermosphere) where the vertical temperature gradient goes to zero

troposphere region of atmosphere characterized by a convective (adiabatic) temperature gradient. This is typically the region where most weather occurs.

UT Universal Time. A measure of time that conforms, within a close approximation, to the mean diurnal motion of the Sun and serves as the basis of all civil time keeping.

UVIS Ultraviolet and Infrared Spectrometer on the Cassini spacecraft

UVS Ultraviolet Spectrometer on the Voyager spacecraft

vignetting the diminution of observed flux due to an obstacle in the optical path

References

Allen, S. J., and R. A. Vincent 1995. Gravity wave activity in the lower atmosphere: seasonal and latitudinal changes. *J. Geophys. Res.* **100**, 1327-1350.

Atreya, S. K. 1986. *Atmospheres and Ionospheres of the Outer Planets and their Satellites*. Springer-Verlag, New York.

Barnes, J. R. 1990. Possible effects of breaking gravity waves on the circulation of the middle atmosphere of Mars. *J. Geophys. Res.* **95**, 1401-1421.

Barnet, C. D., R. F. Beebe, and B. J. Conrath 1992. A seasonal radiative-dynamic model of Saturn's troposphere. *Icarus* **98**, 94-107.

Baum, W. A., and A. D. Code 1953. A photometric observation of the occultation of σ Arietis by Jupiter. *Astron. J.* **58**, 108-112.

Benedict, G. F., E. Nelan, D. Story, B. McArthur, A. L. Whipple, W. H. Jefferys, W. van Altena, P. D. Hemenway, P. J. Shelus, O. G. Franz, A. Bradley, L. W. Fredrick, and R. L. Duncombe 1992. Astrometric Performance Characteristics of the Hubble Space Telescope Fine Guidance Sensors. *Publ. Astron. Soc. Pacific* **104**, 958-975.

Bezard, B., and D. Gautier 1985. A seasonal climate model of the atmospheres of the giant planets at the Voyager encounter time. *Icarus* **61**, 296-310.

Bosh, A. S. 1994. *Stellar occultation studies of Saturn's rings with the Hubble Space Telescope*. Ph. D. Thesis, Department of Earth, Atmospheric, and Planetary Sciences, Massachusetts Institute of Technology, Cambridge.

Bosh, A. S., and S. W. McDonald 1992. Stellar occultation candidates from the Guide Star Catalog. I. Saturn, 1991-1999. *Astron. J.* **103**, 983-990.

Brinkmann, R. T. 1971. Occultation by Jupiter. *Nature* **230**, 515-516.

Broadfoot, A. L., B. R. Sandel, D. E. Shemansky, S. K. Atreya, T. M. Donahue, H. W. Moos, J. L. Bertaux, J. E. Blamont, J. M. Ajello, and D. F. Strobel 1977. Ultraviolet spectrometer experiment for the Voyager mission. *Space Science Reviews* **21**, 183-205.

Buie, M. W., R. L. Millis, L. H. Wasserman, J. L. Elliot, S. J. Bus, E. W. Dunham, E. F. Young, W. B. Hubbard, D. M. Hunten, and W. K. Wells 1993. CCD Camera Occultation System. *Bull. Amer. Astron. Soc.* **25**, 1115.

Campbell, J. K., and J. Anderson 1989. Gravity Field of the Saturnian System from Pioneer and Voyager tracking Data. *Astron. J.* **97**, 1485-1495.

Connerney, J. E. P. 1986. Magnetic connection for Saturn's rings and atmosphere. *Geophys. Res. Lett.* **13**, 773-776.

Conrath, B. J., and J. A. Pirraglia 1983. Thermal structure of Saturn from Voyager infrared measurements: Implications for atmospheric dynamics. *Icarus* **53**, 286-292.

Conrath, B. J., D. Gautier, R. A. Hanel, and J. S. Hornstein 1984. The helium abundance of Saturn from Voyager measurements. *Astrophys. J.* **282**, 807-815.

Conrath, B. J., D. Gautier, T. C. Owen, and R. E. Samuelson 1993. Constraints on N2 in Neptune's atmosphere from Voyager measurements. *Icarus* **101**, 168-171.

Conrath, B. J., P. J. Gierasch, and S. S. Leroy 1990. Temperature and Circulation in the Stratosphere of the Outer Planets. *Icarus* **83**, 255-281.

Conrath, B., R. E. Samuelson, D. Gautier, G. F. Lindal, and W. A. Shaffer 1991. The helium abundance of Neptune from Voyager measurements. *J. Geophys. Res.* **96**, 18,907-18,919.

Conrath, B., R. Hanel, D. Gautier, A. Marten, and G. Lindal 1987. The helium abundance of Uranus from Voyager measurements. *J. Geophys. Res.* **92**, 15,003-15,010.

Cooray, A. R., J. L. Elliot, A. S. Bosh, L. A. Young, and M. A. Shure 1998. Stellar occultation observations of Saturn's north-polar temperature structure. *Icarus* **132**, 298-310.

Dewan, E. 1997. Saturated-cascade similitude theory of gravity wave spectra. *J. Geophys. Res.* **102**, 29,799-29,817.

Dewan, E. M., and R. E. Good 1986. Saturation and the "universal" spectrum for vertical profiles of horizontal scalar winds in the atmosphere. *J. Geophys. Res.* **91**, 2742-2748.

Elliot, J. L. 1979. Stellar occultation studies of the solar system. *Ann. Rev. Astron. & Astrophys.* **17**, 445-475.

Elliot, J. L., A. S. Bosh, M. L. Cooke, R. C. Bless, M. J. Nelson, J. W. Percival, M. J. Taylor, J. F. Dolan, E. L. Robinson, and G. W. van Citters 1993. An occultation by Saturn's rings on 1991 October 2-3 observed with the Hubble Space Telescope. *Astron. J.* **106**, 2544-2572.

Elliot, J. L., and C. B. Olkin 1996. Probing Planetary Atmospheres with Stellar Occultations. In *Annual Review of Earth and Planetary Sciences* (G. W. Wetherill, Ed.), pp. 89-123. Annual Reviews Inc., Palo Alto.

Elliot, J. L., and L. A. Young 1992. Analysis of stellar occultation data for planetary atmospheres. I. Model fitting, with application to Pluto. *Astron. J.* **103**, 991-1015.

Elliot, J. L., H. B. Hammel, L. H. Wasserman, O. G. Franz, S. W. McDonald, M. J. Person, C. B. Olkin, E. W. Dunham, J. R. Spencer, J. A. Stansberry, M. W. Buie, J. M. Pasachoff, B. A. Babcock, and T. H. McConnochie 1998. Global warming on Triton. *Nature* **393**, 765-767.

Elliot, J. L., L. H. Wasserman, J. Veverka, C. Sagan, and W. Liller 1974. The occultation of Beta Scorpii by Jupiter. II. The hydrogen-helium abundance in the Jovian atmosphere. *Astrophys. J.* **190**, 719-729.

Elliot, J. L., R. G. French, E. Dunham, P. J. Gierasch, J. Veverka, C. Church, and C. Sagan 1977. Occultation of ε Geminorum by Mars: Evidence for atmospheric tides? *Science* **195**, 485-486.

Elliot, J. L., R. G. French, E. Dunham, P. J. Gierasch, J. Veverka, C. Church, and C. Sagan 1977. Occultation of ε Geminorum by Mars. II. The structure and extinction of the Martian upper atmosphere. *Astrophys. J.* **217**, 661-679.

Festou, M. C., and S. K. Atreya 1982. Voyager ultraviolet stellar occultation measurements of the composition and thermal profiles of the Saturnian upper atmosphere. *Geophys. Res. Lett.* **9**, 1147-1150.

French, R. G., and J. L. Elliot 1979. Occultation of ε Geminorum by Mars. III. Temperature of the Martian upper atmosphere. *Astrophys. J.* **229**, 828-845.

French, R. G., J. L. Elliot, and P. J. Gierasch 1978. Analysis of stellar occultation data. Effects of photon noise and initial conditions. *Icarus* **33**, 186-202.

Fritts, D. C. 1989. A review of gravity wave saturation processes, effects, and variability in the middle atmosphere. *PAGEOPH* **130**, 343-371.

Fritts, D. C., T. Tsuda, T. Sato, S. Fukao, and S. Kato 1988. Observational evidence of a saturated gravity wave spectrum in the troposphere and lower stratosphere. *J. Atmos. Sci.* **45**, 1741-1759.

Gardner, C. S. 1994. Diffusive filtering theory of gravity wave spectra in the atmosphere. *J. Geophys. Res.* **99**, 20,601-20,622.

Gautier, D., and T. Owen 1989. The composition of outer planet atmospheres. In *Origin and Evolution of Planetary and Satellite Atmospheres* (S. K. Atreya, J. B. Pollack and M. S. Matthews, Ed.), pp. 487-512. University of Arizona Press, Tucson.

Gautier, D., B. Conrath, M. Flasar, R. Hanel, V. Kunde, A. Chedin, and N. Scott 1981. The helium abundance of Jupiter from Voyager. *J. Geophys. Res.* **86**, 8713-8720.

Goldsmith, D. W. 1963. Differential refraction in planetary atmospheres with linear scale height gradients. *Icarus* **2**, 341-349.

Goody, R. M., and Y. L. Yung 1989. *Atmospheric Radiation*. Oxford Univ. Press, New York.

Hanel, R. A., B. J. Conrath, V. Kunde, J. C. Pearl, and J. A. Pirraglia 1983. Albedo, internal heat flux, and energy balance of Saturn. *Icarus* **53**, 262-285.

Harrington, J., M. L. Cooke, W. J. Forrest, J. L. Pipher, E. W. Dunham, and J. L. Elliot 1993. IRTF observations of the occultation of 28 Sgr by Saturn. *Icarus* **103**, 235-252.

Heasley, J. N., and R. W. Milkey 1978. Structure and spectrum of quiescent prominences. III - Application of theoretical models in helium abundance determinations. *Astrophys. J.* **221**, 677-688.

Hines, C. 1991. The saturation of gravity waves in the middle atmosphere, 2, Development of Doppler-spread theory. *J. Atmos. Sci.* **48**, 1360-1379.

Hines, C. 1996. Nonlinearity of gravity wave saturated spectra in the middle atmosphere. *Geophys. Res. Lett.* **23**, 3309-3312.

Hinson, D. P., and J. M. Jenkins 1995. Magellan radio occultation measurements of atmospheric waves on Venus. *Icarus* **114**, 310-327.

Hubbard, W. B., and D. J. Stevenson 1984. Interior structure of Saturn. In *Saturn* (T. Gehrels and M. S. Matthews, Ed.), pp. 47-87. University of Arizona Press, Tucson.

Hubbard, W. B., C. C. Porco, D. M. Hunten, G. H. Rieke, M. J. Rieke, D. W. McCarthy, V. Hammerle, J. Haller, B. McLeod, L. A. Lebofsky, R. L. Marcialis, J. B. Holberg, R. Landau, L. Carrasco, J. Elias, M. W. Buie, E. W. Dunham, S. E. Persson, T. Boroson, S. West, R. G. French, J. Harrington, J. L. Elliot, W. J. Forrest, J. L. Pipher, R. J. Stover, B. Sicardy, A. Brahic, and I. Grenier 1997. Structure of Saturn's mesopshere from the 28 Sgr occultations. *Icarus* **130**, 404-425.

Hubbard, W. B., C. C. Porco, D. M. Hunten, G. H. Rieke, M. J. Rieke, D. W. McCarthy, V. Haemmerle, R. Clark, E. P. Turtle, J. Haller, B. McLeod, L. A. Lebofsky, R. Marcialis, J. B. Holberg, R. Landau, L. Carrasco, J. Elias, M. W. Buie, S. E. Persson, T. Boroson, S. West, and D. J. Mink 1993. The occultation of 28 Sgr by Saturn: Saturn pole position and astrometry. *Icarus* **103**, 215-234.

Hubbard, W. B., J. J. MacFarlane, J. D. Anderson, G. W. Null, and E. D. Biller 1980. Interior structure of Saturn inferred from Pioneer 11 gravity data. *J. Geophys. Res.* **85** [illegible]-5916.

Jacobson. .. 1997. Update of the major Saturian satellite ephemerides. *JPL Interoffice Memorandum 312.1-96-012.*

Jokipii, J. R., and W. H. Hubbard 1977. Stellar occultations by turbulent planetary atmospheres: The Beta Scorpii events. *Icarus* **30**, 537-550.

Karkoschka, E., and M. G. Tomasko 1992. Saturn's Upper Troposphere, 1986-1989. *Icarus* **97**, 161-181.

Kerridge, S. J., W. Flury, L. Horn, J.-P. Lebretor, D. Stetson, R. L. Stoller, and G. H. Tan 1992. Cassini: Mission to Saturn and Titan. *Exobiology in Solar System Exploration*, Ames Research Center, pp 229-248.

Kinney, A. L. 1994. *Hubble Space Telescope Faint Object Spectrograph instrument handbook, version 5.0.*

Koratkar, A. 1996. Pre-COSTAR and post-COSTAR observed point spread functions for the FOS, . *Instrument Science Report CAL/FOS-148.*

Kovalevsky, J., and F. Link 1969. Diamètre aplatissement et propriétés optiques de la haute atmosphère de Neptune d'après l'occultation de l'étoile BD-17° 4388. *Astron. & Astrophys.* **2**, 398-412.

Krasnopolsky, V. A. 1975. On the structure of Mars' atmosphere at 120-220 km. *Icarus* **24**, 28-35.

Kunde, V., and co-authors 1996. Cassini Infrared Fourier Spectroscopic Investigation. *Cassini/Huygens: A Mission to the Saturnian Systems*, Denver, pp 162-177.

Leggett, S., and T. Denault 1996. NSFCAM 256x256 InSb infrared array camera user's guide.

Leitherer, C. 1995. *HST Data Handbook.*

Lellouch, E., J. J. Goldstein, J. Rosenqvist, S. W. Bougher, and G. Paubert 1994. Global circulation, thermal structure, and carbon monoxide distribution in Venus' mesosphere in 1991. *Icarus* **110**, 315-339.

Leroy, S. S. 1994. Convectively generated internal gravity waves in Venus's middle atmosphere. Ph.D. Thesis, California Institute of Technology,

Lindal, G. F., D. N. Sweetnam, and V. R. Eshleman 1985. The atmosphere of Saturn: an analysis of the Voyager radio occultation measurements. *Astron. J.* **90**, 1136-1146.

Lindzen, R. S. 1981. Turbulence and stress owing to gravity wave and tidal breakdown. *J. Geophys. Res.* **86**, 9707-9714.

Makhlouf, U., E. Dewan, J. R. Isler, and T. F. Tuan 1990. On the importance of the purely gravitationally induced density, pressure, and temperature variations in gravity waves: their application to airglow observations. *J. Geophys. Res.* **95**, 4103-4111.

Mansfield, C. R., and E. R. Peck 1969. Dispersion of helium. *J. Opt. Soc. Am.* **59**, 199.

Matcheva, K. I., and D. F. Strobel 1998. Heating of Jupiter's thermosphere by dissipation of gravity waves due to molecular viscosity and heat conduction. *Bull. Amer. Astron. Soc.* **30**, 1075.

Matson, D. 1996. The Cassini/Huygens mission to the Saturnian system. *Cassini/Huygens: A Mission to the Saturnian Systems*, Denver, pp 22-29.

McDonald, S. W., and J. L. Elliot 1992. Triton stellar occultation candidates: 1992-1994. *Astron. J.* 104, 862-879.

McHugh, J. P., and A. J. Friedson 1996. Neptune's energy crisis: gravity wave heating of the stratosphere of Neptune. Division for Planetary Sciences meeting of the American Astronomical Society

Nastrom, G. D., T. E. Van Zandt, and J. M. Warnock 1997. Vertical wavenumber spectra of wind and temperature from high-resolution balloon soundings over Illinois. *J. Geophys. Res.* **102**, 6685-6701.

Nicholson, P. D., and C. Porco 1988. A new constraint on Saturn's zonal gravity harmonics from Voyager observations of an eccentric ringlet. *J. Geophys. Res.* **93**, 10209-10224.

Nicholson, P. D., C. McGhee, and R. G. French 1995. Saturn's central flash from the 3 July 1989 occultation of 28 Sgr. *Icarus* **113**, 57-83.

Niemann, H. B. 1996. The Galileo probe mass spectrometer: composition of Jupiter's atmosphere. *Science* **272**, 846-849.

Olkin, C. B. 1996. *Stellar occultation studies of Triton's atmosphere*. Ph. D. Thesis, Department of Earth, Atmospheric, and Planetary Sciences, Massachusetts Institute of Technology, Cambridge.

Pagel, B. E. J. 1982. Abundances of elements of cosmological interest. *Philos. Trans. R. Soc. London Ser. A.* **307**, 19-35.

Peck, E. R., and S. Huang 1977. Refractivity and dispersion of hydrogen in the visible and near-infrared. *J. Opt. Soc. Am.* **67**, 1550-1554.

Press, W. H., S. A. Teukolsky, W. T. Vetterling, and B. P. Flannery 1992. *Numerical recipes in FORTRAN: The art of scientific computing.* Cambridge Univ. Press, Cambridge.

Rizk, B., and D. M. Hunten 1990. Solar heating of the Uranian mesopause by dust of ring origin. *Icarus* **88**, 429-447.

Roques, F., B. Sicardy, R. G. French, W. B. Hubbard, A. Barucci, P. Bouchet, A. Brahic, J.-A. Gehrels, T. Gehrels, I. Grenier, T. Lebertre, J. Lecacheux, J. P. Maillard, R. A. McLaren, C. Perrier, F. Vilas, and M. D. Waterworth 1994. Neptune's upper stratosphere, 1983-1990: Ground-based stellar occultation observations. *Astron. & Astrophys.* **288**, 985-1011.

Shure, M., D. W. Toomey, J. T. Rayner, P. M. Onaka, and A. T. Denault 1994. NSFCAM: A new infrared array camera for the NASA Infrared Telescope Facility. *Instrumentation in Astronomy VIII*, Kona, HI, pp 25-33.

Sicardy, B., F. Ferri, F. Roques, J. Lecacheux, S. Pau, N. Brosch, Y. Nevo, W. B. Hubbard, H. J. Reitsema, C. Blanco, E. Carreira, W. Beisker, C. Bittner, H.-J. Bode, M. Bruns, H. Denzau, M. Nezel, E. Riedel, H. Struckmann, G. Appleby, R. W. Forrest, I. K. M. Nicolson, A. J. Hollis, and R. Miles 1998. The structure of Titan's stratosphere from the 28 Sgr occultation. *Icarus* submitted,

Slattery, W. L. 1977. The structure of the planets Jupiter and Saturn. *Icarus* **32**, 58-72.

Smith, G. R., D. E. Shemansky, J. B. Holberg, A. L. Broadfoot, B. R. Sandel, and J. C. McConnell 1983. Saturn's upper atmosphere from the Voyager 2 EUV solar and stellar occultations. *J. Geophys. Res.* **88**, 8667-8678.

Smith, J. D. 1995. *Lunar Occultation Timing in a Two-Telescope Observation of Saturn.* S.B. Thesis, Department of Physics, Massachusetts Institute of Technology, Cambridge.

Smith, P. L., M. C. E. Huber, and W. H. Parkinson 1976. Refractivities of H2, He, O2, CO, and Kr for $168 \leq \lambda \leq 288$ nm. Phys. Rev. A **13**, 1422-1434.

Smith, S. A., D. C. Fritts, and T. E. Van Zandt 1987. Evidence for a saturated spectrum of atmospheric gravity waves. *J. Atmos. Sci.* **44**, 1404-1410.

Smoluchowski, R. 1967. Internal structure and energy emission of Jupiter. *Nature* **215**, 691-695.

Stevenson, D. 1980. Saturn's luminosity and magnetism. *Science* **208**, 746-748.

Stevenson, D. J. 1982. Interiors of the giant planets. *Ann. Rev. Earth Planet Sci.* **10**, 257-295.

Taylor, F. W., S. B. Calcutt, P. G. J. Irwin, C. A. Nixon, P. L. Read, P. J. C. Smith, and T. J. Vellacott 1998. Investigation of Saturn's atmosphere by Cassini. *Planet. Space Sci.* **46**, 1315-1324.

Taylor, J. R. 1982. *An Introduction to Error Analysis*. University Science Books, Mill Valley.

Tokunaga, A. T., J. Caldwell, F. C. Gillett, and I. G. Nolt 1978. Spatially resolved infrared observations of Saturn. II - The temperature enhancement at the South Pole of Saturn. *Icarus* **36**, 216-222.

USNO 1997. *The Astronomical Almanac for the Year 1997*. U. S. Government Printing Office, Washington.

USNO 1998. *The Astronomical Almanac for the Year 1998*. U. S. Government Printing Office, Washington.

Van Zandt, T. E. 1982. A universal spectrum of buoyancy waves in the atmosphere. *Geophys. Res. Lett.* **9**, 575-578.

Von Zahn, U., and D. M. Hunten 1996. The helium mass fraction in Jupiter's atmosphere. *Science* **272**, 849-851.

Wasserman, L. H., and J. Veverka 1973a. Analysis of spikes in occultation curves: A critique of Brinkmann's method. *Icarus* **18**, 599-604.

Wasserman, L. H., and J. Veverka 1973b. On the reduction of occultation light curves. *Icarus* **20**, 322-345.

Weinstock, J. 1990. Saturated and unsaturated of gravity waves and scale-dependent diffusion. *J. Atmos. Sci.* **47**, 2211-2225.

Wells, D. C., E. W. Greisen, and R. H. Harten 1981. FITS: A flexible image transport system. *Astron. & Astrophys.* **44**, 363-370.

West, R. A. 1981. Sunlight absorption by aerosols in Jupiter's upper atmosphere. *Geophys. Res. Lett.* **8**, 847-849.

West, R. A., M. Sato, H. Hart, A. L. Lane, C. W. Hord, K. E. Simmons, L. W. Esposito, D. L. Coffeen, and R. B. Pomphrey 1983. Photometry and polarimetry of Saturn at 2640 and 7500 Å. *J. Geophys. Res.* **88**, 8679-8697.

Wolfram, S. 1991. *Mathematica*. Addison-Wesley Publishing Co., Redwood City, CA.

Woodgate, B. E., and co-authors 1997. The Space Telescope Imaging Spectrograph design. *Pub. Astron. Soc. Pacific* **110**, 1183-1204.

Yelle, R. V., L. A. Young, R. J. Vervack, R. Young, L. Pfister, and B. R. Sandel 1996. The structure of Jupiter's upper atmosphere: Predictions for Galileo. *J. Geophys. Res.* **101**, 2149-2161.

Young, L. A., R. V. Yelle, R. Young, A. Seiff, and D. B. Kirk 1997. Gravity waves in Jupiter's thermosphere. *Science* **276**, 108-111.

Young, L. A., R. V. Yelle, R. Young, A. Seiff, and D. B. Kirk 1998a. Dynamics of Jupiter's upper and middle atmosphere from the Atmospheric Structure Instrument on the Galileo probe. *EOS* **79**, S200.

Young, L. A., R. V. Yelle, and R. E. Young 1998b. Can gravity waves heat Jupiter's thermosphere? *Bull. Amer. Astron. Soc.* 30. 1075.

Zharkov, V. N., and V. P. Trubitsyn 1978. *Physics of Planetary Interiors*. Tucson.

THESIS PROCESSING SLIP

FIXED FIELD: ill. _____ name _____

index _____ biblio _____

▶ COPIES: (Archives) (Lindgren) Aero Dewey Eng Hum Music Rotch Science

TITLE VARIES: ▶☐ _____

NAME VARIES: ▶☐ _____

IMPRINT: (COPYRIGHT) _____

▶ COLLATION: 230 p

▶ ADD: DEGREE: _____ ▶ DEPT.: _____

SUPERVISORS: _____

S:

cat'r: _____ date: _____ page: 195

EHPS

1999 ▶ DEGREE: Ph.D.

FAUST, Jeffrey Alan